Atomistic Simulation of Strength and Deformation of Ceramic Materials

by

Dongyi Liao

Submitted to the Department of Nuclear Engineering
in partial fulfillment of the requirements for the degree of

Doctor of Philosophy

at the

MASSACHUSETTS INSTITUTE OF TECHNOLOGY
[September 2001]
August 2001

Author .....
Department of Nuclear Engineering
August 3, 2001

Certified by .....
Sidney Yip
Professor, Department of Nulcear Engineering
Thesis Supervisor

Certified by .....
Sow-Hsin Chen
Professor, Department of Nuclear Engineering
Thesis Reader

Accepted by .....
Jeffery A. Coderre
Department Committee on Graduate Students

Atomistic Simulation of Strength and Deformation of Ceramic Materials

by

Dongyi Liao

Submitted to the Department of Nuclear Engineering
on August 3, 2001, in partial fulfillment of the
requirements for the degree of
Doctor of Philosophy

Abstract

This thesis is a study of atomistic measures of strength and deformation of ceramic materials, utilizing molecular dynamics (MD) simulation that incorporates newly developed theoretical models and computational algorithms to probe the microstructural effects in crystalline, amorphous, and nanocrystalline media. Specific issues of a materials property or mechanics of materials nature are addressed in the context of characterizing the limits to strength and mechanisms of structural failure in two physically rather different model ceramics, SiO_2 described by pairwise ionic interactions and ZrC with many-body covalent interactions. These range from stress-strain responses to various applied loading, determination of fracture toughness, structural relaxation effects, to scaling with grain size. Additionally, a study of the thermal conductivity of ZrC is presented. On the computational side, thesis contributions consist of improved MD algorithms for finding neighbors and integrating the Newton's equations of motion, extension of Ewald summation to a binary ionic lattice for phonon dispersion, elastic constant, and heat current calculations, and a stand-alone scheme for coupled MD-continuum simulations based on domain decomposition and control feedback.

The onset of structural instability in MD simulation of an initially defect-free lattice gives not only the theoretical or ideal strength of the deforming material, but also the mode of deformation and details of the structural defects nucleated afterwards. This provides a systematic basis for determining the effects of temperature on mechanical response, and stoichiometry effects in the case of carbon vacancies in ZrC_{1-x}. In tensile deformation of quartz, the structural transition from α to β phase is observed and analyzed using a pseudo-critical phase transition model, leading to a new interpretation of the structure of the β-quartz. In uniaxial compression of α-quartz a local process of nucleation and growth of disordering is observed which appears to be distinct from the essentially homogeneous crystal-to-amorphous transformation that is well known to occur under hydrostatic compression. This finding also leads to a new interpretation of plastic deformation experiments.

Fracture toughness is studied by introducing a pre-existing nanocrack in the simu-

lations and following the details of crack tip extension under mode I loading. Simulations are shown to be quite consistent with the Griffith model in elementary fracture mechanics, confirming on the one hand the brittle nature of these two ceramics while also revealing the effects of surface relaxation, energy dissipation, and surface energy at the atomistic level. Similarly, simulations performed with initial structures with microstructural disorder, in the form of prepared amorphous and nanocrystalline specimens, also lead to new results pointing to the particular mechanisms, void nucleation and growth as well as strain-rate dependence in structural failure of an amorphous specimen, and grain-boundary sliding in shear deformation in very fine-grained nanocrystals.

Taken together the thesis results demonstrate the feasibility and utility of the investigation of thermal and mechanical behavior of binary solids at the atomistic level. It is hoped that they also provide a quantitative basis for future work generally in the direction of delineating the effects of more complex and physically relevant microstructures, and specifically towards the multiscale modeling of interfacial fracture and high-temperature creep.

Thesis Supervisor: Sidney Yip
Title: Professor, Department of Nulcear Engineering

Acknowledgments

I dedicate this thesis to my mentor Professor Sidney Yip, for his patience toward my immaturity, for his support to my every step, for his encouragement on my every small progress, for his nourishment to my growth, for his knowledge and wisdom that provide a broad base for my research... I can never thank him enough.

I want to thank my thesis committee members, Professor Sow-Hsin Chen, Professor Linn Hobbs and Dr. Richard Lanza. Their support, understanding and guidance during my thesis preparation are invaluable.

I also want to thank my group members: Vasily, Lisa, Justo, JuLi, Wei, Elton, Joshua, Maurice, Gen, Tanya, Sundar, Manabu, Dimitris, Antonino, Dongsheng, Tin... I learned a lot from working and talking with each and every of them.

I would like to acknowledge my sponsors, Air Force Office of Scientific Research, Sandia National Laboratory and Knolls Atomic Power Laboratory. I am thankful for the computing facilities provided by Hondar R&D North America and Boston University Scientific Computing Facility, most of my research are conducted on the supercomputers provided by them.

Lastly, I must thank Lina, she is a constant source of my energy.

Contents

List of Figures

List of Tables

Chapter 1

Introduction

1.1 Background and Motivation

Strength and deformation have always been among the key issues in materials applications. While mechanics of deformation is of course a well developed subject in continuum elasticity, there exists a class of irreversible processes associated with stress-induced structural instability which are not understood at the molecular level. Quite often these processes involve microstructural features such as a crack or the disorder associated with an amorphous or interfacial region. In order to gain fundamental insight to how individual microstructural processes influence the strength of materials, two conditions need to be satisfied. One is the availability of a sufficiently robust interatomic potential model describing the chemical bonding in the material of interest. The other is a suitably developed methodology where the potential model can be applied to first simulate the deformation processes under well characterized conditions, and then to analyze the atomic-level details associated with the observed stress-strain response. This thesis is primarily concerned with the latter challenge, specifically in the context of studying the mechanical behavior of ceramics at finite strain and high temperatures.

Ceramics materials[1] are known for their high strength[2] and outstandingly high melting points. However, their brittleness renders them unsuitable for many structural applications. Designing tough ceramics requires intimate understandings of the

rupturing process down to atomistic scale. New developments in material processing such as nanophase materials pose more challenge in understanding strength and deformation processes. Taking two physically rather different ceramics, SiO_2 and ZrC for case studies, this thesis tries to address the problems of understanding their mechanical behavior by combining simulation results with basic models in solid mechanics and materials science

Molecular dynamics (MD) is an atomistic simulation[3, 4] technique which requires, as its most essential input, a prescribed interatomic interaction potential[5, 6]. Once the potential is specified, MD can be used to probe deformation processes that occur quickly (picoseconds to nanoseconds) and locally (angstroms to tens of nanometers) in response to arbitrary but well-defined loading conditions, and to obtain details of the corresponding microstructural evolutions that are not accessible to experiments. MD simulaion is the methodology with which we intend to achieve the goals of this thesis.

To model SiO_2 we have adopted the widely used pairwise ionic interaction potential developed by van Beest, Kramer and van Santen(BKS)[7]. Based on *ab initio* local force field calculations as well as bulk elastic properties, the model is proven to be suitable for mechanical properties in several different polymorphic phases[8]. Through ten years of existance, it has been used in study of pressure induced phase transformations[9, 10, 11], amorphization[12, 13, 14, 15, 16] and melting[17] of crystals as well as the amorphous phase[18]. In case of ZrC, a new many-body potential has been developed recently by Ju Li[19]. As demonstrated by an extensive validation study of thermal and mechanical properties[20, 21], the model accurately characterizes the nature of Zr-C interactions. It is considered to give meaningful results pertaining to strength and deformation.

For both materials we therefore expect them to be applicable to the structural stability studies in this work.

Through a series of technique developments and applications to strength determination we will demonstrate the feasibility and utility of combining MD simulations with models of deformation mechanisms.

Strength and Deformation of Crystals

Theoretical strength of a material can be defined in terms of the maximum elastic deformation of perfect crystals. It is closely related to the breaking strength of atomic bonding in the material. Theoretical strength is also the upper limit of strength, providing a reference value with which to assess the effects of microstructures in the material which generally cause the strength to be reduced. Because it pertains only to the defect-free material (a crystal lattice), theoretical strength can be accurately calculated from atomistic simulations. Table.1.1 compares the calculated tensile strength of three ceramic materials. Indeed the perfect single crystal states of all three materials can sustain the largest elastic deformation possible and therefore set the upper limit of strength.

		SiO_2	ZrC	SiC[1]
crystal (tension)	hydrostatic	32(0.14)	30(0.10)	38(0.15)
	uniaxial	41(0.26)$\langle 1\bar{1}00\rangle$	28(0.18)$\langle 100\rangle$	72(0.31)$\langle 0001\rangle$
		59(0.35)$\langle 0001\rangle$	49(0.18)$\langle 111\rangle$	
amorphous (tension)	hydrostatic	7(0.12)		22(0.10)
	uniaxial	13(0.23)		26(0.20)
nanocrystal (tension)	hydrostatic			20
	uniaxial		7.5	

[1] Data taken from[19]

Table 1.1: Calculated tensile strength of different ceramic materials from atomistic models, all at 300°K. Values shown are critical stress [GPa] and in parenthesis critical strain if applicable. Uniaxial tension results for crystals are marked with the direction tensile stress is applied.

With direct hydrostatic tension simulation of ZrC, the study of the theoretical strength reveals a changing of failure mechanism from low temperature to high temperature. The low temperature ZrC crystal fails by cleavage through its $\{100\}$ planes while high temperature ZrC cavitates accompanied by plastic deformations.

While simulation observations help to identify failure mechanisms, the external loading conditions that induce instability can be predicted by theories. In 1940, Born[22] proposed the necessary condition for lattice stability, stating that the elastic

constant tensor C_{ijkl} must be positive definite for any stable crystal lattice. Born's stability conditions have since been extended and used in several atomistic simulation studies[23, 24]. These criteria are able to describe structural instabilities arising from homogeneous deformations at long wavelengths. Instability also can be triggered by vibrational modes at finite wavelengths, namely, soft phonons. From the lattice dynamical perspective, Born's criteria correspond to only the Γ point phonons.

The phonon dispersion relations can be obtained from both experiments and simulations. Modeled by partially ionic interactions, the optical phonon dispersion curves of SiO_2 is discontinuous at Γ point, known as LO-TO splitting[25]. This is observed in a study of failure modes in this thesis, where the full phonon dispersion calculation are conducted. The phonon curves obtained from simulations are compared with experimental neutron scattering measurements[26, 27] and used to predict the soft modes under different external mechanical loadings.

In the hydrostatic tension study of quartz, the α to β phase transition is observed to be induced by tension as well as by heat. After discovered in 1889[28], the quartz α to β phase transition is put under various experimental examination. These are well summarized in a review by Dolino[29]. First carried out by Tsuneyuki[30], the atomistic simulation study gives a picture of β-quartz as a disordered coexistance of two different α-quartz states. This is in contradiction with later hard-mode spectroscopy experiment[31]. In this thesis, a "pseudo-critical" transition model, arises from an Ising spin system coupled to lattice vibrations[32], is applied to both the simulation and experiments. The controversy is resolved by attributing the overestimate of the temperature range where disordered β phase observed in simulation to the inadequacy of the interaction potential used. Using experimental data, the "pseudo-critical" model predicts a disordered β-phase to exist only in a range of 6°K, matching well with the observed incommensurate phase.

Atomistic Simulation of Brittle Fracture

When cracks are present, the strength of a brittle solid can be reduced greatly. The reduction of strength is due to the stress concentration around the crack tips. By

creating a crack in a single crystal and applying a load in incremental steps, crack extension can be studied directly and systematically by molecular dynamics simulation. Although it seems to be straightforward, the direct simulation of crack extension in MD is a non-trivial task. The computational power required for this was unthinkable just several years ago. Thanks to the rapid growth of computer technology, the study can now be carried out with moderate effort. The recent availability of direct fracture simulation poses unique challenges and opportunities. With the system size significantly increased, several simulation techniques developed in 1960s and 1970s need to be re-examined. Among the methodology developments presented in the thesis, the Verlet's neighbor finding algorithm[33] and its later developments[34, 35] have been greatly improved by more sophisticated book-keeping algorithm. The predictor-correct integration scheme[36] is taken to higher order accuracy to fully utilize the modern computer's numerical power. Parallel computing is an indispensable tool, without it large scale simulation would be impossible. The considerations in writing a parallel MD program are briefly described in Appendix B.

With the tools developed and readily at hand, we have studied the crack extension problem for both SiO_2 and ZrC. The quartz crystal is found to be brittle with respect to crack extension even close to melting. This is compatible with the experimental observations of "dry" quartz[37]. Due to the computational power requirements, little previous study of SiO_2 fracture can be found except for the preliminary results reported by Simmons *et al.*[38, 39].

In 1920, Griffith[40] proposed a necessary condition for crack extension in a brittle material. It states that without dissipation, the energy released by crack extension must be equal to the energy used to create the new fracture surface. In a planar strain mode I (uniaxial tensile) loading situation, the critical tensile stress σ_c which must act perpendicular to the crack to cause it to propagate can be expressed in terms of crack half-length c, surface energy γ, Poisson's ratio ν and Young's modulus E:

$$\sigma_c = \sqrt{\frac{2E\gamma}{(1-\nu^2)\pi c}} \tag{1.1}$$

In fracture mechanics[41], based on linear elasticity, the stress field of near crack tip can be expressed by stress intensity factors K_{I}, K_{II} and K_{III}

$$\sigma = \frac{K_{\mathrm{I}}}{\sqrt{2\pi r}} f^{\mathrm{I}}(\theta) + \frac{K_{\mathrm{II}}}{\sqrt{2\pi r}} f^{\mathrm{II}}(\theta) + \frac{K_{\mathrm{III}}}{\sqrt{2\pi r}} f^{\mathrm{III}}(\theta) \tag{1.2}$$

In turn, the stress intensity factors can be related to an externally applied stress at "infinity". In the case of planar strain mode I loading, we have

$$K_{\mathrm{I}} = \sigma\sqrt{\pi c} \tag{1.3}$$

The critical stress intensity factor that initiates the crack extension is an inherent material property that does not depend on loading conditions. This can be seen by equating (1.1) and (1.3):

$$K_{\mathrm{Ic}} = \sqrt{2E\gamma/(1-\nu^2)} \tag{1.4}$$

If the critical stress intensity factor K_{Ic} is obtained through direct tensile loading, the Griffith criterion can be verified by (1.4). The verification of Griffith is carried out in this thesis for both SiO_2 and ZrC. In the case of SiO_2, the fracture toughness predicted by (1.4) agrees closely with experiment[42]; the higher fracture toughness derived from direct simulation of crack extension is the result of dissipation originated from surface relaxation. In the case of ZrC, the fracture toughness derived from direct simulation matches the fracture mechanics prediction. Due to the lack of experimental measurements of ZrC fracture toughness, the connection to actual material is made indirectly through a comparison with $TiC_{0.96}$ indentation measurement[43]

Plastic Deformations

Plastic deformation is an irreversible structural change of the material which can be induced by external loading. It determines the lower limit of material strength. Plastic deformation denotes a collection of very different processes usually having very different underlying mechanisms and observable behavior. Among them, crystal compressive failure, amorphous tensile fracture and nanocrystal shear strength are

the three topics that will be studied in detail in the thesis.

As one of most abundant minerals in earth mantle, SiO_2 and its high pressure properties are of great interest to geophysicts. Recently, pressure induced structural transformation and amorphization has been the focus of both experiments[44, 45] and simulations[17, 46, 14]. Most of the simulation studies deal with the phase transformations of SiO_2 under hydrostatic compressive loading, while there are extensive uniaxial compression experimental results[47, 48, 49, 50]. Using a small system ($N = 576$), the uniaxial compression simulation performed by us gives compressive failure by amorphization, confirming similar processes reported by hydrostatic compression simulations. In a somewhat larger study of $N = 1152$ particles, the uniaxial compressive failure occurs at the same external loading but in contrast to the homogeneous amorphization reported in hydrostatic simulations, a new nucleation and growth mechanism is observed. The uniaxial compressive failure first nucleates from the structural disordering in a thin layer perpendicular to the compression direction; then the disordered layer widens and eventually takes over the whole system. With an even larger ($N = 4320$) sample with free surfaces, the layered compressive failure is confirmed. Relating to existing experiments[48], our finding may have implications to the problem of crack extension parallel to compressive loading planes[51], which can not be explained by the Griffith fracture criterion.

In contrast to single crystals, glass has quite different mechanical properties. Lacking an ordered structure, amorphous materials are much less understood from a theoretical point of view, requiring more attention from experiments and simulations. The slow relaxation processes inherent in glassy materials is an issue which has not been addressed extensively in atomistic modeling. In this thesis, we will initiate a study of strain-rate effects. With powerful supercomputers, we are able to study much slower loading than previous simulations of for silica glass[38, 39]. Although still unrealistically high compared to laboratory experiments, our "slow" tension simulation of silica glass gives a converged stress-strain response independent of strain-rate. The maximum tensile strength observed in simulation is now in line with measurements[52, 53]. Using full atomistic information available from simulations, the characteristic stress-

strain response is separated into four stages of deformation processes: elastic, plastic by void nucleation, plastic by void growth/coalescence and fraturing. The understanding of deformation mechanism will help further multiscale modeling efforts toward materials design.

New nanocrystalline materials are popular in many applications for their superior mechanical properties such as enhanced hardness compared with ordinary polycrystals. It is observed in simulation[54] that the conventional Hall-Petch[55, 56] effect, which refers to the fact that strength or hardness of a polycrystalline material increases as the grain size decreases, is reversed in nanocrystalline metals. The controversy still exists concering whether the reverse Hall-Petch effect in nanocrystals and the conventional Hall-Petch behavior in micro-sized polycrystals can be linked by a continuous change in grain size. If so, the strongest grain size[57] should be in range of tens of nanometers. The controversy would be resolved if a single model describing the entire range including the cross-over region could be established. As a first step, simulation of nanocrystal ZrC under shear in this thesis reveals a reverse Hall-Petch effect in nanocrystaline ceramics, with similar grain sliding mechnisms as found in metals[54]. This suggests that the reverse Hall-Petch effect in nanocrystals may be inherent to any grain-sliding process rather than being specific to particular materials.

1.2 Thesis Problem and Scope

This thesis is concerned with the determination of strengths of ceramics and the study of deformation mechanisms, both strongly dependent on the particular microstructural features present in the material. Theoretical strength, the upper limit in the resistance to structural instability, is determined by molecular dynamics simulation in which a defect-free crystal (microstructureless) is subjected to a prescribed external stress. This approach is also useful for assessing the effects of temperature and stoichiometry. Fracture strength, conventionally expressed through fracture toughness, is obtained from the critical stress necessary to induce the extension of a pre-existing

crack. Results of this direct determination match well with an indirect estimate based on the Griffith criterion for brittle cleavage. The comparison also reveals the effects of surface relaxation during crack tip extension and a bias toward fracture on planes with low surface energy. Similar simulations carried out on prepared amorphous and nanocrystalline specimens give results showing plastic deformation arising from structural relaxation in disordered media and small-scale grain boundary sliding events.

Besides addressing materials issues, contributions of an algorithmic and computational nature are presented in this work. Regarding MD simulation, improved methods for finding neighbors and integrating the governing Newton's equations of motion have been developed, along with extension of the Ewald summation to more complicated properties calculations. Regarding a key aspect of multiscale modeling, that of coupling atomistic and continuum simulations, a novel domain decomposition method which incorporates control feedback is proposed.

The thesis is organized as follows. In Chap.2 four new developments in the theory and methodology of atomistic simulation are presented. These form a basis for the later studies. The fast neighbor list implementation (Sec.2.1) and higher order numerical integration scheme (Sec.2.2) arise from the vast improvements of computer technology since the origin of atomistic simulations. These two topics deal how to fully utilize the modern computer power and technology. The coupling between fluid simulation and hydrodynamics (Sec.2.3) shows a new way of extracting information as well as applying controls to the simulations. The Ewald formulations for ionic systems (Sec.2.4) lays the necessary base for the simulation of SiO2, which has a significant part of ionic interactions in its model. Although the Ewald construction scheme was proposed as early as 1921, the octupole moment derivation presented in the thesis has not been reported in the literature; it enables fast calculations of elastic constants. It is also helpful to give explicitly the Ewald formulation and discussions relevant to simulations, which are hard to gather from other sources.

Chap.3 presents the strength and deformation study of SiO2. Starting from background and introduction of the potential model used in this thesis (Sec.3.1), the

theoretical strength is studied by direct stress-strain response simulation (Sec.3.2). Stability study is carried out by phonon dispersion calculations (Sec.3.3). α-quartz to β-quartz phase transition is studied under changing temperatures and pressure (Sec.3.4), a model of Ising-spin like system coupled to a compressible lattice is used to explain the transition. Both the order-parameter curves obtained from atomistic simulations and experiments can be fitted nicely into the model with the same exponent. Following the atomic trajectories in simulation, we are able to understand the structural details of the transition. In Sec.3.5, a detailed look into quartz under uniaxial compression reveals a new amorphization mechanism where a thin layer of amorphous zone perpendicular to the compressive direction nucleates and then grows thicker as more and more compressive strains are imposed. The nucleation and growth mechanism is verified under different loading orientation and boundary conditions in simulation. Experimental evidence of similar (yet much bigger in length scale) amorphous layer perpendicular to compressive direction can be found, with the maximum yielding stress comparable to the simulation results. In Sec.3.6, samples of quartz with pre-existing elliptic crack are studied under uniaxial tension. From the critical stress and crack length in the simulation the calculated stress intensity factor is in line with experimental values. The Griffith criterion[40] of brittle crack propagation can also be verified with modest rate of dissipation. Simulations ranging from room temperature up to close melting all shows brittle crack propagation, which is consistent with experiments on "dry" quartz. Future investigation of effects of water molecules near crack tip could lead to the understanding of hydrolytic weakening problem[58]. In Sec.3.7 the study of tensile strength of amorphous silica, a qualitatively different deformation mechanism from crystalline phases is identified with four distinctive stages. In the first stage the material responds purely elastically, in the second stage elastic response are accompanied by void nucleation. In the third stage void nucleation is taken over by void growth and coalescence. In the last stage the material fails through separation by percolated voids.

In Chap.4, strength and deformation of ZrC is presented. After introducing the new many body interaction model for ZrC (Sec.4.1), the compositional and temper-

ature effects on theoretical strength is studied (Sec.4.2). In a separate study of ZrC thermal conductivity (Sec.4.3), drastic microstructure effects on the phonon heat carriers of ZrC is observed. We conclude that heat is conducted largely by the electrons in ZrC crystals. Single crystal ZrC with pre-existing crack on different planes is studied (Sec.4.4). The Griffith criterion and linear elasticity can accurately predict the propagation of crack tip with the help of surface energy and elastic constants. A series of nanocrystal samples with different grain sizes are subjected to shear (Sec4.5); the observed reverse Hall-Petch effect of grain size dependence of critical stress is similar to results of Schiøzt *et al.*[54]. Although the issue is still controversial, our results suggest that the reverse Hall-Petch effects in nanocrystals are inherent to any grain-sliding process rather than being specific to any particular material.

Chapter 2

Methodologies of MD simulation

2.1 Fast Neighbor List Implementation

Conventional methods of enumerating neighbor in molecular dynamics are re-examined in the context of modern simulation tasks. A new incremental updating scheme of neighbor list maintenance is proposed and compared to the widely used Verlet-cell-list method. The way to deal with shape varying simulation cell in Parrinello and Rahman's NTP ensemble simulation is discussed.

2.1.1 Introduction

Neighbor list is a book-keeping method to accelerate molecular dynamics or Monte Carlo simulations. The idea of the neighbor list is to record all the possible neighbors of each atom, so that one does not need to check the whole system when calculating force of interaction. Neighbor list saves time from unnecessary distance calculations, which can be a significant part in many simulations. Clever schemes for keeping neighbor list can reduce the calculation time significantly. If a *cell list* is used, one can reduce the neighbor calculation from $\mathcal{O}(N^2)$ to $\mathcal{O}(N)$. For this reason every MD simulation code contains some kind of neighbor list algorithm.

The first neighbor list algorithm was developed by Verlet[33] in 1967. Verlet's neighbor keeping method lists all the atoms within r_{L} of each atom, and the list is

recalculated every n time steps. Let r_C be the cut-off distance of interaction, roughly speaking, as long as

$$n\bar{v}\Delta t < (r_L - r_C) \tag{2.1}$$

the atoms not on the list will not move into interaction range during the n steps and few error would be made in the simulation. Following Verlet[33], we call the difference between listing range and interaction range the "skin depth" of the neighbor list. It is easily seen that (2.1) does not strictly guarantee correctness, since it only uses average atom velocity $\bar{v}$. To be strict, one has to make sure no atom can move more than half of the "skin depth" of the neighbor list[35].

$$\max(\Delta r) \leq \frac{1}{2}(r_L - r_C) \tag{2.2}$$

In simulations, error can occur only when a pair of atoms come into interaction without being listed as neighbors. As shown in Fig.2-1, an unlisted pair can come into interaction if $r^0_{AB} > r_L$ and $r_{AB} < r_C$. To prevent this, one needs to make sure that:

$$|\Delta r_B - \Delta r_A| < r_L - r_C \tag{2.3}$$

Because A and B are arbitrary atoms and each may move up to Δr_{MAX}, (2.3) reduces to (2.2).

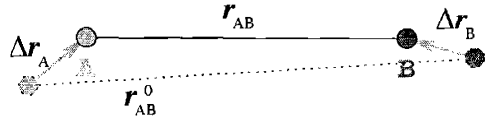

Figure 2-1: Illustration of strict Verlet neighbor list requiring maximum atom displacement less than half the "skin depth".

Various improvements to the original Verlet method are proposed to reduce computational effort, such as the automatic update scheme by Chialvo *et al.*[59]. When strictness of interaction is desired, which is true for most cases, many of these improvements are not applicable. In this section, we will discuss how the strict Verlet

method can be improved by incremental updating the neighbor list.

If the system has N atoms, and each atom has on average m other atoms within its interaction range, then at each step, an MD simulation without any neighbor keeping algorithm needs to compute $\frac{1}{2}N(N-1)$ distances to enumerate all possible interactions. Verlet's neighbor keeping algorithm reduces it to $\frac{1}{2}mN$ at each time step, although it still needs $\frac{1}{2}N(N-1)$ distances calculated when constructing the list. According to Verlet[33], the neighbor list *"cuts the computing time by a factor of the order of 10"*. Still, Verlet's algorithm scales as $\mathcal{O}(N^2)$ when N is large. The essence of Verlet's neighbor algorithms is trading space for time. By storing all the neighbor information that *could* be needed in the near future, one can reduce the time used to enumerate the neighbors. Since in almost all simulations the bottle-neck is indeed the running time rather than space limit, Verlet's method is a step in the right direction.

In 1973 Quentrec *et al.*[34] proposed a method to search the neighbors in $\mathcal{O}(N)$ time. This is achieved by dividing the simulation box into cells, and construct a cell-list, which lists for each cell all the atoms inside it. When the simulation needs to find the neighbors of an atom, it searches all the cells that are within interaction range of the current cell (the cell containing the atom being updated), as shown in Fig.2-2. Constructing cell-list and search neighbors in cells both cost $\mathcal{O}(N)$ time.

Many flavors of the cell-list are implemented for MD simulations. Some choose the cell size to be equal the length of interaction cutoff[1], so that there are only 27 cells (current cell and all the adjacent ones) to consider for any atom[60]. In the original Quentrec *et al.*[34] paper, they took cells so small that only zero or one atoms can be in each cell; this reduces the management of varying length cell-lists to an array of Boolean variables, but excessively small cell size makes the enumeration of cells slow. According to Fincham[61], among all the different implementations, the optimal speed is achieved when the number of particles per cell is about 4.

In many modern MD simulation programs, the Verlet method is used together

[1]Here cell size implies diameter of the largest sphere that can be put into the cell. In the case of rectangular cell, it equals to the shortest edge.

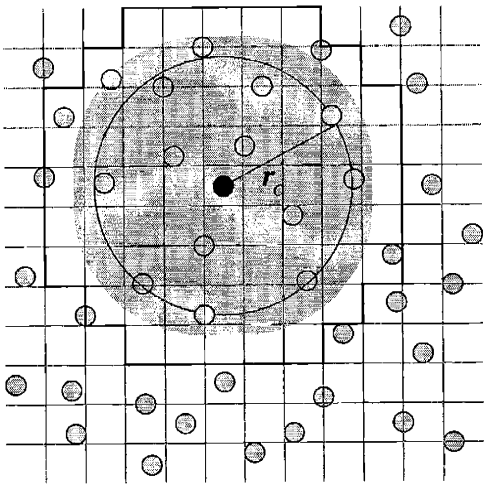

Figure 2-2: Illustration of cell-list method showing all the cells that involved in the neighbor enumeration of an atom. The shaded area represents the region that are within r_L of the *cell* in consideration. All cells in the outlined region needs to be considered when enumerating neighbors for the center atom.

with cell-list method. That is, use Verlet neighbor list at each step; when it is needed to reconstruct the Verlet neighbor list, use a cell-list and collect neighbor information from the cell-list. Combining both Verlet's neighbor list and cell list gives $\mathcal{O}(N)$ time scaling and added performance bonus of Verlet's method. We shall call this the *Verlet-cell-list*(VCL). One thing to notice is, after combining the Verlet list with cell list, because the cells are only accessed when reconstructing Verlet list, the balance discussed in the last paragraph shifted toward bigger cells. Usually, in VCL implementations, cell size is chosen to contain an interaction cutoff so that only 27 cells need be considered. Compared to the conventional Verlet algorithm or the bare cell-list algorithm, VCL performs better in most situations.

In recent years, as the computers become more and more powerful, the system size of typical MD simulations increases significantly. The ability to calculate neighbors quickly is especially important for simulations using relative simple interaction model and millions or more atoms.

Another development is the widely used Parrinello-Rahman's shape varying box scheme[62], which poses new problem for fast neighborlist maintenance.

In this section an efficient scheme of maintaining neighbor list is presented, which can cut the time spent in neighbor list by half when comparing to the Verlet-cell-list approach. With the help of test simulation data, the choice of optimal parameters is considered. Then a way to cope with Parrinello-Rahman's shape varying simulation is introduced followed by various other discussions and possible further developments.

2.1.2 Incremental Verlet Neighbor List

In Verlet's method, the whole neighbor list is reconstructed as soon as *any* atom moves more than Δr_{MAX} from its last updated position. ($\Delta r_{\mathrm{MAX}} = (r_{\mathrm{L}} - r_{\mathrm{C}})/2$) One may ask "Can we update the neighbor list for any individual atom only when it's necessary?" The answer is yes, and by doing so much can be gained.

Naively, in the spirit of Verlet's method, one wants to update neighbor list pertain to any atom that has moved Δr_{MAX} from the place it is last updated, and whenever updating, include all atoms within r_{L}. As in Verlet's methods, for every atom one needs to keep the position when it is last updated. We call this position the *anchor* of an atom. *Anchor* positions are denoted by a superscript ^{A} on the atom positions r_a. There are two ways to do incremental update. When reconstructing the neighbor list of an atom, say atom a, one can either (i) choose to include all the atoms that fall into the range r_{L} within current atom:

$$\text{Include atom } b \text{ if } |\boldsymbol{r}_a - \boldsymbol{r}_b| < r_{\mathrm{L}} \tag{2.4a}$$

or (ii) choose to include all the atoms whose *anchors* fall into the range r_{L} of the current atom. (Note when atom a is being updated, its anchor and its position are the same.)

$$\text{Include atom } b \text{ if } |\boldsymbol{r}_a^A - \boldsymbol{r}_b^A| < r_{\mathrm{L}} \tag{2.4b}$$

In case (i), the atoms will not be updated if it moves within the circle of radius of Δr_{MAX}; thus when an atom is being updated, its neighbors can move up to $2\Delta r_{\mathrm{MAX}}$

since last update event. In light of (2.3), we have:

$$3\Delta r_{\mathrm{MAX}} \leq r_{\mathrm{L}} - r_{\mathrm{C}} \tag{2.5a}$$

Compared to Verlet's condition (2.2), here we have a factor of 3 instead of 2 because each atom is freely moving and neighbor lists for different atoms are updated at different times.

In case (ii), the neighbor list is calculated according to anchor positions, and anchor position will not change unless an update event occurs. This means the anchor position can serve as a *snapshot* of the system; at any time, just like in the conventional Verlet list algorithms, the neighbor list of any atom contains only those atoms whose *anchors* are within r_{L} of the *anchor* of current atom. So, at any time, we can think as if all the *anchors* are the result of one Verlet's neighbor list reconstruction at some early time. In the same picture as the strict Verlet list (see Fig.2-1), we have the condition similar to the original Verlet's

$$2\Delta r_{\mathrm{MAX}} \leq r_{\mathrm{L}} - r_{\mathrm{C}} \tag{2.5b}$$

It is clear that case (ii) is a better way to maintain the neighbor list. It may seem counter-intuitive at first that updating neighbor list with "old" anchored positions could be better than using current ones. The reason is, in case (ii) there is more information on the neighbor list structure than in case (i), because of the *snapshot* described earlier. This additional information enables us to have a more stringent bound on the atom positions. We will see that the concept of *snapshot* for the neighbor list is very useful in shape varying boxes and other situations too. From here on we will take case (ii) to be the chosen method for neighbor list updating.

Similar to the combination of Verlet and cell-list method, we can also use cell-list to achieve $\mathcal{O}(N)$ time scaling. That is, updating an atom only involves checking and maintaining the neighbor lists of atoms that are inside the cells within the cutoff. Because we are using only *anchors* to define neighbors, the cell-list should also be the cell-list of *anchors* instead of real atom positions. This means we only need

to maintain the cell-list once we change the anchor of any atom, which saves time compared to the Verlet-cell-list.

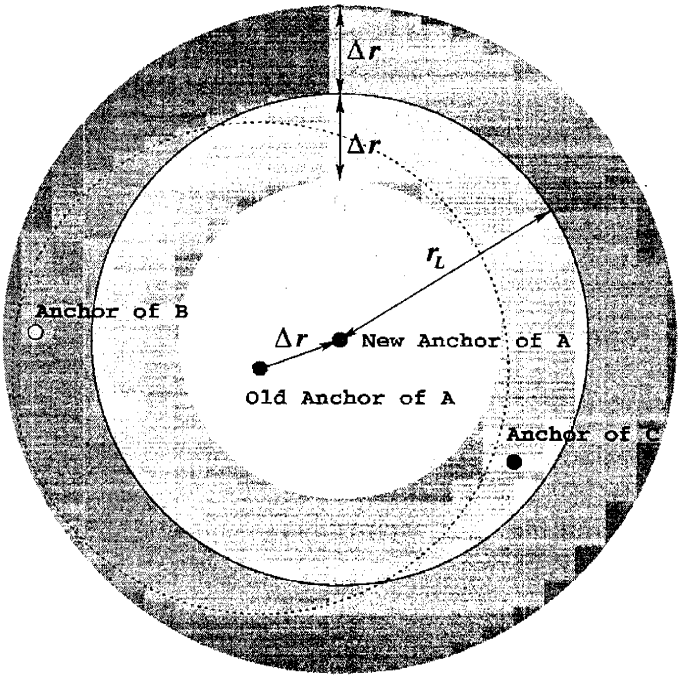

Figure 2-3: Illustration showing the updating of atom A that removes pair A-B and inserts pair A-C. The regions need to consider for insertion and removal of neighbors are shaded.

Contrary to the conventional Verlet method, the new algorithm modifies neighbor lists only when necessary, and when the neighbor list of an atom needs to be modified, its old content is still useful. As shown in Fig.2-3, when atom a is updated, the only atoms that need to be checked are those satisfying the following condition:

$$\begin{aligned} \text{Remove pair } a\text{-}b \text{ if} \quad & r_{\mathrm{L}} < |\boldsymbol{r}_b - \boldsymbol{r}_a| < r_{\mathrm{L}} + \Delta r \\ \text{Insert pair } a\text{-}b \text{ if} \quad & r_{\mathrm{L}} - \Delta r < |\boldsymbol{r}_b - \boldsymbol{r}_a| < r_{\mathrm{L}} \end{aligned} \tag{2.6}$$

Anything else does not need to be changed. Here Δr is the distance between old anchor and new anchor of atom a. According to the rule, update occurs when $\Delta r \geq \Delta r_{\mathrm{MAX}}$. In MD, atoms move continuously, Δr is usually close to Δr_{MAX}. In the case when r_{C} is small, such as in Lennard-Jones Argon, a portion of the time used

to update neighbor list can already be saved. In systems with relatively long-range interactions, such as Coulomb interaction with Ewald summation, the speed gain is of order 10 to 100.

Below is a formal description of the method we have discussed so far:

- In the beginning of simulation, construct the lists:

  1. Choose an optimal parameter Δr_{MAX} according to the interaction potential and density and temperature. Take $r_{\mathrm{L}} = r_{\mathrm{C}} + 2\Delta r_{\mathrm{MAX}}$
  2. Divide the system into cells that contain one r_{L}.
  3. Setup cell-cell list: For each cell create a list of cells that has minimum distance less than r_{L} (there are 27 of them)
  4. Setup cell-atom list: For each cell create a list of all the atoms in the cell.
  5. Set all the anchors to be current atom position
  6. Setup atom-atom list: For each atom, go through the cell-cell list to find all the cells within r_{L}, go through the cell-atom list and list all the atoms within r_{L}.

- During the simulation, if atom a has moved more than Δr_{MAX} from its *anchor*($|\boldsymbol{r}_a - \boldsymbol{r}_a^A| \equiv \Delta r > \Delta r_{\mathrm{MAX}}$), reset its *anchor*.

  1. Check all the atoms that have distance to atom a between r_{L} and $r_{\mathrm{L}} + \Delta r$. If they are listed as neighbors, remove the pair from neighbor list.
  2. Check all the atoms that have distance to atom a between r_{L} and $r_{\mathrm{L}} - \Delta r$. If they are not listed as neighbors, insert the pair into neighbor list.
  3. Update the cell-lists if atom a moved from one cell to another.
  4. Update the anchor position of atom a

To evaluate the difference between the new incremental Verlet-cell-list (`IVL`) and the conventional Verlet-cell-list(`Verlet`), three solid configurations, large ($N = 13500$) medium ($N = 4000$) and small ($N = 864$), are used to test the performance gain of

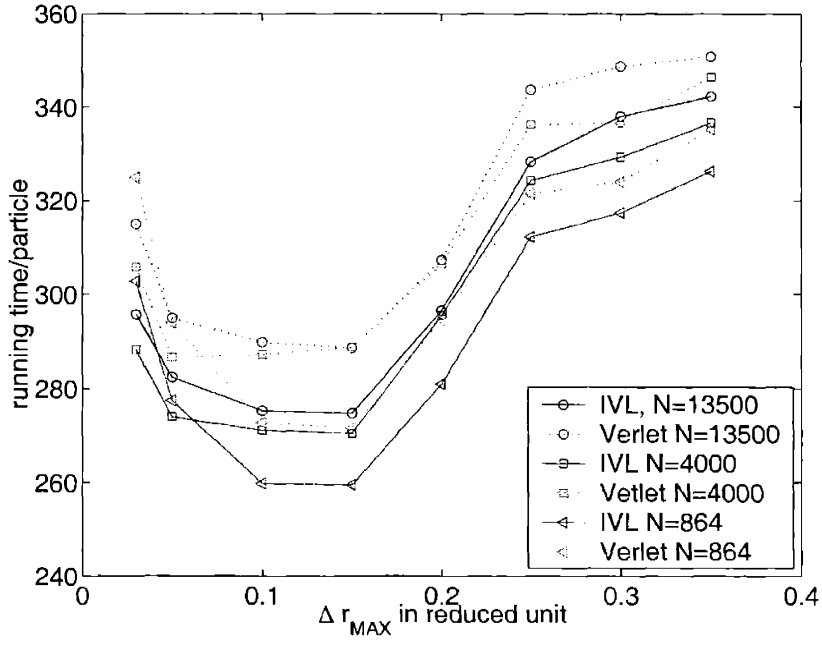

Figure 2-4: Simulation results showing a comparison of different system size between IVL and conventional Verlet-cell neighbor list method. Three Lennard-Jones Argon systems are studied with $N = 13500$, $N = 4000$ and $N = 864$ respectively, all of the system are solid FCC crystals with $T = 60°K$.

IVL over conventional Verlet. Fig.2-4 shows the comparison of running time between IVL and conventional Verlet methods. For an $\mathcal{O}(N)$ method, it is not a trivial gain. In all three systems, the IVL gains 5-10% *total running time*. In all cases, the time spend on neighbor list is more than halved.

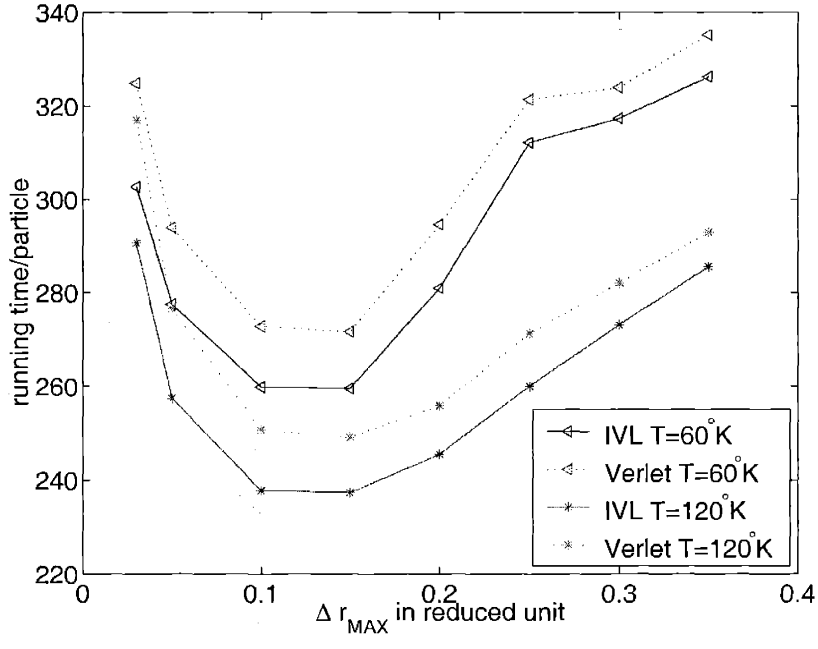

Figure 2-5: Simulation results showing a comparison of solid and liquid systems between IVL and conventional Verlet-cell neighbor list method. Both systems contain 864 atoms, with solid FCC at $T = 60°K$ and liquid at $T = 120°K$.

Fig.2-5 shows the comparison between solid and liquid simulations. A notable feature is that the optimal Δr_{MAX} does not depend much on temperature or density, and it is always the same whether one uses IVL or conventional Verlet.[2]

Fig.2-6 shows the time spent on neighbor enumeration broken down to two parts: time used for neighbor list maintenance and time used for calculating the distance for pair that are out of interaction range.

[2]As a side note, in Verlet's original paper[33], he proposed using $r_{\mathrm{L}} = 3.3$ and $r_{\mathrm{C}} = 2.5$, this gives $\Delta r_{\mathrm{MAX}} = 0.4$, the results shown here imply it is not optimal on modern computers.

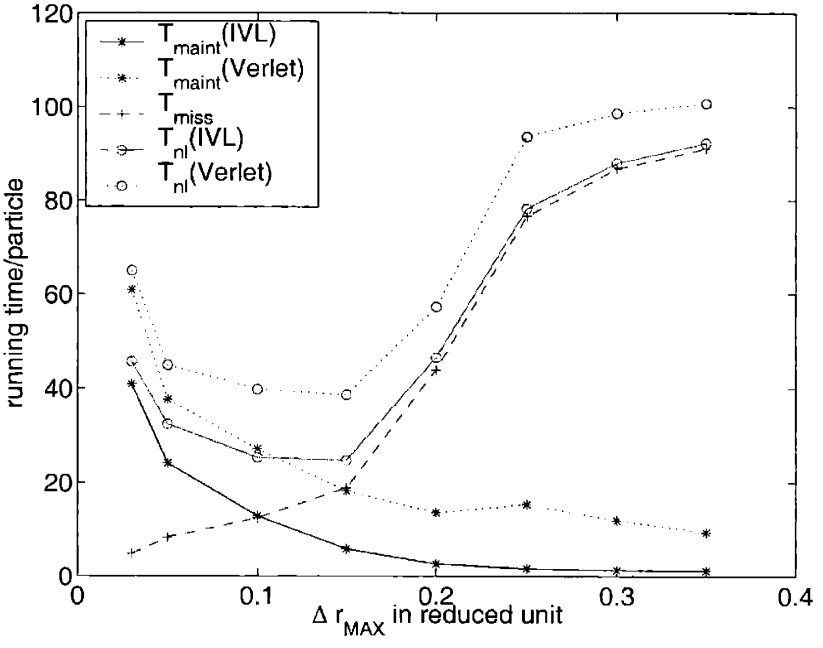

Figure 2-6: Simulation results showing the break down of simulation time spent into neighbor list maintenance time and time spend on neighbors that are out of interaction range (missed neighbor). Both IVL and Verlet are from the big system $N = 135000$.

2.1.3 Neighbor List in Shape Varying Boxes

Since Parrinello and Rahman published the famous NTP ensemble paper[62] in 1981, the application of shape varying box to perform NTP ensemble simulations has been widely adopted. Any useful neighbor list algorithm must be able to deal with the changing simulation box shape. In simulation using a shape varying box, the atom positions are usually represented by the frame matrix $\underline{\underline{h}}$ and internal coordinates $\boldsymbol{s}_a$. The actual position can be expressed as:

$$\boldsymbol{r}_a = \underline{\underline{h}}\boldsymbol{s}_a \tag{2.7}$$

with the frame matrix changing through time. If the frame matrix changed from $\underline{\underline{h}}_0$ to $\underline{\underline{h}}$, any vector $\boldsymbol{r} = \underline{\underline{h}}_0\boldsymbol{s}$ changes to $\boldsymbol{r}' = \underline{\underline{h}}\boldsymbol{s} = \underline{\underline{\kappa}}\boldsymbol{r}$ ($\underline{\underline{\kappa}} \equiv \underline{\underline{h}}\underline{\underline{h}}_0^{-1}$).The distortions $\boldsymbol{r}$ can be bounded by the following limits:

$$\begin{aligned} \max \frac{|\underline{\underline{h}}\boldsymbol{s}|}{|\underline{\underline{h}}_0\boldsymbol{s}|} &= \max \frac{|\underline{\underline{\kappa}}\boldsymbol{r}|}{|\boldsymbol{r}|} = \sqrt{\lambda_{\max}(\underline{\underline{\kappa}}^{\mathrm{T}}\underline{\underline{\kappa}})} \\ \min \frac{|\underline{\underline{h}}\boldsymbol{s}|}{|\underline{\underline{h}}_0\boldsymbol{s}|} &= \min \frac{|\underline{\underline{\kappa}}\boldsymbol{r}|}{|\boldsymbol{r}|} = \sqrt{\lambda_{\min}(\underline{\underline{\kappa}}^{\mathrm{T}}\underline{\underline{\kappa}})} \end{aligned} \tag{2.8}$$

Here $\lambda_{\max}$ and $\lambda_{\min}$ denote the largest and smallest eigenvalue of a matrix. With this knowledge the analysis of neighbor list maintenance criteria can now be carried out.

In the equation of motions of Parrinello-Rahman MD simulations, the frame matrix $\underline{\underline{h}}$ is not treated much differently from the atomic internal coordinates. Similar to the arguments in last section, it is advantageous to have a common frame matrix for all the atom *anchors*, called a *frame anchor* $\underline{\underline{h}}_0$. If the algorithm described in last section is performed under the environment of $\underline{\underline{h}}_0$, the most error one can make is bounded by (2.8). If no atom has moved more than r_{SKIN} from its *anchor* under the measure of $\underline{\underline{h}}_0$, then under the measure of $\underline{\underline{h}}$, if atom a and atom b are not neighbors,

the distance between the two can be bounded:

$$\begin{aligned} |\boldsymbol{r}_a - \boldsymbol{r}_b| &= \left|\underline{\underline{\kappa}}\left[(\boldsymbol{r}_a^0 - \boldsymbol{r}_a^A) - (\boldsymbol{r}_b^0 - \boldsymbol{r}_b^A) + (\boldsymbol{r}_a^A - \boldsymbol{r}_b^A)\right]\right| \\ &> \sqrt{\lambda_{\min}(\underline{\underline{\kappa}}^{\mathrm{T}}\underline{\underline{\kappa}})}\left(|(\boldsymbol{r}_a^A - \boldsymbol{r}_b^A)| - |(\boldsymbol{r}_a - \boldsymbol{r}_a^A)| - |(\boldsymbol{r}_b - \boldsymbol{r}_b^A)|\right) \\ &> (r_{\mathrm{L}} - 2\Delta r_{\mathrm{MAX}})\lambda_{\mathrm{S}} \end{aligned} \tag{2.9}$$

Here λ_{S} is a chosen parameter, so that the neighbor list will be reconstructed as soon as the frame matrix changes so much that

$$\sqrt{\lambda_{\min}(\underline{\underline{\kappa}}^{\mathrm{T}}\underline{\underline{\kappa}})} < \lambda_{\mathrm{S}} \tag{2.10}$$

The neighbor listing criterion changes from (2.5b) to:

$$2\Delta r_{\mathrm{MAX}} \leq r_{\mathrm{L}} - r_{\mathrm{C}}/\lambda_{\mathrm{S}} \tag{2.11}$$

with an additional parameter λ_{S}. Optimal λ_{S} is determined by simulation conditions, *e.g.* one would like to choose a looser λ_{S} in compression simulations and a tighter λ_{S} in tension. In static state simulations, the frame matrix usually moves slowly, making the optimal λ_{S} quite close to unity. A typical choice of λ_{S} is 0.99.

The parameter λ_{S} only constrains the frame matrix from shrinking. Expanding a frame matrix will never violate the integrity of any constructed neighbor list, but it will make the neighbor list contain more and more non-interacting pairs, which in turn cause the simulation to run slower. The optimal performance can be obtained by introducing a similar upper limit of distortion λ_{L} and reconstruct the neighbor list as soon as

$$\sqrt{\lambda_{\max}(\underline{\underline{\kappa}}^{\mathrm{T}}\underline{\underline{\kappa}})} > \lambda_{\mathrm{L}} \tag{2.12}$$

Optimal λ_{L} also depends on simulation conditions, In equilibrium simulation, a value of $\lambda_{\mathrm{L}} = 1/\lambda_{\mathrm{S}}$ is recommended.

2.1.4 Discussion

The reason a neighbor list can speed up the interaction evaluation stems from two facts. First is that interactions are short ranged. If any given atom only interacts with a small number of other atoms independent of the total number of particles, there is no reason to check more than a localized area. This is the idea underlying the cell-list algorithms. With cell-lists, only pairs of atoms that are close enough need to be checked.

The second fact is the nature of continuous motion of atoms. If two atoms interact in the previous timestep, they are probably not too far away this timestep. This fact enables the Verlet neighbor list, which keeps slightly more atoms than actually needed to be valid for longer time.

In the conventional neighbor finding algorithms such as Verlet-cell-list, the two facts are used separately. By incremental maintenance of both the Verlet list and cell list, IVL gains efficiency over conventional Verlet-cell neighbor list by combining and fully utilizing both facts of MD simulation.

The immense computational power required by many large scale MD simulations is usually attained through parallelization. A large portion of overhead of parallelization comes from the neighbor list maintenance and force calculation. The incremental updating feature of IVL can reduce the need of unnecessary communication between processors and help to evenly distribute the load in neighbor list maintenance throughout the course of simulation.

2.2 Higher Order Numerical Integration

2.2.1 Introduction

In 1971 Gear discussed in his book[36] a flavor of predictor-corrector numerical approach to solve the initial value problems of ordinary differential equations. It is widely adopted in the MD simulation to solve the Newton's equation of motion. The Gear's algorithm utilizes higher order derivatives and achieves high accuracy with lit-

tle additional computational cost. The most widely used Gear's method is the 6-value Gear's predictor-corrector, which can achieve 6th-order accuracy ($\mathcal{O}(\Delta t^6)$) if interaction does not depend on atom momenta. The 6-value Gear's predictor-corrector approaches the numerical cutoff error for single precision floating point number, thus can be considered the "optimal" order for MD simulations done with single precision arithmetics. The computational power has increased significantly since then; in modern times, most MD simulations are conducted with double precision, making higher order Gear's predictor-corrector necessary.

In this section we briefly discuss the way to do numerical integration with Gear's predictor-corrector methods; the first few orders are given explicitly and a comparison is made with the symplectic integration methods, which is usually used in astrophysics calculations.

2.2.2 Higher Order Gear's Predictor Corrector

For an N-th order m-th derivative predictor-corrector method, the procedure to calculate is: **Predictor**

$$\begin{pmatrix} r_0^P(t+\delta t) \\ r_1^P(t+\delta t) \\ r_2^P(t+\delta t) \\ \cdots \\ r_N^P(t+\delta t) \end{pmatrix} = \begin{pmatrix} 1 & 1 & 1 & \cdots \\ 0 & 1 & 2 & \cdots \\ 0 & 0 & 1 & \cdots \\ \cdots & \cdots & \cdots & \cdots \\ \cdots & \cdots & \cdots & \cdots \end{pmatrix} \begin{pmatrix} r_0(t) \\ r_1(t) \\ r_2(t) \\ \cdots \\ r_N(t) \end{pmatrix} \tag{2.13}$$

Corrector

$$\Delta R_m(t+\delta t) = r_m(t+\delta t) - \hat{r}_m(t+\delta t) \tag{2.14}$$

$$\begin{pmatrix} r_0^C(t+\delta t) \\ r_1^C(t+\delta t) \\ r_2^C(t+\delta t) \\ \cdots \\ r_N^C(t+\delta t) \end{pmatrix} = \begin{pmatrix} r_0^P(t+\delta t) \\ r_1^P(t+\delta t) \\ r_2^P(t+\delta t) \\ \cdots \\ r_N^P(t+\delta t) \end{pmatrix} + \begin{pmatrix} C_0^m \\ C_1^m \\ C_2^m \\ \cdots \\ C_N^m \end{pmatrix} \Delta R_m(t+\delta t) \qquad (2.15)$$

There is a brief discussion in Gear's book on how to determine the coefficients of arbitrary order. The procedure involves choosing the coefficients to fix all the eigen values of the iteration matrix to be zero, which reduces to a set of linear equations and can be easily solved. Table.2.1 gives a list of coefficients at higher order.

p	k	C_{kl}^p											
2	4	$\frac{1}{6}$	$\frac{5}{6}$	1	$\frac{1}{3}$								
2	6	$\frac{3}{20}$	$\frac{251}{360}$	1	$\frac{11}{18}$	$\frac{1}{6}$	$\frac{1}{60}$						
2	8	$\frac{275}{2016}$	$\frac{19087}{30240}$	1	$\frac{137}{180}$	$\frac{5}{16}$	$\frac{17}{240}$	$\frac{1}{120}$	$\frac{1}{2520}$				
2	10	$\frac{8183}{64800}$	$\frac{1070017}{1814400}$	1	$\frac{121}{140}$	$\frac{469}{1080}$	$\frac{967}{7200}$	$\frac{7}{270}$	$\frac{23}{7560}$	$\frac{1}{5040}$	$\frac{1}{181440}$		
2	12	$\frac{4671}{39424}$	$\frac{26842253}{47900160}$	1	$\frac{7129}{7560}$	$\frac{6515}{12096}$	$\frac{4523}{22680}$	$\frac{19}{384}$	$\frac{3013}{362880}$	$\frac{5}{5376}$	$\frac{29}{435456}$	$\frac{1}{362880}$	$\frac{1}{19958400}$

Table 2.1: Coefficients for even orders Gear's Predictor-Corrector

2.2.3 Comparison and Discussion

Fig.2-7 and Fig.2-8 shows the energy and position error of a one body problem, where a particle is subjected to a $1/r^2$ attractive central force field. The analytic solution gives a perfect periodic elliptical trajectory. Applying different numerical integration scheme, their relative merits can be compared.

A set of higher order symplectic integration algorithms are chosen to compare with the Gear's algorithm[63, 64, 65].

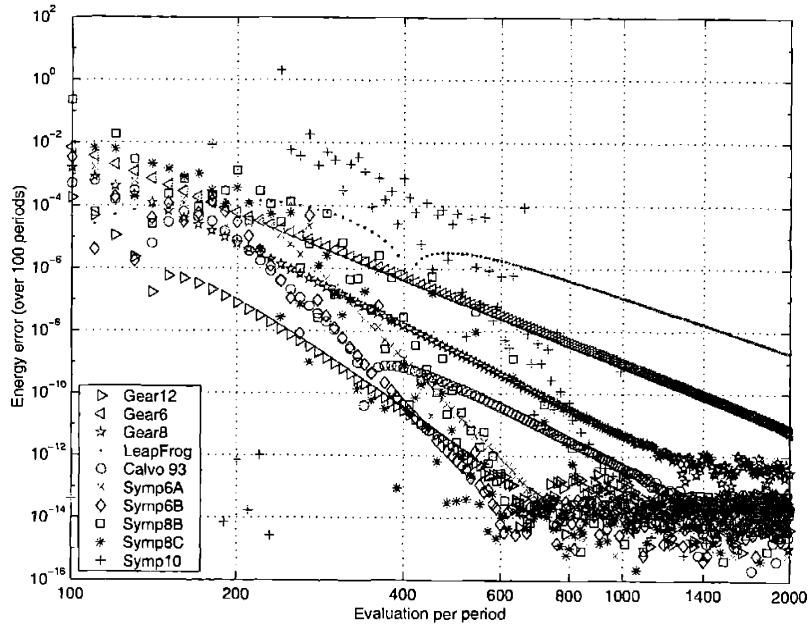

Figure 2-7: Error of energy of different integration schemes after 100 periods

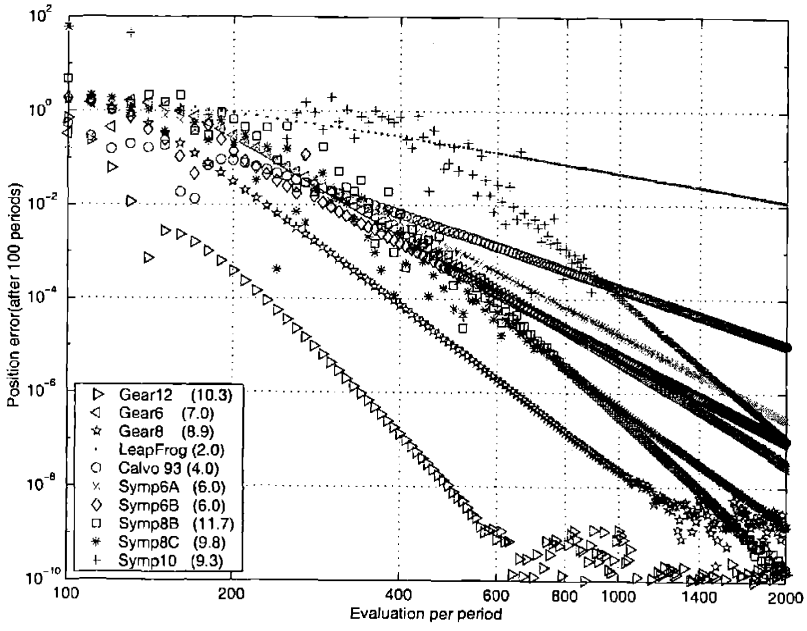

Figure 2-8: Error of position of different integration schemes after 100 periods. In the parenthesis is the calculated order of each integration scheme.

2.3 Coupling Molecular Dynamics with Continuum in Fluid Simulations

In this section we formulate a method for coupling atomistic and continuum simulations in the framework of the classical alternating Schwarz method with domain decomposition. Our approach combines the thermodynamic field estimator, which acts to extract the macroscopic field from the results of atomistic simulation, with a novel procedure, optimal in the sense of least disturbance, for imposing prescribed continuum boundary conditions on the atomistic system. By means of simple feedback control, we further ensure that the desired macroscopic field is achieved at the physical boundary by adjusting the imposed field at an extended boundary. Validity of our method is demonstrated in the example of simple Couette flow where the continuum solution is known analytically.

2.3.1 Introduction

Molecular dynamics (MD) plays a unique role in the simulation of fluids by virtue of its ability to offer insights into atomic-level structure and dynamics that cannot be obtained from continuum calculations. Because only a microscopic region of the fluid can be studied in this manner, there is considerable interest to develop hybrid atomistic-continuum methods. The central issue here is the coupling, or matching, of discrete particles with continuum representation of the system, whose degrees of freedom are very different although physically related. Though this problem has been well recognized[66], there still appears to be no completely satisfactory solution.

Two notable attempts have been made recently to rectify this situation, both invoking the use of an overlapping region but differing in how the molecular and continuum descriptions are to be made compatible. O'Connell and Thompson[67] proposed to constrain the dynamics of atoms in the hybrid layer between the MD and continuum regions to ensure continuity of property averages across the coupling region. Hadjiconstantinou[68, 69] cast their formulation in the framework of alternat-

ing Schwarz method[70] and treated the matching in terms of refining the boundary conditions imposed on each of the overlapping subdomains through an iterative process.

In this section we present a formalism for hybrid atomistic-continuum simulation, also in the spirit of the alternating Schwarz method, and focus on the problem of coupling continuum solution, in the form of phase space distribution (fields), to a system of discrete particles. The essence of the Schwarz method is to solve for the two overlapping subdomains in an iterative fashion (see Fig.2-18), first obtaining the solution in one subdomain using an approximate boundary condition inside the other subdomain, then doing the same for the other subdomain based on the newly obtained solution, and iterating on this sequence of steps until convergence is reached.

In this work the atomistic subdomain will be treated by MD simulation, while the other subdomain will be treated by an appropriate continuum solver. Coupling the two means that the boundary condition for the atomistic region will have a part determined by the continuum solution (on the border joining the overlapping region and the continuum), and vice versa. In order to iterate between continuum and MD solutions, one needs methods to carry out two types of operations, one is to construct the macroscopic field(s) that accurately represents a given set of particle data, and the other is to perform the inverse, which is to make sure that the MD particle trajectories correspond to a prescribed macroscopic field, and is achieved with as little artificial disturbance as possible. A method for the former has been developed[71] in the form of an algorithm called the Thermodynamic Field Estimator (TFE). A method for latter operation is what we will describe below, to be named the Optimal Particle Controller (OPC).

The basis of OPC is a transformation relating two sets of random variables, each governed by a distribution function with certain macroscopic fields serving as parameters. In conjunction with TFE, this transformation allows us to impose arbitrary continuum solution as boundary condition for MD simulation. We regard this particular coupling procedure as optimal in the sense that the resulting artificial disturbance to the particle dynamics, as measured in terms of the square deviation in the two sets

of random variables, is minimal.

Our coupling method incorporates another technique, designed to reduce further the artificial disturbance of imposing a prescribed macroscopic field. This involves applying the boundary condition at a distance extended beyond the MD-continuum interface normally associated with Schwarz-type overlapping domain decompositions. Using a first-order feedback control algorithm relating the field actually imposed at the extended boundary and the intended field at the MD-continuum interface, we show that faster convergence to the prescribed field can be achieved. We will refer to this procedure as the Extended Boundary Condition (EBC).

To demonstrate the validity of our hybrid atomistic-continuum simulation formalism, with emphasis on the atomistic aspects, we consider a particularly simple problem, that of planar Couette flow between two parallel walls. In this case the continuum solution is simply a linear flow velocity field, which conveniently eliminates the need for a real continuum solver, but suffices to illustrate the ideas.

This section is organized as follows. We begin with the development of the Optimal Particle Controller in Sec.2.3.2, first defining a simple measure of disturbance to the particle dynamics, then formulating the optimal transformation, and lastly deriving the various distributions needed for the implementation. Given the OPC as a direct method of imposing field boundary condition on a system of particles with least disturbance, one can proceed in an even more gentle manner by incorporating the Extended Boundary Condition and feedback control, discussed in Sec.2.3.3. Validation of our method which involves all three techniques, TFE, OPC, and EBC, in the case of Couette flow, is first discussed without reference to the larger picture of alternating Schwarz method, in Sec.2.3.4. And then in Sec.2.3.5 we consider specifically the effects of different types of Schwarz iterations on the convergence of the solution. A number of concluding remarks are offered in Sec.2.3.6.

2.3.2 Optimal Particle Controller

Minimal Disturbance to Particle Dynamics

The basic problem we face is the following. Given a set of particle coordinates in phase space, namely the positions and velocities of a system of N particles, which can be reasonably well described by a distribution function characterized by a set of macroscopic fields (density, velocity, and temperature)[71]. How does one modify the particle coordinates such that the corresponding distribution is now characterized by a different set of macroscopic fields? Stated in another way, given that the current particle coordinates are governed by a certain distribution function, how does one find a new set of coordinates which are governed by a different distribution, the one that is prescribed by the continuum subdomain solution? One may try to decouple the two first, and use only the latter to sample the new set of coordinates. While this would indeed lead to a coupling scheme, it is quite conceivable that ignoring the current state will result in a procedure which strongly disturbs the particle dynamics. If decoupling the two distributions, or equivalently, the two sets of particle coordinates, is not a good idea, then one should look for a way to relate them such that the disturbance is minimized. We will now introduce a quantitative measure of this disturbance and suggest a relation connecting the current state and the desired state that minimizes this measure.

To be explicit we consider a coupling scheme where the continuum velocity field is imposed on the atomistic simulation, and for the moment suppose we already know the transformation that are to give the desired continuum field. Then we can define

$$B = \sum_n |\Delta \mathbf{v}_n|^2 = \sum_n |\mathbf{v}_n^{\text{out}} - \mathbf{v}_n^{\text{in}}|^2, \tag{2.16}$$

where $\Delta \mathbf{v}_n$ is the change in particle velocity of the nth particle ($\mathbf{v}_n^{\text{in}}$ and $\mathbf{v}_n^{\text{out}}$ are the velocity before and after the transformation). This quantity will be used as a simple measure of the artificial disturbance to particle dynamics, which should be minimized as much as possible.

For the developments to follow, we note that a reasonable form to take for the distribution which describes the particle coordinates is the local Maxwellian function

$$\begin{aligned} dP = \quad & f_M\left(\mathbf{x},\mathbf{v}|\{\rho(\mathbf{x}),T(\mathbf{x}),\bar{\mathbf{v}}(\mathbf{x}\}\right) d\mathbf{x}d\mathbf{v} \\ = \quad & \rho(\mathbf{x})d\mathbf{x}\cdot\frac{1}{(2\pi T(\mathbf{x}))^{D/2}}\exp\left(-\frac{|\mathbf{v}-\bar{\mathbf{v}}(\mathbf{x})|^2}{2T(\mathbf{x})}\right)d\mathbf{v}, \end{aligned} \tag{2.17}$$

where $\mathbf{x}$, $\mathbf{v}$ are single particle position and velocity, and $\rho(\mathbf{x})$, $T(\mathbf{x})$, $\bar{\mathbf{v}}(\mathbf{x})$ are the macroscopic density, velocity and temperature fields, respectively. In (2.17) D is the dimensionality of the system, and we have taken the mass of particles and the Boltzmann constant to be unity.

Consider now the different ways one can modify the existent particle velocities to achieve a distribution that is characterized by a different macroscopic field. We can think of two criteria which need to be satisfied. First, the resulting macroscopic field must be correct. A common way to estimate the macroscopic field from particle data is to assume a distribution and calculate its averaged moments. In most situations a local Maxwellian form (2.17) provides a good description, and that can always be explicitly checked. Second, correct particle dynamics is desired. If the particle dynamics is strongly disturbed, MD simulation will lose its physical significance. Conforming to a prescribed distribution does not mean that the dynamics is also correct. If a macroscopic field has reached the correct value and can be maintained without further coupling, a good controller should do nothing more to the particles. This means that the modified phase coordinates should not be decoupled from the original ones.

As an illustration let us consider a simple problem of 1D convection-less heat conduction, for which we wish to impose a temperature boundary condition of high temperature T_h on the left ($x = 0$) and low temperature T_l on the right ($x = 1$). Intuitively one could imagine doing the following.

When a particle crosses either boundary ($x = 1$ or $x = 0$), give it a random velocity drawn from distribution (2.17) with parameters $\bar{\mathbf{v}} = 0$ and $T = T_h$ (or $T = T_l$). However, this procedure can be shown not to work. When implemented in

practice, the case of homogeneous heating ($T_h = T_l$) shows that the bulk temperature reaches a value of $T_h/2$.

The above scheme fails because one is dealing with a conditional probability problem. The speed distribution of atoms which cross the boundary is *different* from the speed distribution of atoms in the bulk

$$dP = \frac{1}{\sqrt{2\pi T}} \exp\left(-\frac{v^2}{2T}\right) dv, \qquad -\infty < v < +\infty \tag{2.18}$$

Instead it is weighted by the normal velocity,

$$\begin{aligned} dP = & \frac{v \exp\left(-\frac{v^2}{2T}\right) dv}{\int_0^{+\infty} v \exp\left(-\frac{v^2}{2T}\right) dv} \\ = & \frac{v}{T} \exp\left(-\frac{v^2}{2T}\right) dv, \qquad 0 < v < +\infty. \end{aligned} \tag{2.19}$$

$\langle v^2 \rangle$ from distribution (2.19) is $2T$, not T. Thus, if we sample the *boundary crossing atoms* using bulk distribution (2.18) with parameter $T = T_h = T_l$, the energy can only be balanced (in a statistical sense) when the bulk temperature reaches $T_h/2$.

A more subtle defect of this scheme is that, for whatever the incoming velocity v_{in} of the particle before hitting the boundary, a new velocity v_{out} is drawn from a given distribution, say $g(v)$, entirely *independent* of v_{in}. Thus if we evaluate the disturbance to particle dynamics using (2.16), it is always substantial no matter how long one runs the simulation. In the example of homogeneous heating, where the correct distribution (2.19) is used as $g(v)$ in drawing v_{out}'s, even when the system reaches the desired temperature, the scheme continues to disturb the particles by giving each boundary crossing atom a new v_{out}. On the other hand, if we just let $v_{\text{out}} = v_{\text{in}}$, i.e., do nothing, the system temperature stays at T_h! A more intelligent particle controller should automatically tune down its influence as the system approaches the desired state, a behavior we may call the coalescence property.

The Optimal Transformation

We now formulate the above considerations mathematically. Suppose we have an incoming random variable series $\{X_n\}$, conforming to distribution function $f(X)$:

$$dP(\eta < X < \eta + d\eta) = f(\eta)d\eta, \tag{2.20}$$

and we would like the series to conform to a different distribution g. We propose to achieve this by replacing every X with another variable Y which is distributed according to g. Thus the goal is to find a transformation $\mathcal{T}$,

$$\mathcal{T} : X_n \to Y_n, \tag{2.21}$$

with the requirement that if $\{X_n\}$ conforms to distribution $f(X)$, $\{Y_n\}$ will conform to distribution $g(Y)$:

$$dP(\xi < Y < \xi + d\xi) = g(\xi)d\xi. \tag{2.22}$$

There are many possible $\mathcal{T}$'s. However our previous discussion shows that the following property is desirable: *if $f \equiv g$, then $\mathcal{T}$ gives $Y_n \equiv X_n$.*

To incorporate the idea of *minimally disturbing the dynamics*, we adopt the criterion that

$$B[\mathcal{T}] = \langle (Y - X)^2 \rangle \tag{2.23}$$

be minimized among all possible $\mathcal{T}$'s.

Thus our output series $\{Y_n\}$ is least altered from $\{X_n\}$, while it is still distributed according to $g(Y)$. As f approaches g, Y approaches X.

We see that if $\mathcal{T}$ is randomly drawing Y from $g(Y)$ without reference to X, it satisfies the basic requirement of (2.22) but not the coalescence property. We will call this transformation $\mathcal{T}_1$.

To incorporate coalescence one may consider the transformation $\mathcal{T}_2$,

$$\mathcal{T}_2 : \begin{cases} Y = X : & p \leq \frac{g(X)}{Kf(X)} \\ \text{draw } Y \text{ randomly from } g(Y) : & p > \frac{g(X)}{Kf(X)} \end{cases}$$

where p is a random number uniformly distributed over $[0, 1]$, and K is a constant (scheme fails if K does not exist) such that

$$Kf(X) \geq g(X) \text{ for } -\infty < X < +\infty. \tag{2.24}$$

But is $\mathcal{T}_2$ the best one?

We propose the following transformation, in the form of an implicit relation,

$$\mathcal{T}_3 : X \to Y \sim \int_{-\infty}^{X} f(\xi)d\xi = \int_{-\infty}^{Y} g(\xi)d\xi. \tag{2.25}$$

It can be checked that Y indeed conforms to distribution $g(Y)$ if the incoming random number X conforms to distribution $f(X)$, and it satisfies the coalescence property. In fact this should come as no surprise because it is the only one-to-one continuous mapping which satisfies (2.22), without the extra randomness like in $\mathcal{T}_2$.

We believe that $\mathcal{T}_3$ is the mathematically optimal transformation which minimizes (2.23). A plausibility argument is given in the Appendix. Our experience has shown that while $\mathcal{T}_3$ works rather well, it is an implicit algorithm and could be computationally demanding.

Thus far we have assumed $f(X)$ to be known. In reality it has to be inferred from $\{X_n\}$, and this invokes the separate issue of how we extract continuum representation from the atomistic description. A straightforward approach would be to collect $\{X_n\}$ over a period of time to compile a histograph. For fields with spatial and temporal variations this is not a very good idea, especially if the available data set is small. If one believes that the *actual* field has smooth variation, then particle data outside the point of interest carry useful information about the field at this point and should not

be discarded. One then should use the Thermodynamic Field Estimator introduced in[71]. The continuous representation given by this method is based on the principle of Maximum Likelihood Inference and a judicious choice of basis functions, which makes good use of all available information. It is assumed in this method as well, that the local-equilibrium distribution (2.17) holds, which is the bridge between macroscopic fields (continuum) and microscopic statistical mechanics (MD).

3D Implementation

To implement the foregoing formulation we need to find the coupling distributions f and g that will relate the continuum description to an atomistic system. Since the coupling takes place through the particle velocities, we will give in this section explicit expressions for the velocity distribution. With $D = 3$ and particles conforming to distribution (2.17) with microscopical fields $(\{T(\mathbf{x}), \bar{\mathbf{v}}(\mathbf{x})\})$, we calculate the boundary crossing rate at $\partial\mathcal{C}$ (see Fig.2-9) for any small piece of the surface area. For choice of the coordinate system, we take the transverse basis $\mathbf{s}$ and $\mathbf{t}$ such that the macroscopic field $\bar{\mathbf{v}}(\mathbf{x})$ lies entirely in the place of $\mathbf{n}$ and $\mathbf{s}$. Thus, in this local frame,

$$\bar{\mathbf{v}} = (\bar{v}_n, \bar{v}_s, 0), \tag{2.26}$$

(from now on we will omit $\mathbf{x}$ but it is implicitly understood that everything is local). In the same frame the particle velocities can be expressed as

$$\mathbf{v} = (v_n, v_s, v_t). \tag{2.27}$$

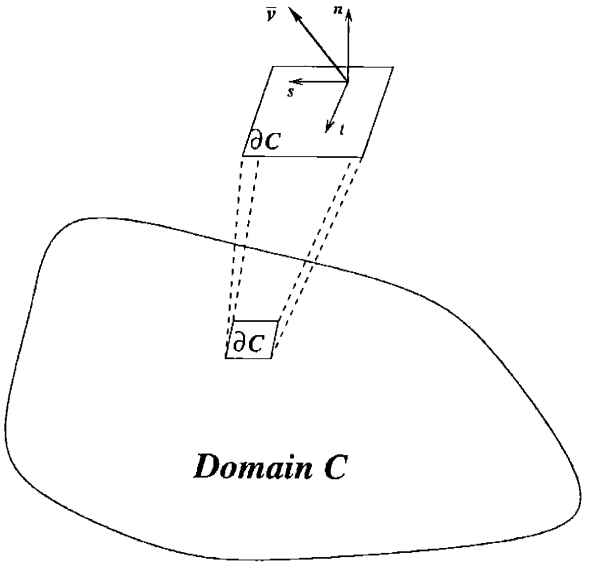

Figure 2-9: In the direct approach, $\mathcal{C}$ is our domain of interest, $\partial\mathcal{C}$ is its boundary which the particle controller acts on to achieve the desired macroscopic fields. For any small piece of the boundary, we choose the local coordinate frame to express the prescribed macroscopic velocity field as $\bar{\mathbf{v}} = (\bar{v}_n, \bar{v}_s, 0)$. In the same frame the actual, or current velocity field is $\bar{\mathbf{v}}' = (v'_n, v'_s, v'_t)$.

The boundary crossing rate from interior to exterior is

$$\begin{aligned}
& \left.\frac{dN}{dSdt}\right|_{-\mathbf{n}\to\mathbf{n}} \\
= \quad & \rho \int_{v_n>0} \exp\left(-\frac{(v_n-\bar{v}_n)^2+(v_s-\bar{v}_s)^2+v_t^2}{2T}\right) \frac{v_n dv_n dv_s dv_t}{(2\pi T)^{3/2}} \\
= \quad & \frac{\rho}{\sqrt{2\pi T}} \int_0^{+\infty} v_n \exp\left(-\frac{(v_n-\bar{v}_n)^2}{2T}\right) dv_n \\
= \quad & \frac{1}{2}\rho\bar{v}_n\left(1+\mathrm{erf}(\frac{\bar{v}_n}{\sqrt{2T}})\right) + \frac{\rho T}{\sqrt{2\pi T}} \exp(-\frac{\bar{v}_n^2}{2T}),
\end{aligned} \tag{2.28}$$

where the error function is defined as

$$\mathrm{erf}(x) = \frac{2}{\sqrt{\pi}} \int_0^x \mathrm{e}^{-\eta^2} d\eta.$$

Similarly the reverse crossing rate is

$$\begin{aligned} & \left.\frac{dN}{dSdt}\right|_{\mathbf{n}\to-\mathbf{n}} \\ = \quad & -\frac{1}{2}\rho\bar{v}_n(1+\mathrm{erf}(\frac{-\bar{v}_n}{\sqrt{2T}}))+\frac{\rho T}{\sqrt{2\pi T}}\exp(-\frac{\bar{v}_n^2}{2T}). \end{aligned} \tag{2.29}$$

With the boundary crossing rate depending only on the normal component of the field velocity, the distribution function which relates the particle and field variables becomes three decoupled distributions. For the boundary hitting ($-\mathbf{n}\to\mathbf{n}$) atoms, they are

$$\begin{aligned} & g_n(v_n)=\frac{(2\pi T)^{-1/2}v_n\exp(-(v_n-\bar{v}_n)^2/2T)}{\frac{1}{2}\bar{v}_n(1+\mathrm{erf}(\frac{\bar{v}_n}{\sqrt{2T}}))+\sqrt{\frac{T}{2\pi}}\exp(-\frac{\bar{v}_n^2}{2T})} \\ & v_n\in(0,+\infty), \end{aligned} \tag{2.30}$$

$$\begin{aligned} & g_s(v_s)=\frac{1}{\sqrt{2\pi T}}\exp(-(v_s-\bar{v}_s)^2/2T) \\ & v_s\in(-\infty,+\infty), \end{aligned} \tag{2.31}$$

$$\begin{aligned} & g_t(v_t)=\frac{1}{\sqrt{2\pi T}}\exp(-v_t^2/2T) \\ & v_t\in(-\infty,+\infty). \end{aligned} \tag{2.32}$$

Notice we use symbol g here to indicate that $(T,\bar{\mathbf{v}})$ are the *desired* macroscopic fields. In order to achieve these fields using $\mathcal{T}_3$ transformation (2.25) we need to know the f's, i.e., the *actual*, or current, velocity distribution functions of boundary hitting atoms. They are also given by (2.17) but with different parameters $(T',\bar{\mathbf{v}}')$. If we express

$$\bar{\mathbf{v}}'=(\bar{v}_n',\bar{v}_s',\bar{v}_t') \tag{2.33}$$

in the same coordinate frame and repeat the steps (2.28) to (2.32), we get correspond-

ing results for the distributions describing the current state,

$$f_n(v_n) = \frac{(2\pi T')^{-1/2} v_n \exp(-(v_n - \bar{v}'_n)^2/2T')}{\frac{1}{2}\bar{v}'_n(1 + \mathrm{erf}(\frac{\bar{v}'_n}{\sqrt{2T'}})) + \sqrt{\frac{T'}{2\pi}}\exp(-\frac{\bar{v}'^2_n}{2T'})}$$
$$v_n \in (0, +\infty), \tag{2.34}$$

$$f_s(v_s) = \frac{1}{\sqrt{2\pi T'}}\exp(-(v_s - \bar{v}'_s)^2/2T')$$
$$v_s \in (-\infty, +\infty), \tag{2.35}$$

$$f_t(v_t) = \frac{1}{\sqrt{2\pi T'}}\exp(-(v_t - \bar{v}'_t)^2/2T')$$
$$v_t \in (-\infty, +\infty). \tag{2.36}$$

Because the distributions in v_n, v_s, v_t are decoupled, we can apply (2.25) separately on the three variables, for each $-\mathbf{n} \rightarrow \mathbf{n}$ boundary hitting particle. The situation for $\mathbf{n} \rightarrow -\mathbf{n}$ is exactly the same after $v_n \rightarrow -v_n$ substitution.

All the above derivations for imposing boundary conditions do not include density coupling. To couple density, one has to inject or remove particles, then the disturbance to particle dynamics cannot be quantified by what we are proposing here. Maintaining certain density field is in general more difficult than maintaining temperature or velocity field. On the other hand, one usually are not required to apply density boundary condition explicitly. In most problems, the density field rather comes as a response to the other fields through the equation of state, for example in the micro-channel Poiseuille flow problem discussed in[71].

2.3.3 Extended Boundary Condition

In Section 2.3.2 a method was proposed to control the field boundary condition of an MD simulation which results in least disturbance to the particle dynamics in the sense of (2.16). Nevertheless the disturbance is still existent for particles in the skin region near the boundary, which can be shown to be proportional to the rate of dissipation

in the system. In this Section we will formulate a procedure which eliminates that disturbance entirely at the specified boundary. Since any artificial action necessarily alters the particle dynamics in the vicinity where it is imposed, the best one can do is to act some distance away from the intended boundary and cause the macroscopic field at the boundary to be what is prescribed.

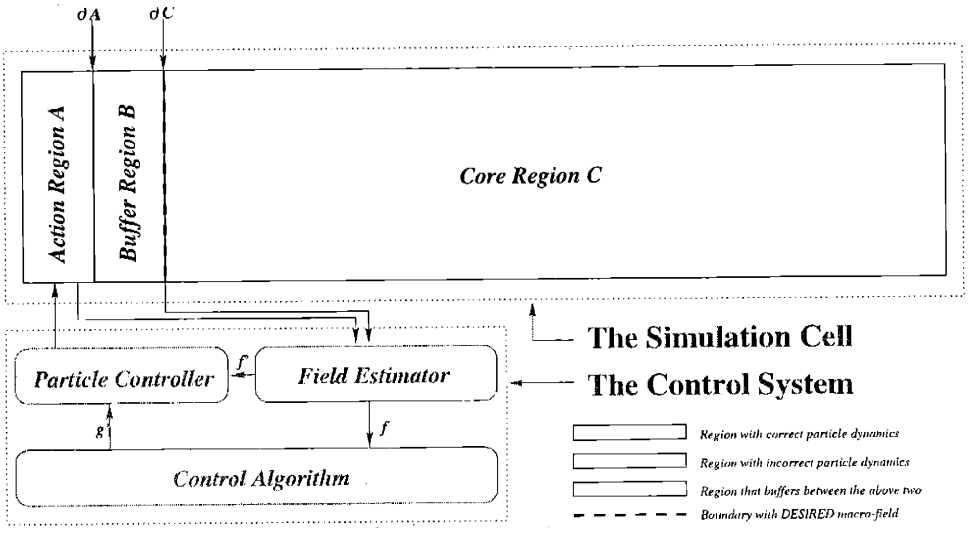

Figure 2-10: Schematic diagram of the Extended Boundary Condition (EBC), which incorporates a field estimator, a particle controller and a feedback control algorithm.

This can be done using a three-region approach which we will call the *Extended Boundary Condition (EBC)*, shown in Fig.2-10, and through a feedback control mechanism. The physical region of interest, $\mathcal{C}$ (core), is surrounded by a buffer zone $\mathcal{B}$. Actions are applied on an outer MD region $\mathcal{A}$ which is sufficiently separated from $\mathcal{C}$, its aim being to induce the prescribed field boundary conditions on the core boundary $\partial\mathcal{C}$. Due to molecular chaos in fluids, perturbation to particle dynamics will decay over a distance of a few mean free paths, thus setting a lower limit for $\mathcal{C}$-$\mathcal{A}$ separation. The action in $\mathcal{A}$ is in general a matter of choice, but here we will use the OPC developed in last section because it minimizes the disturbance, thus $\mathcal{B}$ could be as thin as possible. The TFE serves as the detector of the control loop, inferring current fields on $\partial\mathcal{C}$ based on particle data from the entire $\mathcal{C}$ region. A Control Algorithm compares the estimated current field with the prescribed field on $\partial\mathcal{C}$, and gives instructions to

the particle controller.

Note that although $\mathcal{A}$ and $\mathcal{B}$ are discrete particle regions governed by the same molecular dynamics as $\mathcal{C}$, they are conceptual constructs which have no physical correspondence and do not appear explicitly anywhere in Fig.2-18. They exist solely to ensure that the physical region of interest $\mathcal{C}$ has the correct field boundary conditions and evolves according to natural particle dynamics. Properly implemented, it could be a powerful tool for studying fluid systems because a fluid atom in $\mathcal{C}$ has no way to tell any difference from reality. It in turn can be used as a perfect benchmark for comparing the actual performance of $\mathcal{T}_1$ and $\mathcal{T}_3$, as we will see below.

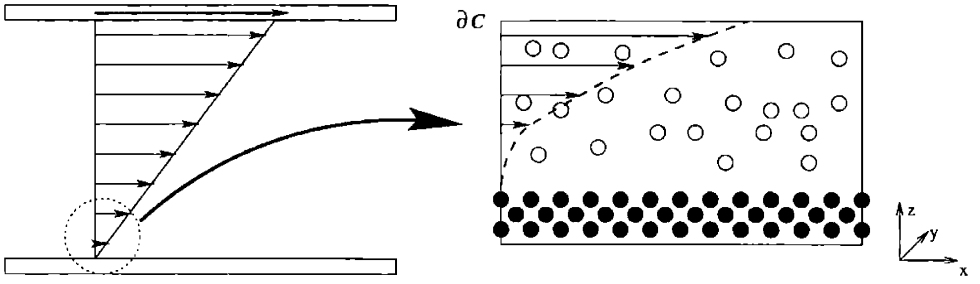

Figure 2-11: Geometry for simulation of planar Couette flow. The continuum solution is a linear velocity profile, $\bar{v}_x(z)$. In the atomistic description, the fluid is represented by N particles evolving according to molecular dynamics, and the wall is modeled by three layers of stationary particles which interact with the fluid. Dashed line depicts qualitatively the expected flow velocity profile on the molecular scale.

We now demonstrate how such a procedure could be implemented in the context of simulation of shear flow. In classic Couette flow problem, the continuum fluid moves between parallel sliding plates with a linear velocity profile as shown in Fig.2-11. The entire fluid is of macroscopic dimension ($> \mu$m). The part of the problem which is appropriate for MD simulation is only a small region at the fluid-wall interface. This atomistic region is depicted as consisting of three layers of atoms representing the wall and a fluid of N atoms. To maintain the flow field, a boundary action representing the continuum-atomistic coupling acts at plane $\partial\mathcal{A}$ in Fig.2-13 which, as we saw, need not to be the outer boundary of the physical core (subdomain) $\partial\mathcal{C}$. But as a comparison, we will also implement the direct Particle Controller (PC) approach

shown in Fig.2-12, where $\partial\mathcal{A}$ *is* $\partial\mathcal{C}$ and there is no buffer zone.

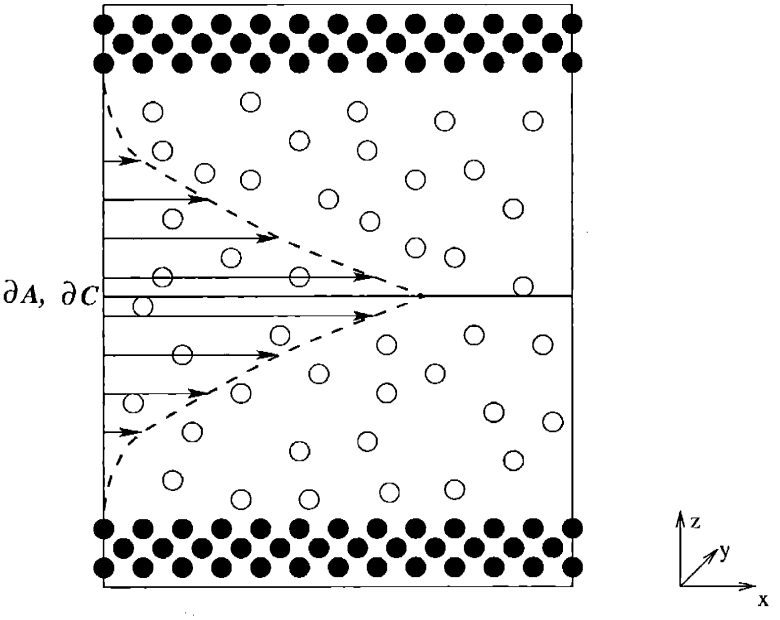

Figure 2-12: Direct particle controller boundary condition, where ∂A and ∂C are brought together and there is no buffer.

In practice it is more convenient to work with a simulation cell that is periodic in the z-direction, for this reason our MD simulation will be carried out in a symmetric geometry as shown in Fig.2-13 and 2-12. Since our MD program is $\mathcal{O}(N)$[71], this merely doubles the computational effort but we get twice as much particle data as well; and with each side serving as a particle reservoir for the other. It is important to keep in mind the connection between this particular simulation setup and the Couette flow problem in the framework of Schwarz coupling (Fig.2-18); otherwise, the significance of simulating a periodic system of fluids flowing between static walls driven by a velocity field along the center line may not be apparent.

In applying the EBC (Fig.2-13), the buffer region is between $\partial\mathcal{A}$ and $\partial\mathcal{C}$. Actions are applied on $\partial\mathcal{A}$ instead of $\partial\mathcal{C}$ in such a way that the desired field at $\partial\mathcal{C}$ is obtained (see Fig.2-13). The question then becomes, given the desired flow velocity at $\partial\mathcal{C}$, v_C^*, how does one control the flow velocity at $\partial\mathcal{A}$ (prescribed value of the OPC), v_A^*?

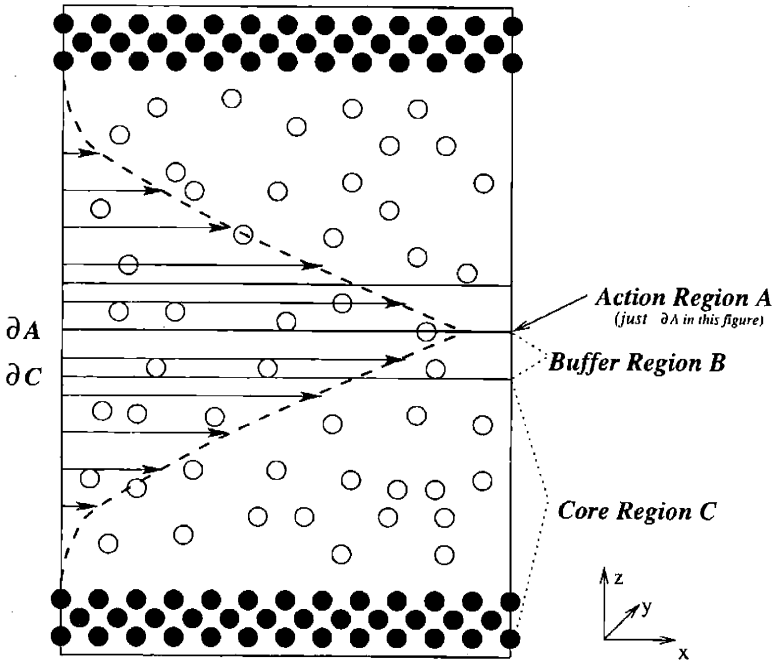

Figure 2-13: MD simulation cell incorporating the Extended Boundary Condition (EBC). A buffer region $\mathcal{B}$ (between $\partial\mathcal{A}$ and $\partial\mathcal{C}$) is inserted between the physical region of interest $\mathcal{C}$ and the action region $\mathcal{A}$ (just a plane $\partial\mathcal{A}$). The simulation cell is symmetric with respect to $\partial\mathcal{A}$.

Adopting a first-order feedback control algorithm, we may write

$$\frac{dv_A^*(t)}{dt} = -\kappa(v_C(t) - v_C^*), \tag{2.37}$$

where the rate constant κ should be picked according to the response time at $\partial\mathcal{C}$ due to an action on $\partial\mathcal{A}$, to make (2.37) converge as quickly as possible without oscillations [72, see, e.g.]. This simple equation allows us to control the action on $\partial\mathcal{A}$ based on current values at $\partial\mathcal{C}$ and $\partial\mathcal{A}$ (from TFE), as well as prescribed value at $\partial\mathcal{C}$.

A further drawback of the direct approach (Fig.2-12) besides disturbing the particle dynamics is that in a system with finite dissipation, we have to "overshoot" in the prescribed field value by some unknown amount in order to achieve the desired value at the same locale, because dissipation is always dragging the gradients down, and the particle controller only acts when the current value is off, so the time-averaged value is always below what is prescribed. The problem is, we do not know beforehand how much overshooting is needed to achieve the desired field. If the dissipation is zero (as in the homogeneous heating case), then we do not need overshooting at all and the coalescence property works perfectly. But in case of finite dissipation, its influence on the results of direct PC approach is significant (see Fig.2-15 in the following section). This problem can only be satisfactorily handled by the EBC, where the feedback control mechanism automatically takes care of the overshooting, and not on $\partial\mathcal{C}$ but $\partial\mathcal{A}$.

2.3.4 Couette Flow Test

In this Section we demonstrate how the above ideas are implemented for Couette flow. The process is somewhat reversed: we first implement the direct approaches (Fig.2-12) using $\mathcal{T}_1$ and OPC, obtain the actual flow velocity value at $\partial\mathcal{C}$ which has dropped somewhat from the prescribed value due to dissipation, and use EBC to reproduce that actual value at $\partial\mathcal{C}$ by acting on $\partial\mathcal{A}$ (Fig.2-13). We then in turn calculate a specially defined particle velocity auto-correlation function with EBC, and compare with those of the direct approaches, to show that OPC is indeed much more effective

than $\mathcal{T}_1$ in preserving the particle dynamics.

Consider a fluid of atoms which interact through a Lennard-Jones 6-12 interatomic potential with a cutoff at $r_c = 2.2\sigma$,

$$V = \begin{cases} 4\varepsilon\left[(\frac{\sigma}{r})^{12} - (\frac{\sigma}{r})^{6} - (\frac{\sigma}{r_c})^{12} + (\frac{\sigma}{r_c})^{6}\right] & (r < r_c) \\ 0 & (r \geq r_c). \end{cases}$$

The interaction parameters define a set of reduced units: length in terms of σ, energy in terms of ε, mass in terms of single fluid particle mass m. Thus one reduced time unit is $\tau = (m\sigma^2/\varepsilon)^{1/2}$, one reduced velocity unit is $(\varepsilon/m)^{1/2}$, etc. All numbers given in this section are in reduced units unless otherwise specified.

The wall consists of three layers of atoms fixed in fcc structure which interact with the fluid atoms also through a Lennard-Jones 6-12 potential but with parameters $\varepsilon_{wf} = 2\varepsilon$ and $\sigma_{wf} = \sigma$. This choice of parameters gives a more pronounced nonlinear effect near the fluid-wall interface.

The core region $\mathcal{C}$ has size $(L_x, L_y, L_z) = (8, 8, 10)$, with the wall occupying 20% and the fluids 80%. The buffer zone $\mathcal{B}$ has size $(8, 8, 1)$. The action region $\mathcal{A}$ is just a plane $\partial\mathcal{A}$ here, meaning that we only act on particles passing through the plane. As mentioned above, the real simulation cell contains two identical, mirror-reflected systems, so the size of simulation cell is $(8, 8, 22)$ for EBC simulations (Fig.2-13) and $(8, 8, 20)$ for direct PC simulations (Fig.2-12); the total number of particles is $N = 979$ and 870, respectively. For the fluid state, we choose density $\rho = 0.81$ and temperature $T = 1.2$ to ensure that it is in stable liquid phase.

As a check of the simulations, we plotted in Fig.2-14 the fluid density profile across the simulation cell with and without an imposed velocity field the centerline. One sees the familiar layering effect near the wall[73]; apparently the presence of a flow field has no discernible effect on the density profile.

Fig.2-15 shows the profile of shear flow velocity with distance normal to the fluid-wall interface, which starts at the interface ($z = 2$) and extends into the bulk. A continuum field boundary condition $v_x = 0.12$ is to be achieved on the $\partial\mathcal{C}$ plane. Three sets of simulation results are shown. Two (stars and circles) are obtained by

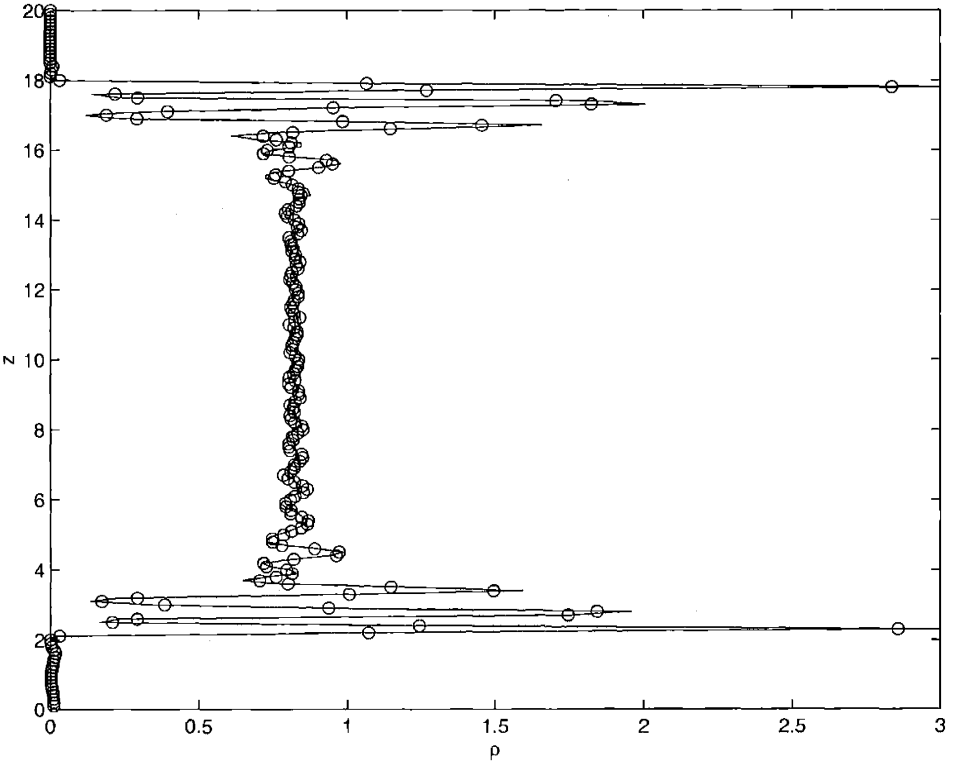

Figure 2-14: Density profile of the fluid in the simulation cell with (circles) and without (solid line) shear flow. The solid wall end at $z = 2$ and $z = 18$.

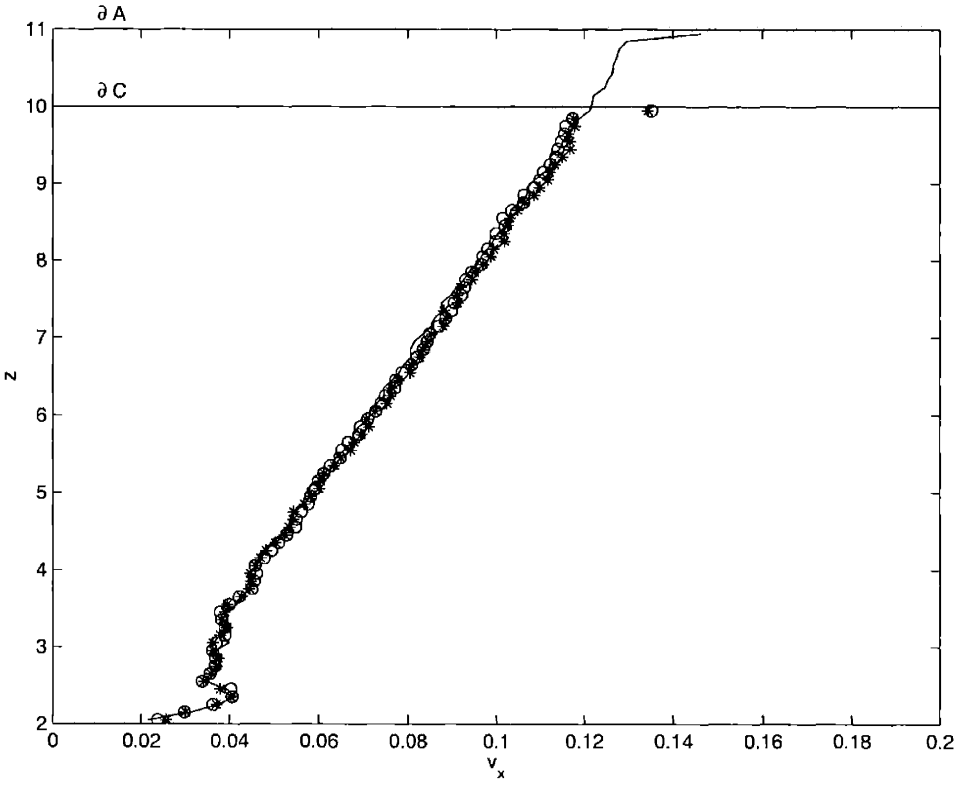

Figure 2-15: Profile of shear flow velocity $\bar{v}_x(z)$ obtained from three different MD simulations: smooth line is result from EBC (Fig. 2-13); stars and circles are results from direct particle controller simulations (Fig.2-12) using $\mathcal{T}_1$ and OPC.

directly applying the particle controllers $\mathcal{T}_1$ and OPC on plane $\partial\mathcal{C}$ (Fig.2-12), with prescribed velocity value $v_x = 0.2$ ("overshooting") to counteract the dissipation. The third (solid line) result is obtained by using the EBC (Fig.2-13) to achieve $v_x = 1.2$ on $\partial\mathcal{C}$, and serves as the benchmark of this test. It can be seen that overall, all three results agree well away from the artificial action region, with linear velocity profile in the bulk and strongly nonlinear behavior near the fluid-wall interface. However, the direct approaches have no way to determine the amount of overshooting *a priori*; and the deleterious effects of sudden velocity drop near the action zone boundary due to dissipation, and the artificial disturbance to particle dynamics, are completely avoided in the EBC simulation for $\partial\mathcal{C}$, to be replaced by what is happening near $\partial\mathcal{A}$.

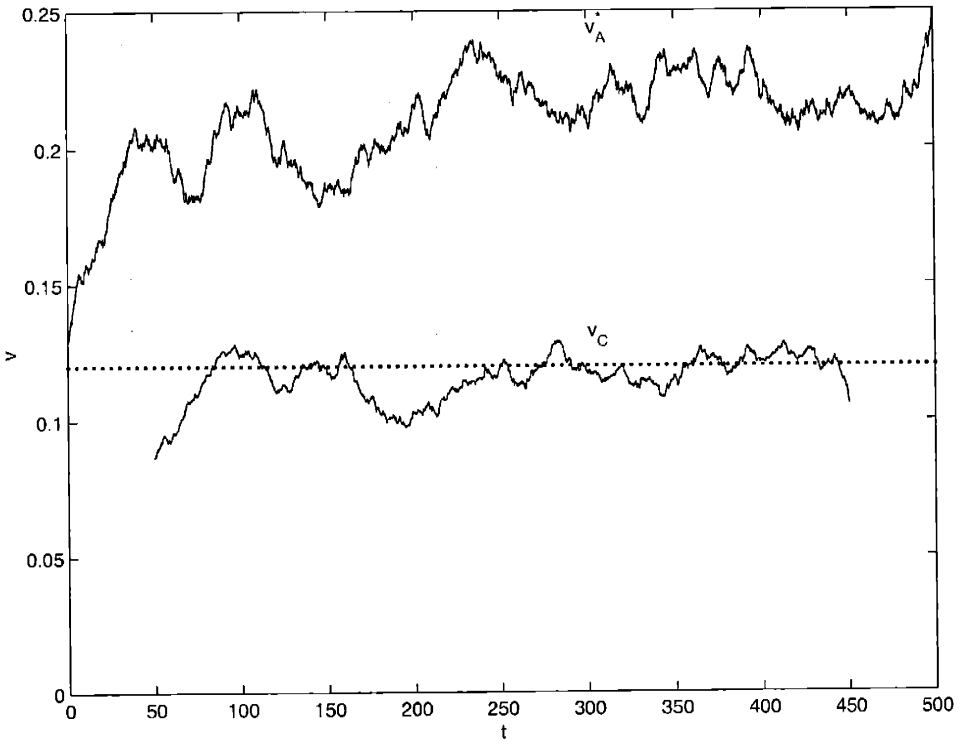

Figure 2-16: Starting with zero flow velocity $v_C(0) = 0$ and the prescribed velocity $v_A^*(0) = 0.12$, this plot shows how v_A^* and v_C evolves in time. $v_C(t)$ in this graph is the sliding bin average over $\Delta t = 50\tau$. For comparison, v_C^* is plotted in dotted line. Convergence in both v_C and v_A^* is obtained at around $t = 80$.

To show how the feedback control mechanism works, we start with a stationary

fluid, and let the desired boundary condition at $\partial\mathcal{C}$ to be $v_C^* = 0.12$. Starting with $v_A^*(0) = 0.12$, Fig.2-16 shows how $v_A^*(t)$ evolves according to (2.37), and how $v_C(t)$ responds to that action on $\partial\mathcal{A}$, separated by a buffer. A rate constant of $\kappa = 0.024$ is picked for the current buffer thickness of 1. To filter out the large thermal noises residing in instantaneous $v_C(t)$, it is plotted in Fig.2-16 after a sliding bin average of $\Delta t = 50$. We can see that $v_C(t)$ converges to the desired value of $v_C^* = 0.12$ at about $t = 80$, while $v_A^*(t)$ has also converged to a value of about 0.21.

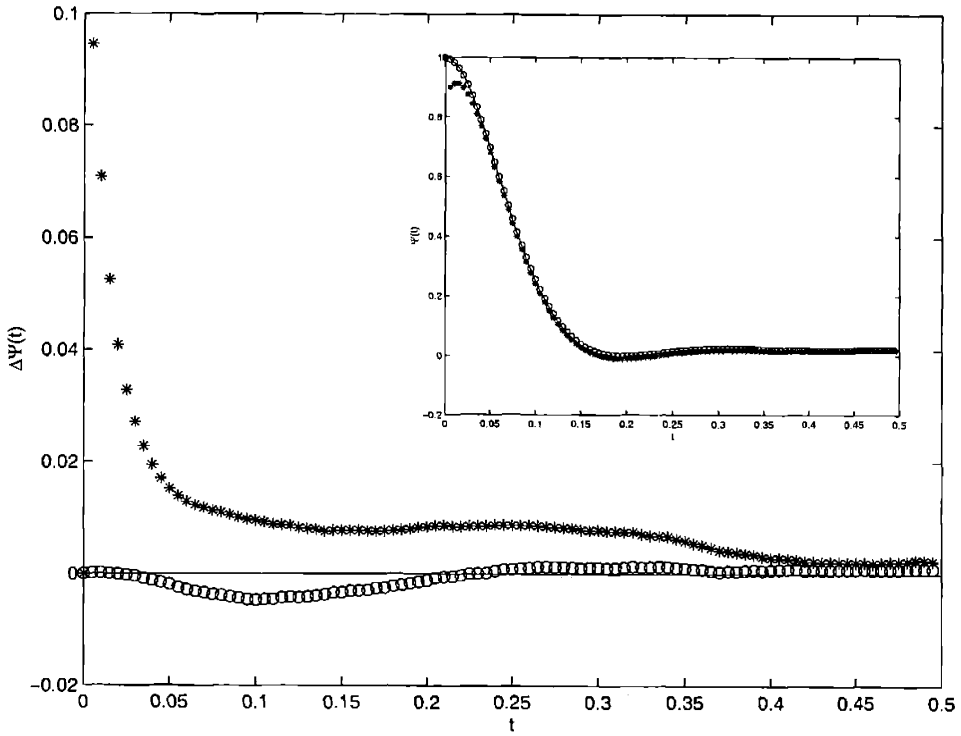

Figure 2-17: Comparison of the change to the normalized velocity autocorrelation function $\Psi(t)$ due to $\mathcal{T}_1$ and OPC. $\Psi_{\text{EBC}}(t) - \Psi_{\mathcal{T}_1}(t)$ is plotted in stars and $\Psi_{\text{EBC}}(t) - \Psi_{\text{OPC}}(t)$ is plotted in circles. In the inset, $\Psi_{\text{EBC}}(t)$, $\Psi_{\mathcal{T}_1}(t)$ and $\Psi_{\text{OPC}}(t)$ are plotted in solid line, stars and circles respectively. Notice that $\Psi_{\mathcal{T}_1}(0) = 1$, but it is quickly scattered in the ensuing period.

To quantify the effectiveness of OPC in preserving the particle dynamics, let us consider a quantity which represents the microscopic dynamics much better than the overall flow velocity. The velocity autocorrelation function is a quantity in the theory of liquids which is an important characteristic of single-particle motion. We can define

its localized and normalized version

$$\Psi(t) = \frac{\langle \mathbf{v}_i(0) \cdot \mathbf{v}_i(t) \rangle}{\langle \mathbf{v}_i(0)^2 \rangle}, \tag{2.38}$$

for any ith particle which crosses the $\partial\mathcal{C}$ plane and comes into $\mathcal{C}$ region at a certain moment; its contribution to $\Psi(t)$ is terminated whenever the particle re-crosses that plane. Since the EBC acts on $\partial\mathcal{A}$ instead of $\partial\mathcal{C}$, $\Psi_{\text{EBC}}(t)$ should be the same as that of nature where no artificial disturbance is discernible locally. On the other hand, it is not so if we directly act on $\partial\mathcal{C}$. However, $\Psi(t)$ of OPC direct should be better than that of $\mathcal{T}_1$ direct in comparing with $\Psi_{\text{EBC}}(t)$. Fig.2-17 shows the difference $\Psi_{\text{EBC}}(t) - \Psi_{\mathcal{T}_1}(t)$ in stars and $\Psi_{\text{EBC}}(t) - \Psi_{\text{OPC}}(t)$ in circles; the three functions themselves are plotted in the upper right inset. Notice that $\Psi_{\mathcal{T}_1}(t = 0)$ is 1 as expected, but there is a drastic loss of correlation in the first $0.05ps$, clearly attributable to the drastic reaction of surrounding atoms when its direction is suddenly altered without considering its original motion. On the other hand, $\Psi_{\text{OPC}}(t)$ is almost indistinguishable from $\Psi_{\text{EBC}}(t)$. This is reasonable since $\Psi(t)$ is normalized, and the shear flow velocity is only a fraction of the particle total velocity.

2.3.5 The Schwarz Coupling Method

Hadjiconstantinou[68, 69] have proposed to couple atomistic and continuum simulations of fluid flow based on a classical procedure known as domain decomposition and the alternating Schwarz method[70]. In this approach one divides the domain into two or more overlapping subdomains and treats each one separately through an iterative procedure where the boundary conditions for one subdomain are derived from the solutions for the other subdomains. Suppose our domain of interest is decomposed into two subdomains $\mathcal{C}$ and $\mathcal{U}$, with an overlapping region bounded by two boundaries, $\partial\mathcal{C}$ and $\partial\mathcal{U}$, as shown in Fig.2-18. To obtain the solution for the entire domain, one iterates on the following. Starting with a trial boundary condition on $\partial\mathcal{C}$ which we denote as v_C^0, one obtains the solution for the subdomain $\mathcal{C}$. With this initial solution one then determines what is the boundary condition on $\partial\mathcal{U}$, denoted as v_U^1. Knowing

this, one obtains the solution in subdomain $\mathcal{U}$. Now a refined value for the boundary condition on $\partial\mathcal{C}$, v_C^1, can be determined to go on with the next iteration. The alternating process continues until convergence is reached in both subdomains. For a large class of problems where both subdomains are treated by continuum solvers, convergence can be proved[70]. When one of the subdomains is treated atomistically, convergence should be similarly achieved so long as the overlapping region is describable by both continuum and atomistic representations.

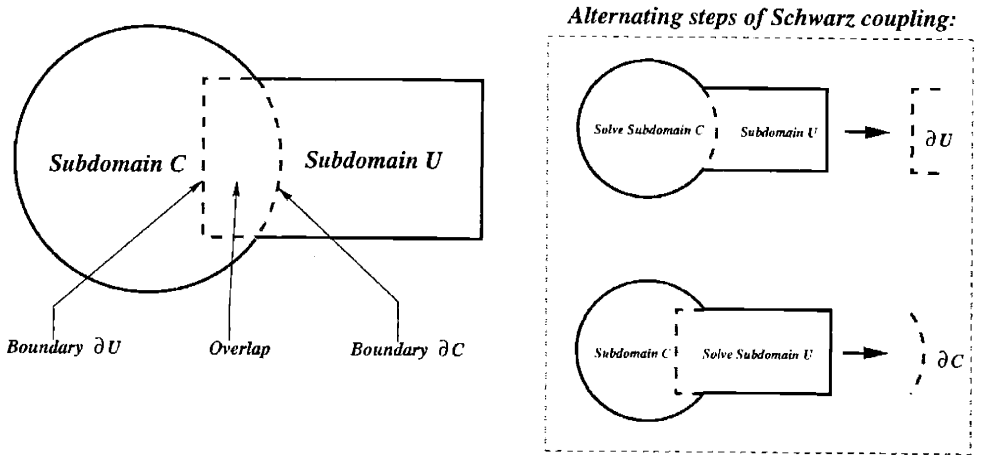

Figure 2-18: Classical alternating Schwarz method, which joins the two overlapping regions/solvers $\mathcal{C}$ and $\mathcal{U}$ through iteration of boundary conditions.

To implement the alternating Schwarz method in our simulation of shear flow we consider the system is decomposed into two overlapping regions (Fig.2-19), with $\mathcal{C}$ being the atomistic region, $\mathcal{U}$ the continuum, and an overlapping region bounded by planes $\partial\mathcal{C}$ and $\partial\mathcal{U}$. In the event that the computational costs involved in determining the velocity fields in the two regions are markedly different, we have found (see below) it is more efficient not to wait for the slow solver to converge, since the initial boundary conditions for the subdomains are not likely to be accurate. With the present continuum region always characterized by a linear velocity field, the calculation required for the continuum part of the iteration is just a linear interpolation. Given the current or averaged velocity field at plane $\partial\mathcal{U}$, the desired boundary value at plane

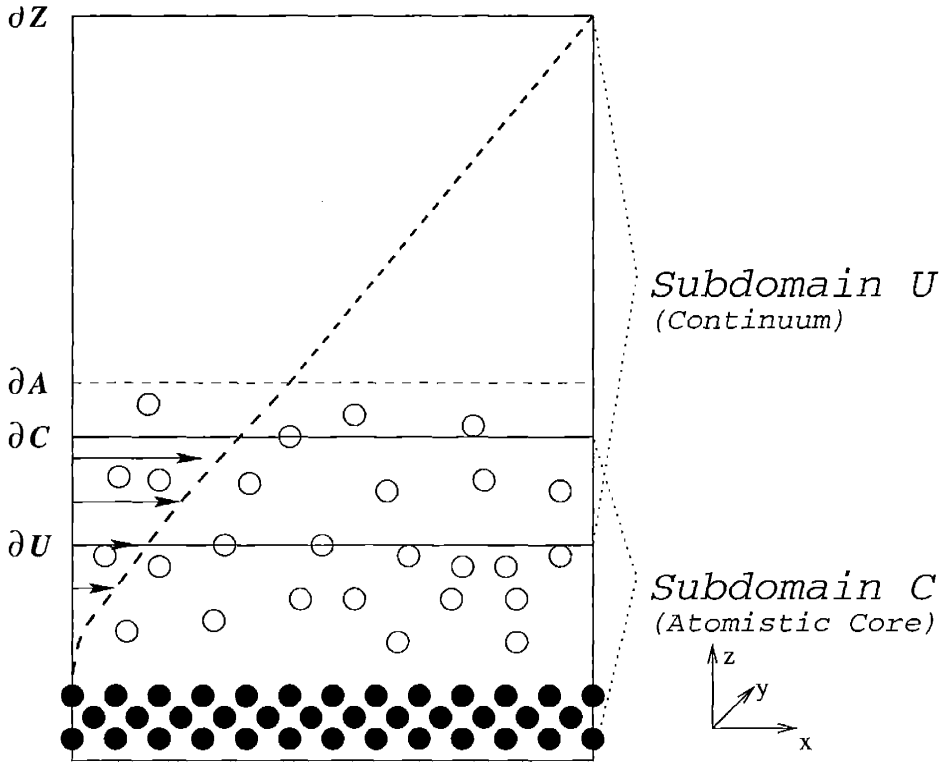

Figure 2-19: Geometry of Schwarz coupling in simulating shear flow.

$\partial\mathcal{C}$ is readily obtained as

$$v_C^* = \frac{(d_{CU}v_Z + d_{ZC}v_U)}{d_{ZU}}, \tag{2.39}$$

where v_Z is a constant which sets the magnitude of the velocity on the real boundary $\partial\mathcal{Z}$ of continuum region (see Fig. 2-19), d_{CU} is the distance between $\partial\mathcal{C}$ and $\partial\mathcal{U}$, etc. In the following simulations, the values are $v_Z = 0.2$, $d_{CU} = 3$, $d_{ZC} = 8$ and $d_{ZU} = 11$ (in a real simulation d_{ZU} should be much larger). Taking advantage of the fact that the the continuum solver requires no computational effort, we update the boundary condition at plane $\partial\mathcal{C}$ after every MD step. This is tantamount to relaxing both boundary conditions simultaneously. The MD solver is realized using EBC and (2.37) developed in section 2.3.3.

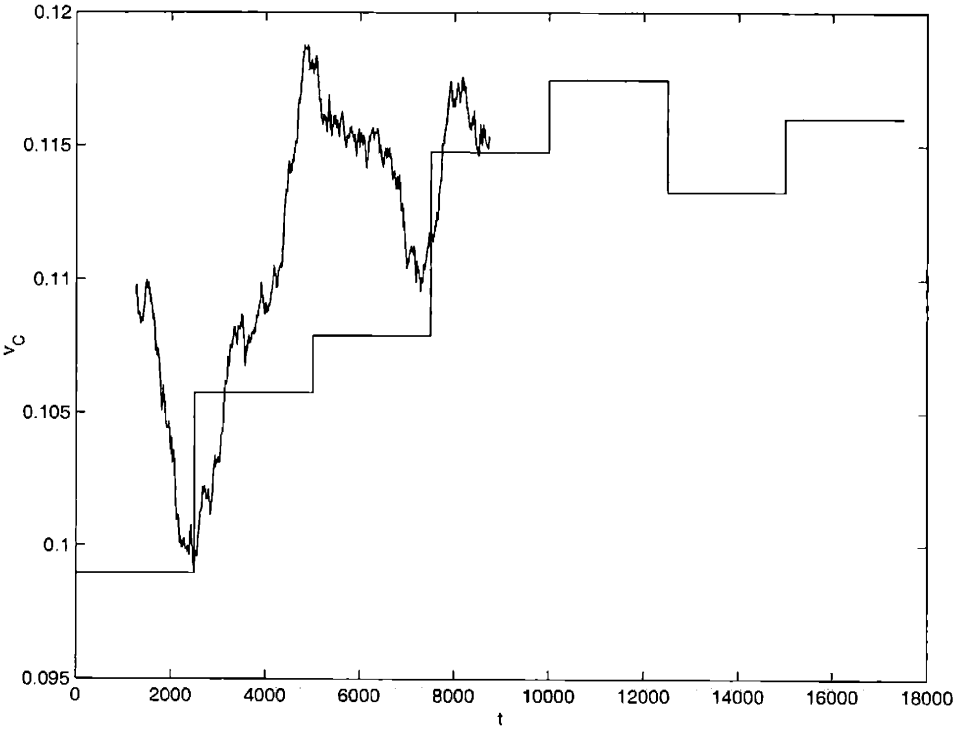

Figure 2-20: Comparison of convergence speed using classical alternating Schwarz method (straight lines), and the simultaneous relaxation method (zigzag lines) which takes advantage of the fact that the continuum solver takes no time at all for this simple scenario.

Fig.2-20 shows the convergence of shear flow velocities at plane $\partial\mathcal{C}$ to the value

given by the continuum solution. The fluid atoms are given initial velocities sampled from (2.17) according to a uniform temperature field and a linear velocity field. At beginning of the simulation the desired velocity at plane $\partial\mathcal{C}$ is set to a value of 0.1 based on the above initial guess. A simulation is taken following the classical alternating Schwarz method, where at each iteration the MD calculation is carried out to convergence. At this point the flow velocity at $\partial\mathcal{U}$ is averaged for previous $500,000$ timesteps or 2500τ. This average v_U is used in (2.39) to update the desired value at plane $\partial\mathcal{C}$, for the next period of MD simulation. The resultant v_C^* is shown in Fig.2-20 in straight solid line.

One could also proceed in a slightly different manner, that is to adjust v_C^* using (2.39) after every MD step, as the continuum solution costs nothing here. The resultant v_C^* is shown in Fig.2-20 as the zigzag solid line, after a sliding bin average of $\pm 1250\tau$. Convergence is achieved after a coupling time of 5000τ. One can see that the classical alternating Schwarz coupling may have a slower convergence here, by a factor of about 2, compared to the method of simultaneous relaxation at each MD step. Thus, invoking the two subdomain solvers in an asymmetrical fashion (one always converges, the other very little) leads to a more efficient scheme.

The fully converged, uniform hybrid continuum-atomistic solution is plotted in Fig.2-21, for both the classical alternating Schwarz coupling (circles) and the new simultaneous coupling (stars). One should note the perfect matching between MD and continuum solution in the overlapping region.

In general, if the continuum solver also requires finite amount of computational effort, the continuum to MD coupling can be updated at intervals of n MD steps, with adjustable n. If $n = 1$, it is the simultaneous relaxation method; if n is a large number such that the MD solver fully converges each time, we recover the classical alternating Schwarz method. An optimal n can be chosen according to the ratio of computational costs of the two solvers in achieving respective convergence. Also notice that one needs to take care of the thermal noises coming out of the MD solution, although it may have been reduced somewhat by the TFE. In general, even if the continuum solver is very fast, one may still need to wait for a while for the MD solver to average out

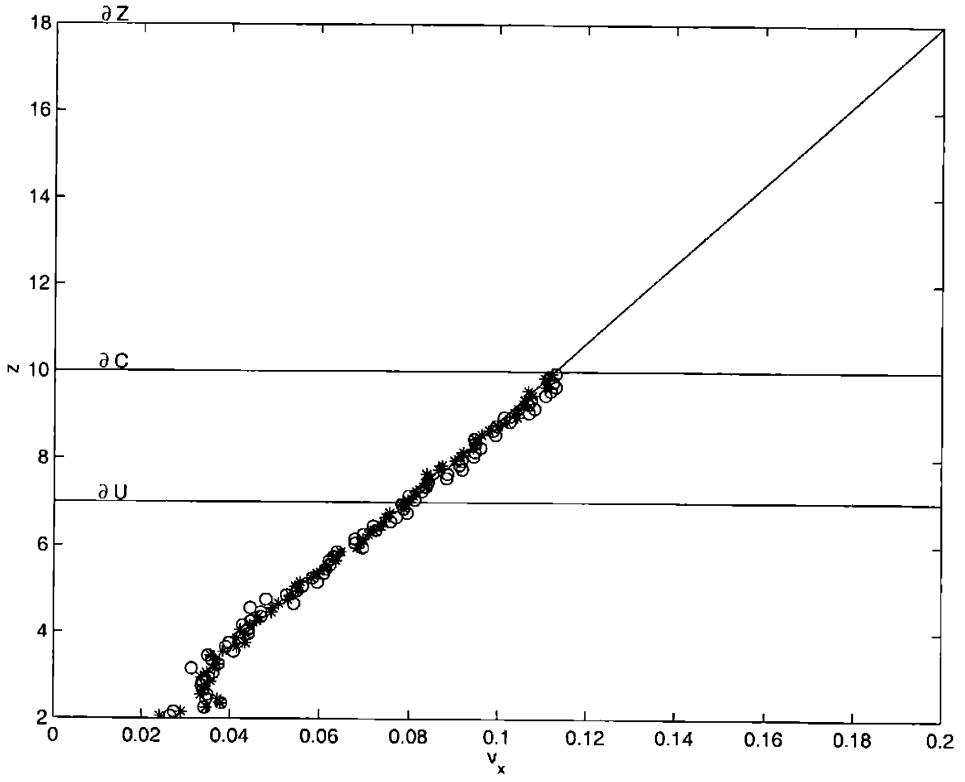

Figure 2-21: Fully converged hybrid continuum-atomistic solution. The classical alternating Schwarz method (circles) and the simultaneous relaxation method (stars) give essentially the same result, and there is good matching with the continuum solutions in the overlapping region.

the thermal noises. Feeding large fluctuations into the continuum solver may likely cause oscillatory behavior or divergence. In our case, the continuum solver is linear and does not have a convergence problem, because the fluctuations which come into the continuum solver will go back linearly and be filtered out by feedback loop.

2.3.6 Discussions

We have developed a hybrid continuum-atomistic simulation scheme based on the concept of domain decomposition, in the same spirit as Hadjiconstantinou and Patera. Such methods are useful for problems where much of the region of interest can be treated by continuum description, but a small critical, embedded part requires atomistic simulation. While Hadjiconstantinou and Patera implemented their method with attention to both the atomistic and continuum representations, we have focused our efforts on techniques for coupling continuum boundary conditions to atomistic simulations. In this work matching of the two different levels of representation, each with its own set of degrees of freedoms, takes place in the overlap region through an implicit transformation which we have called the Optimal Particle Controller, with the local Maxwellian distribution serving as the bridge, which depends on both particle and field variables. Relative to the conventional method of sampling from a desired distribution, such as the $\mathcal{T}_1$ transformation, OPC has the advantage that it is least disturbing to the particle dynamics, and that disturbance is proportional to the rate of dissipation, i.e., field gradients in the system instead of the absolute magnitude of the fields.

We have incorporated OPC along with the Thermodynamic Field Estimator and the Extended Boundary Condition into the framework of alternating Schwarz method and implemented our formalism in a study of shear flow. We should regard the numerical results presented here as proof of principle of the entire hybrid scheme. Since each one of these three techniques has its own novel features, further applications, including separate investigations of each technique, will be worthwhile to bring out their capabilities and limitations. We believe that relative to the other hybrid methods recently proposed [67, 68, 69] our method should be the most gentle as far as

treating the atomistic subdomain is concerned. For this reason the method should be most useful when one is interested in delicate or subtle molecular effects where minimizing local disturbance to particle dynamics is a significant concern.

Up to now we have only concerned with ourselves steady state fluid problems. One may wonder if a continuum solver could be dynamically coupled with an MD solver using the above techniques in real time. We do not have the solution yet but it seems quite difficult. On the other hand, the timescale of an macroscopic dynamical event is usually much greater than that of its underlying microscopic mechanism, thus to the critical microscopic region at any given moment of the event, the outside would seem to be in a steady state flow condition and could be modeled by our techniques. Such is in fact the rationale behind constitutive equations; but it should be able to handle more complex databases as well, such as stick-slip motion and chemisorption.

The case for solids is different. Solids, unlike fluids, have long range order. The assumption of molecular chaos is invalid here, and a buffer zone cannot cover up the disturbed dynamics elsewhere, which is the underpinning of the Extended Boundary Condition. Thus, it is quite difficult to isolate a region in a crystalline material since the phonons have very long mean free paths, and their scattering and reflections determine important macroscopic properties such as the thermal conductivity. Although researchers have developed successful techniques to couple continuum with atomistic regions for static calculations[74, 75], no one has yet claimed to successfully implement such a scheme to study finite temperature properties.

Proof that $\mathcal{T}_3$ is optimal

By our definition, a transformation is an operation which gives an output Y from an input X, but not necessarily in a deterministic manner, which differs from the concept of a function. $\mathcal{T}_1, \mathcal{T}_2$ and $\mathcal{T}_3$ in section (2.3.2) are all examples of such transformations. Mathematically it is equivalent to a mapping from a real number $x = X$ to a real *function* in y, which is the conditional probability distribution $W(y|x)$, from which

Y is drawn. The joint probability distribution function is simply

$$W(x,y) = W(y|x)f(x) \tag{2.40}$$

for the two random variables on xy plane.

$W(x,y)$ has the properties of:

1. Non-negativeness:

$$\forall x, y \in (-\infty, +\infty) \quad W(x,y) \geq 0 \tag{2.41}$$

2. Normalization:

$$\int_{-\infty}^{+\infty} W(x,y)dy = f(x) \tag{2.42}$$

$$\int_{-\infty}^{+\infty} W(x,y)dxdy = 1 \tag{2.43}$$

3. To satisfy the basic requirement (2.22), there must be:

$$\int_{-\infty}^{+\infty} W(x,y)dx = g(y) \tag{2.44}$$

Now, we want to find the $W_{\min}(x,y)$ which minimizes "disturbance" to the sequence, quantified as

$$B[W] = \int_{-\infty}^{+\infty} (x-y)^2 W(x,y)dxdy \tag{2.45}$$

We want to show that the distribution $W_{\min}$ must be zero almost everywhere on the xy plane. Suppose we have found such a $W_{\min}$, and $W_{\min}(x,y) > 0$ everywhere in a small region $\mathcal{A}$. We can always find some function $S_{\mathcal{A}}(x,y)$ which is nonzero only inside $\mathcal{A}$ and satisfies

$$\int_{\mathcal{A}} S_{\mathcal{A}}(x,y)dx = 0 \tag{2.46}$$

$$\int_{\mathcal{A}} S_{\mathcal{A}}(x,y)dy = 0 \tag{2.47}$$

For instance in a rectangular area $(x_1, y_1) - (x_2, y_2)$ we can pick $S_{\mathcal{A}}$ to be

$$S_{\mathcal{A}}(x, y) = \sin(2\pi n_x \frac{x - x_1}{x_2 - x_1}) \sin(2\pi n_y \frac{y - y_1}{y_2 - y_1}) \tag{2.48}$$

where n_x, n_y are non-zero integers, and zero elsewhere. Since the expression for $B[W]$ contains $(x - y)^2$, it can not be that

$$B[S_{\mathcal{A}}] = 0 \tag{2.49}$$

for all valid $S_{\mathcal{A}}$'s, and we can always choose a small enough λ to ensure that $|\lambda S_{\mathcal{A}}(x, y)| \leq W(x, y)$ everywhere. Let

$$W_{\text{new}} = W_{\text{min}} + \lambda S_{\mathcal{A}} \tag{2.50}$$

W_{new} will also satisfy the constraints (2.41) to (2.44). Lastly let us pick the sign of λ to make $\lambda B[S_{\mathcal{A}}] < 0$, so

$$B[W_{\text{new}}] = B[W_{\text{min}}] + \lambda B[S_{\mathcal{A}}] < B[W_{\text{min}}] \tag{2.51}$$

which is a contradiction. So, a finite area $\mathcal{A}$ where $W_{\text{min}}(x, y) > 0$ does not exist, and W_{min} must equal to zero almost everywhere, which can only be satisfied if $W_{\text{min}}(x, y)$ are combinations of δ-functions; that is, the optimal transformation $\mathcal{T}$ is a function-like mapping from X to Y, without any randomness.

Now, assuming W_{min} takes the form

$$W_{\text{min}} \sim \delta(y - H(x)) \tag{2.52}$$

which is equivalent to saying that the transformation is in fact a function $y = H(x)$. Then the problem simplifies to finding a function H_{min} which minimizes the sum (for illustrative purposes we use summation here instead of integration)

$$B[H] = \lim_{N \to \infty} \sum_i (x_i - H(x_i))^2 / N \tag{2.53}$$

with the requirement that x_i's are randomly drawn from distribution f and $H(x_i)$'s are randomly distributed with distribution g.

We want to show that $H_{\min}(x)$ must be a monotonically non-decreasing function: because if there exists a pair

$$x_1 > x_2 \text{ but } H(x_1) < H(x_2)$$

we can construct an $\tilde{H}(x)$ with x_1, x_2 exchanged

$$\tilde{H}(x) = \begin{cases} H(x) & (x \neq x_1, x \neq x_2) \\ H(x_2) & (x = x_1) \\ H(x_1) & (x = x_2) \end{cases} \tag{2.54}$$

without influencing g, but

$$\begin{aligned} (x_1 - \tilde{H}(x_1))^2 + (x_2 - \tilde{H}(x_2))^2 &= (x_1 - H(x_2))^2 + (x_2 - H(x_1))^2 \\ &= (x_1 - H(x_1))^2 + (x_2 - H(x_2))^2 \\ &\quad -(x_1 - x_2)(H(x_2) - H(x_1)) \\ &< (x_1 - H(x_1))^2 + (x_2 - H(x_2))^2 \end{aligned}$$

So $B[\tilde{H}] < B[H]$, which means $H_{\min}(x)$ must be a monotonically non-decreasing function.

Thus there is a unique, one-to-one relation between x and y, and there must be, because of (2.22),

$$dP = f(x)dx = g(y)dy \tag{2.55}$$

because any small interval $(x, x + dx)$ is uniquely and deterministically mapped into $(y, y + dy)$ by the optimal transformation. So if we integrate from $x, y \to -\infty$ where $P = 0$, there must be

$$\int_{-\infty}^{x} f(\xi)d\xi = \int_{-\infty}^{y} g(\xi)d\xi$$

which is the $\mathcal{T}_3$ transformation of (2.25).

2.4 Ewald Formulation for Ionic Systems

In this section the algorithm of the Ewald lattice summation is formulated in a form suitable for ionic crystalline solids. The derivation of phonon dispersion relations, elastic constants and thermal conductivity is presented, applied to the SiO_2, and tested against with experimental results.

2.4.1 Ewald Summation

Consider a system with Coulombic interaction, let's examine how the total energy of system can be calculated. (Our derivation follows[76], see also [5, 77, 78, 79])

We can write the total energy as:

$$U^C_{sum} = \sum_{ab}^{\text{all pairs}} \frac{e_a e_b}{r_{ab}} \tag{2.56}$$

Now suppose the system has a periodic crystal lattice. The total energy will be a summation over all the lattices. Introduce $\boldsymbol{k}$ as the Bloch phase between adjacent lattices (for introduction to Bloch theorem etc., see[80]).

$$U^C_{\text{sum}} = \sum_{\boldsymbol{R}} \sum_{ab} e_a e_b \frac{e^{i\boldsymbol{k}\cdot\boldsymbol{R}}}{|\boldsymbol{r}_{ab} + \boldsymbol{R}|} = \sum_{ab} e_a e_b \left\{ \sum_{\boldsymbol{R}} \frac{e^{i\boldsymbol{k}\cdot\boldsymbol{R}}}{|\boldsymbol{r}_{ab} + \boldsymbol{R}|} \right\} \tag{2.57}$$

We are interested in calculating the value inside the curly bracket. Without confusion, we can omit the $\sum_{ab}$ and the subscripts $_{ab}$ on all the $\boldsymbol{r}$. We define

$$U^C = \sum \frac{1}{r} = \sum_{\boldsymbol{R}} \frac{e^{i\boldsymbol{k}\cdot\boldsymbol{R}}}{|\boldsymbol{r} + \boldsymbol{R}|} \tag{2.58}$$

Following Ewald, we introduce the identity:

$$\frac{2}{\sqrt{\pi}} \int_0^\infty e^{-x^2\rho^2} \mathrm{d}\rho = \frac{1}{x} \tag{2.59}$$

so,

$$
\begin{aligned}
U^C &= \sum_{\boldsymbol{R}} e^{i\boldsymbol{k}\cdot\boldsymbol{R}} \frac{2}{\sqrt{\pi}} \int_0^\infty e^{-(\boldsymbol{r}+\boldsymbol{R})^2\rho^2} \mathrm{d}\rho \\
&= \int_0^\infty \left\{ \frac{2}{\sqrt{\pi}} \sum_{\boldsymbol{R}} e^{-(\boldsymbol{r}+\boldsymbol{R})^2\rho^2 + i\boldsymbol{k}\cdot(\boldsymbol{r}+\boldsymbol{R})} \right\} e^{-i\boldsymbol{k}\cdot\boldsymbol{r}} \mathrm{d}\rho
\end{aligned} \tag{2.60}
$$

The expression in the curly bracket is a periodic function of $\boldsymbol{r}$, with the periodicity of the lattice. So we can expand it into a Fouriour series.

$$
\left\{ \frac{2}{\sqrt{\pi}} \sum_{\boldsymbol{R}} e^{-(\boldsymbol{r}+\boldsymbol{R})^2\rho^2 + i\boldsymbol{k}\cdot(\boldsymbol{r}+\boldsymbol{R})} \right\} = \sum_{\boldsymbol{K}} C(\boldsymbol{K}) e^{i\boldsymbol{K}\cdot\boldsymbol{r}} \tag{2.61}
$$

From the othorgonality of $e^{i\boldsymbol{K}\cdot\boldsymbol{r}}$ we have

$$
C(\boldsymbol{K}) = \frac{1}{V_{allspace}} \int_{allspace} \left\{ \frac{2}{\sqrt{\pi}} \sum_{\boldsymbol{R}} e^{-(\boldsymbol{r}+\boldsymbol{R})^2\rho^2 + i\boldsymbol{k}\cdot(\boldsymbol{r}+\boldsymbol{R})} \right\} e^{-i\boldsymbol{K}\cdot\boldsymbol{r}} \mathrm{d}^3 r \tag{2.62}
$$

Change integration variables $\boldsymbol{r} \to \boldsymbol{r} - \boldsymbol{R}$, so that every term in the summation of $\sum_{\boldsymbol{R}}$ becomes the same. (Remember the definition of $\boldsymbol{K}$, for any $\boldsymbol{K}$ or $\boldsymbol{R}$ we have $e^{i\boldsymbol{K}\cdot\boldsymbol{R}} = 0$.) So now we have $\frac{1}{V_{allspace}} \sum_{\boldsymbol{R}} \to \frac{1}{V}$, here V is the volume of unit cell. So

$$
\begin{aligned}
C(\boldsymbol{K}) &= \frac{1}{V} \int \frac{2}{\sqrt{\pi}} e^{-r^2\rho^2 + i(\boldsymbol{k}-\boldsymbol{K})\cdot\boldsymbol{r}} \mathrm{d}^3 r = \frac{1}{V} \int \frac{2}{\sqrt{\pi}} e^{-\rho^2\left[\boldsymbol{r} - \frac{i(\boldsymbol{k}-\boldsymbol{K})}{2\rho^2}\right]^2 - \frac{(\boldsymbol{k}-\boldsymbol{K})^2}{4\rho^2}} \mathrm{d}^3 r \\
&= \frac{1}{V} e^{-\frac{(\boldsymbol{k}-\boldsymbol{K})^2}{4\rho^2}} \int \frac{2}{\sqrt{\pi}} e^{-\rho^2 r^2} \mathrm{d}^3 r
\end{aligned} \tag{2.63}
$$

The integration in the last equation can be performed:

$$
\int \frac{2}{\sqrt{\pi}} e^{-\rho^2 r^2} \mathrm{d}^3 r = \int_0^\infty \frac{2}{\sqrt{\pi}} e^{-\rho^2 r^2} 4\pi r^2 \mathrm{d}r = \frac{2\pi}{\rho^3} \tag{2.64}
$$

so we get $C(\boldsymbol{K})$

$$
C(\boldsymbol{K}) = \frac{2\pi}{V} \frac{1}{\rho^3} e^{-\frac{(\boldsymbol{k}-\boldsymbol{K})^2}{4\rho^2}} \tag{2.65}
$$

Thus far we have proven an important equality

$$\frac{2}{\sqrt{\pi}}\sum_{\boldsymbol{R}} e^{-(\boldsymbol{r}+\boldsymbol{R})^2\rho^2+i\boldsymbol{k}\cdot(\boldsymbol{r}+\boldsymbol{R})} = \frac{2\pi}{V}\sum_{\boldsymbol{K}}\frac{1}{\rho^3}e^{-\frac{1}{4\rho^2}(\boldsymbol{k}-\boldsymbol{K})^2+i\boldsymbol{K}\cdot\boldsymbol{r}} \tag{2.66}$$

Now back to the calculation of potential energy in (2.60), lets break the integration of ρ into 2 parts, $(0,\alpha)$ and (α,∞), denote

$$\mathcal{R}(U^C) = \int_\alpha^\infty \left\{\frac{2}{\sqrt{\pi}}\sum_{\boldsymbol{R}} e^{-(\boldsymbol{r}+\boldsymbol{R})^2\rho^2+i\boldsymbol{k}\cdot(\boldsymbol{r}+\boldsymbol{R})}\right\} e^{-i\boldsymbol{k}\cdot\boldsymbol{r}}\mathrm{d}\rho \tag{2.67}$$

$$\mathcal{K}(U^C) = \int_0^\alpha \left\{\frac{2}{\sqrt{\pi}}\sum_{\boldsymbol{R}} e^{-(\boldsymbol{r}+\boldsymbol{R})^2\rho^2+i\boldsymbol{k}\cdot(\boldsymbol{r}+\boldsymbol{R})}\right\} e^{-i\boldsymbol{k}\cdot\boldsymbol{r}}\mathrm{d}\rho \tag{2.68}$$

the expression for $\mathcal{R}(U^C)$ is just the definition of $\mathrm{erfc}(x)$ function:

$$\mathrm{erfc}(x) = \frac{2}{\sqrt{\pi}}\int_x^\infty e^{-\rho^2}\mathrm{d}\rho \tag{2.69}$$

so the real-space part of U^C is evaluated as

$$\mathcal{R}(U^C) = \sum_{\boldsymbol{R}}\frac{\mathrm{erfc}(\alpha|\boldsymbol{r}+\boldsymbol{R}|)}{|\boldsymbol{r}+\boldsymbol{R}|}e^{i\boldsymbol{k}\cdot\boldsymbol{R}} \tag{2.70}$$

Substitute the expression in the curly bracket of (2.68) by (2.66), we get

$$\mathcal{K}(U^C) = \int_0^\alpha \left\{\frac{2\pi}{V}\sum_{\boldsymbol{K}}\frac{1}{\rho^3}e^{-\frac{1}{4\rho^2}(\boldsymbol{k}-\boldsymbol{K})^2+i\boldsymbol{K}\cdot\boldsymbol{r}}\right\} e^{-i\boldsymbol{k}\cdot\boldsymbol{r}}\mathrm{d}\rho \tag{2.71}$$

Integrate out the ρ, we have

$$\mathcal{K}(U^C) = \frac{4\pi}{V}\sum_{\boldsymbol{K}}\frac{1}{(\boldsymbol{k}-\boldsymbol{K})^2}e^{-\frac{(\boldsymbol{k}-\boldsymbol{K})^2}{4\alpha^2}}e^{-i(\boldsymbol{k}-\boldsymbol{K})\cdot\boldsymbol{r}} \tag{2.72}$$

putting (2.70) and (2.72) together, the Ewald's construction for $U^C = \sum 1/r$ is

$$U^C = \underbrace{\sum_{\boldsymbol{R}}\frac{\mathrm{erfc}(\alpha|\boldsymbol{r}+\boldsymbol{R}|)}{|\boldsymbol{r}+\boldsymbol{R}|}e^{i\boldsymbol{k}\cdot\boldsymbol{R}}}_{Real-space-term} + \underbrace{\frac{4\pi}{V}\sum_{\boldsymbol{K}}\frac{1}{(\boldsymbol{k}-\boldsymbol{K})^2}e^{-\frac{(\boldsymbol{k}-\boldsymbol{K})^2}{4\alpha^2}}e^{-i(\boldsymbol{k}-\boldsymbol{K})\cdot\boldsymbol{r}}}_{Reciprocal-space-term} \tag{2.73}$$

put back the lattice cell summation, we then get

$$\begin{aligned} U^C_{sum} &= \sum_{ab} e_a e_b U^C \\ &= \sum_{ab} e_a e_b \underbrace{\sum_{\boldsymbol{R}} \frac{\mathrm{erfc}(\alpha|\boldsymbol{r}+\boldsymbol{R}|)}{|\boldsymbol{r}+\boldsymbol{R}|} e^{i\boldsymbol{k}\cdot\boldsymbol{R}}}_{Real-space-term} \\ &+ \sum_{ab} e_a e_b \underbrace{\frac{4\pi}{V} \sum_{\boldsymbol{K}} \frac{1}{(\boldsymbol{k}-\boldsymbol{K})^2} e^{-\frac{(\boldsymbol{k}-\boldsymbol{K})^2}{4\alpha^2}} e^{-i(\boldsymbol{k}-\boldsymbol{K})\cdot\boldsymbol{r}}}_{Reciprocal-space-term} \end{aligned} \tag{2.74}$$

In actual simulations, the Block $\boldsymbol{k}$ vector is always taken to be 0, thus there is a divergence when $\boldsymbol{K}$ takes the value of 0. This comes from the infinitely mirrored electric charges. The divergence no longer exists when there is no monopole in the simulation, i.e. the summation of all charges is 0. Taking

$$\sum_{a}^{\text{unit cell}} e_a = 0 \tag{2.75}$$

as a precondition, let's now examine closely what the Ewald term ends up to be at the $\boldsymbol{k} \to 0$ limit (only the $\boldsymbol{K} = 0$ term in $\boldsymbol{K}$ summation has problem)

$$\begin{aligned} &\lim_{k\to 0} \sum_{ab} e_a e_b \frac{4\pi}{V} \frac{1}{k^2} e^{-\frac{k^2}{4\alpha^2}} e^{-i\boldsymbol{k}\cdot\boldsymbol{r}} \\ &= \sum_{ab} e_a e_b \lim_{k\to 0} \frac{4\pi}{V} \frac{1}{k^2} \left\{ (1 - \frac{k^2}{4\alpha^2}) \left[1 - i\boldsymbol{k}\cdot\boldsymbol{r} + \frac{1}{2}(-i\boldsymbol{k}\cdot\boldsymbol{r})^2 \right] \right\} + \mathcal{O}(k) \\ &= \sum_{ab} e_a e_b \lim_{k\to 0} \frac{4\pi}{V} \frac{1}{k^2} \left[1 - i\boldsymbol{k}\cdot\boldsymbol{r} - \frac{k^2}{4\alpha^2} - \frac{1}{2}(\boldsymbol{k}\cdot\boldsymbol{r})^2 \right] + \mathcal{O}(k) \end{aligned} \tag{2.76}$$

There are 4 terms inside the square bracket in (2.76), first and third is 0 from (2.75)[3],

[3]For simulations which have monopole, esp. with changing charge, people simply ignore the divergence part (first term) and keep the convergence part (third term), so in many books, there is a charged system correction term

$$-\frac{1}{2V\alpha^2} \left(\sum_a e_a \right)^2 \tag{2.77}$$

second is pure imaginary, which is just an artifact of our construct (as we will mention later, all the imaginary parts in the fomulae will be ignored in calculation).

Thus, only the last term contributes. But one will quickly realize that this term is sensitive to the direction in which $\boldsymbol{k}$ goes to zero! This is not surprising if we know that there is an arbitrary surface dipole at infinity. The direction of $\boldsymbol{k}$ indicates the direction of the dipole. If we consider our sample to be surrounded by metals (dielectric constant $\varepsilon = 0$), there will be no surface dipole, so this term can be dropped too.

So at last, we can write:

$$U^C_{sum} = \sum_{ab} e_a e_b \underbrace{\sum_{\boldsymbol{R}} \frac{\mathrm{erfc}(\alpha|\boldsymbol{r}+\boldsymbol{R}|)}{|\boldsymbol{r}+\boldsymbol{R}|} e^{i\boldsymbol{k}\cdot\boldsymbol{R}}}_{Real-space-term} + \sum_{ab} e_a e_b \underbrace{\frac{4\pi}{V} \sum_{\boldsymbol{K}\neq 0} \frac{1}{K^2} e^{-\frac{K^2}{4\alpha^2}} e^{i\boldsymbol{K}\cdot\boldsymbol{r}}}_{Reciprocal-space-term} \tag{2.78}$$

we can further simplify this formula as following: in $\boldsymbol{K}$ summation, $\boldsymbol{r} = \boldsymbol{r}_a - \boldsymbol{r}_b$ and $\sum_{ab} = \frac{1}{2}\sum_a \sum_b$, $\sum_{\boldsymbol{K}} = 2\sum_{\boldsymbol{K}>0}$ [4]. In $\boldsymbol{R}$ summation, all terms are short-ranged, for an MD simulation with big enough unit cell, we can ignore summation over mirror images altogether. The final formula for Ewald energy used in MD is:

$$U^C_{sum} = \sum_{ab} \frac{e_a e_b}{r} = \sum_{ab} e_a e_b \frac{\mathrm{erfc}(\alpha r)}{r} + \frac{4\pi}{V} \sum_{\boldsymbol{K}>0} \frac{1}{K^2} e^{-\frac{K^2}{4\alpha^2}} \left| \sum_{a=1}^{N} e_a e^{i\boldsymbol{K}\cdot\boldsymbol{r}_a} \right|^2 \tag{2.79}$$

The force on particle a is given by

$$\begin{aligned} \boldsymbol{f}^C_a &= -\nabla_{\boldsymbol{r}_a} U^C_{tot} \\ &= e_a \sum_{b\neq a} e_b \left\{ \left[\frac{\mathrm{erfc}(\alpha r)}{r} + \frac{2\alpha}{\sqrt{\pi}} e^{-\alpha^2 r^2} \right] \frac{\boldsymbol{r}}{r^2} e^{i\boldsymbol{k}\cdot\boldsymbol{R}} + \frac{8\pi}{V} \sum_{\boldsymbol{K}>0} \frac{-i\boldsymbol{K}}{K^2} e^{-\frac{K^2}{4\alpha^2}} \left(e^{i\boldsymbol{K}\cdot\boldsymbol{r}}\right) \right\} \end{aligned} \tag{2.80}$$

We should keep in mind that in all the formulae, only the real part is taken, the imaginary part exists just to simplify the derivation, i.e. it is cleaner to deal with exponentials than trigonometric funtions. So effectively, $e^{i\boldsymbol{k}\cdot\boldsymbol{r}}$ should be $\cos(\boldsymbol{k}\cdot\boldsymbol{r})$ and $-ie^{i\boldsymbol{k}\cdot\boldsymbol{r}}$ should be $\sin(\boldsymbol{k}\cdot\boldsymbol{r})$, etc.

[4] By $\sum_{\boldsymbol{K}>0}$ we mean sum over any half of the Brillouin zone.

2.4.2 Quadruple Moments

In the formulae of internal stress and elastic constants, some of the important terms have the form $\frac{r_i r_j}{r}\frac{\partial U}{\partial r}$ and $\frac{r_i r_j r_k r_l}{r^2}\frac{\partial^2 U}{\partial r^2}$. For a Coulombic system, these terms also go like $1/r$ thus need Ewald's construction to calculate. Because we will be dealing with lengthy expressions from now on, let's introduce some short-hand notations first

$$\boldsymbol{r}^{\boldsymbol{R}} \equiv \boldsymbol{r} + \boldsymbol{R} \qquad \boldsymbol{k}^{\boldsymbol{K}} \equiv \boldsymbol{k} - \boldsymbol{K} \tag{2.81}$$

Define:

$$X_{ij}^{C} = \sum \frac{r_i r_j}{r^3} \tag{2.82}$$

as in (2.57),we can write (2.82) for the periodic crystal system

$$X_{ij}^{C} = \sum_{\boldsymbol{R}} \frac{r_i^{\boldsymbol{R}} r_j^{\boldsymbol{R}}}{(r^{\boldsymbol{R}})^3} e^{i\boldsymbol{k}\cdot\boldsymbol{R}} = -\sum_{\boldsymbol{R}} r_i^{\boldsymbol{R}} \frac{\partial}{\partial r_j} \frac{e^{i\boldsymbol{k}\cdot\boldsymbol{R}}}{r^{\boldsymbol{R}}} \tag{2.83}$$

apply (2.59), we get

$$X_{ij}^{C} = -\sum_{\boldsymbol{R}} r_i^{\boldsymbol{R}} \frac{\partial}{\partial r_j} \left[e^{i\boldsymbol{k}\cdot\boldsymbol{R}} \frac{2}{\sqrt{\pi}} \int_0^{\infty} e^{-(r^{\boldsymbol{R}})^2\rho^2} \mathrm{d}\rho \right] \tag{2.84}$$

similar to Ewald's construction of $1/r$, we split the integration with a parameter α as $\int_0^{\infty} = \int_{\alpha}^{\infty} + \int_0^{\alpha}$. Then try to keep $\int_{\alpha}^{\infty}$ in real-space $\boldsymbol{R}$ summation and convert $\int_0^{\alpha}$ into reciprocal-space $\boldsymbol{K}$ summation. Define

$$\mathcal{R}(X_{ij}^{C}) = -\sum_{\boldsymbol{R}} r_i^{\boldsymbol{R}} \frac{\partial}{\partial r_j} \left[e^{i\boldsymbol{k}\cdot\boldsymbol{R}} \frac{2}{\sqrt{\pi}} \int_{\alpha}^{\infty} e^{-(r^{\boldsymbol{R}})^2\rho^2} \mathrm{d}\rho \right] \tag{2.85}$$

$$\mathcal{K}(X_{ij}^{C}) = -\sum_{\boldsymbol{R}} r_i^{\boldsymbol{R}} \frac{\partial}{\partial r_j} \left[e^{i\boldsymbol{k}\cdot\boldsymbol{R}} \frac{2}{\sqrt{\pi}} \int_0^{\alpha} e^{-(r^{\boldsymbol{R}})^2\rho^2} \mathrm{d}\rho \right] \tag{2.86}$$

where $\mathcal{R}(X_{ij}^C)$ is evaluated as

$$\begin{aligned}\mathcal{R}(X_{ij}^C) &= -\sum_{\boldsymbol{R}} r_i^{\boldsymbol{R}} \frac{\partial}{\partial r_j}\left[e^{i\boldsymbol{k}\cdot\boldsymbol{R}}\frac{2}{\sqrt{\pi}}\frac{\mathrm{erfc}(\alpha r^{\boldsymbol{R}})}{r^{\boldsymbol{R}}}\right] \\ &= \sum_{\boldsymbol{R}}\left[\frac{\mathrm{erfc}(\alpha r^{\boldsymbol{R}})}{r^{\boldsymbol{R}}}+\frac{2\alpha}{\sqrt{\pi}}e^{-\alpha^2(r^{\boldsymbol{R}})^2}\right]\frac{r_i^{\boldsymbol{R}} r_j^{\boldsymbol{R}}}{(r^{\boldsymbol{R}})^2}e^{i\boldsymbol{k}\cdot\boldsymbol{R}} \qquad (2.87)\end{aligned}$$

To calculate the reciprocal-space part, notice the commutation relation

$$r_i\frac{\partial}{\partial r_j}A(\boldsymbol{r}) = \frac{\partial}{\partial r_j}\left[r_i A(\boldsymbol{r})\right] - \delta_{ij}A(\boldsymbol{r}) \qquad (2.88)$$

where $A(\boldsymbol{r})$ denote any function of $\boldsymbol{r}$. We can put the $\frac{\partial}{\partial r_j}$ outside the summation

$$\begin{aligned}\mathcal{K}(X_{ij}^C) &= \delta_{ij}\sum_{\boldsymbol{R}} e^{i\boldsymbol{k}\cdot\boldsymbol{R}}\frac{2}{\sqrt{\pi}}\int_0^\alpha e^{-(r^{\boldsymbol{R}})^2\rho^2}\mathrm{d}\rho \\ &\quad -\frac{\partial}{\partial r_j}\sum_{\boldsymbol{R}} r_i^{\boldsymbol{R}} e^{i\boldsymbol{k}\cdot\boldsymbol{R}}\frac{2}{\sqrt{\pi}}\int_0^\alpha e^{-(r^{\boldsymbol{R}})^2\rho^2}\mathrm{d}\rho \qquad (2.89)\end{aligned}$$

The first term (δ_{ij} term) is same as in (2.60), so we can just write down the result as

$$\delta_{ij}\frac{4\pi}{V}\sum_{\boldsymbol{K}}\frac{1}{(k^{\boldsymbol{K}})^2}e^{-\frac{(k^{\boldsymbol{K}})^2}{4\alpha^2}}e^{-i(k^{\boldsymbol{K}})\cdot\boldsymbol{r}} \qquad (2.90)$$

For the second term, notice that

$$r_i^{\boldsymbol{R}}e^{i\boldsymbol{k}\cdot(r^{\boldsymbol{R}})} = -i\frac{\partial}{\partial k_i}e^{i\boldsymbol{k}\cdot(r^{\boldsymbol{R}})} \qquad (2.91)$$

So the second term of (2.89) can be written as

$$
\begin{aligned}
& -\frac{\partial}{\partial r_j}\sum_{\boldsymbol{R}}\left[(-i)\frac{\partial}{\partial k_i}e^{i\boldsymbol{k}\cdot(\boldsymbol{r}^{\boldsymbol{R}})}\right]e^{-i\boldsymbol{k}\cdot\boldsymbol{r}}\frac{2}{\sqrt{\pi}}\int_0^{\alpha}e^{-(r^{\boldsymbol{R}})^2\rho^2}\mathrm{d}\rho \\
= \; & i\frac{\partial}{\partial r_j}e^{-i\boldsymbol{k}\cdot\boldsymbol{r}}\frac{\partial}{\partial k_i}\int_0^{\alpha}\left\{\frac{2}{\sqrt{\pi}}\sum_{\boldsymbol{R}}e^{-(r^{\boldsymbol{R}})^2\rho^2+i\boldsymbol{k}\cdot(\boldsymbol{r}^{\boldsymbol{R}})}\right\}\mathrm{d}\rho \\
= \; & i\frac{\partial}{\partial r_j}e^{-i\boldsymbol{k}\cdot\boldsymbol{r}}\frac{\partial}{\partial k_i}\int_0^{\alpha}\left\{\frac{2\pi}{V}\sum_{\boldsymbol{K}}\frac{1}{\rho^3}e^{-\frac{1}{4\rho^2}(k^{\boldsymbol{K}})^2+i\boldsymbol{K}\cdot\boldsymbol{r}}\right\}\mathrm{d}\rho \\
= \; & i\frac{\partial}{\partial r_j}e^{-i\boldsymbol{k}\cdot\boldsymbol{r}}\frac{\partial}{\partial k_i}\frac{4\pi}{V}\sum_{\boldsymbol{K}}\frac{1}{(k^{\boldsymbol{K}})^2}e^{-\frac{(k^{\boldsymbol{K}})^2}{4\alpha^2}}e^{i\boldsymbol{K}\cdot\boldsymbol{r}} \\
= \; & -\sum_{\boldsymbol{K}}\frac{8\pi}{V}\left[\frac{1}{(k^{\boldsymbol{K}})^2}+\frac{1}{4\alpha^2}\right]\frac{k_i^{\boldsymbol{K}}k_j^{\boldsymbol{K}}}{(k^{\boldsymbol{K}})^2}e^{-\frac{(k^{\boldsymbol{K}})^2}{4\alpha^2}}e^{-i\boldsymbol{k}^{\boldsymbol{K}}\cdot\boldsymbol{r}}
\end{aligned}
\tag{2.92}
$$

Now we put the two terms together to obtain the expression for $\mathcal{K}(X_{ij}^C)$:

$$
\mathcal{K}(X_{ij}^C)=\sum_{\boldsymbol{K}}\frac{4\pi}{V}\left\{\delta_{ij}-2\left[\frac{1}{(k^{\boldsymbol{K}})^2}+\frac{1}{4\alpha^2}\right]k_i^{\boldsymbol{K}}k_j^{\boldsymbol{K}}\right\}\frac{e^{-\frac{(k^{\boldsymbol{K}})^2}{4\alpha^2}-i\boldsymbol{k}^{\boldsymbol{K}}\cdot\boldsymbol{r}}}{(k^{\boldsymbol{K}})^2} \tag{2.93}
$$

Finally we get the Ewald construction for r_ir_j/r^3

$$
\begin{aligned}
X_{ij}^C \; = \; & \underbrace{\sum_{\boldsymbol{R}}\left[\frac{\mathrm{erfc}(\alpha r^{\boldsymbol{R}})}{r^{\boldsymbol{R}}}+\frac{2\alpha}{\sqrt{\pi}}e^{-\alpha^2(r^{\boldsymbol{R}})^2}\right]\frac{r_i^{\boldsymbol{R}}r_j^{\boldsymbol{R}}}{(r^{\boldsymbol{R}})^2}e^{i\boldsymbol{k}\cdot\boldsymbol{R}}}_{Real-space-term} \\
& + \underbrace{\frac{4\pi}{V}\sum_{\boldsymbol{K}}\left[\delta_{ij}-2\left(\frac{1}{(k^{\boldsymbol{K}})^2}+\frac{1}{4\alpha^2}\right)k_i^{\boldsymbol{K}}k_j^{\boldsymbol{K}}\right]\frac{e^{-\frac{(k^{\boldsymbol{K}})^2}{4\alpha^2}-i\boldsymbol{k}^{\boldsymbol{K}}\cdot\boldsymbol{r}}}{(k^{\boldsymbol{K}})^2}}_{Reciprocal-space-term}
\end{aligned}
\tag{2.94}
$$

Similar to the U^C case, in simulation, we take $\boldsymbol{k}$ to be 0, remove the divergence, and convert the $\boldsymbol{K}$ summation over pairs into summation over single atoms by writing $\boldsymbol{r}=\boldsymbol{r}_a-\boldsymbol{r}_b$, omit $\boldsymbol{R}$ summation for the short range charactor of every term in it.

The final formula to use in simulation is:

$$\begin{aligned}\sum_{ab} e_a e_b \frac{r_i r_j}{r^3} &= \sum_{ab} e_a e_b \left[\frac{\operatorname{erfc}(\alpha r)}{r} + \frac{2\alpha}{\sqrt{\pi}} e^{-\alpha^2 r^2}\right] \frac{r_i r_j}{r^2} \\ &+ \frac{4\pi}{V} \sum_{\boldsymbol{K}>0} \left\{\delta_{ij} - 2\left[\frac{1}{K^2} + \frac{1}{4\alpha^2}\right] K_i K_j\right\} \frac{1}{K^2} e^{-\frac{K^2}{4\alpha^2}} \left|\sum_{a=1}^{N} e_a e^{i\boldsymbol{K}\cdot\boldsymbol{r}_a}\right|^2\end{aligned} \tag{2.95}$$

2.4.3 Octupole Moments

Define:

$$F^C_{ijkl} = \sum \frac{3 r_i r_j r_k r_l}{r^5} \tag{2.96}$$

Let's first examine the second derivative of $\frac{1}{r}$

$$\begin{aligned}\frac{\partial^2}{\partial r_i \partial r_j}\frac{1}{r} &= \frac{\partial}{\partial r_i}\left[\left(\frac{\partial}{\partial r}\frac{1}{r}\right)\frac{r_j}{r}\right] \\ &= \left(\frac{\partial^2}{\partial r^2}\frac{1}{r}\right)\frac{r_i r_j}{r^2} - \left(\frac{\partial}{\partial r}\frac{1}{r}\right)\frac{r_i r_j}{r^3} + \frac{1}{r}\left(\frac{\partial}{\partial r}\frac{1}{r}\right)\delta_{ij} \\ &= \frac{3 r_i r_j}{r^5} - \frac{1}{r^3}\delta_{ij}\end{aligned} \tag{2.97}$$

So we have

$$\begin{aligned}F^C_{ijkl} &= \sum r_k r_l \left(\frac{\partial^2}{\partial r_i \partial r_j}\frac{1}{r} + \frac{1}{r^3}\delta_{ij}\right) \\ &= \sum_{\boldsymbol{R}} r^{\boldsymbol{R}}_k r^{\boldsymbol{R}}_l \frac{\partial^2}{\partial r_i \partial r_j}\left(\frac{e^{i\boldsymbol{k}\cdot\boldsymbol{R}}}{r^{\boldsymbol{R}}}\right) + \delta_{ij} X^C_{kl}\end{aligned} \tag{2.98}$$

Naturally we define real-space and reciprocal-space parts of F^C_{ijkl} as:

$$\mathcal{R}(F^C_{ijkl}) = \sum_{\boldsymbol{R}} r^{\boldsymbol{R}}_k r^{\boldsymbol{R}}_l \frac{\partial^2}{\partial r_i \partial r_j}\left[e^{i\boldsymbol{k}\cdot\boldsymbol{R}}\frac{2}{\sqrt{\pi}}\int_\alpha^\infty e^{-(r^{\boldsymbol{R}})^2\rho^2}\mathrm{d}\rho\right] + \delta_{ij}\mathcal{R}(X^C_{kl}) \tag{2.99}$$

$$\mathcal{K}(F^C_{ijkl}) = \sum_{\boldsymbol{R}} r^{\boldsymbol{R}}_k r^{\boldsymbol{R}}_l \frac{\partial^2}{\partial r_i \partial r_j}\left[e^{i\boldsymbol{k}\cdot\boldsymbol{R}}\frac{2}{\sqrt{\pi}}\int_0^\alpha e^{-(r^{\boldsymbol{R}})^2\rho^2}\mathrm{d}\rho\right] + \delta_{ij}\mathcal{K}(X^C_{kl}) \tag{2.100}$$

First evaluate $\mathcal{R}(F^C_{ijkl})$:

$$\begin{aligned}\mathcal{R}(F^C_{ijkl}) &= \sum_{\boldsymbol{R}} r^{\boldsymbol{R}}_k r^{\boldsymbol{R}}_l \frac{\partial^2}{\partial r_i \partial r_j}\left[\frac{\operatorname{erfc}(\alpha r^{\boldsymbol{R}})}{r^{\boldsymbol{R}}} e^{i\boldsymbol{k}\cdot\boldsymbol{R}}\right] + \delta_{ij}\mathcal{R}(X^C_{kl}) \\ &= -\sum_{\boldsymbol{R}} r^{\boldsymbol{R}}_k r^{\boldsymbol{R}}_l \frac{\partial}{\partial r_i}\left\{\left[\frac{\operatorname{erfc}(\alpha r^{\boldsymbol{R}})}{r^{\boldsymbol{R}}} + \frac{2\alpha}{\sqrt{\pi}} e^{-\alpha^2 (r^{\boldsymbol{R}})^2}\right]\frac{r^{\boldsymbol{R}}_j}{(r^{\boldsymbol{R}})^2} e^{i\boldsymbol{k}\cdot\boldsymbol{R}}\right\} \\ &\quad +\delta_{ij}\mathcal{R}(X^C_{kl}) \end{aligned} \tag{2.101}$$

Recall (2.88), this δ_{ij} term can be absorbed into the first term by exchanging $\frac{\partial}{\partial r_i}$ with $r^{\boldsymbol{R}}_j$

$$\begin{aligned}\mathcal{R}(F^C_{ijkl}) &= -\sum_{\boldsymbol{R}} r^{\boldsymbol{R}}_j r^{\boldsymbol{R}}_k r^{\boldsymbol{R}}_l e^{i\boldsymbol{k}\cdot\boldsymbol{R}} \cdot \\ &\quad \frac{\partial}{\partial r_i}\left[\frac{\operatorname{erfc}(\alpha r^{\boldsymbol{R}})}{(r^{\boldsymbol{R}})^3} + \frac{2\alpha}{\sqrt{\pi}} e^{-(\alpha r^{\boldsymbol{R}})^2}\frac{1}{(r^{\boldsymbol{R}})^2}\right] \\ &= \sum_{\boldsymbol{R}} r^{\boldsymbol{R}}_i r^{\boldsymbol{R}}_j r^{\boldsymbol{R}}_k r^{\boldsymbol{R}}_l e^{i\boldsymbol{k}\cdot\boldsymbol{R}}\left[\frac{3\operatorname{erfc}(\alpha r^{\boldsymbol{R}})}{(r^{\boldsymbol{R}})^5} + \right. \\ &\quad \left.\frac{6\alpha}{\sqrt{\pi}(r^{\boldsymbol{R}})^4} e^{-\alpha^2 (r^{\boldsymbol{R}})^2} + \frac{4\alpha^3}{\sqrt{\pi}(r^{\boldsymbol{R}})^2} e^{-\alpha^2 (r^{\boldsymbol{R}})^2}\right] \end{aligned} \tag{2.102}$$

To evaluate $\mathcal{K}(F^C_{ijkl})$ we need to move $\frac{\partial^2}{\partial r_i \partial r_j}$ out of the $\boldsymbol{R}$ summation.

$$\begin{aligned} r_k r_l \frac{\partial^2}{\partial r_i \partial r_j} A(r) &= \frac{\partial^2}{\partial r_i \partial r_j}[r_k r_l A(r)] - (\delta_{jk}\delta_{il} + \delta_{ik}\delta_{jl})A(r) - \delta_{jk} r_l \frac{\partial}{\partial r_i} A(r) \\ &\quad - \delta_{ik} r_l \frac{\partial}{\partial r_j} A(r) - \delta_{jl} r_k \frac{\partial}{\partial r_i} A(r) - \delta_{il} r_k \frac{\partial}{\partial r_j} A(r) \end{aligned} \tag{2.103}$$

Notice that each $-r_i \frac{\partial}{\partial r_j} A(r)$ corresponds to a $\mathcal{K}(X^C_{ij})$ term. So the reciprocal space part is:

$$\begin{aligned}\mathcal{K}(F^C_{ijkl}) &= \sum_{\boldsymbol{R}} \frac{\partial^2}{\partial r_i \partial r_j} r^{\boldsymbol{R}}_k r^{\boldsymbol{R}}_l e^{i\boldsymbol{k}\cdot\boldsymbol{R}} \frac{2}{\sqrt{\pi}} \int_0^\alpha e^{-(r^{\boldsymbol{R}})^2\rho^2} \mathrm{d}\rho - (\delta_{jk}\delta_{il} + \delta_{ik}\delta_{jl})\mathcal{K}(U^C) \\ &\quad +\delta_{jk}\mathcal{K}(X^C_{li}) + \delta_{ik}\mathcal{K}(X^C_{lj}) + \delta_{jl}\mathcal{K}(X^C_{ki}) + \delta_{il}\mathcal{K}(X^C_{kj}) + \delta_{ij}\mathcal{K}(X^C_{kl}) \end{aligned} \tag{2.104}$$

The only non-trivial term is the first term,

$$\begin{aligned}
&\sum_{\boldsymbol{R}} \frac{\partial^2}{\partial r_i \partial r_j} r_k^{\boldsymbol{R}} r_l^{\boldsymbol{R}} e^{i\boldsymbol{k}\cdot\boldsymbol{R}} \frac{2}{\sqrt{\pi}} \int_0^{\alpha} e^{-(r^{\boldsymbol{R}})^2\rho^2} \mathrm{d}\rho \\
= & -\frac{\partial^2}{\partial r_i \partial r_j} e^{-i\boldsymbol{k}\cdot\boldsymbol{r}} \sum_{\boldsymbol{R}} \frac{\partial^2}{\partial k_k \partial k_l} e^{i\boldsymbol{k}\cdot(r^{\boldsymbol{R}})} \frac{2}{\sqrt{\pi}} \int_0^{\alpha} e^{-(r^{\boldsymbol{R}})^2\rho^2} \mathrm{d}\rho \\
= & \frac{4\pi}{V} \sum_{\boldsymbol{K}} k_i^{\boldsymbol{K}} k_j^{\boldsymbol{K}} k_k^{\boldsymbol{K}} k_l^{\boldsymbol{K}} \left[\frac{8}{(k^{\boldsymbol{K}})^4} + \frac{2}{\alpha^2 (k^{\boldsymbol{K}})^2} + \frac{1}{4\alpha^4}\right] \frac{e^{-\frac{(k^{\boldsymbol{K}})^2}{4\alpha^2} - i\boldsymbol{k}^{\boldsymbol{K}}\cdot\boldsymbol{r}}}{(k^{\boldsymbol{K}})^2} \\
& + \delta_{kl}(\mathcal{K}(X_{ij}^C) - \delta_{ij})
\end{aligned} \tag{2.105}$$

Collect all the terms and substitute (2.72) and (2.93), we finally get

$$\mathcal{K}(F_{ijkl}^C) = \frac{4\pi}{V} \sum_{\boldsymbol{K}} \frac{e^{-\frac{(k^{\boldsymbol{K}})^2}{4\alpha^2} - i\boldsymbol{k}^{\boldsymbol{K}}\cdot\boldsymbol{r}}}{(k^{\boldsymbol{K}})^2} \left[S_{ijkl}^A - 2S_{ijkl}^B(k^{\boldsymbol{K}}) + S_{ijkl}^C(k^{\boldsymbol{K}})\right] \tag{2.106}$$

with the following short hand notations

$$S_{ijkl}^A = (\delta_{ij}\delta_{kl} + \delta_{ik}\delta_{jl} + \delta_{il}\delta_{jk}) \tag{2.107}$$

$$S_{ijkl}^B(q) = (q_i q_j \delta_{kl} + q_i q_k \delta_{jl} + q_i q_l \delta_{jk} + q_j q_k \delta_{il} + q_j q_l \delta_{ik} + q_k q_l \delta_{ij}) \left[\frac{1}{q^2} + \frac{1}{4\alpha^2}\right] \tag{2.108}$$

$$S_{ijkl}^C(q) = q_i q_j q_k q_l \left[\frac{8}{q^4} + \frac{2}{\alpha^2 q^2} + \frac{1}{4\alpha^4}\right] \tag{2.109}$$

In simulation, the simplified version of this formula is

$$\begin{aligned}
\sum_{ab} e_a e_b \frac{3 r_i r_j r_k r_l}{r^5} = & \sum_{ab} e_a e_b \frac{r_i r_j r_k r_l}{r^4} \left[\frac{3\,\mathrm{erfc}(\alpha r)}{r} + \left(3\alpha + 2\alpha^3 r^2\right) \frac{2}{\sqrt{\pi}} e^{-\alpha^2 r^2}\right] \\
& + \frac{4\pi}{V} \sum_{\boldsymbol{K}>0} \left[S_{ijkl}^A - 2S_{ijkl}^B(K) + S_{ijkl}^C(K)\right] \frac{1}{K^2} e^{-\frac{K^2}{4\alpha^2}} \left|\sum_{a=1}^{N} e_a e^{i\boldsymbol{K}\cdot\boldsymbol{r}_a}\right|^2
\end{aligned} \tag{2.110}$$

2.4.4 Heat Current

Atomic heat current is a linear function of the interaction potentials, defined as

$$\boldsymbol{J} = \frac{\mathrm{d}}{\mathrm{d}t} \sum_{a}^{N} (E_a \boldsymbol{r}_a) \tag{2.111}$$

In ionic systems, the heat current can be seperated into a short ranged interaction part and a Coulomb part.

$$\boldsymbol{J} = \boldsymbol{J}^C + \boldsymbol{J}^S = \frac{\mathrm{d}}{\mathrm{d}t} \sum_a^N \left[\left(E_a^C + E_a^S \right) \boldsymbol{r}_a \right] \tag{2.112}$$

The Coulomb part is pairwise, which can be expreseed as:

$$\boldsymbol{J}^C = \frac{1}{2} \sum_{a<b}^N \left[U^C(r_{ab})(\boldsymbol{v}_a + \boldsymbol{v}_b) - \frac{1}{r_{ab}} \frac{\partial U^C(r_{ab})}{\partial r_{ab}} [\boldsymbol{r}_{ab} \cdot (\boldsymbol{v}_a + \boldsymbol{v}_b)] \boldsymbol{r}_{ab} \right] + \frac{1}{2} \sum_a \left(m_a v_a^2 \right) \boldsymbol{v}_a \tag{2.113}$$

Putting in $U(r) = e_a e_b / r$, then the i-th (i = 1,2,3) component of $\boldsymbol{J}^C$ is (below $r \equiv r_{ab}$):

$$J_i^C = \frac{1}{2} \sum_{a<b}^N e_a e_b \frac{v_{ai} + v_{bi}}{r} + \frac{1}{2} \sum_{a<b}^N e_a e_b \frac{r_i r_j}{r^3} (v_{ai} + v_{bi}) + \frac{1}{2} \sum_a \left(m_a v_a^2 \right) \boldsymbol{v}_a \tag{2.114}$$

The first and second terms in (2.114) are conditional convergent and thus require Ewald construction. Using the dipole and quadruple moments developed in previous sections, namely (2.73) and (2.94), the $\boldsymbol{J}^C$ can be calculated in MD simulations directly.

2.4.5 Phonon Dispersion

Starting from the formula for the dynamic matirx (A.34), in ionic system, the second derivative of the Coulomb potential is

$$V_{ij}(r) = \frac{\partial^2}{\partial r_i \partial r_j} \frac{e_a e_b}{r} + U_{ij}(r) \tag{2.115}$$

where $U(r)$ is the short term interaction. From what we have done in the previous sections, it is not hard to write down the Ewald construction for each term in the $\sum_{\boldsymbol{R}}$ in (A.34). Putting everything together, the Ewald construction for the ionic system

dynamic matrix can be written as:

$$
\begin{aligned}
\tilde{C}_{ai;bj}(\boldsymbol{k}) &= -\frac{1}{\sqrt{m_a m_b}} \sum_{\boldsymbol{R}} W_{ij}(|\boldsymbol{r}+\boldsymbol{R}|) e^{i\boldsymbol{k}\cdot(\boldsymbol{r}+\boldsymbol{R})} + \\
&\quad + \frac{e_a e_b}{\sqrt{m_a m_b}} \frac{4\pi}{V} \sum_{\boldsymbol{K}\neq 0} \frac{(k_i - K_i)(k_j - K_j)}{(\boldsymbol{k}-\boldsymbol{K})^2} e^{-\frac{(\boldsymbol{k}-\boldsymbol{K})^2}{4\alpha^2} + i\boldsymbol{K}\cdot\boldsymbol{r}} \\
&\quad + \frac{e_a e_b}{\sqrt{m_a m_b}} \frac{4\pi}{V} \frac{k_i k_j}{k^2} e^{-\frac{k^2}{4\alpha^2}} \quad (a \neq b) \\
\tilde{C}_{ai;aj}(\boldsymbol{k}) &= \frac{1}{m_a} \left[\sum_{b\neq a} \sum_{\boldsymbol{R}} W_{ij}(|\boldsymbol{r}+\boldsymbol{R}|) + \sum_{\boldsymbol{R}\neq 0} W_{ij}(R) \left(1 - e^{i\boldsymbol{k}\cdot\boldsymbol{R}}\right) \right] \\
&\quad + \frac{e_a}{m_a} \frac{4\pi}{V} \sum_{\boldsymbol{K}\neq 0} \left[e_a \frac{(k_i - K_i)(k_j - K_j)}{(\boldsymbol{k}-\boldsymbol{K})^2} e^{-\frac{(\boldsymbol{k}-\boldsymbol{K})^2}{4\alpha^2}} - \frac{K_i K_j}{K^2} e^{-\frac{K^2}{4\alpha^2}} \left(\sum_{b=1}^{N} e_b e^{i\boldsymbol{K}\cdot\boldsymbol{r}} \right) \right] \\
&\quad + \frac{e_a^2}{m_a} \frac{4\pi}{V} \frac{k_i k_j}{k^2} e^{-\frac{k^2}{4\alpha^2}}
\end{aligned}
\tag{2.116}
$$

Here $W(r)$ is the short range potential plus short range portion of Coulomb interaction:

$$
W(r) \equiv U(r) + e_a e_b \frac{\mathrm{erfc}(\alpha r)}{r} \tag{2.117}
$$

and the last terms of both equations in (2.116) is dependent on the direction when k approaches 0. This direction dependant means approaching Γ point from different directions will give different frequency, a well known effect called LO-TO splitting[25].

Chapter 3

Strength and Deformation of SiO_2

3.1 Introduction

3.1.1 Potential Models for silica

In 1988, Tsuneyuki *et al.*[81] proposed a Buckingham style pair potential with the partial ionic interactions for silica from *ab initio* calculations of SiO_4 clusters, two years later, in 1990, van Beest *et al.*[7] modified the Tsuneyuki potential for better bulk properties, and proposed a potential model with even simpler forms (BKS potential).

The two pair potential are in similar forms:

- TTAM Potential[81]

$$U_{ab}(r) = e_a e_b / r + A_{ab} \exp(-B_{ab} r) - C_{ab} / r^6 \tag{3.1}$$

The parameters are defined in Table. 3.1.

- BKS Potential[7]

The BKS potential has the same functional form as the TTAM, with a new set of parameters, notably, there is no Si-Si interaction besides Coulomb forces, this is a reflection of the fact that in most stable configurations, distance between silicon atoms are greater than their covalent bond length.

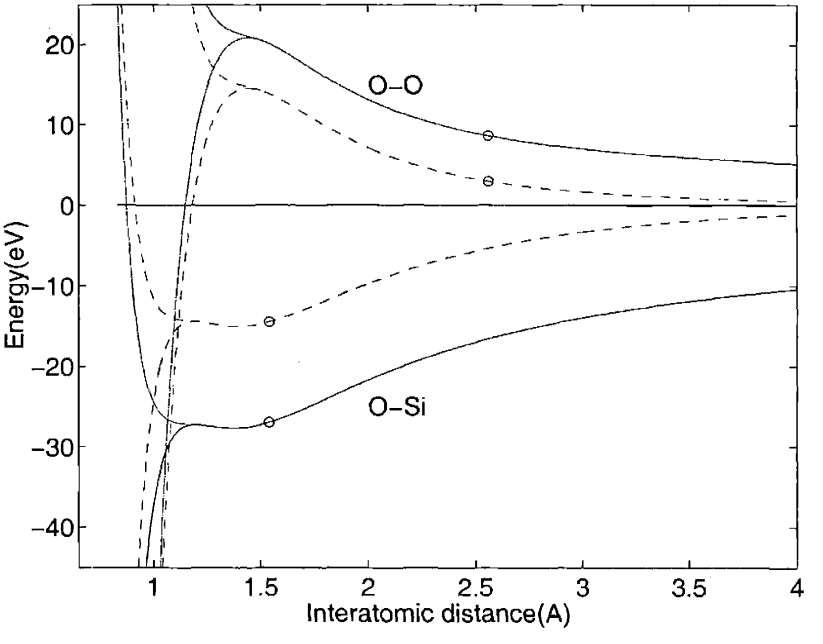

Figure 3-1: The BKS potential function for SiO_2. The solid lines are original form, the dashed lines are effective short range real space part after Ewald construction with $\alpha = 0.284954$. Also shown the added hard core used to prevent atoms from coming too close to each other.

	A_{ab}[eV]	B_{ab}[Å^{-1}]	C_{ab}[eVÅ^6]	
Si-Si	8.72930×10^8	15.2207	23.3154	$e_{\mathrm{Si}} = 2.4e$
Si-O	1.07286×10^4	4.79593	70.7810	$e_{\mathrm{O}} = -1.2e$
O-O	1758.02	2.84641	214.877	

Table 3.1: Parameters for the TTAM potential model

	A_{ab}[eV]	B_{ab}[Å^{-1}]	C_{ab}[eVÅ^6]	
Si-O	18003.7572	4.87318	133.5381	$e_{\mathrm{Si}} = 2.4e$
O-O	1388.7730	2.76000	175.0000	$e_{\mathrm{O}} = -1.2e$

Table 3.2: Parameters for the BKS potential model

A detailed discussion of how to deal with long range Coulomb interaction by Ewald construction is described in section 2.4.

3.2 Stress-Strain Responses

Several stress-strain response studies are carried out with a relative small system of 576 atoms. Fig.3-2 is the hydrostatic tension response of quartz at 300°K and 800°K. The kinks exist for both curve at about 3% strain is a manifestation of the α-quartz to β-quartz transition, which is studied in detail in Sec.3.4. It is notable that the temperature dependence is quite weak for quartz crystals. The change in theoretical strength from 300°K to 800°K, which spans about 1/3 of melting temperature, is only about 10%. As we will see in next chapter, the temperature effect on theoretical strength of ZrC is more pronounced.

Fig.3-3 the hydrostatic stress-strain curve obtained through static calculation in contrast to MD simulation. The anisotropy is shown. Fig.3-4 shows the stress-strain curves of uniaxial tension at 300°K for two directions $(11\bar{2}0)$ and (0001). Fig.3-5 is a combination of three shear responses. The three shear simulations corresponds to three shear stress components, acting on $\{1\bar{1}00\}\langle 11\bar{2}0\rangle$, $\{11\bar{2}0\}\langle 0001\rangle$

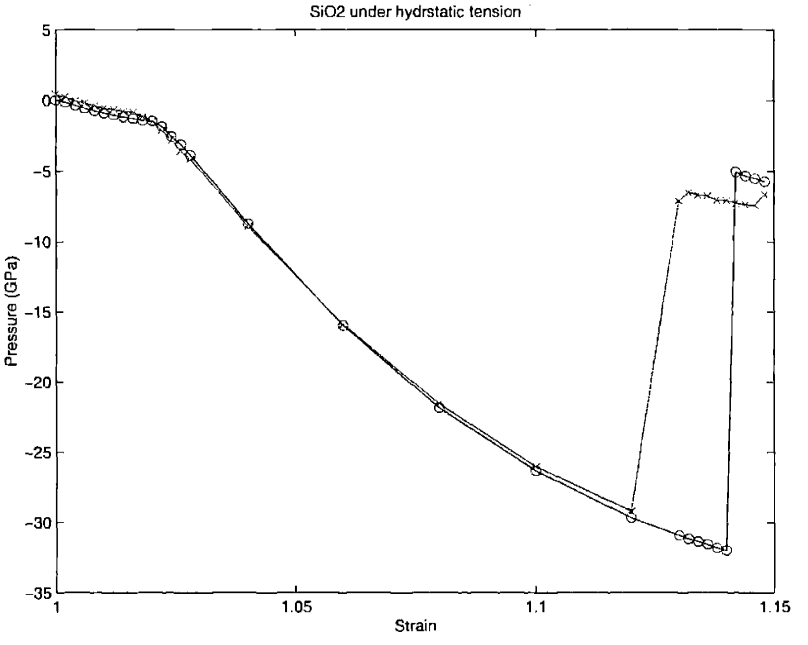

Figure 3-2: Stress-strain curves of quartz under hydrostatic tension at 300°K and 800°K.

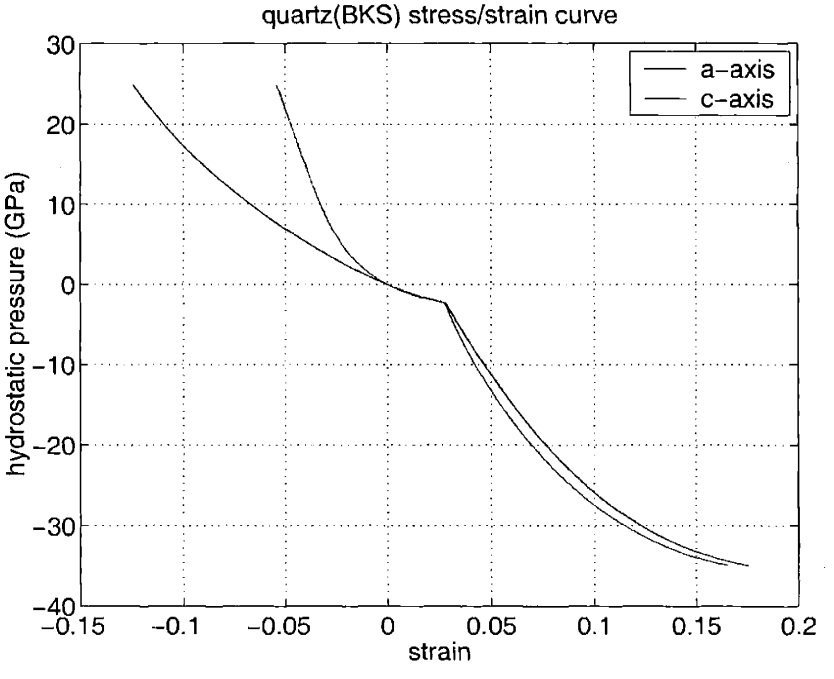

Figure 3-3: The 0°K quartz hydrostatic stress strain curves with BKS model. The anisotropy of a-axis and c-axis is shown.

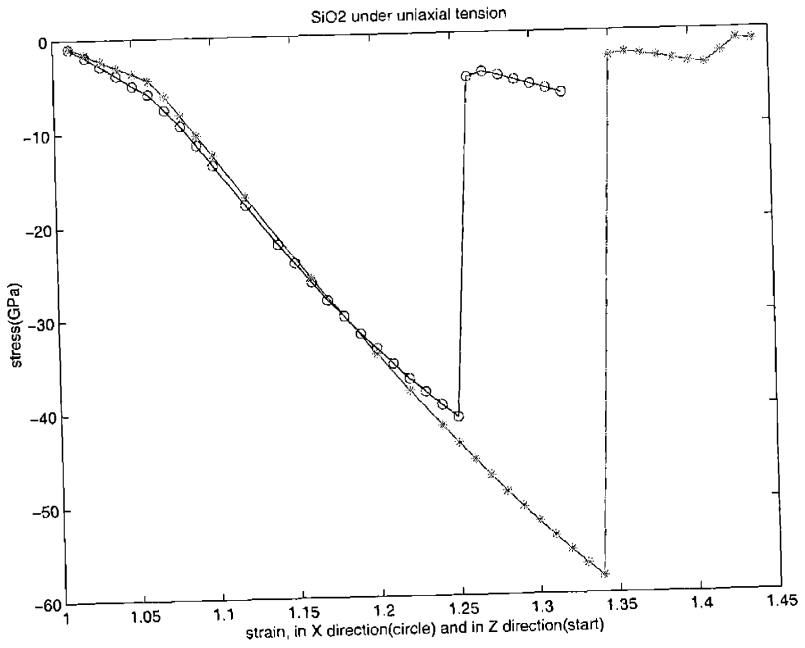

Figure 3-4: Stress-strain curves of quartz under uniaxial tension at 300°K. tensile stress is applied in $(11\bar{2}0)$(circle) and (0001)(star) directions.

and $\{0001\}\langle 1\bar{1}00\rangle$ respectively. Failures happen in first two loading conditions by structural disorder; for the third loading, conducted on the primary slip system of quartz[82, 83], release the shear stress by clean slips, signified by the repeating pattern of stress-strain curve. Due to the small system size, we are not able to see any dislocation activity; rather, the system slips all together. A large system is needed to studied any possible dislocations in quartz.

Another feature on the shear stress-strain curve is the kinks at lower strains. From atomistic configurations, this kink is identified as a structural transition between the two *Dauphiné twins* of the quartz. At zero external shear the two structures have same energy, with shear stress applied, the symmetry is broken. The higher energy structure becomes metastable as soon as non-zero shear is applied; but to overcome the potential barrier, significant amount of shear stress needs to be applied before the transition could occur. The transition seen in simulation could be observed in experiments if a pure single crystal is subjected to carefully designed shear loading where slip systems are avoided.

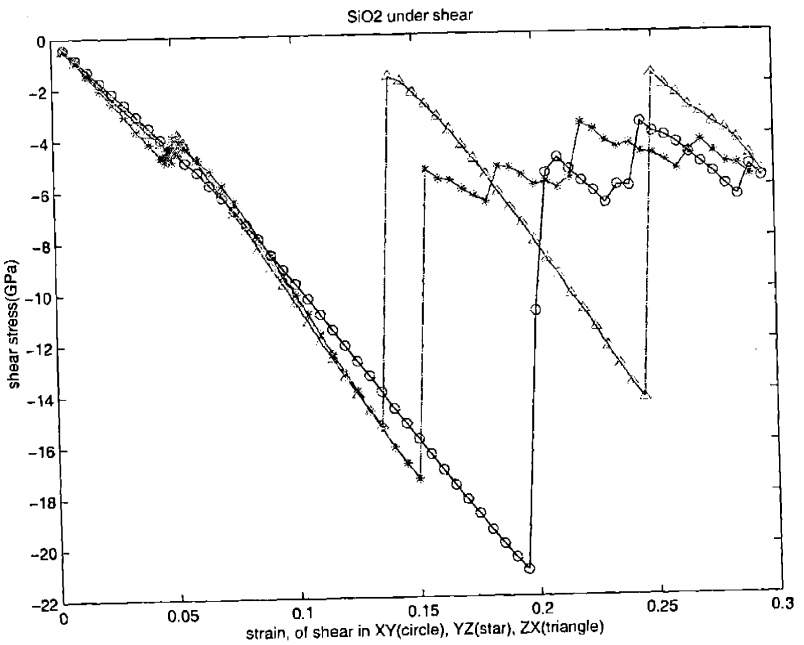

Figure 3-5: stress strain curves of quartz under shear.

3.3 Phonon Dispersion Relations

Phonon dispersion calculations are carried out by the formulation given in Sec.2.4, the phonon modes is calculated for both relaxed system and loaded system.

Because there are 9 atoms (3 SiO_2 molecules) in the unit-cell of quartz, the complete phonon has 27 different branches.

Fig.3-6 shows the complete phonon dispersion curves calculated from the BKS potential model. Due to the ionic nature of the interaction, the LO-TO splitting[25] at Γ point is seen. Compared with experimental neutron scattering measurements, shown in Fig.3-7[26] and Fig.3-8[27], we can see that besides differences in higher optical bands, the dispersion matches fairly well.

Having verified the model with experiments, we can use the model to study the system under external stress. If traced through the continuous increasing of external stress, the individual phonon bands can be identified as they cross each other and move up or down in response to external stress. Fig.3-9 and Fig.3-10 shows the hydrostatic tension and compression soft phonon modes. Compared with the normal condition

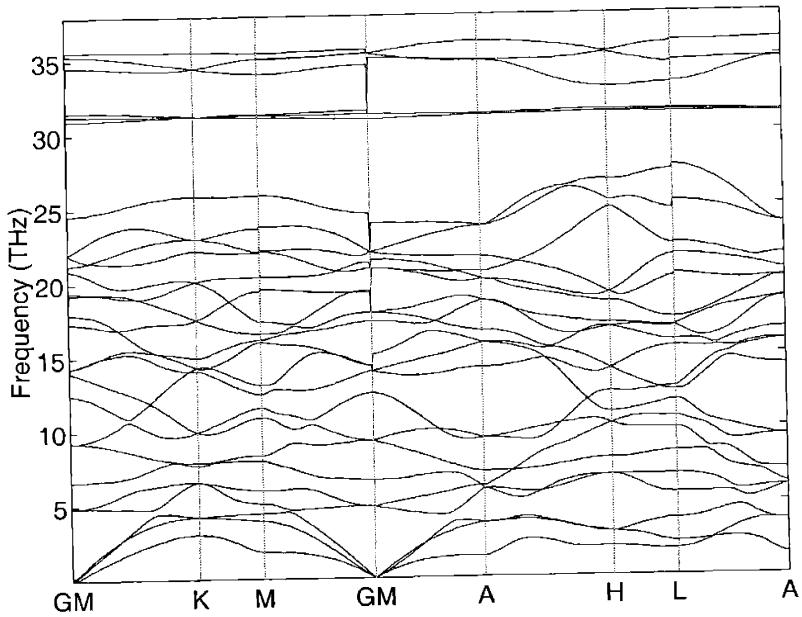

Figure 3-6: The phonon dispersion relations of quartz with BKS model. No external pressure

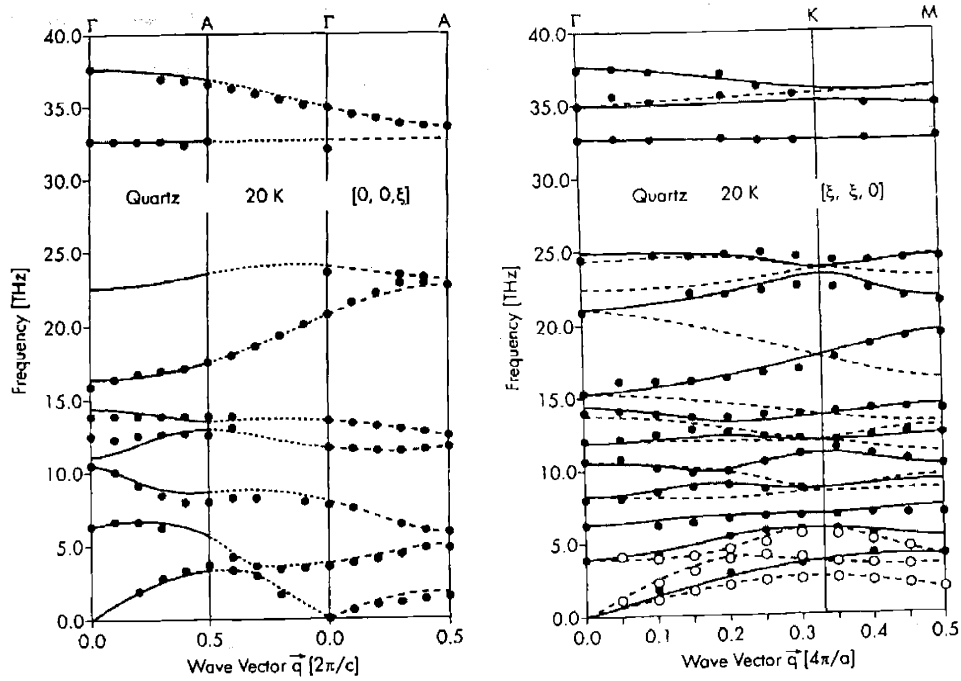

Figure 3-7: Inelastic neutron scattering experimental results (points) of quartz phonon dispersion curve. Reproduced from[26]

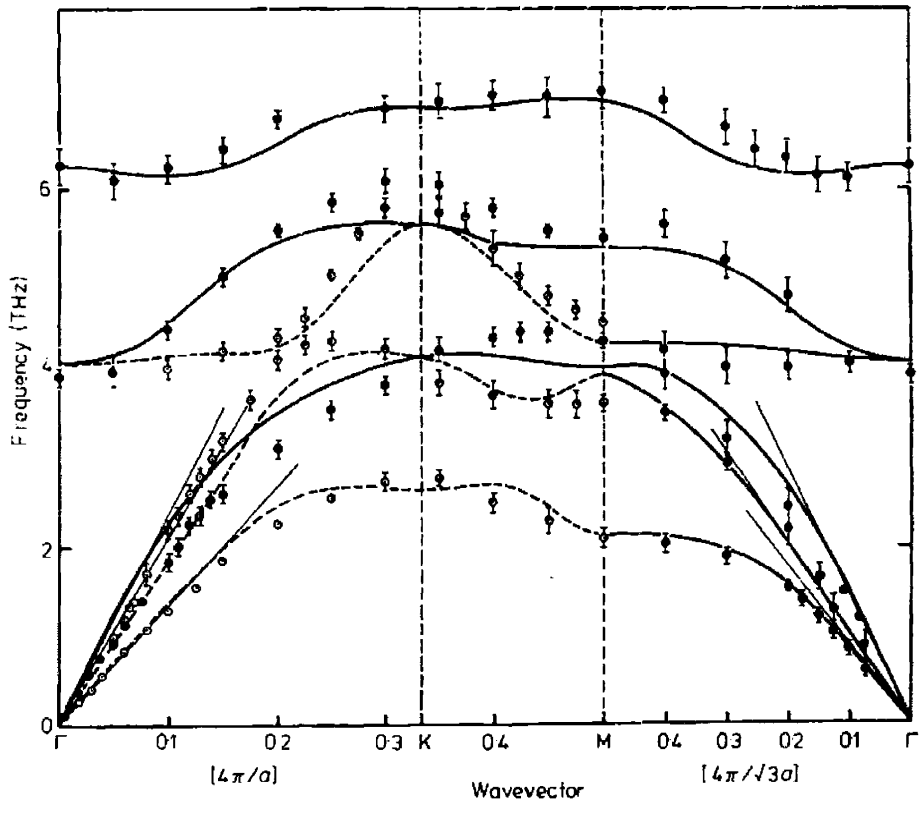

Figure 3-8: Neutron scattering experimental results (points) of six lowest phonon dispersion branches of α-quartz at room temperature. Reproduced from[27].

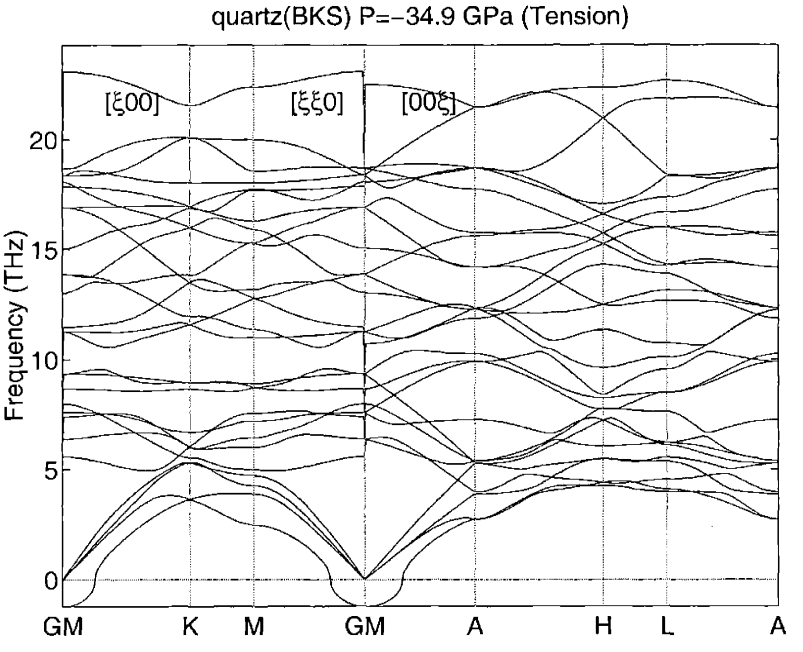

Figure 3-9: The phonon dispersion relations of quartz with BKS model. 34.9GPa external hydrostaic tension, the first appearance of soft mode correspond to a Γ point optical phonon.

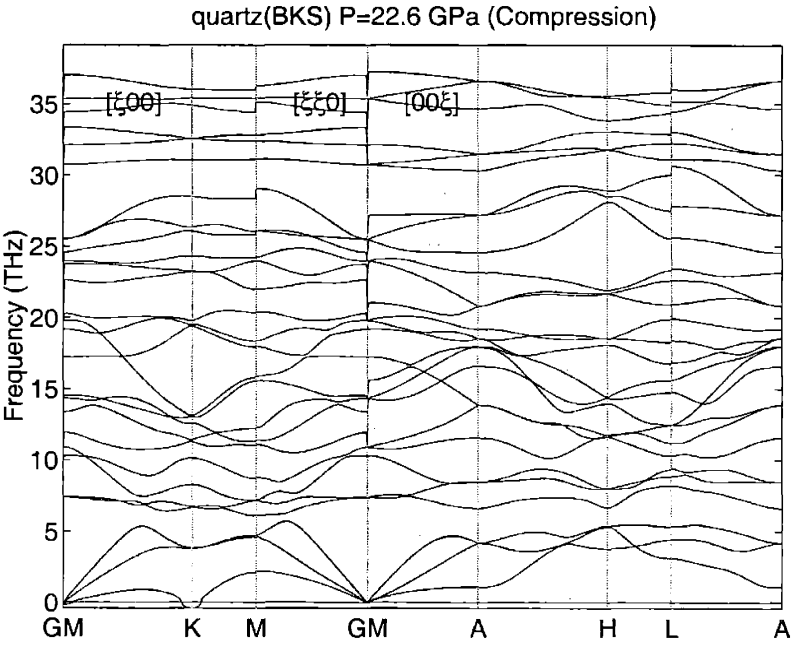

Figure 3-10: The phonon dispersion relations of quartz with BKS model. 22.6GPa external hydrostaic compression, the first appearance of soft mode corresponds to K point acoustic phonon.

dispersion curves in Fig.3-6, we can see that under tension, the atoms are separated further, the far-field interactions between atoms are relatively flat, giving rise to the uniform decrease of all phonon bands. At near failure, the hardest phonon, originally has frequency of 30 to 35[THz], decreases drastically and eventually becomes the soft phonon mode. This relates to the bond breaking that occurs at the point of failure. In the hydrostatic compression, the phonon bands goes up to higher frequencies as the atoms are pushed together. The near degenerate top optical modes is spread out during the process. As the stress increases, both K point acoustic phonons and A point acoustic phonons are getting softer, indicating the compression comes in all directions. Eventually the first soft mode turns out to be a K point phonon.

Admittedly, the phonon dispersion calculations are best performed using first principles, the continuous phonon band evolution through large ranges of external condition can be prohibitively expansive. Considering that it is extremely hard to get to finite temperatures with first principles calculations, the molecular dynamics and other atomistic simulation techniques can be a valuable tool to study phonon dispersion curve in connection with both solid state theories and neutron scattering experiments.

Studying soft phonon modes can give valuable insights to both structural transformations (Sec.3.4) and lattice instabilities (Sec.3.5).

3.4 Quartz Under Tension: α to β Phase Transition

In normal conditions, α quartz will transform into β quartz at 847°K. Through a series of molecular dynamics(MD) simulations, we have reproduced this transition by tension as well as by heating. The study of free energy at 0°K tension induced transition reveals the double potential well mechanism for the transition. A model of Ising-like system coupled to compressible lattices is used to explain this near critical first order transition. The order parameters can be fitted very well on the basis of

a pseudo-critical behavior. We have shown that a non-Γ point vibration mode leads to an instability of the crystal at the transition point, before the critical point can be reached. After the transition, the system breaks into regions of the two Dauphiné twins. The system becomes homogeneous again further down the transition path, where all atoms oscillate around the true β-quartz structure positions. By applying the pseudo-critical transition model to experimentally measured order parameters, we find that the pair potentials used in MD gives a lower transition temperature relative to the pseudo-critical point. With the use of experiments, we propose that the range of inhomogeneity is actually very small and the structure of β-quartz is an ordered one.

3.4.1 Introduction

The low-temperature phase of silica, α-quartz, has a trigonal symmetry of space group $P3_121$, with three SiO_2 molecules in each unit cell. As a consequence of the symmetry, only one parameter u is enough to describe the atom positions of the three silicon atoms. As in Wyckoff[84], the three atoms are at (u, 0, 0), (0, u, 2/3) and (1-u, 1-u, 1/3) within a trigonal frame, forming an order 3 screw axis along Z direction. The experimental value of u given by Wyckoff at room temperature is 0.465. Rotating the crystal by 180° degrees the along Y axis restores the crystal structure with u changing to 1-u. Historically, the two α-quartz structure with u and 1-u are called *Dauphiné twins*.

When α-quartz is heated to 847°K, it transforms into a higher symmetry hexagonal structure known as β-quartz[28], with space group $P6_221$. Constrained by the sixfold symmetry, parameter u in β-quartz is exactly 0.5. It is well established that the α to β transition is first order, although very close to second order[29]. As to the true structure of β-quartz, there has been controversy over whether the structure stays at the true β positions with only thermal vibration, or it fluctuates between the two Dauphiné twins of α-quartz structures. In other words, is the transition displacive or order-disorder? A review by Dolino *et al.*[85] presents experimental evidence on both sides.

In 1980, a new incommensurate phase was discovered between the α and β phases that exists only in a temperature range about 2-3°K[85]. In this incommensurate phase the two Dauphiné twins of α-quartz structures are arranged in triangular (called $3q$ phase) or striped (called $1q$ phase) patterns about 200Å in size [86, 29, 85]. Landau's theory of phase transition was successfully applied to explain the incommensurate phase[87], detailed understanding of the various features seen in experiments[85] is still lacking.

There are numerous molecular dynamics(MD) studies of silica. First Tsuneyuki *et al.*[81] proposed an interatomic pair potential from *ab initio* force field calculation of SiO_4 clusters. Later van Beest *et al.*(BKS)[7] obtained another pair potential by empirically taking account of the bulk properties of silica in addition to the *ab initio* force field data. Tse *et al.*[8] studied the structure and dynamics of silica using the BKS potential and compared it with the Tsuneyuki potential. They summarized that the BKS potential gave very good equilibrium structures for different polymorphic forms of silica and worked very well in predicting the structural instabilities as a function of pressure and temperature. This makes BKS potential a suitable choice to the study α to β transition in quartz. More complicated many body potentials are proposed afterwards[88, 8], which are however not widely adopted.

Recent works on quartz have been mostly focused on high pressure induced effects such as phase transformation[89, 9, 10, 11], amorphization[12, 13, 14, 15, 16] and melting[17]. In modeling α to β quartz transition, Tsuneyuki *et al.*[30] studied thermally induced process and concluded that in the β-quartz structure the system is hopping between the two Dauphiné twins of α-quartz structure through anharmonic motions with temperature-dependent temporal and spatial correlations. Other studies at 0°K have been reported using volume constrained static MD relaxation[90], and first principles methods[91]. These works also confirmed the view of the order-disorder transition.

In this work, we used the BKS potential to study the α to β quartz transition induced by both temperature and pressure. Similar to Tsuneyuki's results, we have found that right after the transition β-quartz appears temporally and spatially chang-

ing between the two Dauphiné twins of α-quartz structures. From the order parameter curve we discovered a critical behavior which is cut off by the discontinuous transition. Using an Ising-like model coupled to compressible crystals, we explain the critical behavior and the discontinuous transition at the same time. According to our model, the discontinuous transition is due to a lattice instability, and the subsequent structure is inhomogeneous, as observed in MD. Apply the model to experimental measurements, we find that the transition in our simulation occurs at a lower temperature than experiment. This can be attributed to our use of a pair potential model, which does not treat properly the bond bending forces. We believe the present simulation gives an overestimate of the range of inhomogeneous structure, which corresponds to the range of incommensurate phase actually observed. On this basis we propose that the β-quartz structure seen in experiments is ordered.

3.4.2 Details of Simulation

In this study, we used the BKS potential[7],

$$U_{ij} = q_i q_j / r_{ij} + A_{ij} exp(-b_{ij} r_{ij}) - c_{ij} / r_{ij}^6 \tag{3.2}$$

The long-range Coulomb interaction is dealt with by Ewald summation method[92], with a real space cutoff $r_C = 10$Å.

All the calculations are conducted with a simulation consisting of $5 \times 5 \times 5$ unit cells and containing 1125 atoms. The finite temperature data are obtained with constant volume MD simulations. The Nosé-Hoover constant temperature scheme is implemented to maintain the desired temperature and the Parrinello-Rahman constant pressure simulation is used to achieve desired pressure[93]. In each simulation, the stress tensor is calculated as well as the average atomic position of each atom. In order to obtain detailed information near the α to β transition with high accuracy, an integration time step of 0.5fs is used together with the 6-value Gear's integration scheme[36]. Good convergence usually requiring 10-100ps of simulation, the points close to the transition requires significantly longer time to converge. The zero tem-

perature data are obtained by conjugate gradient(CG) relaxation. All CG results are accurate to 0.01%.

To calculate the silicon Wyckoff position parameter $\langle u \rangle$ used to define order parameter, we first map all the averaged silicon atomic positions to the (u, 0, 0) position with appropriate symmetry operation, then $\langle u \rangle$ is obtained by a simple average. The error is calculated as the standard deviation of all the mapped atom positions from the averaged ($\langle u \rangle$, 0, 0) position.

Each atom position is expressed by a 3×3 frame matrix H and an internal unit cell coordinate (s_a, s_b, s_c). Real coordinates are calculated as $(x, y, z)' = H(s_a, s_b, s_c)'$. Zero strain reference state is taken as the zero pressure, zero temperature state, with $a_0 = 4.9534\mathring{A}$ and $c_0 = 5.449\mathring{A}$.

$$H = \begin{bmatrix} a_0 & -a_0/2 & 0 \\ 0 & a_0\sqrt{3}/2 & 0 \\ 0 & 0 & c_0 \end{bmatrix} \tag{3.3}$$

In constant strain simulations, all the strains are imposed by changing the frame matrix H uniformly. A hydrostatic tension of ε changes the frame matrix to $(1+\varepsilon)H$.

3.4.3 Results and Discussion

Through a series of constant strain MD simulations at different temperatures, we obtain the stress-strain curves of quartz under hydrostatic tension, shown in Fig.3-11(a). The cusp in each curve is a clear indication of a possible phase transition. Indeed the transition of the α-quartz to β-quartz is confirmed from the atomic configurations.

Following Tsuneyuki *et al.*[30] we define the order parameter as $\eta = \langle u \rangle - 1/2$ where u is the Wyckoff[84] position parameter of the silicon atoms. Thus, η is non-zero for α-quartz and zero for β-quartz. Fig.3-11(b) shows the change of order parameter at different temperatures under tension. We can see that at 0°K, the order parameter goes to zero continuously whereas at high temperature, there is a discontinuous jump. This confirms that the transition is first order at finite temperature. One should note

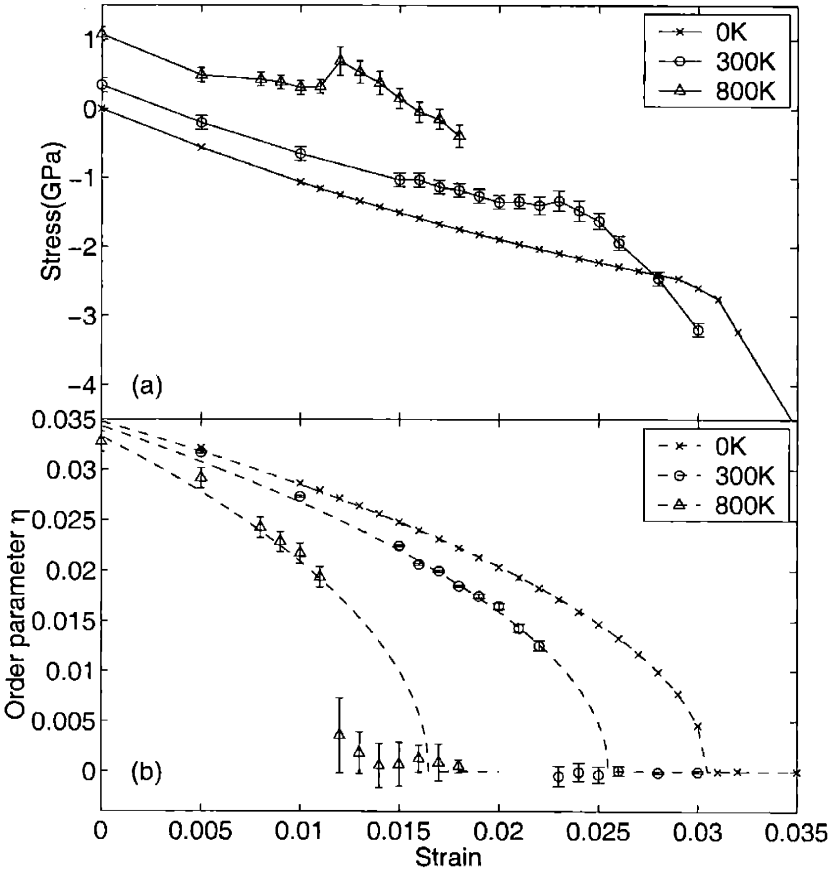

Figure 3-11: (a) Stress-strain curves of quartz through constant volume simulations. Data for 0°K, 300°K and 800°K are shown. All the relative strain are define from one standard 0°Kzero stress state. (b) The order parameter at various strains for 0°K, 300°K and 800°K. Solid and dashed lines are the α-quartz phase data fitted to $\eta \sim (S_c - S)^{0.5}$. At finite temperature the transition is discontinuous and happens before the fitted curve goes to zero.

also that the transition appears to be close to second order in the vicinity of 0°K.

It is desirable to characterize the transition by explicitly calculating the free energy of the system as a function of order parameters or temperatures and pressures. At finite temperature, it is not easy to calculate the free energy, and furthermore, it is quite difficult to constrain the system to an energetically unfavorable order parameter, which is needed to obtain a curve of free energy variation with order parameters. On the other hand, we can always calculate the free energy at 0°K, which is just the internal energy. The energy *vs.* order parameter curve can also be plotted by constraining the system to any prescribed order parameter value. In our case, once the order parameter η is chosen, all the positions of silicon atoms are fixed, then we can relax the oxygen atoms with conjugate gradient method to obtain the system internal energy. Fig.3-12 is the 0°K energy curve $E(\eta)$ at two different strains.

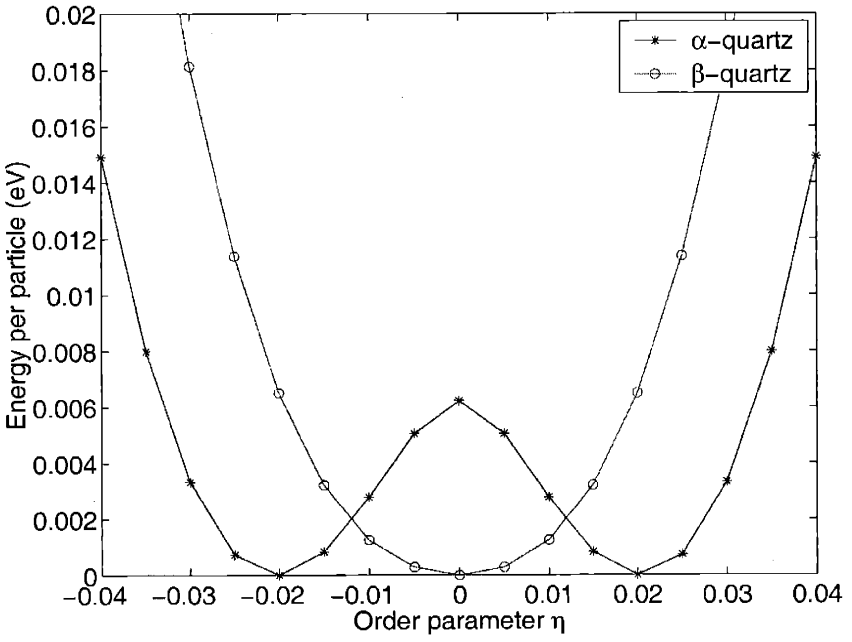

Figure 3-12: Energy per particle curve for α-quartz and β-quartz, all at $T = 0$. α-quartz corresponds to 2% strain and β-quartz corresponds to 3.5% strain in Fig.3-11(b) $T = 0°K$ curve

In view of the symmetry of Dauphiné twins, it is not surprising to see the double potential well result. With increasing tension, the potential barrier between the two

wells becomes shallower. At the transition point, the potential barrier completely vanishes, and the whole curve becomes a fourth order anharmonic potential.

Another set of MD simulations has been performed under constant temperature and constant pressure. This showed the temperature induced α to β transition. Fig.3-13 shows the thermal expansion of quartz. Both the x-direction and the z-direction linear expansion match the experiments. It is worth pointing out that in our constant strain simulations, we have ignored the difference in compressibility in x and z directions. We have confirmed this make no difference in our simulation results. Fig.3-14 is the order parameter versus temperature curve. Again, the weak first order phase transition is reproduced. At zero pressure, the phase transition occurs at $T^* = 700°\text{K}$, this is lower than the experimentally observed 847°K. We will explain this discrepancy later on. From the data points of order parameters, a seemingly critical behavior can be observed before the transition.

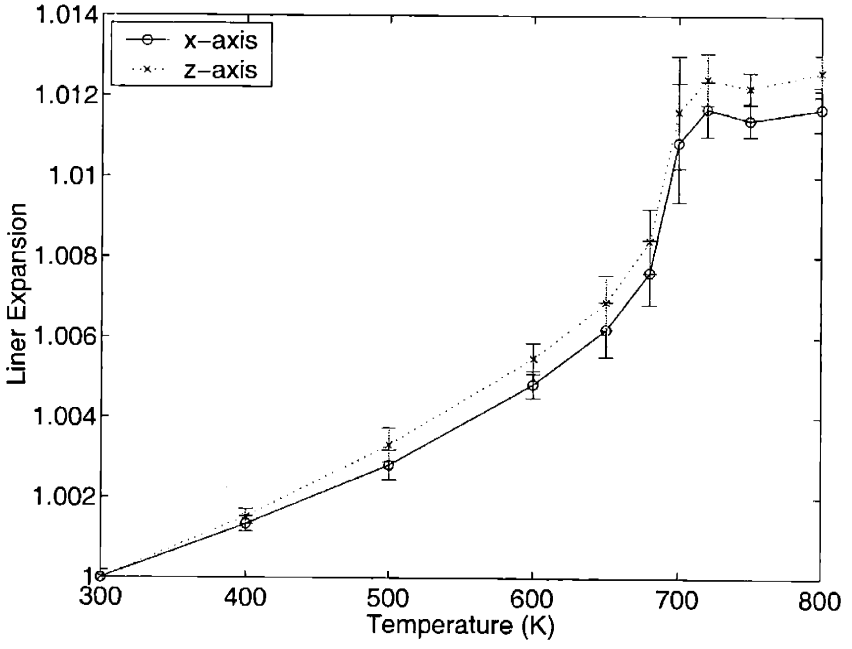

Figure 3-13: The thermal linear expansion of quartz at constant zero external pressure.

In 1970s, people have studied the critical behavior of an Ising model on a cubic compressible lattice. According to Bergman *et. al.*[32], if one assumes that C_v diverges

at the Ising critical point, then the bulk modulus B will go negative when the system comes close enough to T^c, the Ising critical temperature. Thus the system will undergo a weak first order phase transition to avoid a negative bulk modulus, and end up in an inhomogeneous state. This weak first order transition temperature T^* is usually close to T^c and the discontinuity of order parameter is very small. If this is the case one can observe critical behavior in a range of temperature before the transition.

This scenario is what we have seen in quartz simulation. In the quartz system, one can view the two minima in the free energy variation with order parameter as two spin states. It can be shown that two neighboring silicon atoms will be favored to stay in the same spin state. So the quartz system can be characterized by an Ising-like model on a compressible lattice. It is not strictly Ising because the long range interaction of the charge dipoles and the extra degrees of freedoms of each SiO_4 cluster. We can try to fit the order parameters near the transition point to:

$$\eta \sim (T^c - T)^{-\beta} \tag{3.4}$$

where T^c is the non-reachable critical temperature. Surprisingly, we get a close fit all the way to $T = 0$, as shown in Fig.3-14. The fit gives $T^c = 740°\text{K}$ while the transition temperature measured in MD is $T^* = 700°\text{K}$. The weak first order transition occurs at $T^* < T^c$. From the fitted curve we can predict T^c without ever reaching it. The fitted value of $\beta = 0.2$ is universal, independent of applied tension.

Landau's phenomenological theory of first order transition has been used[94] to explain the quartz transition by writing free energy as

$$F(\eta) = a(T^* - T)\eta^2 + b\eta^4 + c\eta^6 \tag{3.5}$$

and solving for the point where $\eta = 0$ minimum has lower free energy than the $\eta \neq 0$ minima. Aside from the observed transition temperature, a, b and c are treated as empirical parameters. In our model (3.4), we also need three parameters, T^c, β and the pre-factor. But unlike the Landau's theory, our parameters T^c and β are intrinsic to the dynamics of system, and the critical exponent β is universal. We will see that

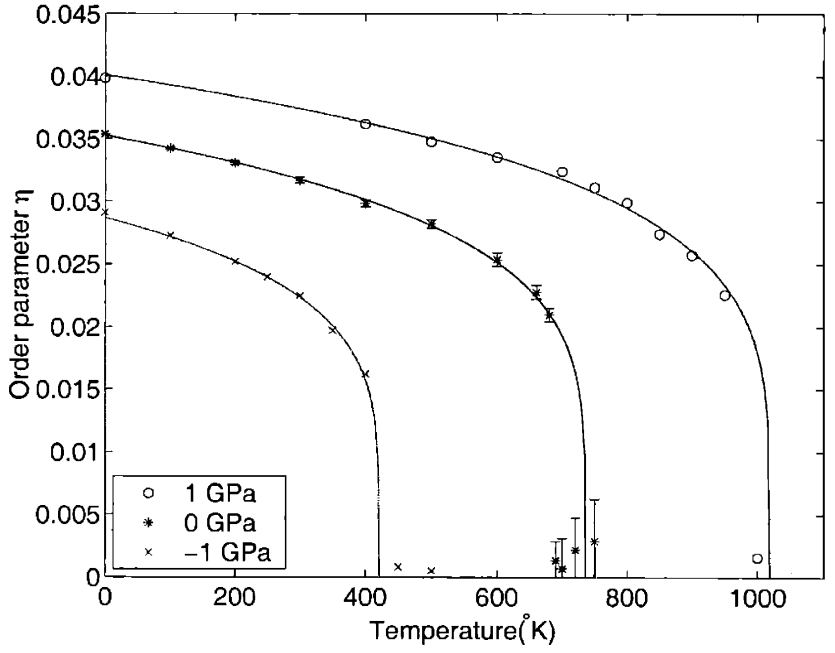

Figure 3-14: The order parameter at various temperatures for constant pressures of 1GPa, 0GPa, and -1GPa. Solid lines are the α-quartz data fitted to $\eta \sim (T^c - T)^{-\beta}$, where β is fitted as 0.2. The weak first order transition happens before T^c

the same $\beta = 0.2$ applies to experimental measured order parameter curve as well.

The small discontinuous transition is caused by the instability of the system with respect to certain vibrational mode. Fig.3-15 shows the calculated bulk modulus at different temperatures. Before T^*, the bulk modulus is decreasing toward 0. After transition, the bulk modulus stops decreasing, but does not increase until $100°K$ after the transition. The fact bulk modulus is never zero means the first unstable vibrational mode is not a homogeneous deformation; it corresponds to an Γ-point optical phonon mode which gives the motion of each atom to accomplish the phase transformation. Fig.3-16 shows the negative phonon mode of 0°K quartz at the point of transition. The negative phonon mode occurs between T^* and T^c, indicating the homogeneous lattice structure is unstable, confirming our observation of the coexisting Dauphiné twins. After T^c, no negative phonon modes can be observed, implying that the system resumes homogeneity.

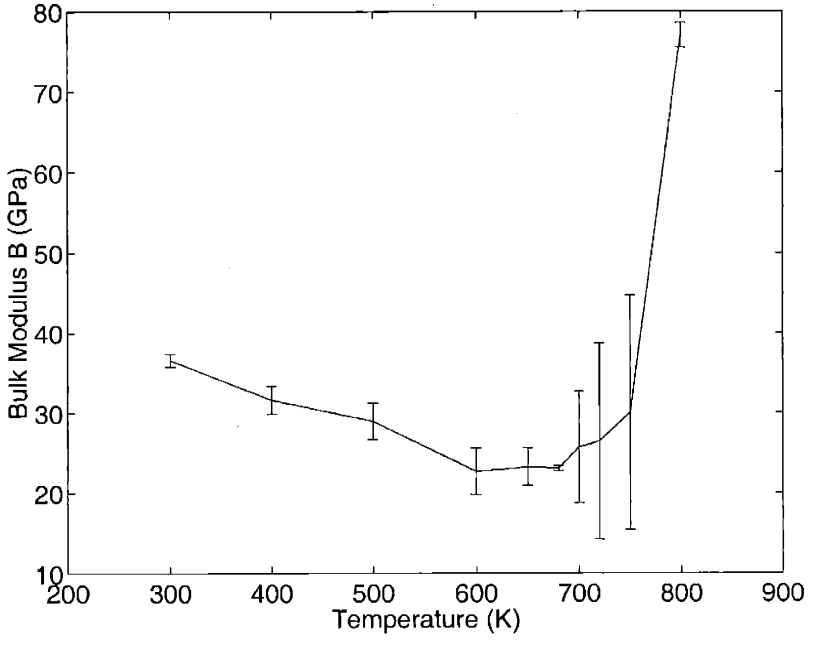

Figure 3-15: The bulk modulus of quartz at different temperature.

We have observed that the system is inhomogeneous with clusters of the two α-quartz structures of Dauphiné twins. Right after the transition, the correlation

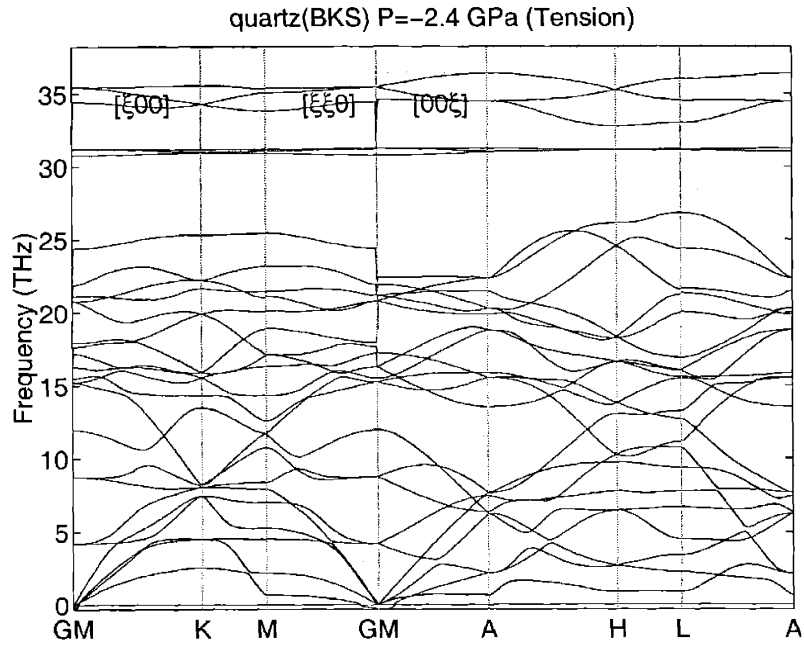

Figure 3-16: The phonon dispersion relations of quartz at 0°K and 2.4GPa tension, the point of α to β transition induced by tension. An optical phonon mode at Γ point goes negative while the three acoustic phonon modes stay positive.

length is presumably larger than the simulation cell, so we can only see the whole system jumping between the two Dauphiné twins structures. When temperature is increased, the cluster size became smaller and we can observe separations between the two phases in our simulation cell. At around 800°K, no clusters are visible in simulation and each atom oscillate independently. Equivalently, we can say at this point the cluster size is comparable with a single SiO_4 tetrahedron. The changing of order parameter with time is shown in Fig.3-17. The enhanced oscillation of order parameter right after α to β transition indicates a large portion of the system is changing from one α phase to the other α phase. Further down the transition path, the oscillation becomes small, where no cluster of the α structure is observable, the system is no longer disordered. It is observed that beyond T^c each atom seems to oscillate freely around the β-quartz position instead of staying at either of the two α-quartz sites.

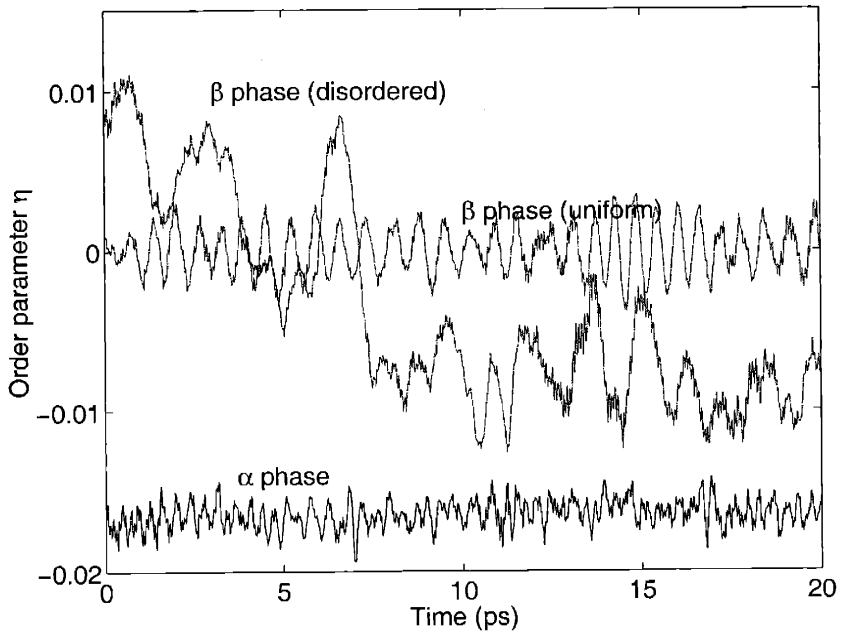

Figure 3-17: Fluctuation of order parameter of there different quartz states are shown for 300°K. α, dynamic-β and static-β phase are chosen to be 2%, 2.3% and 3% strain respectively. α to β quartz transition happens at 2.2% for 300°K.

It is apparent from our simulations that right after the transition, the system

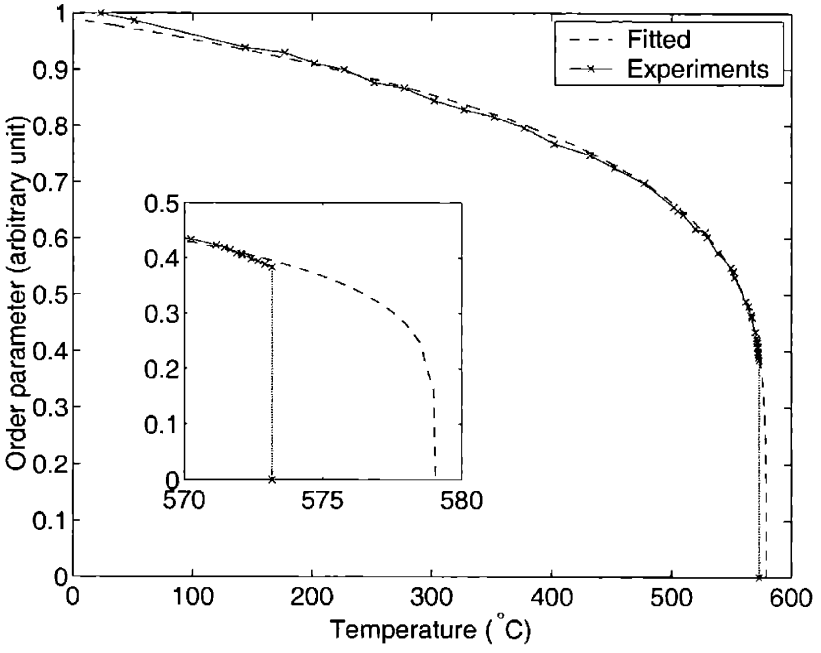

Figure 3-18: Experimental measurements of order parameter at different temperatures[94]. Dashed line is fitted to $\eta \sim (T_0 - T)^\beta$ with $\beta = 0.2$ and $T_0 = 852.3°\text{K}$. The phase transition region is enlarged in the inset, which gives the incommensurate phase a range of 5.9°K.

consists of two different α-structure regions separated by phase boundaries. Since we have used a pair potential that can not accurately reflect the subtle interactions of atoms, we can not draw our conclusion so concisely. One indication of the inaccuracy is that we get a transition temperature about 150°K lower than experimental value. The quantitative numbers aside, we suggest that the underlying physics is captured properly by the potential, and the model of an Ising-like system coupled with lattice is appropriate. To check this, we fit the model $\eta \sim (T^c - T)^{-\beta}$ with experimentally measured order parameters. As shown in Fig.3-18, using the exponent fitted from MD simulation $\beta = 0.2$ we fit the experimental data very accurately. But the difference between T^c and T^* is only 5.9°K instead of 40°K, directly obtained from the MD simulations. We believe that the BKS pair potential does not well represent the bond-bending force. This will result in a weaker system than the physical one. So it is perhaps not surprising that the discontinuous phase transition occurs earlier in our simulation.

Now we want to consider more carefully what is going on between T^* and T^c. It is safe to say that between T^* and T^c the system is inhomogeneous and separated into two α phases. Using the experimental data, we have found that the inhomogeneous range is only about 5.9°K. This matches with the observed incommensurate phase at 2-3°K above the discontinuous transition, and it consists of patterns of two α quartz structures. From this understanding, we propose that the β phase is ordered, with atoms oscillating around it's sites in thermal vibration.

It would not be easy to fully investigate the inhomogeneous phase between α and β quartz. The first logical step is to use a many body potential which gives accurate bond bending forces. Also, if one expects to reproduce the incommensurate phase in MD simulation, a much larger simulation cell size is required, which is only feasible with the fastest supercomputers.

3.4.4 Conclusion

As a summary, we have probed α to β quartz phase transition in MD simulation, using tension as a driving force, in addition to temperature. We show explicitly the

system internal energy has the double potential well structure for *alpha*-quartz. A model of Ising-like spin system coupling with compressible elastic lattice is applied to explain the transition at finite temperature. In the model, the transition is weakly discontinuous and the critical behavior is observable before transition. The MD results can be accurately fitted by a pseudo-critical curve $\eta \sim (T^c - T)^{-\beta}$, with the transition occurring at $T^* < T^c$. The transition is triggered by a Γ point soft optical phonon mode corresponding to the atomic motion accompanying the change from α-quartz to β quartz structure. After the transition the system become inhomogeneous and appears as clusters of two α quartz structures. At around the pseudo-critical point, the system become homogeneous again where atoms oscillate around β-quartz sites in thermal vibration.

By comparing the model results to experimental measurements, we find that the MD simulation over estimate the range between transition point T^* and pseudo-critical point T^c. From the experimental data, we deduced the inhomogeneous range is only around 6°K. We suggest this inhomogeneous state manifests itself as the incommensurate phase observed in experiment.

The present model leads to a picture of α-inc-β phase transition as a sequence. A first order phase transition occurs when α phase transforms into an incommensurate phase which then transforms into the β phase continuously. In this picture, β-quartz is an ordered phase, where atoms oscillate around their lattice positions with thermal vibration. This interpretation is compatible with the available experiments data[31].

3.5 Quartz Under Uniaxial Compression: New Deformation Mechanism

Molecular dynamics simulation study of stress-strain response of single crystal α-quartz has been reported for hydrostatic and uniaxial compressive loadings. While we reproduce the pressure-induced amorphization under hydrostatic compression observed by earlier works, a new anisotropic layered amorphization response is reported

first under uniaxial compression. We have observed under uniaxial compression that, past the point of stability of the lattice, a block of atoms oriented perpendicular to applied stress direction disorders before spreading to the entire cell, suggesting an symmetry-breaking nucleation and growth process. From our simulation results, we propose a possible instability-assisted fracture in experiments to explain certain anomalous observations with respect to fractures parallel to compressive plane.

3.5.1 Introduction

Structural transitions and properties of SiO_2 have been studied by molecular dynamics simulations[89, 95, 96, 9, 97, 98] and force-field calculations[99, 12, 13] using empirical interatomic potentials[81, 7]. Most of the previous works have focused on the phenomenon of pressure-induced amorphization and the related crystal-crystal transformations in quartz prior to amorphization. While these involve hydrostatically loading the quartz structure to high pressures at room temperature, there have been only few simulations of uniaxially compressive loadings on any structure[100, 101, 102, 103]. Simulations of uniaxial deformation behavior at high stresses and high temperature is of interest from the standpoint of understanding the plastic deformation of quartz, particularly given the extensive experimental data[104, 47, 105, 48, 58, 106, 49, 107, 50]. Before the specific effect of hydrolytic weakening of quartz, i.e. the reduction of strength by about an order of magnitude in the presence of water, can be understood, the deformation behavior of dry quartz crystals should be first established.

We observed in our simulation that under uniaxial compression, beyond 14GPa compressive stress, the quartz crystal lattice becomes disordered and loses resistance in the compression direction. However unlike under hydrostatic loading, there was a layered amorphization process in which a region of the cell (several layers of atoms) oriented perpendicular to compression direction disordered first before spreading to the entire cell leading to a full amorphization, suggesting a nucleation and growth process.

From these results, we suggest an instability-assisted failure method possible to observe in single-crystal experiments, which provides support for certain planar frac-

ture features, new zones of glassy material and a few high strength observations, observed in room temperature experiments[48]. These observations have not been addressed in detail.

3.5.2 Layered Compressive Failure

Molecular dynamics simulations are performed using the pair potential given by van Beest *et al.*[7]. A number of studies[95, 96, 9, 97, 98, 99, 12, 13, 108, 10, 109] have shown that this description is able to account for structural phenomena in SiO_2 such as the pressure-induced amorphization and elastic instability observed in quartz[95, 99, 12], the properties of the evolved amorphous structure[96], the intermediate crystal-crystal transitions that exist before amorphization[9], the mechanism of this amorphization[13], other new stable structures[108, 10, 109], and the structure and phase transformations of other silica polymorphs[97, 108]. We use the Nosé-Hoover thermostat[110, 111] and Parrinello-Rahman constant stress molecular dynamics method[62], in a periodic simulation cell with 1152 atoms and 4320 atoms. The long-range Coulomb interactions were treated with the Ewald method. A suitably small time-step of 0.001ps was chosen to ensure energy conservation. At each state point on the stress-strain curve the system was equilibrated for 10ps and run for 5ps, followed by static relaxation and the strain was measured with this equilibrium structure.

To avoid the unnecessary restrictions imposed by periodic boundary conditions, another simulation was carried out on a quartz slab with two free surfaces. When the sample is compressed, again an amorphous layer forms perpendicular to the compressive direction, as shown in 3-21. The amorphous part the system has higher density, thus it can relieve the applied strain. In constant strain simulations, the thickening of the amorphous layer only happens when more strains are introduced to the system.

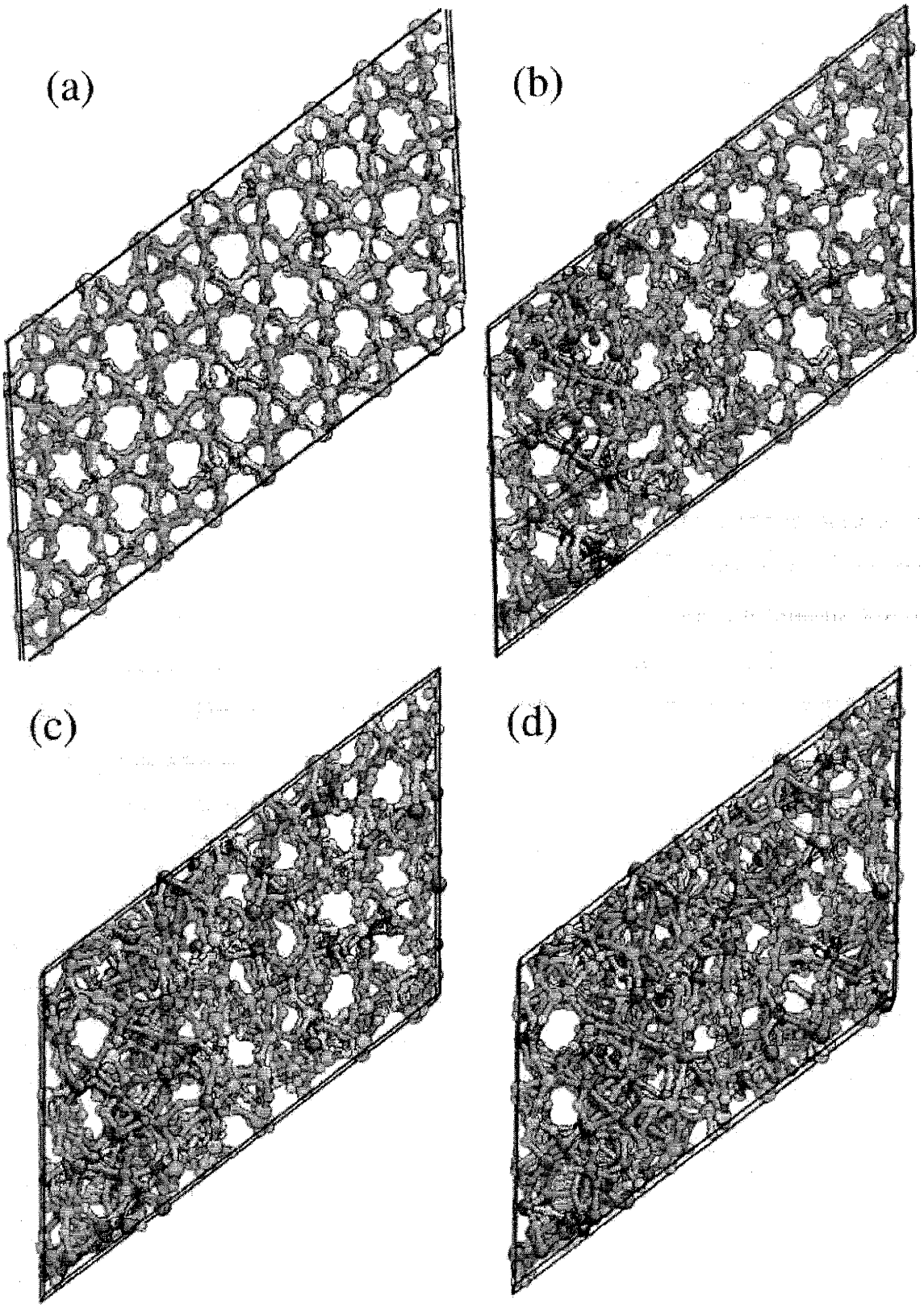

Figure 3-19: The time evolution from original configuration to final configuration of the x-axial uniaxial compression of bulk quartz. (a) Initial state. (b) 1.0ps after applied 16GPa uniaxial compression. (c) 1.5ps. (d) 1.75ps.

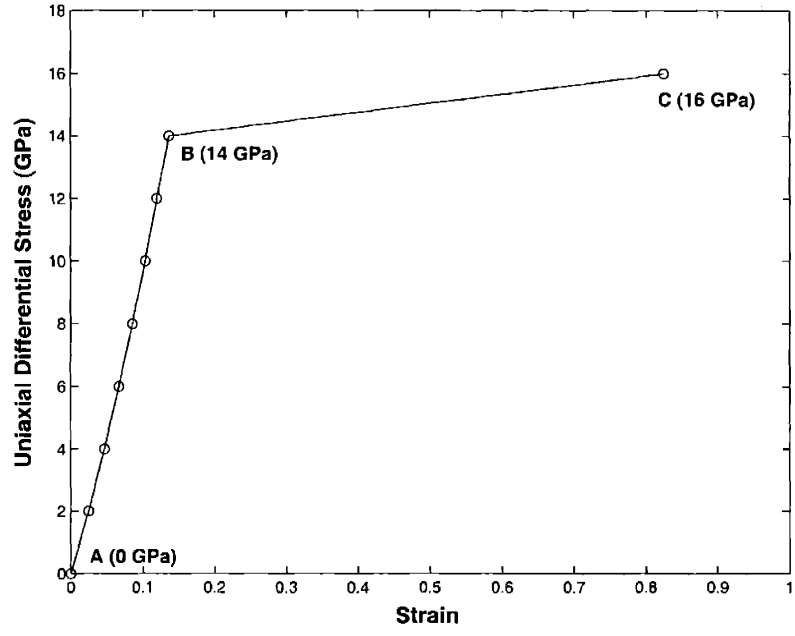

Figure 3-20: Stress-strain response of bulk quartz crystal under uniaxial compression at 300°K

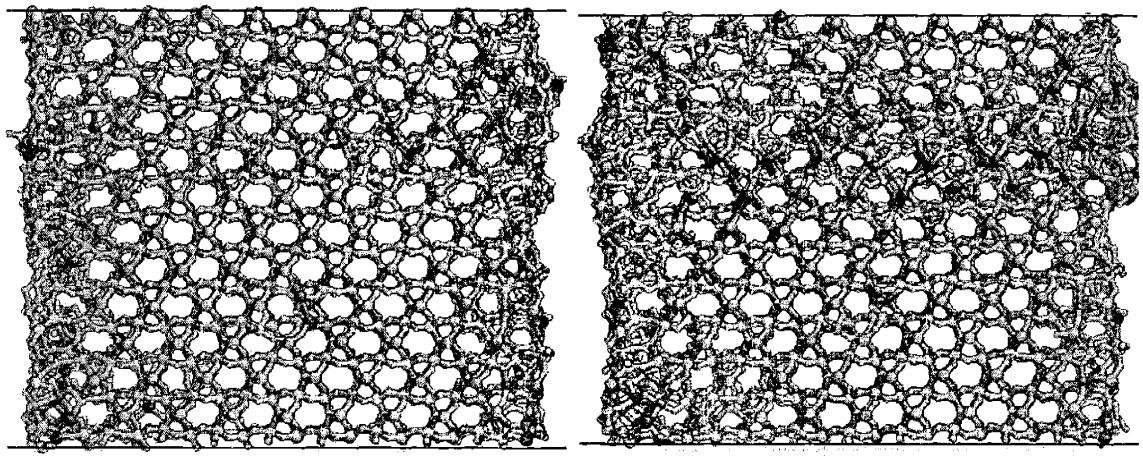

Figure 3-21: A comparison between original configuration and failure configuration of the y-axis uniaxial compression of a slab of quartz with free surface

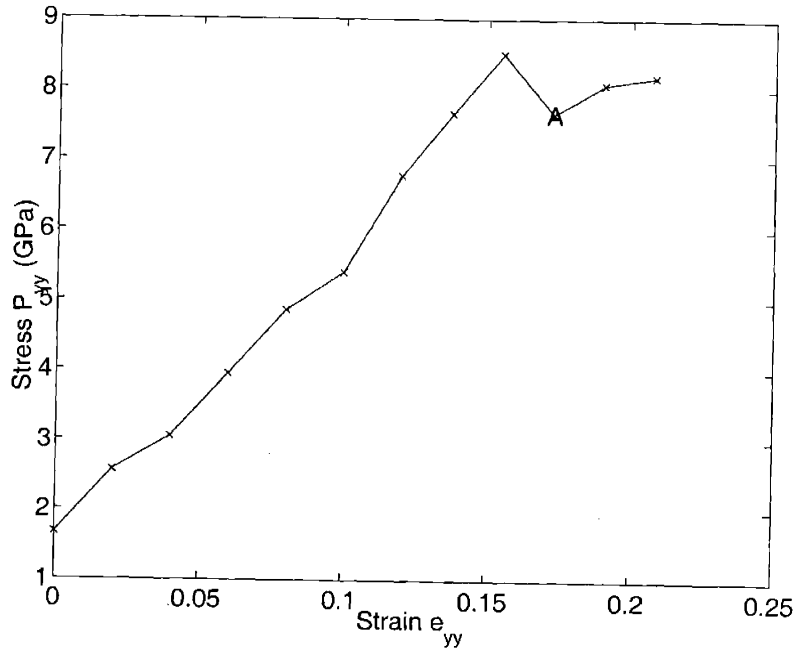

Figure 3-22: Stress-strain response of quartz slab under uniaxial compression at 300°K

3.5.3 Instability-Induced Failure in Experiment

In order to make contact with deformation features seen in experiments, we recall first some background information on slip systems[82, 83]. Quartz crystal structure falls in the trigonal-hexagonal lattice type with α-quartz having a $P3_121$ space group. The slip planes for hexagonal lattice type are given by $\{0001\}$, $\{10\bar{1}0\}$, $\{10\bar{1}1\}$ and the slip directions by $\langle a \rangle$ or $\langle a+c \rangle$. Out of these, the $\{0001\}$ basal slip is most commonly observed. When plastic deformation was first recorded in quartz crystals[104], it was observed that the crystals had predominantly slipped in the basal plane or the $\{0001\}$[47, 105] as slip along the basal plane requires lower shear stress than other slip planes.

Experimental studies on uniaxial compression in quartz crystals or aggregates are extensive. Features such as deformation lamellae, bands, undulatory extinction[47], faulting along particular planes, isotropic zones[48], and recrystallization[106] have been recorded in these experiments. Here we will consider two such features (isotropic zones, fracture planes) in the context of our simulation results.

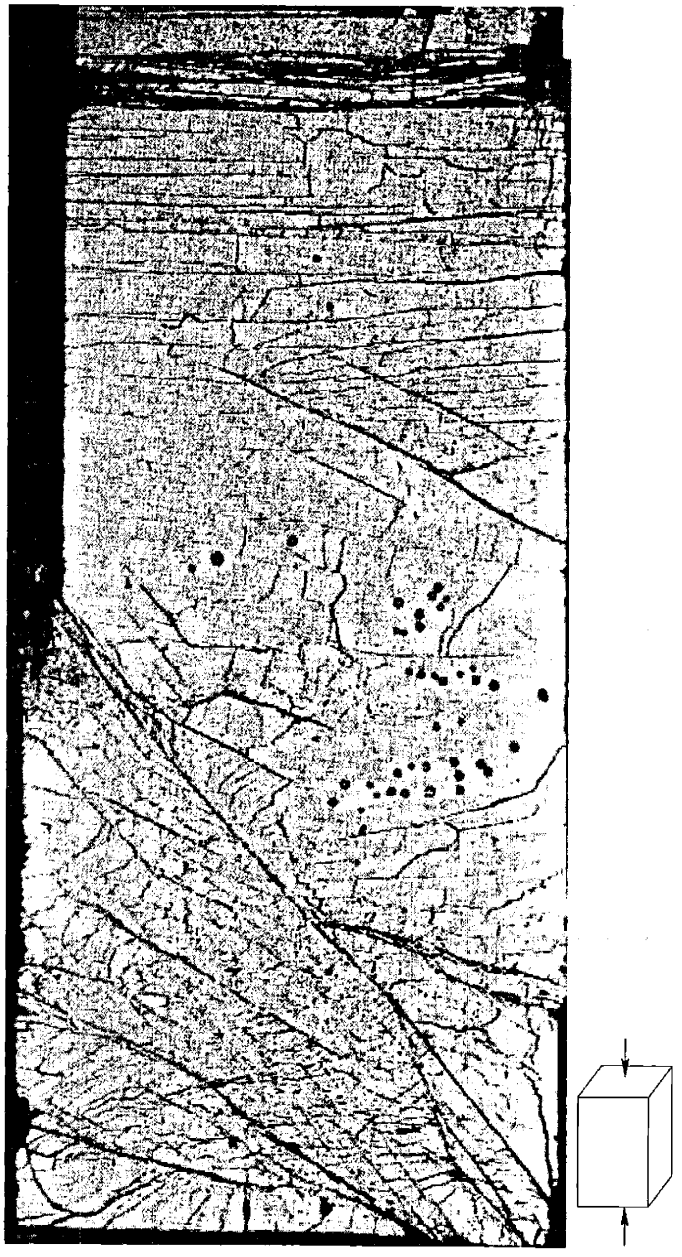

Figure 3-23: Experimental result of single crystal quartz uniaxial compression failure, taken from [48]. Features seen include: below activated slip bands, top glassy zone.

Christie *et al.*[48] have made experimental deformation studies of quartz at room temperature. Fig.3-23 is a figure reproduced from Christie *et al.*[48]. Although this length scale is one million times bigger than what we have done, our simulation may explain the 40 old experiment. Any in fact, with more and more simulation studies, many existing experiments can be better explained or understood.

We have suggested here an instability-assisted failure possible to observe in pure single crystal quartz with no dislocations and defects, with specific characteristics (fracture plane perpendicular to compressive stress, isotropic zones along fracture surface, high strength) particularly loaded along the c-axis, which has more chances to preempt slip. Further experiments with purer samples maybe possible to reproduce this failure. We have also underlined certain observations and situations in experiments that could possibly signify the ideal strength failure from our simulation, even with defects in the material. Further experimental verification of this subjective proposition for fracturing and the instability-assisted failure is required. We have already observed supporting results under free boundary simulations and study is underway to simulate this effect with more complex microstructures in simulation.

3.6 Crack Extension in Crystalline Quartz

Mechanical behavior of fracture in quartz on the atomistic level is studied through molecular simulations by placing an elliptical nanocrack in the lattice, and applying mode I (uniaxial tension) loading at different temperatures. No dislocation nucleation is observed as the crack advances in a brittle manner even up to a high temperature of 1500°K.

3.6.1 Brittle crack extension in Quartz

An elliptical crack of 6nm long and 1nm wide is put into the bulk quartz crystal by removing all the atoms within an elliptical hole. The simulation cell is 14.75 × 5.11 × 3.24[nm] consists of 19440 atoms. 336 silicon atoms and 666 oxygen atoms within the elliptical crack area is removed. To preserve electric neutrality, additional

6 oxygen atoms are removed, selected based on their distance to the ellipse. The original configuration is shown in Fig.3-24(a), containing 18432 atoms. The atoms on the crack surface has lower coordination number.

The system is then heated to 300°K and 1500°K respectively. Fig.3-24(b) shows the relaxed 300°K configuration. It is noticeable that the relaxation heals most of the dangling bonds on the surface. Both systems are put into mode I plane strain loading. Fig.3-25 shows the stress-strain response at both temperatures. Before the critical stress, the system strains elastically, the crack widens but otherwise stays unchanged. When the critical stress is reached, the crack starts to extend in a brittle manner. This is signified from the rapid decrease of stress in the stress-strain response. From the low temperature and high temperature stress-strain curves, it is evident that quartz remains brittle up to very close to melting temperature ($T_m = 1850$°K). This can also be verified by looking at the atomistic configurations of crack tip for both temperatures, as shown in Fig.3-26. The crack tip for both temperature is sharp to atomistic level. The low temperature crack tip is bound by only a few Si-O bonds, the crack extension involves breaking those bonds, as shown in Fig.3-26(b).

The brittleness of quartz at high temperature observed in simulation is consistent with the experiments on "dry" quartz[37], where no plastic deformation can be observed at all.

3.6.2 Verifying Griffith Criteria

From the critical crack propagation stress of 16[GPa] and crack length $2c = 6$[nm], the stress intensity factor predicted by the simulation is:

$$K_{\mathrm{Ic}} = \sigma_{\mathrm{C}}\sqrt{\pi c} = 1.55[\mathrm{MPa}\cdot\mathrm{m}^{1/2}] \tag{3.6}$$

Because quartz is always brittle, the Griffith criteria[40] can be checked.

The following properties can be calculated within the simulation model: surface energy $\gamma = 0.3412[\mathrm{eV/\AA}^2] = 5.4592[\mathrm{J/m}^2]$, Young's modulus $E = 74.47$[GPa], Poisson's ratio $\nu = 0.085$. Using (1.4), this gives $K_{\mathrm{Ic}} = 0.91[\mathrm{MPa}\cdot\mathrm{m}^{1/2}]$. This is in line

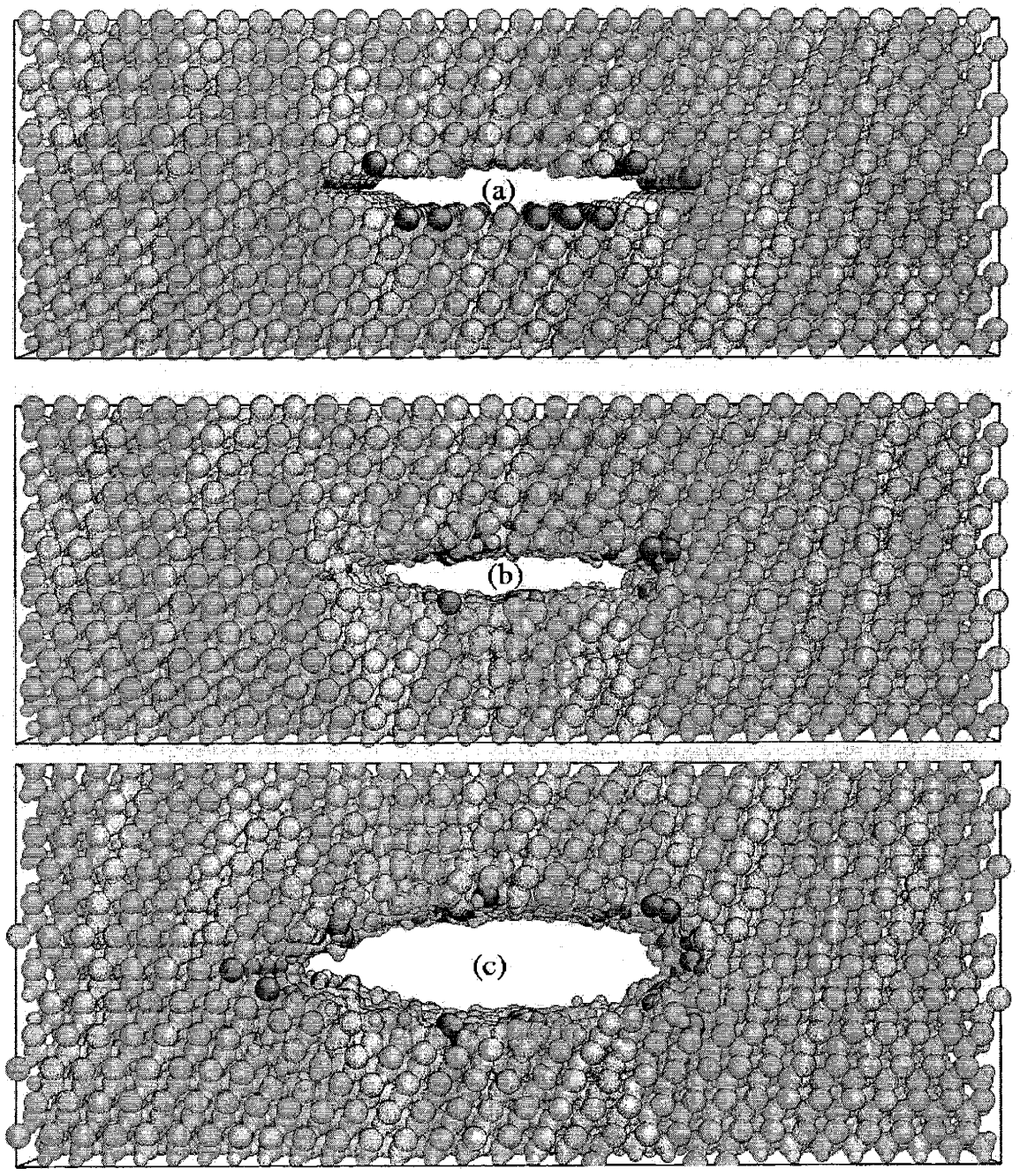

Figure 3-24: Atomistic configurations of 300°K crack in quartz. (a) The original unrelaxed elliptical crack configuration. Cell size $14.75 \times 5.11 \times 3.24$[nm], 18432 atoms. Big atoms are silicons and small ones are oxygens. The color of each atom is based on coordination number. (b) The relaxed elliptical crack unstressed configuration. (c) The configuration when the crack tip starts to extend.

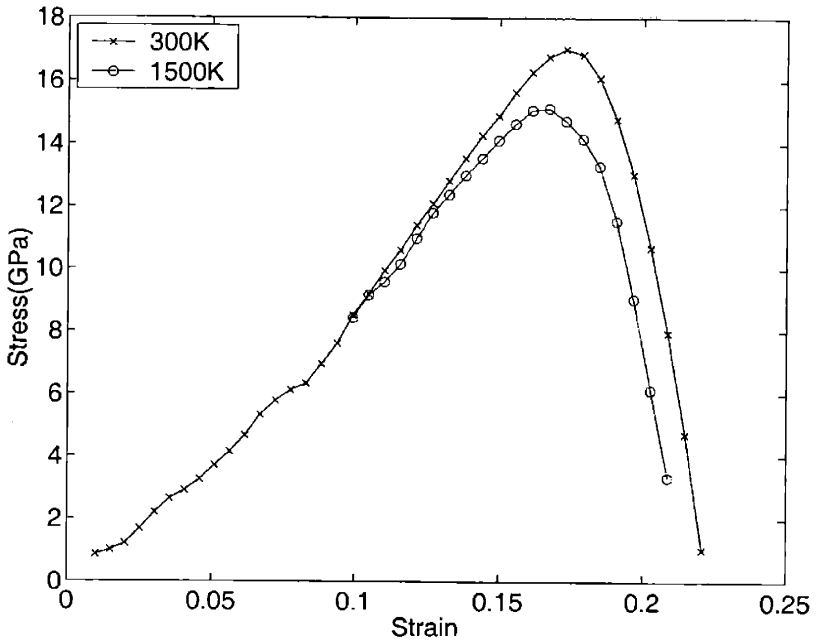

Figure 3-25: Stress-strain curve of 6nm elliptical crack in bulk quartz crystal at 300°K and 1500°K.

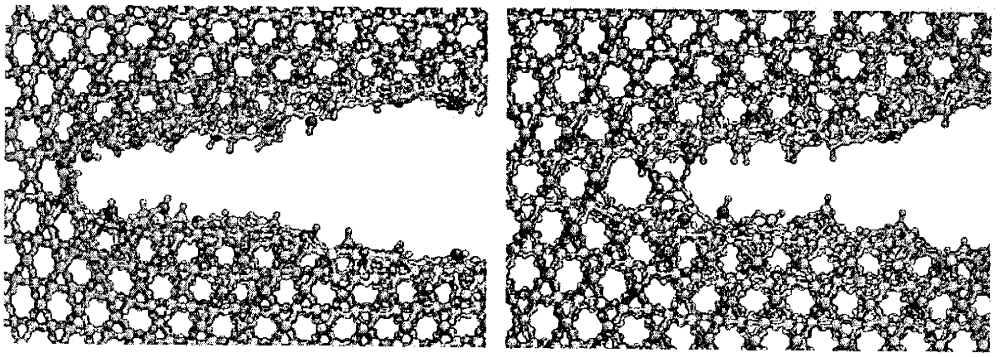

Figure 3-26: The detailed extending crack tip configuration for 300°K (left) and 1500°K (right) extending crack.

with the direct simulation result in (3.6).

The experimental measured stress intensity factor quartz is $0.97[\text{MPa} \cdot \text{m}^{1/2}]$[42]. This matches perfectly with the value predicted by fracture mechanics, the significance of this agreement is, in the first formula we have used the simulation surface energy and matches the experiments very closely. This implies our model is quite reliable.

Furthermore, the difference can be understood if we remember that the Griffith law assumes there is no dissipation. Our results of higher stress intensity factor indicates that in the quartz fracture propagation, there is energy dissipation. To quantify the dissipation, we need to modify the Griffith criteria with dissipated energy per unit crack propagation G:

$$K_{\text{Ic}} = \sqrt{E(2\gamma + G)/(1-\nu^2)} \tag{3.7}$$

Following this formula, our 16[GPa] crack propagation stress gives $G = 1.31[\text{eV}/\text{Å}^2]$.

Using the *relaxed* surface energy in (1.4), implies a thermodynamic equilibrium. In perfectly sharp cracks where no defects present at the crack tip, crack propagation creates *unrelaxed* surface at first. To get the mechanical stress barrier we should use unrelaxed surface energy. The unrelaxed surface energy of quartz $\{1\bar{1}00\}$ surface is $\gamma_{\text{unrelaxed}} = 1.1077[\text{eV}/\text{Å}^2] = 17.75[\text{J}/\text{m}^2]$. This leads to $K_{\text{Ic}} = 1.63[\text{MPa} \cdot \text{m}^{1/2}]$. This means, all the dissipated energy comes from surface relaxation after the crack propagates.

In this study, it is verified that in brittle materials, Griffith criteria and fracture mechanics is applicable down to atomistic scales and very high stresses. In addition, the mechanism of dissipation for fast crack extension is identified to be surface relaxation. Furthermore, the amount of dissipation is quantized from the unrelaxed surface energy, which matches closely to the value predicted by direct simulation.

3.6.3 Nano-notch on Quartz Surface

In order to eliminate the effects of small periodic boundary conditions, a nano-notch geometry is setup for mode I loading.

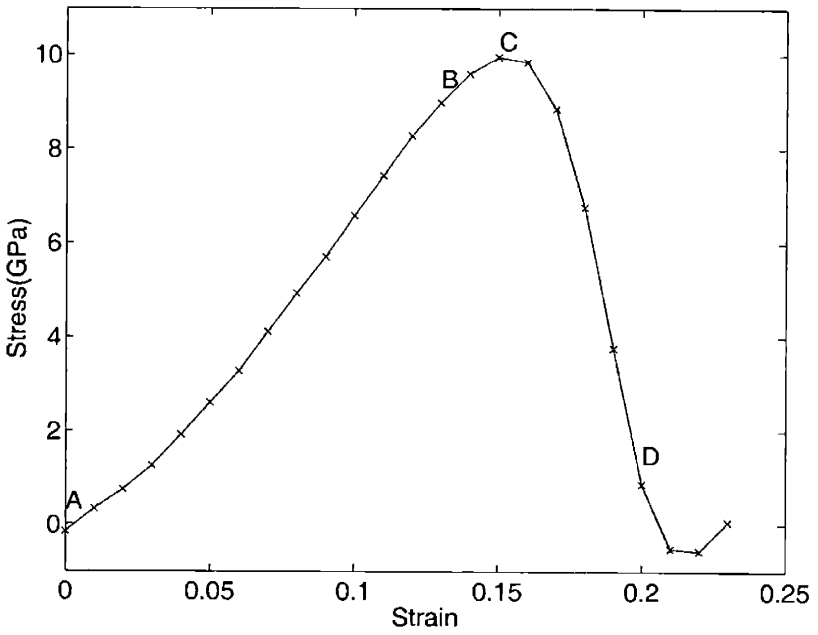

Figure 3-27: Stress-strain curve of notched surface quartz slab at different temperatures

3.7 Fracture of Amorhpous Silica

Unlike crystals, amorphous materials have an irregular structure characterized by a variety of local structures on the atomistic scale. In turn this gives rise to structural relaxiation processes that are usually much slower than the vibrational relaxations in an ordered lattice. In studying the strength and deformation of amorphous silica, we will focus on the strain-rate dependence of the stress-strain response. A strain-rate independent response may be expected for strain rates small enough to allow local relaxation to proceed through thermal vibrations. Indeed we are able to observe this convergence. By looking closely at the "converged" stress-strain curve, four distinct stages of deformations response involving void nucleation and growth are identified. The effects of high temperature and pre-existing crack are also studied.

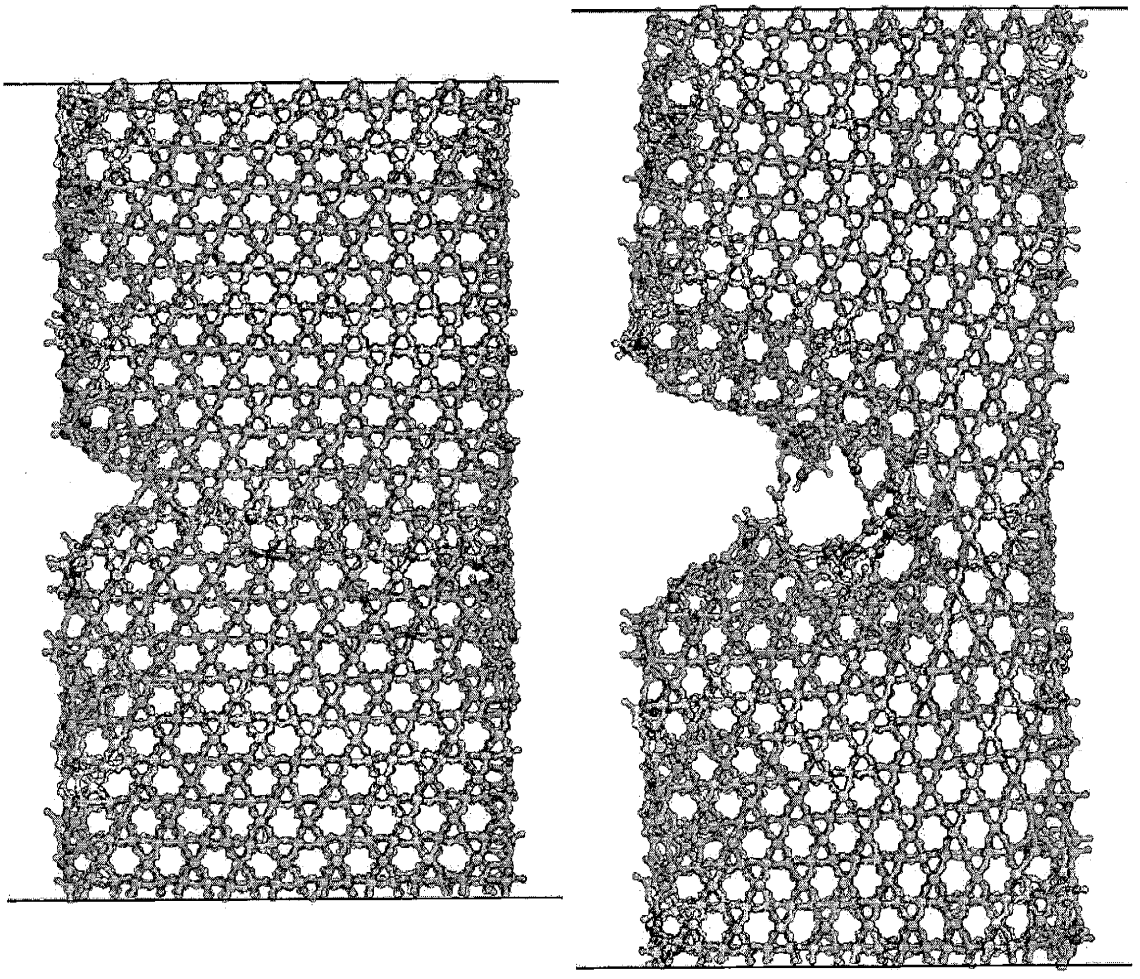

Figure 3-28: (a) Initial configuration of nano-notch simulation on quartz surface. (b) Propagating fracture under mode I loading.

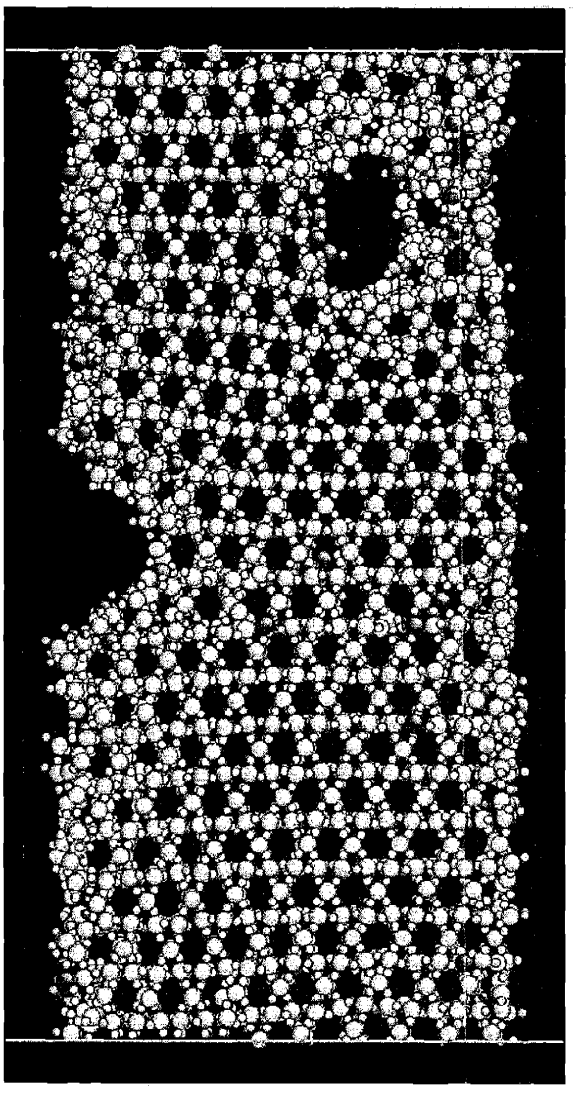

Figure 3-29: Configuration showing a void and a surface crack both starting to move when subject to external mode I loading

3.7.1 Structures and Initialization

Amorphous materials such as fused silica are usually obtained by quenching from the liquid state. Although the quenching rate in experiments is fast enough to prevent crystallization, it is still many orders of magnitude slower than the time that can be simulated in MD. We will adopt the simple criterion based on considerations of the radial distribution function (RDF) and the system density. When these two are reasonably close to the experimental values, we will consider it meaningful to compare the other properties between MD simulation and experiments.

The sample used for simulation is produced by heating a 9999 atom quartz sample to 10000°K for 10ps while maintaining around 3[GPa] containing pressure. This ensures the system has completely melted and in a typically molten state. Then it is brought down to 300°K at constant zero pressure with an averaged cooling rate around 1×10^{15}[°K/s]. For a detailed study of cooling rate effect, see[18]. After the melting and quenching, the sample is given another 10ps to equilibrate.

The equilibrated sample has a density of $\rho = 2.3$[g/cm^3]. A smaller sample prepared through same procedure have higher density. Looking at the 9999 atom sample, we discovered that local density of the amorphous can be as high as 2.6[g/cm^3], which is comparable to quartz crystals ($\rho_{\text{quartz}} = 2.65$[g/cm^3][112]). The presence of many existing voids accounts for the overall lower density. The experimental density of fused silica is about 2.2[g/cm^3][112]. We believe the same degree of heterogeneity could also exist in the fused silica used in experiments, namely, the local density can be as high as in quartz crystal.

Fig.3-30 shows the RDF of the sample, compared with peak values obtained from neutron scattering experiments[113, 114]. The radial distribution functions of our sample agree well with the ones of similar quenching rate reported by Vollmayr *et al.*[18].

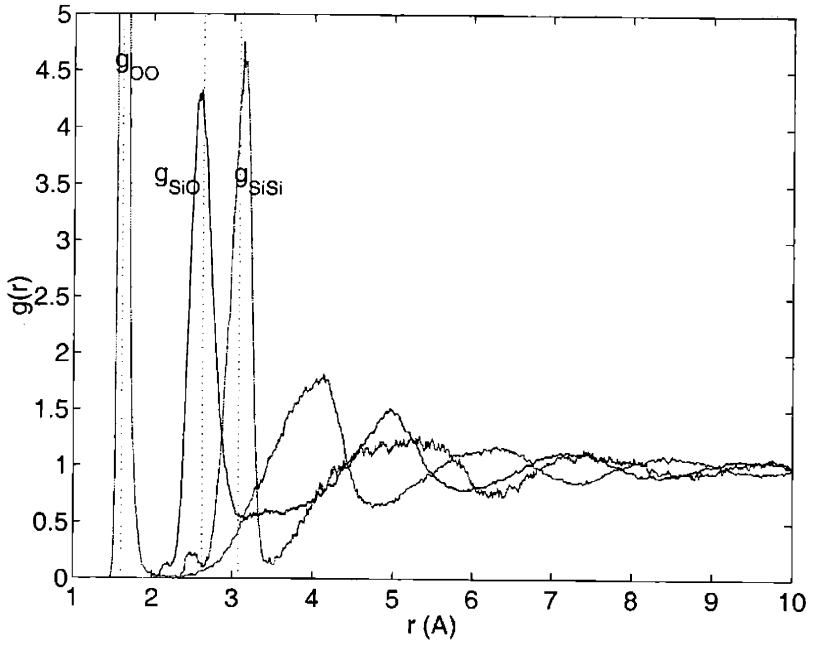

Figure 3-30: The radial distribution function(RDF) of the amorphous sample used. Measured at 300°K, three RDF functions are shown: g_{OO}, g_{SiO}, g_{SiSi}. The dotted lines are the first peaks measured by neutron scattering.[113, 114]

3.7.2 Strain-rate Dependence

Uniaxial constant strain-rate tensile loading is applied to the prepared amorphous sample. Seven strain rates ranging from $5 \times 10^{11}/s$ to $1 \times 10^{9}/s$ are applied. The stress-strain responses are shown in Fig.3-31.

Significant strain rate variation is seen at the very high strain rates. The sound speed in solid silica glass is about $6000m/s$. If we take the effective short range interaction cutoff as $\sim$ 12Å, then a sound wave can propagate across the cutoff range for about 0.2ps. Our results show that strain rate dependence of tensile strength only appears when the strain rates are higher than $2 \times 10^{10}/s$, which amounts to 0.4% strains for the time it take a phonon to transverse interaction range. Thus the observed strain rate dependence may be attributed to local structural rearrangements that do not have sufficient time to relax. If the strain rates are smaller than $2 \times 10^{10}/s$, there is no more discernible rate dependence, implying the local rearrangements have time to complete.

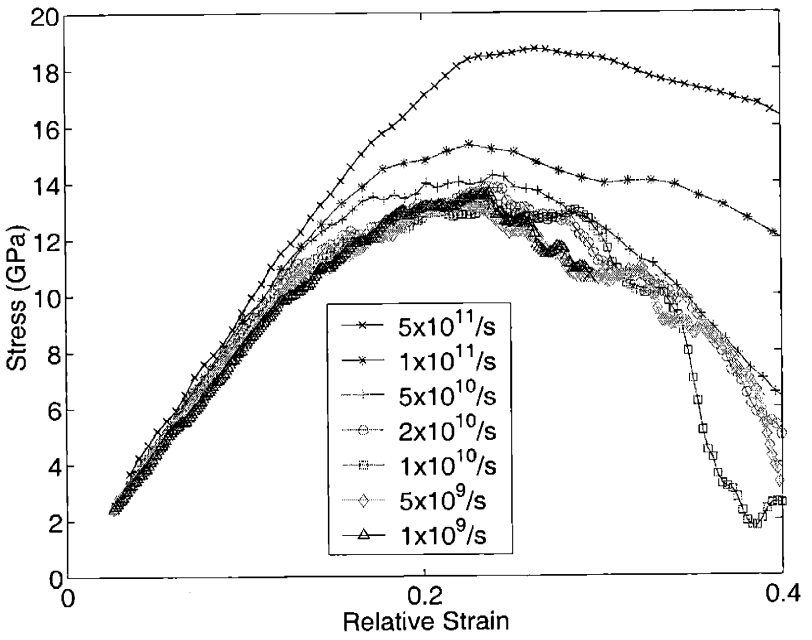

Figure 3-31: Stress-strain response of amorphous silica under tensile loading at 300°K. Seven sets of simulation runs at different strain-rates are shown together.

From the strain rate independent results, we get a converged tensile strength of 13[GPa]. Experimental maximum tensile strengths of silica fibers lie in range of 10-15[GPa][52, 53]

3.7.3 Deformation Mechanisms

In the low strain region, the stress-strain response is elastic where the slope of the curve (C_{11}) are constant. When the loading is reversed, the atoms return back to the original configuration. After around 0.14 strain, the slope changes visibly. Then, at around 0.23 strain, the critical tensile strength is reached. After about 0.35 strain, the strength decreases drastically.

To understand better the four apparently distinct stress-strain response stages, we look into the atomic configurations of the system during the deformation process. Taking one of the slowest strain rate simulations, strain rate $5 \times 10^9/s$, we show in Fig.3-33 a four stage process of deformation under tensile loading. In stage I, the

stress-strain response is linear $\sigma = C\varepsilon$, with $C = 78$[GPa]. This agrees perfectly well with the measured elastic constant for glass: $C_{11} = 78.75$[GPa] (calculated from Young's modulus $E = 73.5$ and Poisson's ratio $\nu = 0.16$[2]). If the strain is relaxed by reversing the loading at same constant strain rate, the system will get back to original state (i.e. zero strain and zero stress) as shown by the circles from point A in Fig.3-33(a). In stage II, the slope changes, and the stress strain relation can be written as

$$\sigma = C\varepsilon - P(\varepsilon - \varepsilon_0) \tag{3.8}$$

Here $P = 56$[GPa] is the ratio of stress release by plastic deformation after threshold strain $\varepsilon_0 = 0.14$. If the loading is reversed after plastic deformation, only the elastic part of (3.8) can be recovered, this is shown by the stars from point B in Fig.3-33(a). The reverse curve having a slope very close to C implies that only the elastic strains are released.

We will adopt the criterion that an interatomic space is called *void space* if there is no atom within 3[Å]. All the connected void space forms a single *void*. With this definition, the number of voids can be counted for any configuration. Fig.3-32 shows a 2D illustration of how the voids are defined.

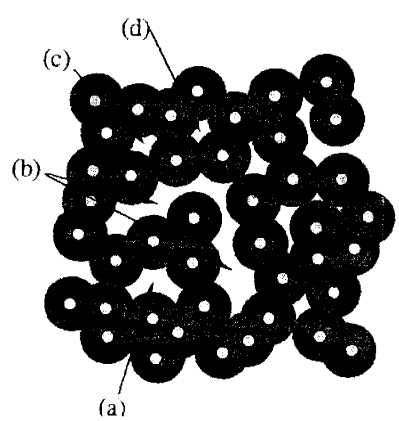

Figure 3-32: Illustration of a two dimensional amorphous system. The space within certain distance to an atom is shaded, the *connected* space not covered by any atom's shade is considered one void. Four voids are marked by (a), (b), (c) and (d)

Fig.3-33(b) is a plot of the number of voids in the whole system. In stage I, even

with only elastic deformations, more interatomic space will qualify as voids as the material takes on tensile strain. In stage II, the number of voids increases faster than that in stage I, implying the onset of void nucleation. With more and more void created, the material can still take higher stress.

At 0.23 strain, on enters stage III where the density of void reaches the limit and no more voids can be created. The existing voids then start to grow and coalesce, with the number of voids remaining the same. When the voids are growing, the material starts to yield to the applied stress. This is similar to the onset of fracture propagation. The critical stress is reached at the boundary of stages II and III. At 0.35 strain, the largest void extends across the system and causes a fracture to occur. As the crack propagates and widens, the loading stress is released quickly, elastic strain is reversed and the total number of voids decrease.

In summary, we have identified four stages of amorphous silica, pure elastic deformation, plastic deformation by voids nucleation, plastic deformation by void growth and coalescence, failure by material separation.

3.7.4 Crack in Amorphous Silica

Another simulations is performed with an elliptic crack in the system. With the crack the tensile strength are greatly reduced, from 13[GPa] to 7[GPa]. Furthermore, the four stages process is reduced to three stages. The main reason for the reduction of the strength is the crack serves as a "seed" void, and at as low as 7[GPa], it's starting to extend, cutting short the stage I and skipping over the stage II previously discussed.

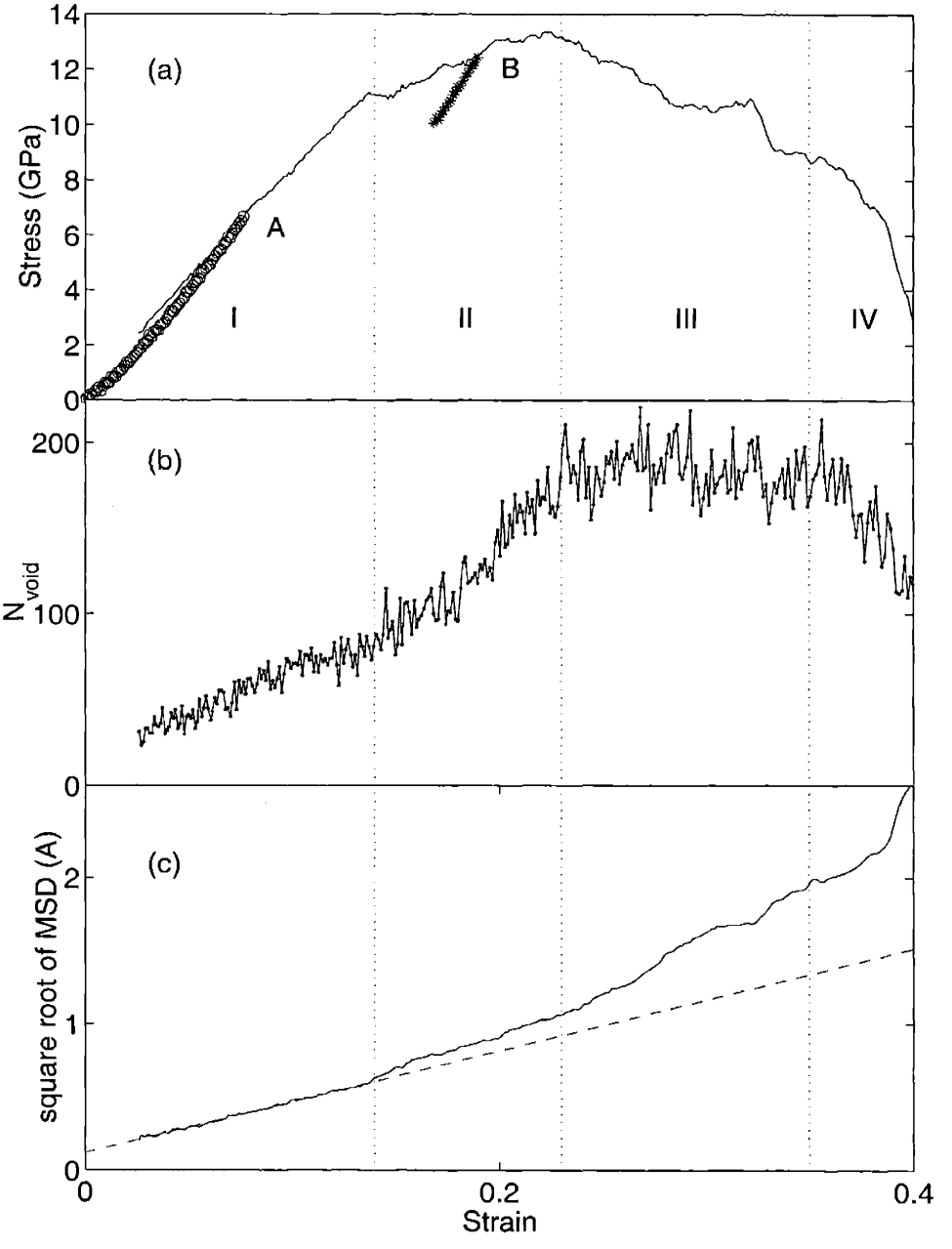

Figure 3-33: The deformation mechanism for amorphous silica: (a) Stress-strain response of amorphous silica under tensile loading of constant strain rate at $5 \times 10^9/s$. Also plotted the stress-strain response when stress are released at same constant strain rate from both point A and B. (b) The number of voids in the whole system. (c) Square root of mean-square displacements of the atoms, dashed line shows the linear extrapolation of stage I.

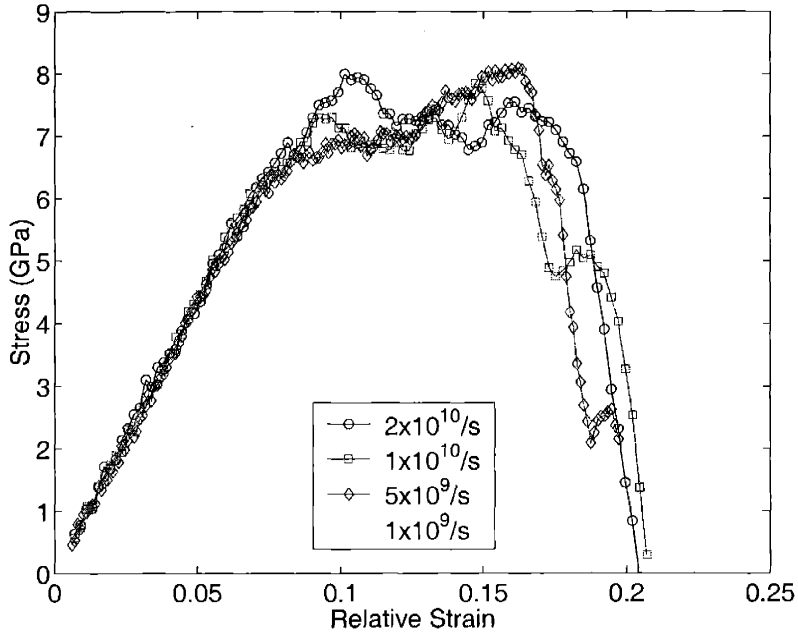

Figure 3-34: Stress-strain response of amorphous silica under tensile loading at 300°K.

Chapter 4

Strength and Deformation of ZrC

4.1 Introduction

The ZrC potential model

A new many-body potential has been developed recently by Ju Li[19] for ZrC_{1-x} system which is based in the so-called Finnis-Sinclair[115] potential or second moment approximation in the description of interatomic binding in transition metals. Such a potential was fitted to pure hcp Zr by Willaime and Massobrio[116, 117] using only four free parameters. The new ZrC model adds only six additional parameters in which four are used to described Zr-C bonding strengths, and two used to describe the angular screening. Described in full details by Ju Li *et al.*[19, 20], the new potential model is fitted to cohesive energies, elastic constants and most importantly, selected atomic force constants given by first-principles electronic structure calculations. Although involving only altogether 10 parameters, the resulting description accurately characterizes the nature of Zr-C interactions as demonstrated by an extensive validation study of thermal and mechanical properties of ZrC systems.

The new potential has the following form[1]:

$$\begin{aligned} U^{\text{total}} &= \sum_{a\in \text{Zr}} U_a^{\text{Zr}} + \sum_{p\in \text{C}} U_p^{\text{C}} \\ U_a^{\text{Zr}} &= \sum_{b\neq a} f(r_{ab}) + \sum_p \phi(r_{ap}) - \sqrt{X_a} \\ X_a &= \sum_{b\neq a} m^2(r_{ab}) + \sum_p \tilde{\mu}_{ap}^2 \\ U_p^{\text{C}} &= \sum_a \phi(r_{ap}) - \sqrt{X_p} \\ X_p &= \sum_a \tilde{\mu}_{ap}^2 \end{aligned} \tag{4.1}$$

The definition of pair interaction and second moments are[2]:

$$\begin{aligned} f(r) &= \exp\left(A_{\text{ZrZr}}(B_{\text{ZrZr}} - r) + \frac{K}{r - r_{\text{C}}^{\text{ZrZr}}}\right) \\ m^2(r) &= \exp\left(C_{\text{ZrZr}}(D_{\text{ZrZr}} - r) + \frac{K}{r - r_{\text{C}}^{\text{ZrZr}}}\right) \\ \phi(r) &= \exp\left(A_{\text{ZrC}}(B_{\text{ZrC}} - r) + \frac{K}{r - r_{\text{C}}^{\text{ZrC}}}\right) \\ \mu(r) &= \exp\left(C_{\text{ZrC}}(D_{\text{ZrC}} - r) + \frac{K}{r - r_{\text{C}}^{\text{ZrC}}}\right) \end{aligned} \tag{4.2}$$

The screened second moment $\tilde{\mu}_{ap}$ is defined with environment dependent terms as:

$$\tilde{\mu}_{ap} = \mu(r_{ap}) \exp\left(-\frac{\sqrt{\sigma_{ap}}}{\mu(r_{ap})}\right) \tag{4.3}$$

[1]To clarify the formulas, we will denote Zirconium atom subscript and Carbon atom subscript by different notations: a,b... for zirconium atoms and p, q ... for carbons. In summation is present, the index runs over all the atoms of that type. Similarly, X_a and X_p denote different functions without further reminder. Also to assist the reader, the function names in roman, $f(r)$, $m(r)$ are understood to pertain zirconium-zirconium interaction with distance between two zirconium atoms as argument, while function names in Greek $\phi(r)$, $\mu(r)$ pertain to zirconium-carbon interactions with distance between one zirconium and one carbon atom as argument. There is no carbon-carbon interaction in the model.

[2]There are many ways to write down the interaction. Although the present form seems awkward in terms of dimensions (each term has to be multiplied by either 1[eV] or 1[eV^2]), it is quiet efficient for implementation; by writing things in this way, every parameter is of order unity and therefore incurs least round-off error.

Here s_{ap} is the screening strength:

$$\sigma_{ap} = \sum_{q \neq p} \left(\frac{1 + \cos\theta_{qap}}{E} \right)^F \mu^2(r_{aq}) + \sum_{b \neq a} \left(\frac{1 + \cos\theta_{bpa}}{E} \right)^F \mu^2(r_{bp}) \tag{4.4}$$

Three parameters are picked by hand:

$$K = 0.1 \text{ [Å]} \qquad r_C^{ZrZr} = 7 \text{ [Å]} \qquad r_C^{ZrC} = 3.5 \text{ [Å]}$$

The fitted parameters are listed below:

$$\begin{aligned} A_{ZrZr} &= 2.9296875 \text{ [Å}^{-1}\text{]} & B_{ZrZr} &= 2.58787395638939 \text{ [Å]} \\ C_{ZrZr} &= 1.32308467741935 \text{ [Å}^{-1}\text{]} & D_{ZrZr} &= 4.3672464262563 \text{ [Å]} \\ A_{ZrC} &= 3.24589393669854 \text{ [Å}^{-1}\text{]} & B_{ZrC} &= 2.05679804919117 \text{ [Å]} \\ C_{ZrC} &= 0.82303818052368 \text{ [Å}^{-1}\text{]} & D_{ZrC} &= 4.15482225815134 \text{ [Å]} \\ E &= 1.80853303846249 & F &= 14.59345494373451 \end{aligned} \tag{4.5}$$

The force on each atom can be derived following (A.15). Here we can write the total energy as a function of the explicit variables r_{ab}, r_{ap}, θ_{apb} and θ_{qap}:

$$U(\{r_{ab}, r_{ap}, \theta_{apb}, \theta_{qap}\}) = \sum_{ab}^{\text{pairs}} 2f(r_{ab}) + \sum_{ap} 2\phi(r_{ap}) - \sum_a \sqrt{X_a} - \sum_p \sqrt{X_p} \tag{4.6}$$

Thus the force on each atom can be written as:

$$\begin{aligned} -\boldsymbol{f}_a^{Zr} &= \frac{\partial U^{\text{total}}}{\partial \boldsymbol{r}_a} \\ &= \sum_{b \neq a} F_{ab}^{ZZ} \frac{\boldsymbol{r}_{ab}}{r_{ab}} + \sum_p F_{ap}^{ZC} \frac{\boldsymbol{r}_{ap}}{r_{ap}} + \sum_{b \neq a} \sum_p F_{apb}^{ZCZ} \left(\frac{\partial \cos\theta_{apb}}{\partial r_{ab}} \frac{\boldsymbol{r}_{ab}}{r_{ab}} + \frac{\partial \cos\theta_{apb}}{\partial r_{ap}} \frac{\boldsymbol{r}_{ap}}{r_{ap}} \right) + \\ &\quad \sum_{pq}^{\text{pair}} F_{paq}^{CZC} \left(\frac{\partial \cos\theta_{paq}}{\partial r_{ap}} \frac{\boldsymbol{r}_{ap}}{r_{ap}} + \frac{\partial \cos\theta_{paq}}{\partial r_{aq}} \frac{\boldsymbol{r}_{aq}}{r_{aq}} \right) \end{aligned} \tag{4.7}$$

$$
\begin{aligned}
-\boldsymbol{f}_p^{\mathrm{C}} &= \frac{\partial U^{\mathrm{total}}}{\partial \boldsymbol{r}_p} \\
&= \sum_a F_{ap}^{\mathrm{ZC}} \frac{\boldsymbol{r}_{pa}}{r_{ap}} + \sum_{q\neq p}\sum_a F_{paq}^{\mathrm{CZC}} \left(\frac{\partial \cos\theta_{paq}}{\partial r_{pa}} \frac{\boldsymbol{r}_{pa}}{r_{pa}} + \frac{\partial \cos\theta_{paq}}{\partial r_{pq}} \frac{\boldsymbol{r}_{pq}}{r_{pq}} \right) + \\
&\quad \sum_{ab}^{\mathrm{pair}} F_{apb}^{\mathrm{ZCZ}} \left(\frac{\partial \cos\theta_{apb}}{\partial r_{pa}} \frac{\boldsymbol{r}_{pa}}{r_{pa}} + \frac{\partial \cos\theta_{apb}}{\partial r_{pb}} \frac{\boldsymbol{r}_{pb}}{r_{pb}} \right)
\end{aligned} \tag{4.8}
$$

with the following definitions:

$$
\begin{aligned}
F_{ab}^{\mathrm{ZZ}} &\equiv \frac{\partial U}{\partial r_{ab}} = 2f'(r_{ab}) - \left(\frac{1}{\sqrt{X_a}} + \frac{1}{\sqrt{X_b}} \right) m(r_{ab}) m'(r_{ab}) \\
F_{ap}^{\mathrm{ZC}} &\equiv \frac{\partial U}{\partial r_{ap}} = 2\phi'(r_{ap}) - \left(\frac{1}{\sqrt{X_a}} + \frac{1}{\sqrt{X_p}} \right) \tilde{\mu}_{ap}^2 \left[\frac{\mu'(r_{ap})}{\mu(r_{ap})} \left(1 + \frac{\sqrt{\sigma_{ap}}}{\mu(r_{ap})} \right) \right] + \\
&\quad \left[\sum_{q\neq p} \Gamma_{aq} \left(\frac{1+\cos\theta_{qap}}{E} \right)^F + \sum_{b\neq a} \Gamma_{bp} \left(\frac{1+\cos\theta_{apb}}{E} \right)^F \right] \mu(r_{ap}) \mu'(r_{ap}) \\
F_{apb}^{\mathrm{ZCZ}} &\equiv \frac{\partial U}{\partial \cos\theta_{apb}} = \left[\Gamma_{ap}\mu^2(r_{bp}) + \Gamma_{bp}\mu^2(r_{ap}) \right] \left(\frac{1+\cos\theta_{apb}}{E} \right)^{F-1} \frac{F}{2E} \\
F_{paq}^{\mathrm{CZC}} &\equiv \frac{\partial U}{\partial \cos\theta_{paq}} = \left[\Gamma_{ap}\mu^2(r_{aq}) + \Gamma_{aq}\mu^2(r_{ap}) \right] \left(\frac{1+\cos\theta_{paq}}{E} \right)^{F-1} \frac{F}{2E} \\
\Gamma_{ap} &\equiv \left(\frac{1}{\sqrt{X_a}} + \frac{1}{\sqrt{X_p}} \right) \frac{\tilde{\mu}_{ap}^2}{\mu(r_{ap})\sqrt{\sigma_{ap}}}
\end{aligned} \tag{4.9}
$$

At last, notice the following:

$$
\begin{aligned}
\frac{\partial \cos\theta_{apb}}{\partial r_{ap}} &= \frac{1}{r_{bp}} - \frac{\cos\theta_{apb}}{r_{ap}} \\
\frac{\partial \cos\theta_{apb}}{\partial r_{ab}} &= -\frac{r_{ab}}{r_{ap} r_{bp}}
\end{aligned} \tag{4.10}
$$

4.2 Composition Effects ZrC_{1-x}

4.2.1 Setup of the ZrC_{1-x} Systems

The ZrC_{1-x} systems have NaCl structure with certain amount of carbon vacancies. To study any off-stoichiometric system in simulation, a stoichiometric system is first prepared, then according the the desired x value, a specific amount of carbon atoms

is removed *randomly*. To equilibrate the carbon vacancy positions, the prepared off-stoichiometric sample is heated to near melting (3500°K) where carbon vacancies should be is relatively mobile for about 10ps followed by cooling down to the desired temperatures. Doing this is intended to avoid getting unphysical carbon vacancy configurations. Several samples of same stoichiometry are prepared randomly to test for convergence. For systems with more than 1000 atoms, no visible difference in the properties of off-stoichiometric ZrC systems could be found.

4.2.2 Structure Stability and Melting

As is the case of many other refractory carbides, ZrC_{1-x} has rock salt structure under normal conditions, the NaCl-like lattice is stable over a wide range of x, from 0 to about 0.39. The experimentally determined phase diagram is shown in Fig.4-1[118].

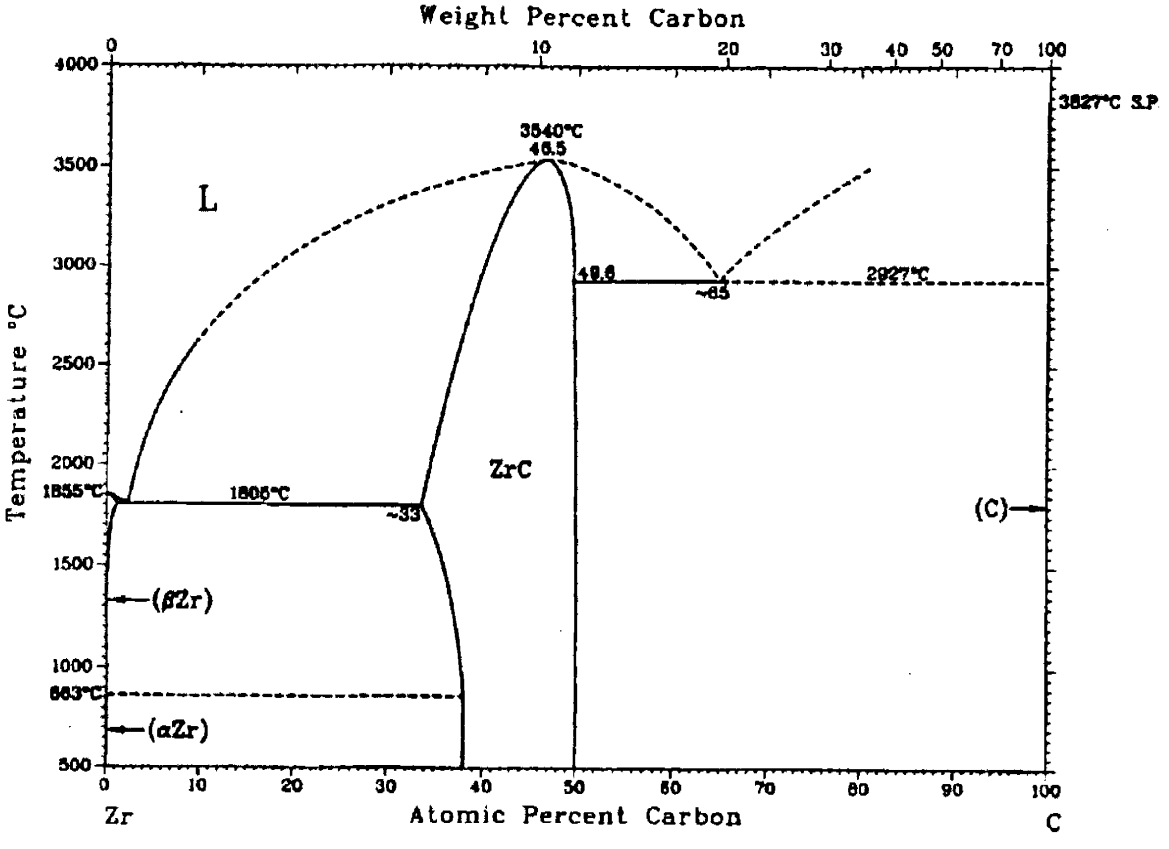

Figure 4-1: The phase diagram of ZrC_{1-x} determined by experiments[118]

In the ZrC crystals, according to the empirical atomic radii[119] zirconium atom is about twice as large as carbon, the former forms an FCC sublattice that by itself is close packed. Zirconium metal has close packed HCP structure in normal conditions, and transforms to FCC when heated above 936°K. Acting as small patches of glue, carbon atoms cause the close packed zirconium atoms to favor FCC instead of HCP structure.

With the new potential model, MD simulation can determine the structural stability and melting of the system. A series of high temperature simulations are performed to determine the melting temperature of the potential model. With two (001) free surfaces, the prepared ZrC system consists of 2000 atoms. At temperatures higher than melting, the mean square displacement (MSD) will increase linearly with time, signifying diffusion of atoms in liquid phase. In contrast, the MSD of a solid will approach a constant at long times. The onset of melting can be defined as the low temperature limit when slope of MSD in the liquid phase goes to zero. Fig.4-2 shows the MSD of different temperatures for the free surface melting simulations; the limit of zero slope is at 3643°K, agrees well with experimental value of $T_m \sim 3800$°K[120]. Fig.4-3 shows a melting free surface system, where the surfaces melts while the interior still remains solid.

4.2.3 Temperature and Stoichiometry Effects

For off-stoichiometric systems, the first thing to test is the relative change of lattice constants of different. Fig.4-4 shows the lattice constant versus composition parameter x. The absent of any effect (less than 0.3%) on lattice constants confirms our view of the carbon atoms acting as glue and zirconium atoms forming a rather rigid frame.

Thermal expansion is the first temperature effect of the system, which is shown in Fig.4-5. Again there is little influence from compositional variation. Furthermore, at higher temperatures the lattice constant difference becomes even smaller, implying the carbon atoms play even smaller parts in determining the distance between zirconium atoms.

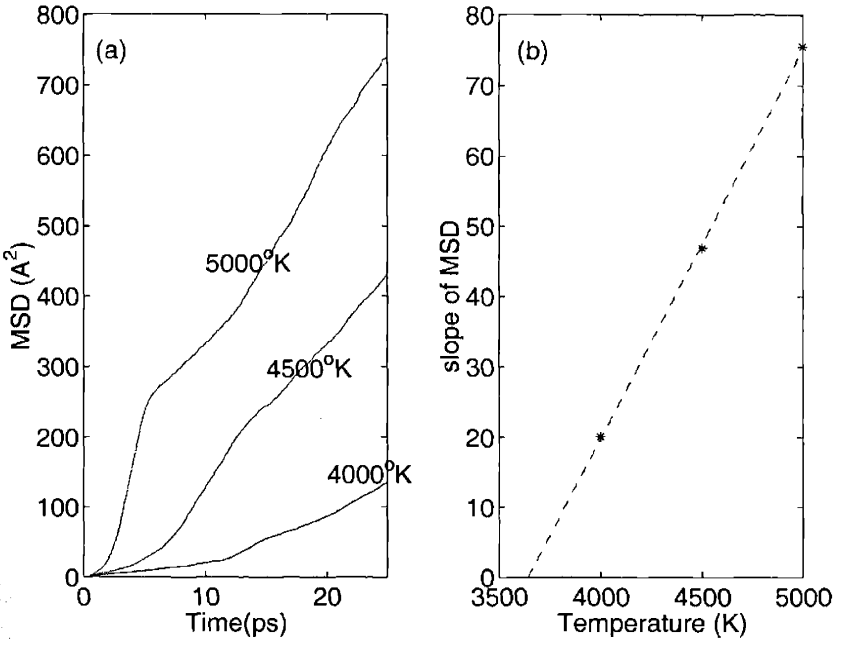

Figure 4-2: The melting of ZrC system with two free surfaces. (a) the mean square displacement(MSD) versus time, higher temperature the MSD increases faster. (b) The slope of MSD versus temperature, the extrapolated line intersect zero slope at 3643°K is the predicted melting temperature of the potential model.

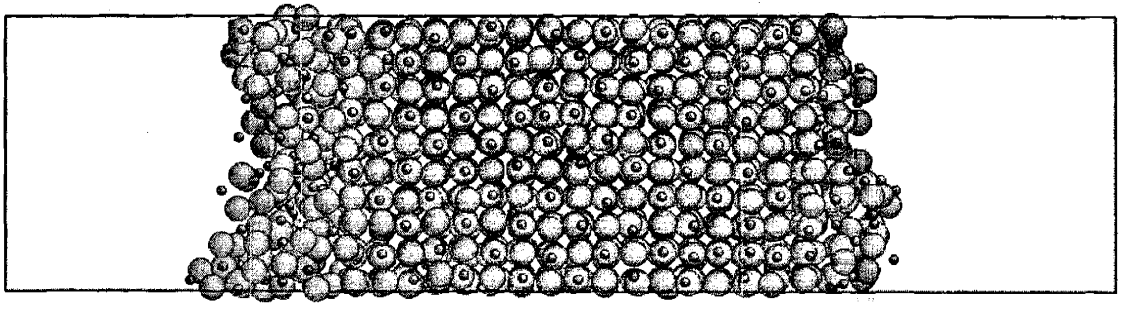

Figure 4-3: The configuration of a melting slab of ZrC with two free surfaces at 4500°K. The liquid-solid interface progress to the inside linearly with a speed proportional to the slope of MSD versus time curve.

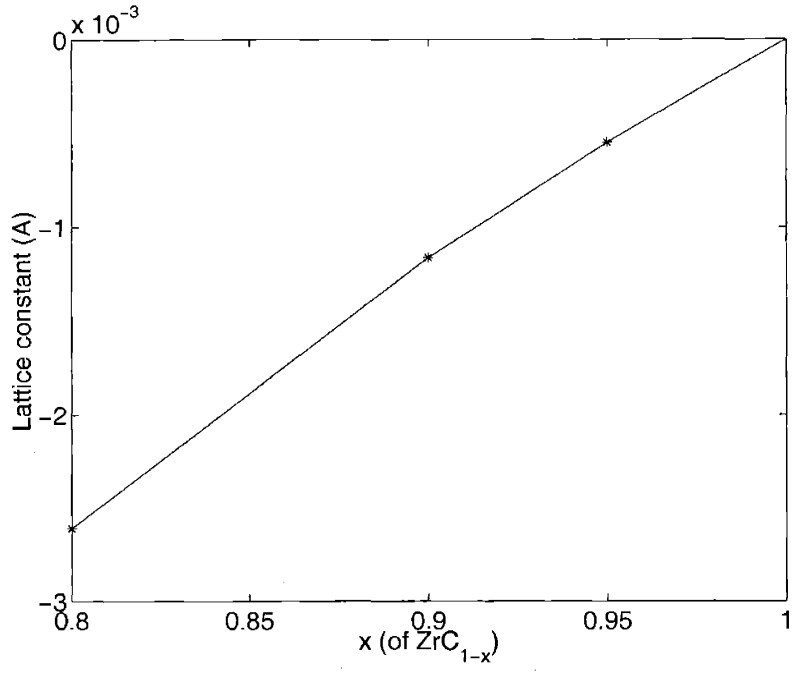

Figure 4-4: The lattice constants of ZrC_{1-x}, the experimental measurements of TiC_{1-x} is also shown.

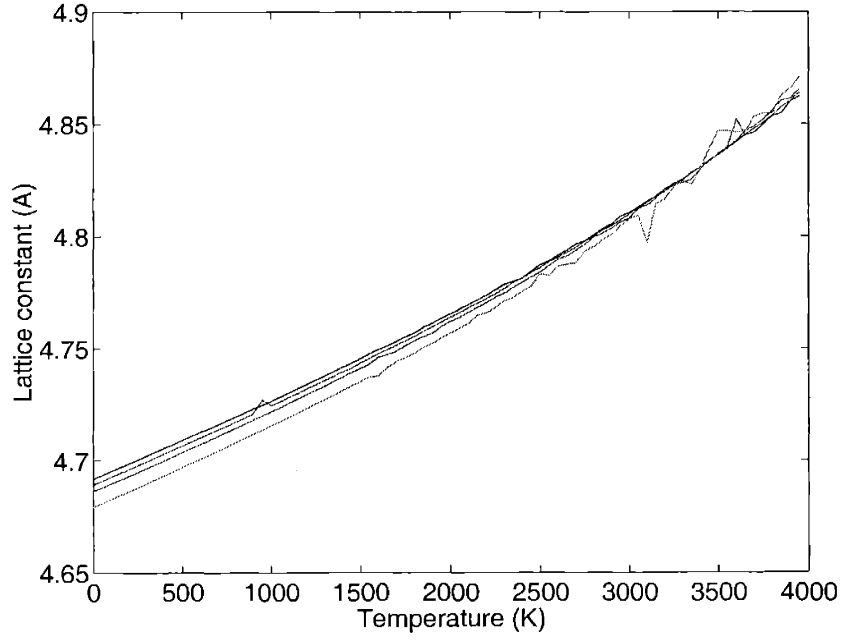

Figure 4-5: The linear thermal expansion of the ZrC_{1-x} system. Experimental values are shown as comparison.

4.2.4 Stress-Strain Responses

Hydrostatic Tensile Strength

Four systems of different stoichiometry used in previous sections are put under tension loading. Fig.4-6 shows the hydrostatic tension response of the on stoichiometry system at different temperatures. At low stress, linear elastic behavior is seen, as expected, while at high stress the systems still deform elastically with non-linear variation. For each system, at a critical stress structural failure occurs suddenly by an abrupt stress reduction. The temperature effect decrease is to both the theoretical strength and the critical strain in a linear manner. Notice that stress-strain response curve after the system failure is somewhat different at 3500°K compared to the three lower temperature curves, thus suggesting a change in the failure mechanism.

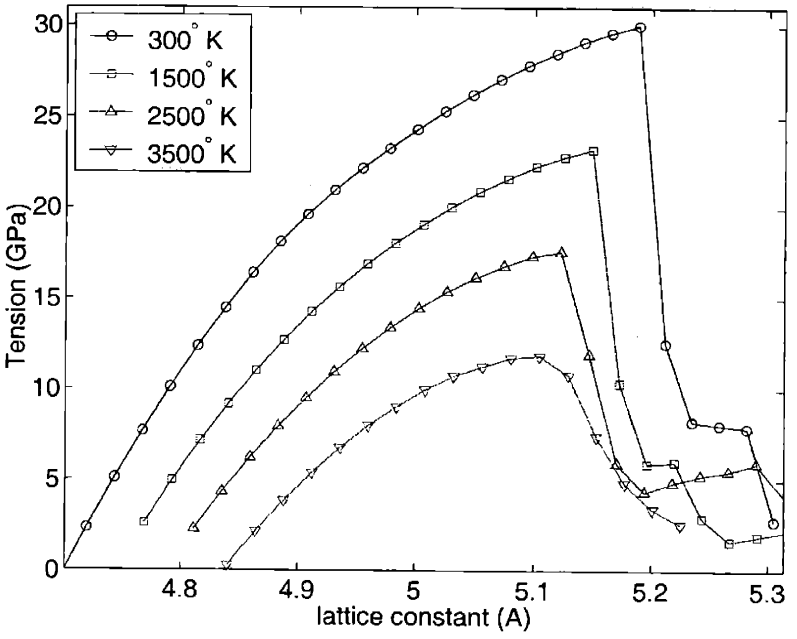

Figure 4-6: Stress-strain response of ZrC under hydrostaic tension, at different temperatures.

Fig.4-7 shows the failed configuration of the four systems, at 300°K, the cleavage plane is very clean. At higher temperatures (1500°K and 2500°K) the cleavage plane gets rougher, due to the higher thermal fluctuations, but the failure mechanism

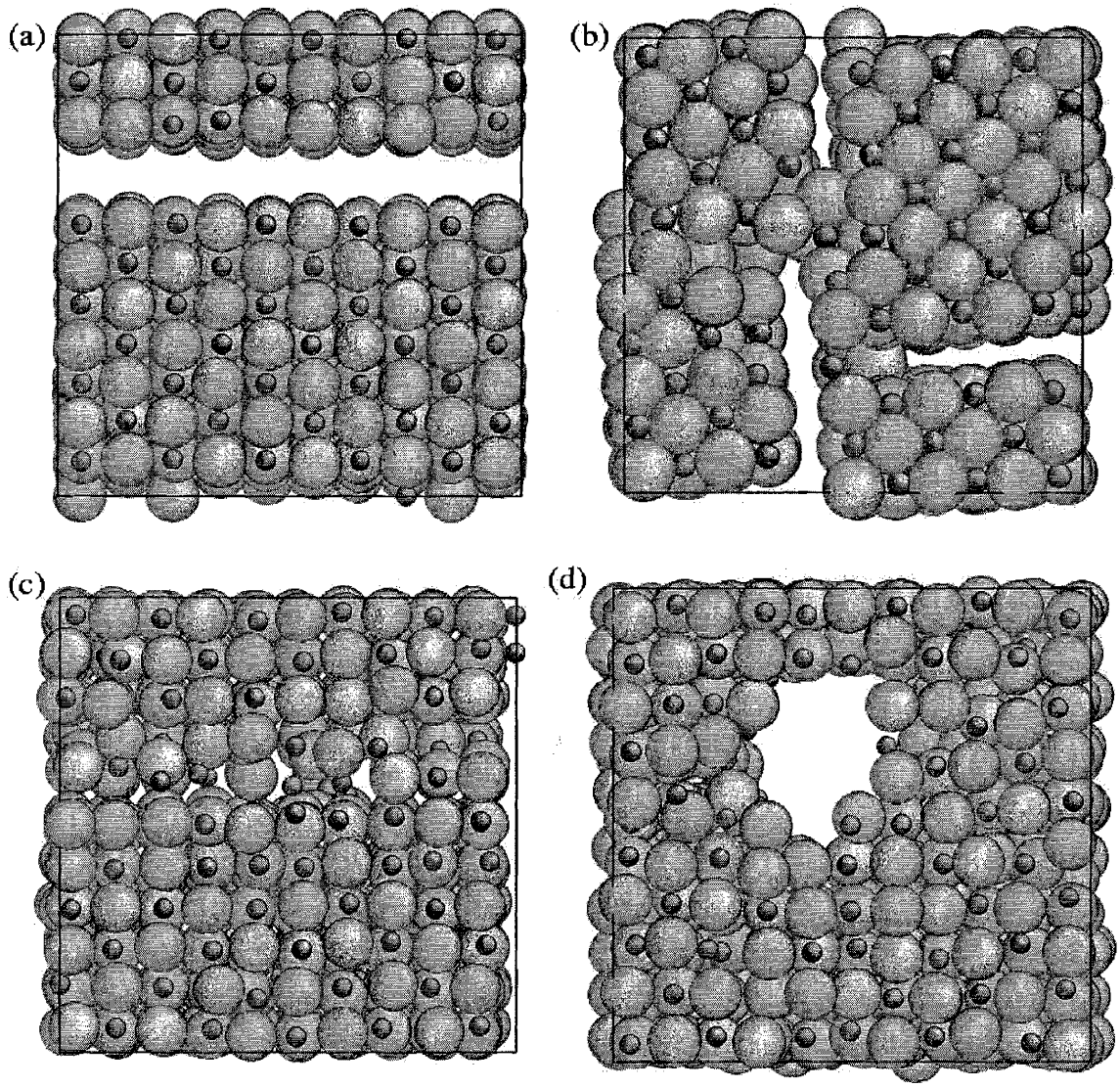

Figure 4-7: The failed configurations of ZrC crystal under hydrostatic tension at different temperatures (a) 300°K (b) 1500°K (c) 2500°K (d) 3500°K

is still planar cleavage. At 3500°K, the system now apparently fails through cavitation. The observation of changing of failure mechanism under simple hydrostatic tension suggests a possible existence of a brittle-to-ductile transition in ZrC around a temperature 2500°K-3500°K.

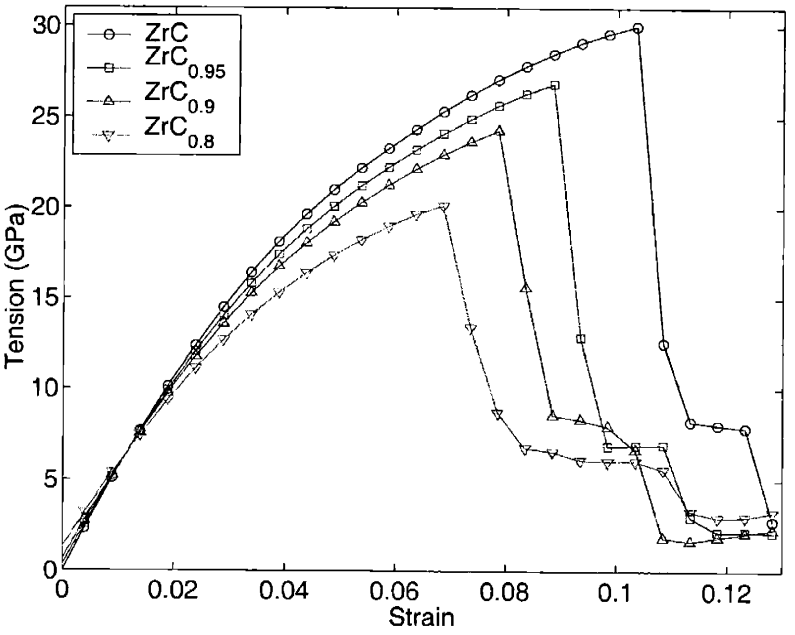

Figure 4-8: Stress-strain response of ZrC_{1-x} under hydrostatic tension at 300°K at different compositions x

The off-stoichiometric systems show a more pronounced compositional dependence in the strength and deformation behavior than the thermal properties like thermal expansion. Fig.4-8 shows the 300°K stress-strain response of four systems. In the low stress linear elastic region, there is little deviation among the different stoichiometric systems. Most of the stoichiometric effects appear in the high stress non-linear elastic region: the more off-stoichiometric, the larger of non-linear deformation, which implies a greater elastic constants softening with increasing strain. Its notable that at the failure point, all four systems have similar bulk modulus values (slope of the stress-strain curve).

At very high temperature (3500°K), stoichiometry effect, as shown in Fig.4-9, is rather systematic, with non-linear deformation setting in at lower strain when carbon

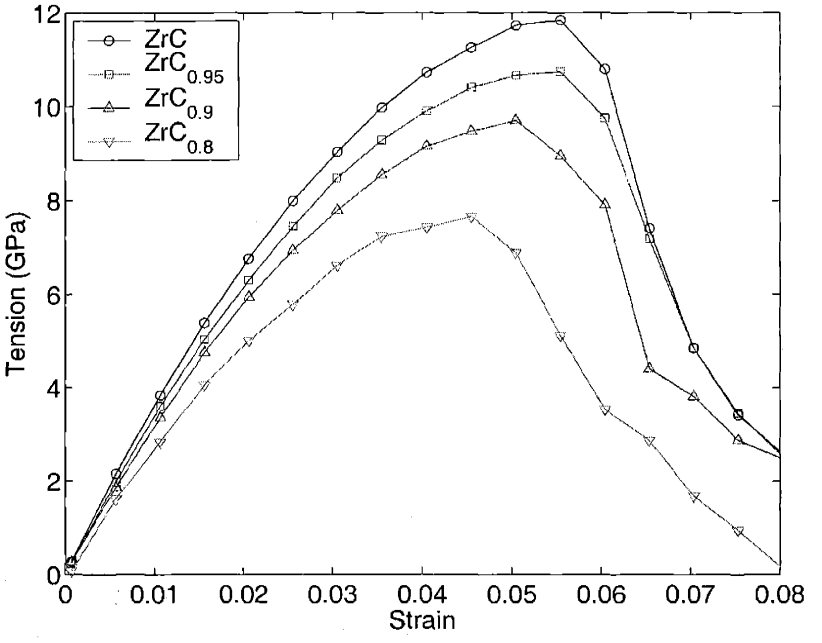

Figure 4-9: Stress-strain response of ZrC_{1-x} under hydrostatic tension at 3500°K at different compositions x

vacancies increase. Stoichiometry apparently has no strong influence on the brittle versus ductile failure behavior of the system.

ZrC_{1-x}	300°K	1500°K	2500°K	3500°K
$x = 0$	30.04(0.103)	23.22	17.58	11.84(0.055)
$x = 0.05$	26.85(0.089)	21.43	16.14	10.74(0.055)
$x = 0.1$	24.26(0.079)	19.62	14.94	9.70(0.051)
$x = 0.2$	20.11(0.069)	16.14	12.38	7.66(0.046)

Table 4.1: Values of critical stress[GPa] and critical strain of ZrC under hydrostatic tension at different temperatures and composition

Table.4.1 and Fig.4-10 summarize the theoretical strength dependence on temperature and composition. Variation of critical stress is largely linear in both T and x. To investigate possible correlation between temperature and stoichiometric effects, we have fitted the critical stress to the form:

$$\sigma_C = \sigma_C^0 + C_T T + C_x x \tag{4.11}$$

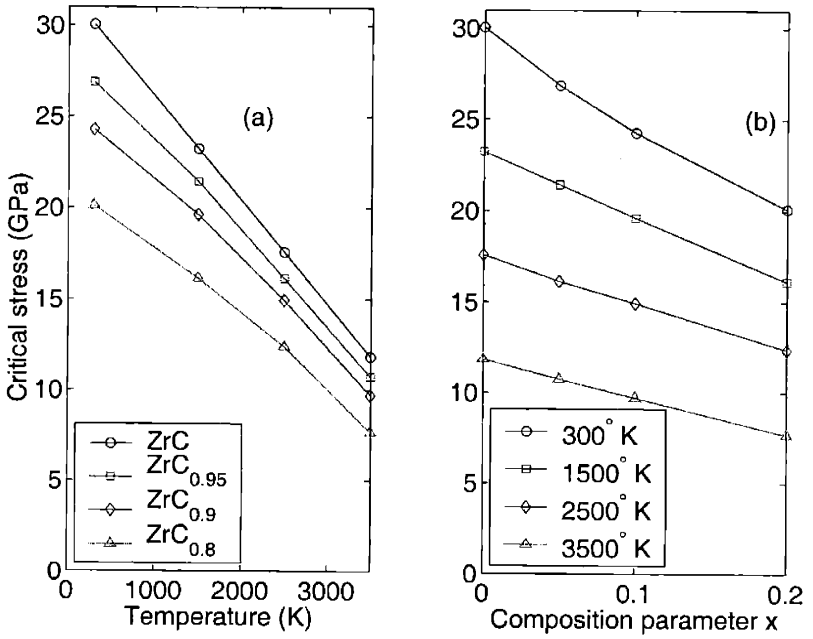

Figure 4-10: Critical stress of ZrC_{1-x} under hydrostaic tension, at different temperatures. Same set of data plotted in two forms, (a) plot of temperature dependence at different composition x. (b) Stoichiometry dependence at different temperature.

The results show that over a large temperature and composition range, the effects of temperature and composition on theoretical stress can be considered independently. This observation, obtained relatively easily by simulations, could be a valuable insight for materials design.

Uniaxial Tensile Strength

Similar to hydrostatic tension studies, the four stoichiometric systems are also examined under uniaxial tensile loading. Because of the anisotropic nature of ZrC crystal, two orientations are studied, namely, $\langle 100 \rangle$ and $\langle 111 \rangle$ directions.

Fig.4-11 shows the stoichiometric effect on uniaxial tensile strength at low temperature (300°K) and high temperature (3500°K). Similar to hydrostatic cases, the theoretical strength decrease linearly with both temperature and stoichiometric composition. Yet the failure mechanism is different from the hydrostatic cases. Even at temperature close to melting ($T_m \sim 3800$°K), the system fails through cleavage. We

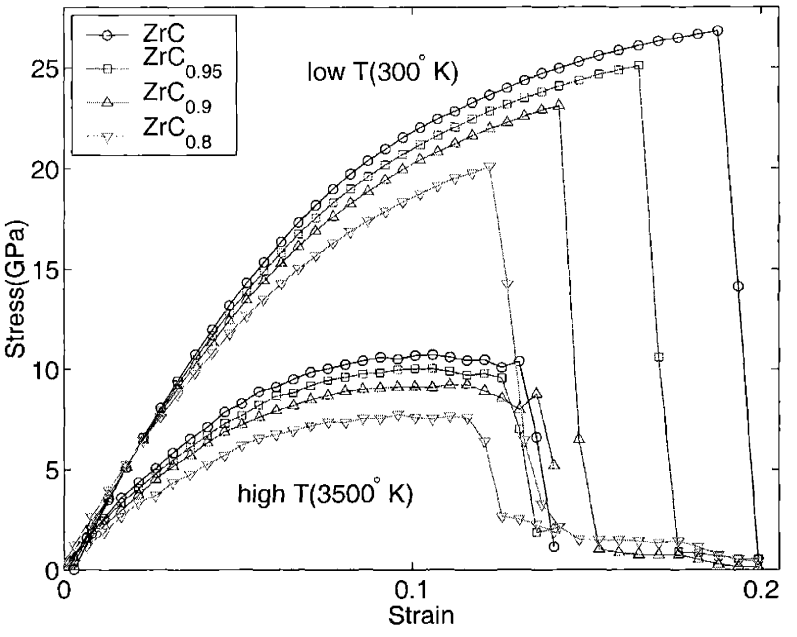

Figure 4-11: Stress-strain response of ZrC_{1-x} under uniaxial tension in $\langle 100 \rangle$ directions at 300°K and 3500°K at different stoichiometries

attribute this behavior to the more anisotropic nature of uniaxial loading, favoring planar decohesion.

For $\langle 111 \rangle$ directions tensile loading, the stress strain response is shown in Fig.4-12. The critical strength is much higher than the $\langle 100 \rangle$ directions tensile loadings; this implies the surface cohesion force is stronger. A calculation of surface energy of different planes of ZrC crystal confirms that surface energy of $\{111\}$ planes are indeed much higher than $\{100\}$ planes. The calculated surface energies at 300°K are shown in Table.4.2

Surface	$\gamma[\text{eV}/\text{Å}^2]$
$\{100\}$	0.1025
$\{210\}$	0.1318
$\{110\}$	0.1397
$\{112\}$	0.1563
$\{111\}$	0.3256

Table 4.2: Surface energy of various orientation of ZrC crystal is calculated at 300°K.

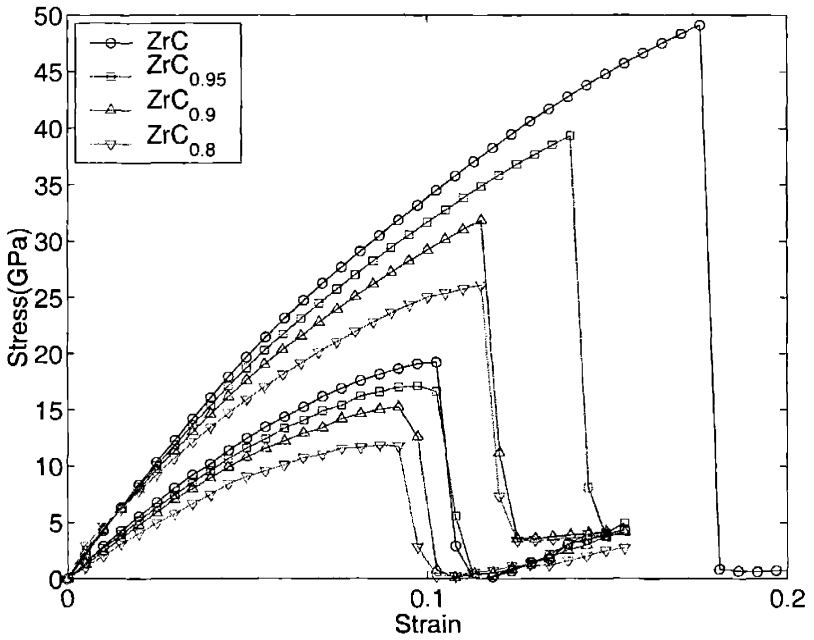

Figure 4-12: Stress-strain response of ZrC_{1-x} under uniaxial tension in $\langle 111 \rangle$ directions at 300°K and 3500°K at different stoichiometries

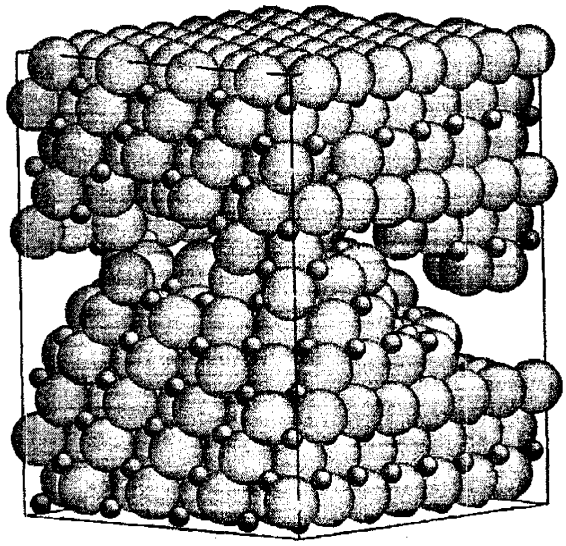

Figure 4-13: Failure configuration of ZrC under $\langle 111 \rangle$ directions uniaxial loading at 300°K. The cleavage happens on several $\{100\}$ planes.

When the systems eventually fail, the cleavage can initiate on several {100} planes, as shown in the configuration Fig.4-13. In a later section we will show that, for the same reason, cracks originally on {111} planes can also change direction under mode I (unaxial tensile) loading.

4.3 Thermal Conductivity of ZrC

The thermal conductivity study described in this section predates the development of the new ZrC potential model and is conducted with an pairwise interaction model fitted to ZrC, named as "ZrC-II" model. A brief summary of the potential can be found in Appendix A.

Some preliminary calculations of ZrC thermal conductivity with the new potential model has been presented by Ju Li *et al.*[19, 21], which give slightly lower conductivity values but otherwise confirms the conclusions arrived at in this section.

Having a very high melting point ($T_m \sim 3800$°K), ZrC finds many high temperature applications such as nuclear power plants or waste incinerators, where good thermal conduction is either desired or to be avoided. Understanding the underlying mechanism and the controlling factors that determine the thermal conductivity[121] of ZrC is therefore considered important to these applications. Using atomistic simulations, we can carry out the study of ZrC thermal conductivity with idealized microstructures and single out every thermal conduction process and study them individually.

In a crystal, thermal energy can be carried by electronic and phonon carriers. Electronic carrier is the dominant heat conduction mechanism in metals, where free electrons exist throughout the system. For insulators, when most electrons are tightly bond, electronic heat current is negligible. On the other hand, phonons with finite lifetime carry heat current through anharmonic lattice vibrations; these can be studied effectively by direct atomistic simulations. In this section, we will investigate the lattice thermal conductivity of ZrC and the effects of microstructures on it.

4.3.1 Thermal Conductivity Calculation

The definition of thermal conductivity κ is based on linear response theory of heat current

$$\boldsymbol{J}^q = -\kappa \nabla T \tag{4.12}$$

As for SiC [122], the method we use to calculate κ is based on the formalism of time-correlation functions where transport coefficients of a system of N interacting atoms are given by the time integrals of appropriate equilibrium correlation functions [123]. The thermal conductivity is proportional to the time integral of heat current correlation function

$$\kappa = \frac{1}{T^2 V} \int_0^\infty \mathrm{d}\tau \, \langle \boldsymbol{J}^q(0) \boldsymbol{J}^q(\tau) \rangle \tag{4.13}$$

The microscopic heat current is defined by

$$\boldsymbol{J}^q = \frac{\mathrm{d}}{\mathrm{d}t} \left(\sum_{a=1}^{N} E_a \boldsymbol{r}_a \right). \tag{4.14}$$

For pairwise potentials, we can write the single particle energy as the sum of kinetic and potential energies

$$E_a = \frac{1}{2} m_a \dot{\boldsymbol{r}}_a^2 + \frac{1}{2} \sum_{b \neq a} U(r_{ab}), \tag{4.15}$$

and by explicitly doing the time derivative, taking account of the equation of motion, we arrive at the expression for pairwise interactions:

$$\boldsymbol{J}^q = \frac{1}{2} \sum_{a<b}^{N} \left[U(r_{ab})(\boldsymbol{v}_a + \boldsymbol{v}_b) - \frac{1}{r_{ab}} \frac{\partial U(r_{ab})}{\partial r_{ab}} [\boldsymbol{r}_{ab} \cdot (\boldsymbol{v}_a + \boldsymbol{v}_b)] \boldsymbol{r}_{ab} \right] + \frac{1}{2} \sum_a \left(m_a v_a^2 \right) \boldsymbol{v}_a. \tag{4.16}$$

Thermal conductivity calculations are performed for twelve systems at different temperatures, which can be specified by ZrC_{1-x} with y% Zr vacancies. Value of x is either 0, 0.05, 0.10 or 0.20, value of y is one of 0%, 0.2% and 0.6%. The perfect crystal system consists of 1000 atoms, with Zr and C each 500. The ZrC_{1-x} systems are set up by removing carbon or zirconium atoms similar to the process described in Section.4.2.1. Molecular dynamics runs of a few picoseconds are first performed

in canonical ensemble at the desired temperature; the simulations are then changed to micro-canonical ensemble. First 10ps is taken to relax any possible transitional effects from one ensemble to another; after that the trajectory data are used to construct the heat current vectors of the entire system at each timestep (a timestep is chosen to be 1.0 femtosecond) for about 1000 picoseconds. After obtaining the heat current of all 1000 picoseconds (which is 1000000 data points), the correlation function $\langle \mathbf{J}^q(0)\mathbf{J}^q(\tau)\rangle$ is calculated for τ values ranging from 0 to 40 picoseconds. Then the thermal conductivity κ is obtained from (4.13).

All the calculated values of thermal conductivity are summarized in Table.4.3 and plotted in Fig.4-14

description	300 K	500 K	1000 K	1500 K	2000 K
ZrC(no Zr vac)	146.6 ± 9.5	75.18 ± 2.3	36.52 ± 0.9	16.47 ± 0.8	9.83 ± 0.2
ZrC(.2% Zr vac)	N/A	34.73 ± 3.3	23.18 ± 1.9	13.95 ± 0.5	10.38 ± 0.5
ZrC(.6% Zr vac)	N/A	21.09 ± 2.0	N/A	9.82 ± 0.4	8.31 ± 0.4
$ZrC_{0.95}$(no Zr vac)	30.00 ± 4.4	21.40 ± 1.4	12.40 ± 0.5	7.19 ± 0.3	7.80 ± 0.2
$ZrC_{0.95}$(.2% Zr vac)	N/A	17.53 ± 2.8	13.44 ± 0.8	N/A	7.84 ± 0.2
$ZrC_{0.95}$(.6% Zr vac)	N/A	14.51 ± 2.8	9.80 ± 0.9	6.94 ± 0.5	5.87 ± 0.3
$ZrC_{0.9}$(no Zr vac)	20.18 ± 3.0	16.05 ± 2.8	10.88 ± 0.7	8.39 ± 0.2	5.36 ± 0.2
$ZrC_{0.9}$(.2% Zr vac)	N/A	14.58 ± 1.7	9.20 ± 0.7	7.09 ± 0.2	7.96 ± 0.2
$ZrC_{0.9}$(.6% Zr vac)	N/A	13.34 ± 1.5	7.24 ± 0.3	5.81 ± 0.5	4.78 ± 0.2
$ZrC_{0.8}$(no Zr vac)	14.37 ± 1.3	10.40 ± 1.1	6.84 ± 0.4	5.28 ± 0.1	5.21 ± 0.2
$ZrC_{0.8}$(.2% Zr vac)	N/A	9.90 ± 0.4	7.27 ± 0.4	6.92 ± 0.2	4.64 ± 0.2
$ZrC_{0.8}$(.6% Zr vac)	N/A	8.80 ± 1.1	N/A	5.96 ± 0.2	4.18 ± 0.1

Table 4.3: Thermal conductivities of single crystal and off-stoichiometric ZrC calculated using ZrC-II.

4.3.2 Microstructure Effects on Phonon Heat Carriers in ZrC

For perfect crystals, the thermal conductivity decreases roughly as $1/T$ at high T, which can be understood from anharmonic phonon lifetime estimation in transport theory[124]. The existence of vacancies, either zirconium or carbon, quickly suppresses the temperature dependence of thermal conductivity because of phonon scattering by the defects. As seen in Fig.4-14, even 0.2% zirconium vacancy can greatly reduce the

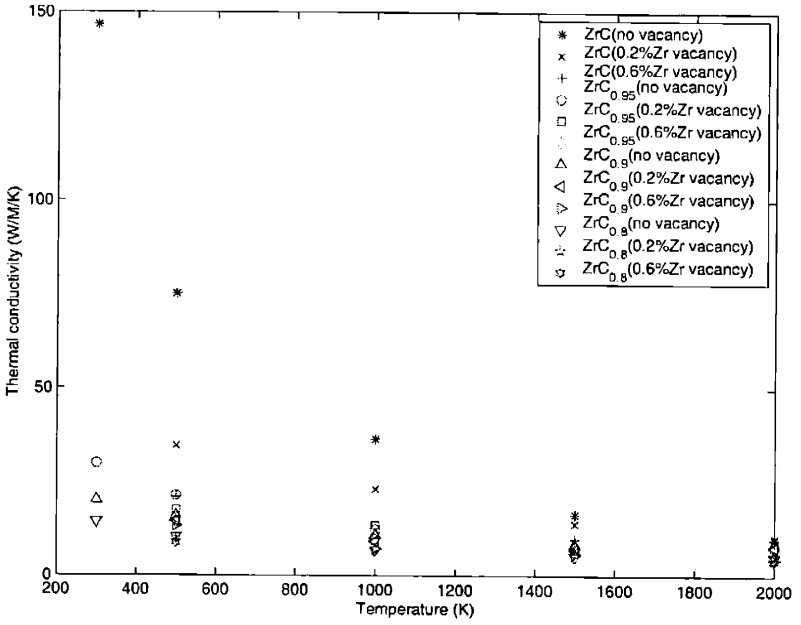

Figure 4-14: All the thermal conductivity data calculated by ZrC-II potential.

thermal conductivity at low temperatures. Similar effects is discovered in a previous study of SiC thermal conductivity by Li, Porter and Yip[122]. The drastic decrease of thermal conductivity by small amount of point defects is understood to be the scattering and decay of heat conducting phonons by the defects.

Fig.4-15 shows a collection of experimental data of ZrC thermal conductivity measurements[125]. An examination of the specimen specifications of the 14 different sets of data indicates that none of the specimens are pure, all containing a few percents of carbon vacancies (i.e. off-stoichiometric) as well as chemical impurities.

Comparing the experimental measurements with the simulation results of ZrC lattice conductivity, we find in the non-pure ZrC crystals, the phonon heat carrier only amounts to about 10-20% of the total heat conductivity. On this basis we conclude that the dominant heat conduction mechanism is electronic.

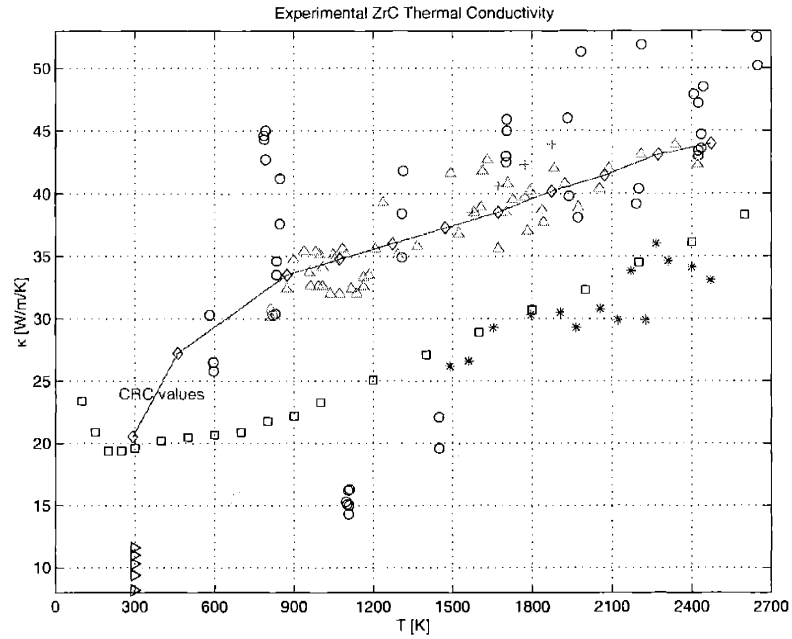

Figure 4-15: A collection of experimental measurements of ZrC thermal conductivity as a function of temperature[125]. *CRC Handbook* [126] recommended values are plotted in solid line.

4.4 Crack Extension in Crystalline ZrC

Similar to our study of crack extension in quartz, cracks are prepared in ZrC crystals. Two sets of simulations are performed, with cracks on either {100} planes or {111} planes. The fracture is observed to be brittle up to 2500°K ($T_m \sim 3800$°K). In the {100} simulations, the crack propagates within the original plane, perpendicular to loading. While for the {111} plane cracks, as shown in Fig.4-16, the fracture choose to propagate along one of the {210} planes that are 45° to the loading direction. This can be understood by the Griffith criteria for brittle fracture.

Using MD results, for the {100} planes, we have the Young's modulus E and Poisson's ratio ν:

$$E^{\{100\}} = \frac{(C_{11}-C_{12})(C_{11}+2C_{12})}{C_{11}+C_{12}} = 332.8[\text{GPa}] \tag{4.17}$$

$$\nu^{\{100\}} = \frac{C_{12}}{C_{11}+C_{12}} = 0.24 \tag{4.18}$$

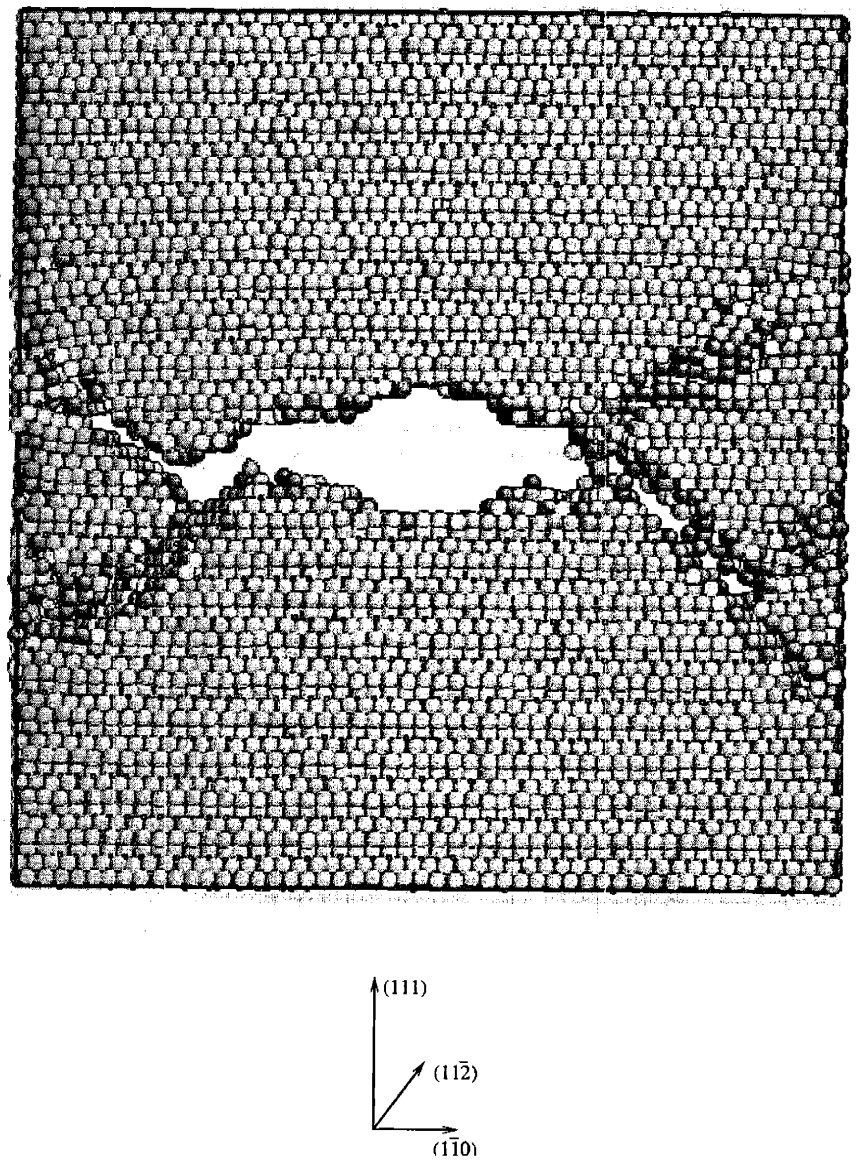

Figure 4-16: The brittle propagation of crack at 1500°K. The crack chooses to move on the plane where the critical stress for propagation is the lowest.

The surface energy of $\{100\}$ is $\gamma^{\{100\}} = 0.1025[\text{eV/Å}]$. The stress intensity factor for mode I loading fracture can be calculated according to (1.4), $K_{\text{IC}}^{\{100\}} = 1.076[\text{MPa} \cdot \text{m}^{1/2}]$

For cracks on any other surface, the stress intensity factor can be calculated similarly. Table.4.2 listed the calculated values for surface energy. It is a non-trivial task to accurately derive the elastic energy release by crack propagation on arbitrary surface in anisotropic material (for details, see[127]). For all practical purpose, we can assume the material to be isotropic, so the difference of planes comes mostly from the surface energy. From (1.4), the K_{IC} are roughly proportional to the square root of the surface energy.

The fact that a crack originally on (111) surface will choose to propagate on (201) surfaces is because the critical stress obtained from fracture mechanics for $\{111\}$ plane crack propagation is larger than the critical stress for a $\{210\}$ plane crack even under 45° tilted loading situation. Roughly speaking, in this loading situation we have:

$$\frac{\sigma_{\text{C}}(\text{propagate along } (111))}{\sigma_{\text{C}}(\text{propagate along } (201))} = \frac{\sqrt{\gamma^{\{111\}}}}{\sqrt{\gamma^{\{210\}}}\sqrt{2}} > 1$$

This explains why the crack choose to propagate along $\{210\}$. Although $\{100\}$ has even smaller surface energy, the crack front does not lie on any $\{100\}$ surfaces, thus unable to extend on $\{100\}$ plane.

In this work we have shown that for brittle crack propagation problems, the Griffith law and relevant linear elasticity theories is applicable even in atomistic length scales.

4.5 Strength and Deformation of Nanocrystal ZrC

4.5.1 Structural Initialization and Verification

Nanocrystal systems for MD studies can be created by putting randomly oriented grains on body centered cubic(BCC) lattice positions and compressing under hydrostatic pressure of 10GPa for 10ps. Then the systems are allowed to equilibrate at 300°K to zero external pressure state. This procedure is not too different from what

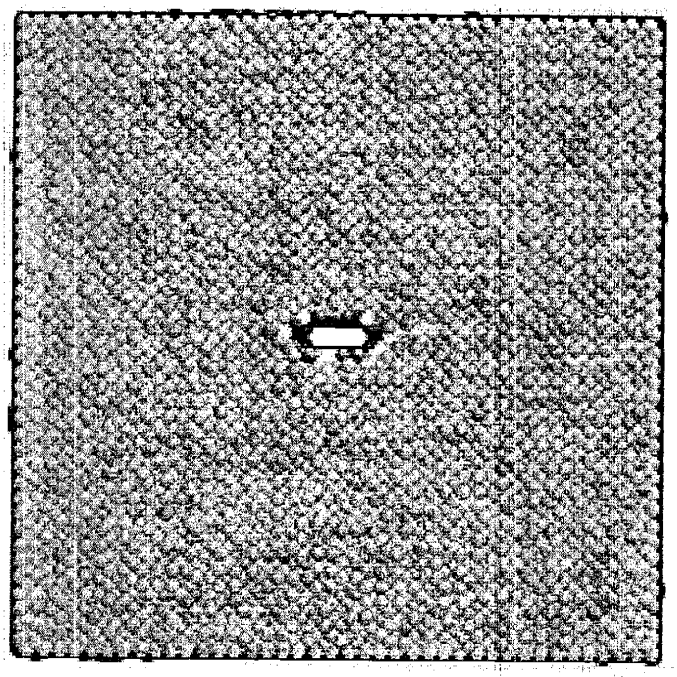

Figure 4-17: The 3nm crack on {001} plane of ZrC. Equilibrated at 1500°K.

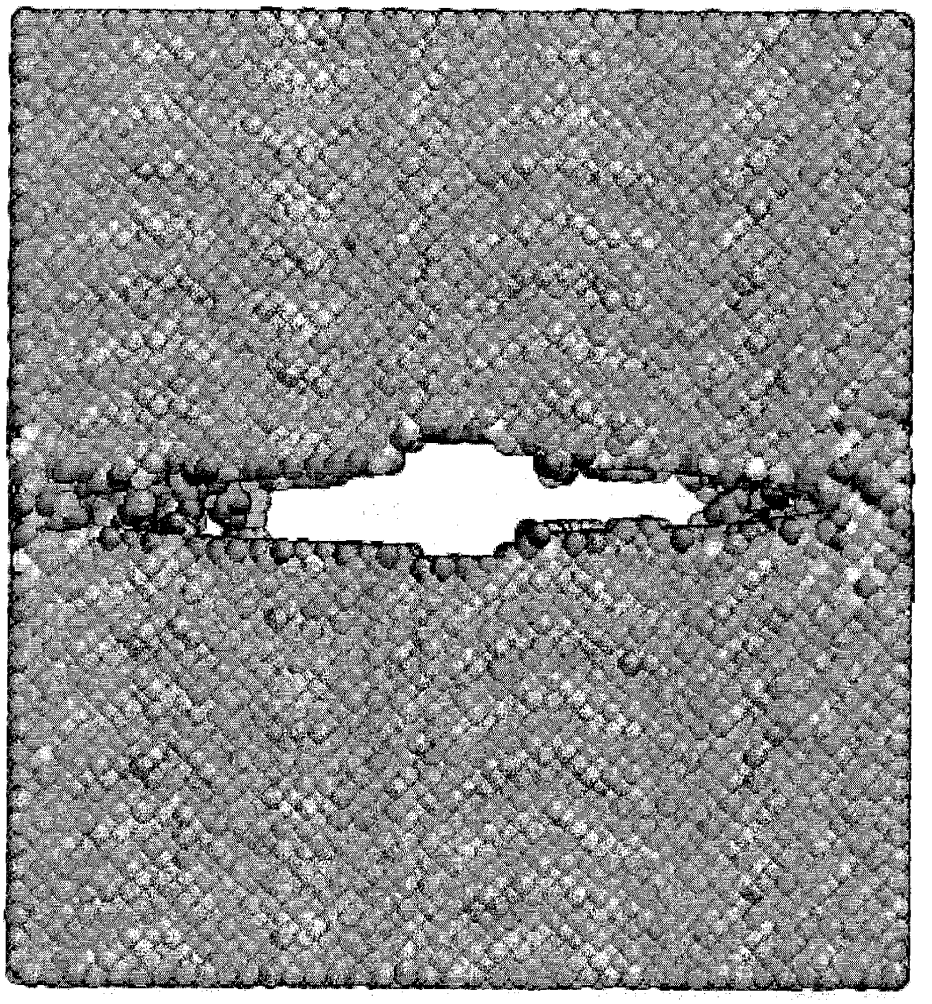

Figure 4-18: The brittle propagation of crack at 1500°K.

nanocrystal is created in experiments[128].

Four systems all with 16 grains have been prepared in this way. The detailed configuration information is listed in Table.4.4. The number of carbon atoms and zirconium atoms slightly disagree because of the randomly cut surfaces of all the grains. It is notable that the density increases as the grain size increases. Recall the density for crystalline ZrC is about 6.6[g/cm^3]. This implies the disordered material in the grain boundaries has lower density. It is also evident that at smaller grain sizes a nanocrystal has a larger portion of grain boundary material, as one would expect.

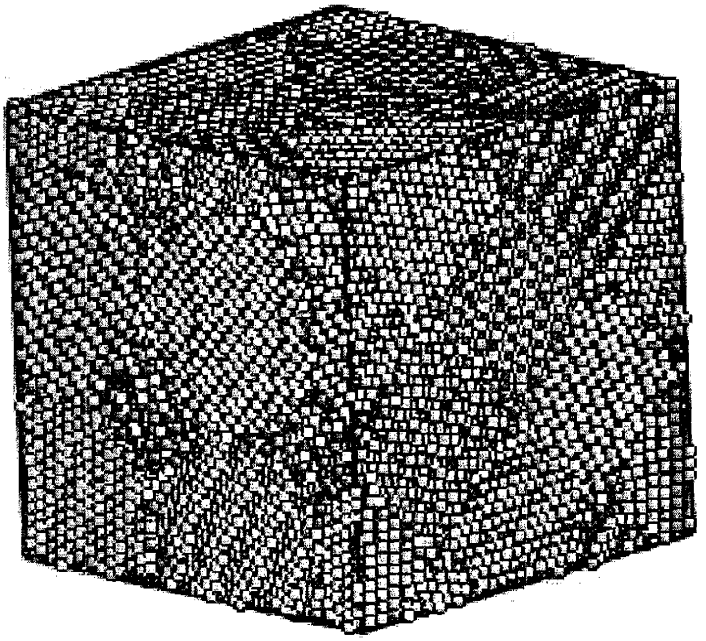

Figure 4-19: The configuration of a nanocrystal sample. 16 grains are arranged in BCC lattice to achieve spherical grain shapes, each grain is roughly 5.9nm in diameter.

Fig.4-19 shows the equilibrated nanocrystalline ZrC sample of 5.9[nm] grain. By choosing completely random grain orientation, large portion of grain boundaries are high angle grain boundaries, making the grain boundary relaxation a complex process. From the configuration it is observed that almost all grain boundaries are amorphous. This will not be the case if the grain boundaries are small-angle boundaries.

Qualitatively, the portion of grain boundary depends on the exact definition of the grain boundary. If we assume all the atoms inside the grain to have coordination number for rock salt structure, and those in grain boundary have other coordination numbers, we can calculate the number of atoms on grain boundaries and get the portion. Alternatively, since the grain boundary consists of amorphous material, we can use the densities of amorphous and crystalline of ZrC to deduce the portion of the system that is grain boundary. In an attempt to get amorphous ZrC by heating and quenching of a 1000 atoms ZrC crystal, we produced a disordered ZrC system above 3000°K. When quenched below 3000°K, the system quickly recrystalized. Fig.4-20 shows the disordered system at 3000°K and partially recrystalized system at 2500°K. Nonetheless, the density of partial recrystalized system at 300°K is 5.4[g/cm^3]. If we take that value as the density of grain boundary, we have a second measure of grain boundary portion in our nanocrystalline system.

d_{grain}[nm]	N_{Zr}	N_{C}	Geometry[nm^3]	ρ[g/cm^3]	GB1	GB2
2.4	3715	3689	$4.76 \times 4.76 \times 4.76$	5.91	56.3%	57.5%
3.6	12792	12837	$7.11 \times 7.11 \times 7.11$	6.11	41.1%	40.8%
4.7	30808	30739	$9.47 \times 9.47 \times 9.47$	6.22	32.0%	31.7%
5.9	60607	60571	$11.82 \times 11.82 \times 11.82$	6.30	26.3%	25.0%

Table 4.4: The details of four nanocrystalline ZrC system prepared in the simulation. GB1 gives the portion of grain boundary deduced from atomic coordination. GB2 gives the portion of grain boundaries is deduced by assuming grain boundary density to be 5.4[g/cm^3]

In Table.4.4 both measures of grain boundary portion are shown, and agree with each other. This result is consistent with previous studies of nanocrystal by both theoretical estimates[129] and simulations[54]. This agreement serves as a verification of the prepared nanocrystalline structures.

4.5.2 Reverse Hall-Petch Effect in Nanocrystalline ZrC

Conventionally, Hall-Petch[55, 56] effect refers to the increase in strength or hardness of a polycrystalline material as the grain size decreases. It is believed to be the result

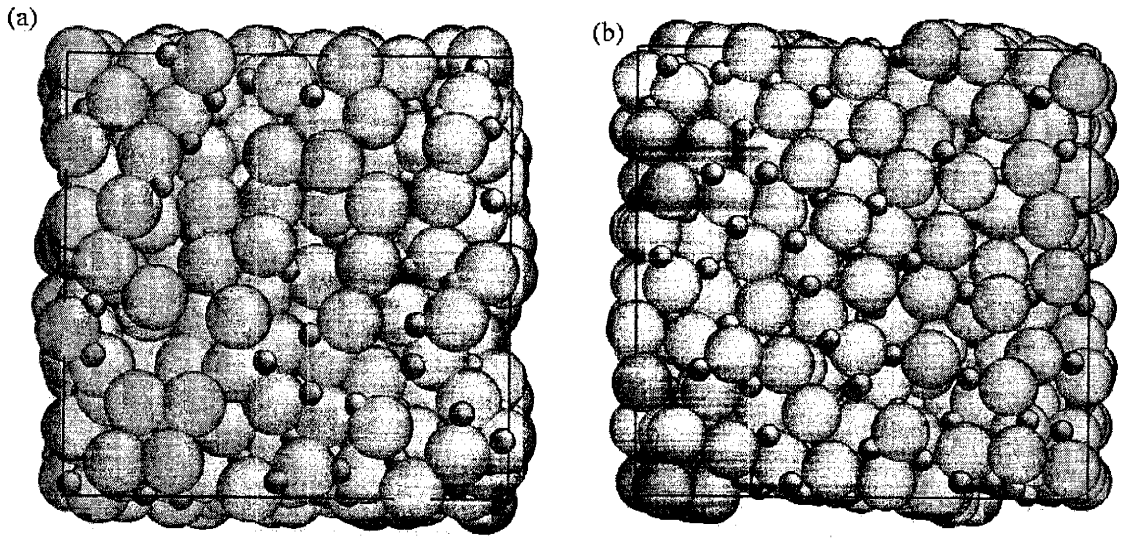

Figure 4-20: The recrystalization of amorphous ZrC. (a) Amorphous ZrC at 3000°K, obtained through melting and quench. (b) Partially recrystalized ZrC at 2500°K.

of dislocation pile-up within each grain, making the grain more resistant to yield. In nanocrystals, a reversed strength versus grain size relation, i.e. the reverse Hall-Petch effect, has been observed[54].

We have performed both tensile and shear simulations on ZrC nanocrystals. The nanocrystal sample is prepared by taking a cubic simulation cell and at 16 "seed points" forming BCC structures in the cube. At each "seed point", an orientation is randomly chosen and filled in the ZrC crystal structure in the Voronoi of that point.[3] The shape of each grain is essentially spherical (the same shape as first Brillouin zone of an FCC crystal). Four different of grain sizes are studied, with grain diameter 2.4, 3.6, 4.7 and 5.9[nm] respectively. At the interface between grains, when two atoms are too close, one of them is randomly removed. After initialization, the system is given 10 picoseconds for equilibration at constant zero external pressure.

Under tensile loading, we have used constant strain rate simulations in which any

[3]A Voronoi of a "seed point" A contains all the space that is closest to A than any other "seed point", the same concept is used in free volume definition of atoms or Brillouin zone of reciprocal lattices.

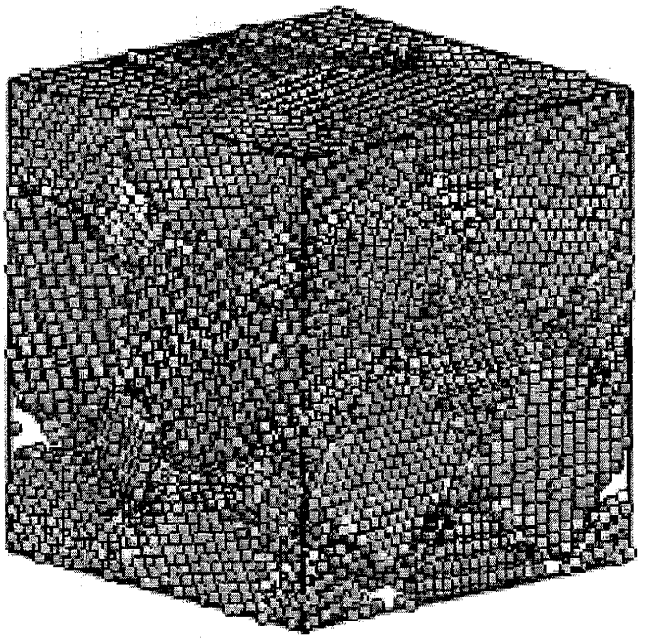

Figure 4-21: The failure configuration after tension loading at 300°K, the cleavage are visible along grain boundaries.

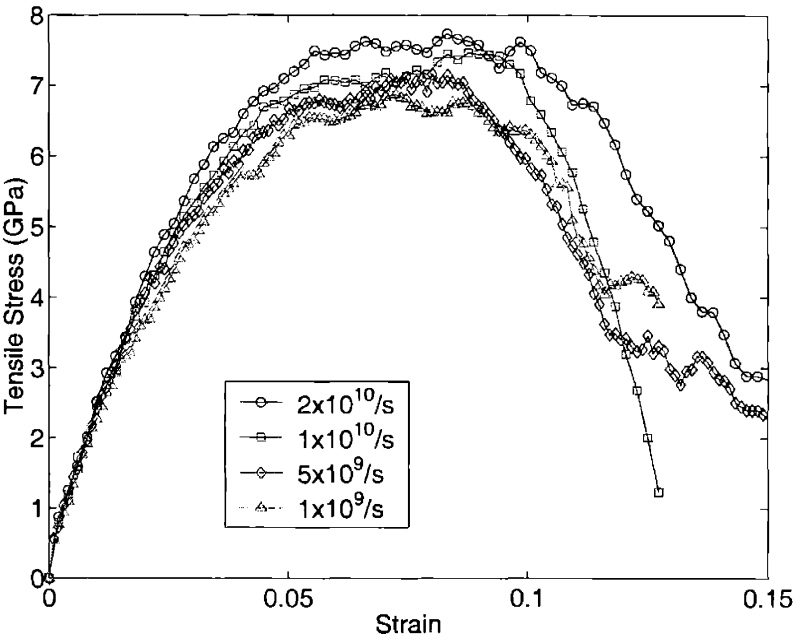

Figure 4-22: A nanocrystalline sample ZrC under constant strain rate uniaxial tension at different strain rates. The sample consists of 16 grains each about 2.4nm in diameter.

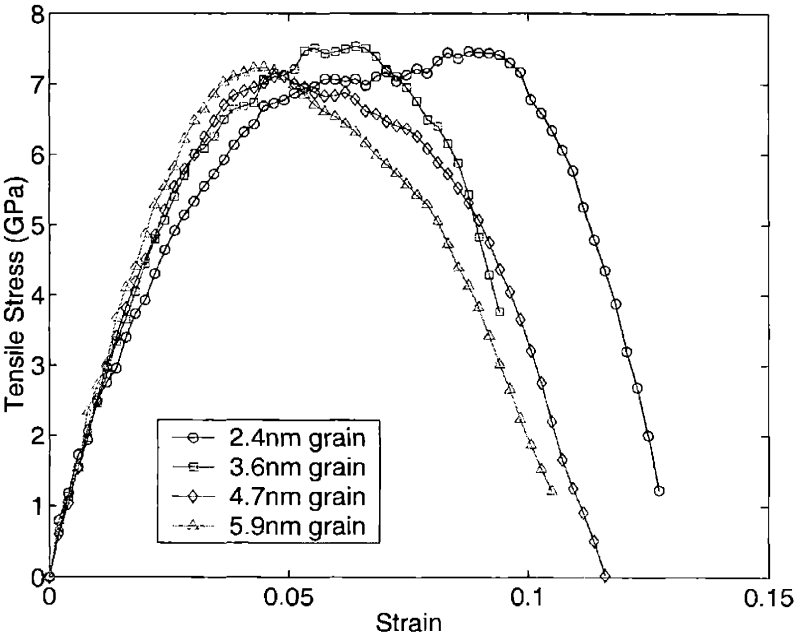

Figure 4-23: Four different sized nano-crystalline system under uniaxial tension of constant strain rate $1 \times 10^{10}/s$

lateral contraction is not allowed. No grain size variation in the critical stress is observed under such loading condition. The critical strains are different because the strains mostly concentrate on the grain boundaries, and different grain size systems have different proportions of grain boundaries. Effectively, all the deformation occurs at the grain boundaries, and there is no dependence on grain size.

Under shear loading, we have observed the reverse Hall-Petch effect. As shown in Fig.4-24, the critical shear stress increases with increasing grain size. The effect can be explained by sliding events in the grain boundaries. The larger the grains the more difficult it is for them to slide against each other, as can be expected.

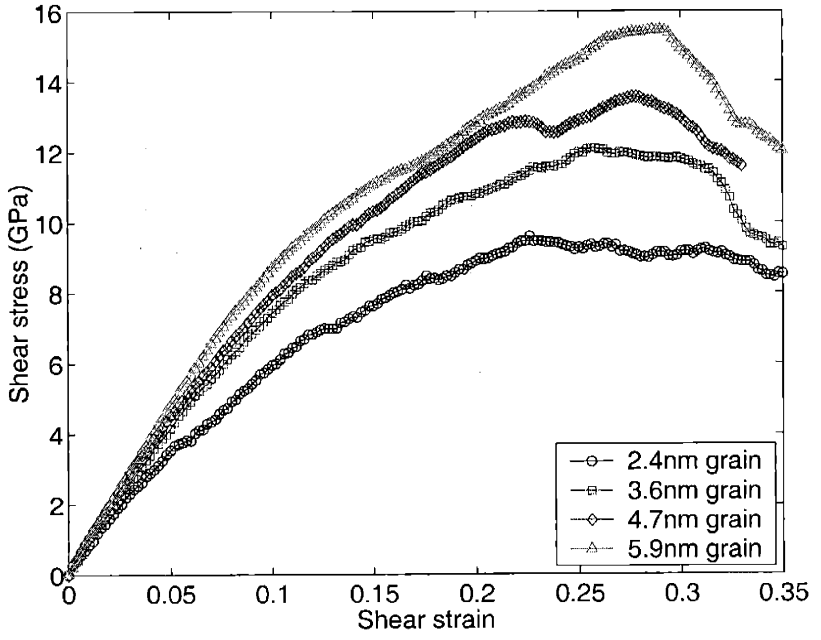

Figure 4-24: Stress-strain response of nanocrystal ZrC under shear. Four systems with grain sizes 2.4, 3.6, 4.7 and 5.9nm are shown.

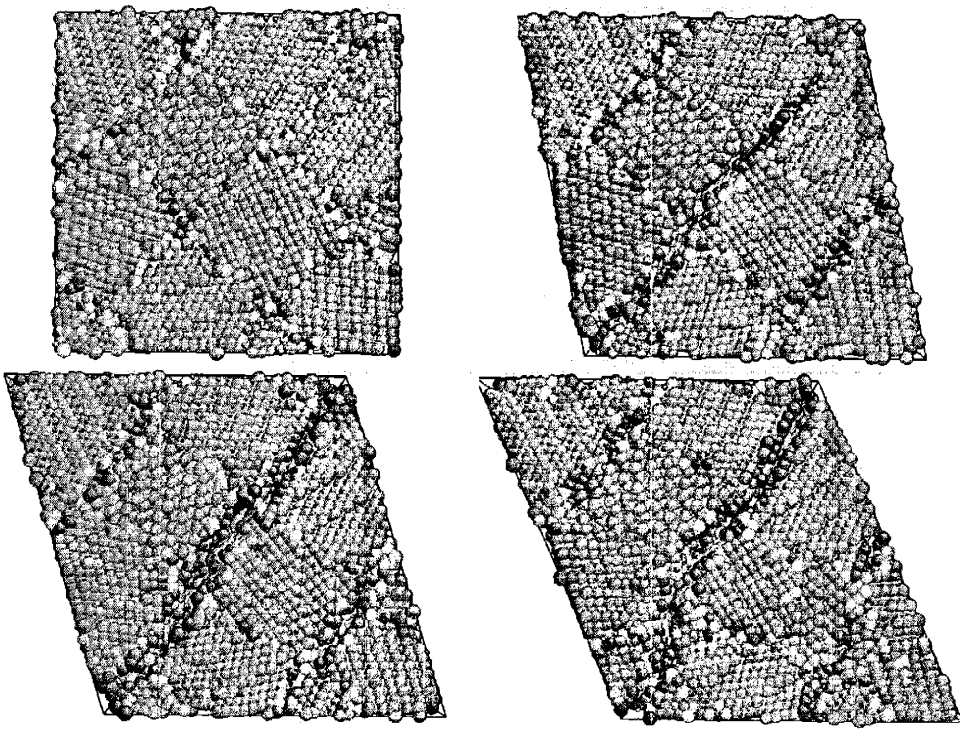

Figure 4-25: Atomistic configurations of nanocrystalline ZrC under shear, at 0, 20%, 30% and 40% respectively.

Chapter 5

Conclusion and Future Work

Through the study of various aspects of strength and deformation of ceramic materials, we have gone through several types of microstructures.

The perfect crystals, when under external stress, exhibit different deformation responses. With the help of stress-strain curves, we have studied compressive failure, where quartz crystal disorders under external uniaxial compression through a nucleation and growth process; the layered amorphization is put into contrast with the well known essentially homogeneous crystal-to-amorphous transformation under hydrostatic compression. We have studied tension induced phase transition, where a pseudo-critical model is applied to quartz to resolve a controversy between simulations and experiments. We have briefly discussed the shear deformation of crystalline quartz (Sec.3.3), where disorder, slip and structure transformation could all happen. In the study of ZrC_{1-x} off-stoichiometric systems, which have carbon vacancies, we have found that theoretical strength are linearly effected by large amount vacancies while heat transfer is suppressed by even tiny amount of impurities.

Putting a nanoscale elliptical crack in crystals, the fracture toughness of both SiO_2 and ZrC are studied. The verification of Griffith crack extension criterion not only gives a much wider range of application to fracture mechanics, but also reveals the underlying dissipation which is directly related to the surface relaxation process.

In the study of amorphous silica tensile strength, we have used the full atomistic positions of every atoms to determine the void structures and from that identified four

distinct stages of stress-strain response. The comparison of large range of strain-rates that can be studied in simulation enables us to successfully connect simulation with the experiments.

Nanocrystalline ZrC are put under shear stress load, where we have observed the reverse Hall-Petch effect. Helped by the atomistic configurations, we attribute the effect to intergranular shearing. Connecting with previous simulation studies on metals, the grain sliding nature in the nanophase shear deformation is considered independent to the underlying materials.

Many of the large scale simulation tasks are assisted by the newly developed simulation methodologies, on the other hand, the need to study increasingly larger systems through more and more complicated data analysis stimulates the grows of new techniques. This duality is best seen in the fast growth of multiscale materials modeling; for example the coupling method of fluid simulation arises from the need to extend the hydrodynamics to the solid-liquid interface.

The contributions of the thesis come in two flavors. First of all it is a study of strength and deformation of ceramics; for the two ceramics SiO_2 and ZrC, it clarifies deformation mechanisms under various microstructures, as well as gives predictions to strength and toughness quantitatively. Secondly, it is a development and demonstration of the atomistic simulation methodology; in addition to the pure methodological improvements discussed in Chap.2, it shows what needs to be done to study strength and deformation in atomistic simulations, how it is carried out and verified, and how to make connections to theories and experiments.

The methodology of atomistic simulation study of strength and deformation developed in this thesis can be directly applied to other ceramic materials. A good candidate is Al_2O_3 for which an appropriate potential already exists[130]. With a reasonable potential description for GeO_2[131], it would be very interesting to study the α to β transition in a manner similar to our simulation and analysis of SiO_2. In this case only the β phase is expected to be stable. SiC is another important ceramic that has been studied in simulation intensively[132, 122] for bulk properties in small systems; direct large scale modeling of its fracture behavior would be valuable. In

another direction, the complicated potential model carefully constructed for ZrC is proven to be quite accurate and transferable in thermal and mechanical studies. This should be extended to TiC which has very similar chemical binding characteristics and lattice structure. Aside from the oxides and carbides, Si_3N_4 is another industrially important ceramic that can be studied using the methods demonstrated in the present thesis.

While the brittleness of quartz at high temperature observed in simulation is consistent with the experiments on "dry" quartz[37], the "wet" quartz can be ductile at high temperatures. When in contact with water molecules, the strength of quartz can be greatly reduced, known as the process of "hydrolytic weakening"[58]. Important to material science as well as geology and earth science, the hydrolytic weakening phenomenon remains to be explained in the atomistic scale.

Further understanding of strength and deformation can come from linking the atomistic simulations to mesoscale methods such as finite-element or kinetic Monte Carlo. Multiscale Material Modeling (MMM) is currently an active area of development and applications. The coupling scheme presented in Sec.2.3 is an example of MMM. Specifically, having studied the crack extension in single crystals, we would like to see additional work in the direction of interfacial fractures and grain boundary/crack interactions. The successful understanding of fracture propagation in polycrystals with micron-sized grains will involve mesoscale modeling, which will need the information provided by the atomistic simulations carried out in the thesis.

In the studies of nanocrystals under shear studies, fast propagation of dislocations is observed within the grains. By speculation[57], the transition from Hall-Petch effect to reverse Hall-Petch effect lies in the competition between intragranular dislocation dominated deformation and intergranular sliding. Dislocation motions are being actively studied by both atomistic and mesoscale modeling, mostly in metals and semiconductors[133]. Similar studies in ceramics represent another open door with many questions waiting to be answered.

Finally, creep[134, 135, 136] is a very important strength determining process in high-temperature ceramics. This phenomenon has yet to be attacked on the atomistic

scale. The gap between the strain rate that can be studied in atomistic modeling ($1 \times 10^9/s$) and the strain rate where creep usually takes place ($1 \times 10^{-5}/s$) has yet to be bridged. Facing a prohibitive 14 orders of magnitude difference, we still have something to do as a first step. The study of the diffusion of single vacancy or interstitial, which is believed to be the carrier of slow creep, can be attacked in atomistic simulation by cleaver acceleration methods such as hyperMD[137, 138].

It is impossible to enumerate all the possibilities provided by the atomistic simulation or multiscale materials modeling. All we can say is: it is a privilege to be on the frontier with great discoveries ahead of us.

Appendix A

Formalism for MD simulations

A.1 Molecular Dynamics

Crystals and Unit Cells

A crystal system is formed by spacial repetition of a unit-cell defined by three frame vectors $\boldsymbol{h}^1$, $\boldsymbol{h}^2$ and $\boldsymbol{h}^3$. The position of any atom can be expressed as:

$$\boldsymbol{r}_a^{\boldsymbol{R}} = \boldsymbol{R} + \boldsymbol{r}_a \tag{A.1}$$

$$\boldsymbol{R} = n_1\boldsymbol{h}^1 + n_2\boldsymbol{h}^2 + n_3\boldsymbol{h}^3 \ (n_1, n_2, n_3 \text{ integers}) \tag{A.2}$$

$$\boldsymbol{r}_a = s_1\boldsymbol{h}^1 + s_2\boldsymbol{h}^2 + s_3\boldsymbol{h}^3 = \underline{\underline{h}}\ \boldsymbol{s}_a \ (0 \leq s_1, s_2, s_3 < 1) \tag{A.3}$$

The set of all possible lattice vectors are denoted by $\{\boldsymbol{R}\}$. And $\underline{\underline{h}}$ is the *frame matrix* converting internal coordinates $\boldsymbol{s}$ into real coordinates $\boldsymbol{r}$.

$$\underline{\underline{h}} = \left[\boldsymbol{h}^1\boldsymbol{h}^2\boldsymbol{h}^3\right] = \begin{bmatrix} h_1^1 & h_1^2 & h_1^3 \\ h_2^1 & h_2^2 & h_2^3 \\ h_3^1 & h_3^2 & h_3^3 \end{bmatrix} \tag{A.4}$$

The frame matrix is not uniquely defined because there is a freedom to choose frame vectors $\boldsymbol{h}^1$, $\boldsymbol{h}^2$, $\boldsymbol{h}^3$ (e.g. $\boldsymbol{h}^1 \rightarrow \boldsymbol{h}^1 + \boldsymbol{h}^2$ can specify the same system). Also, there are 3 degrees of freedom in choosing the real coordination system. To uniquely specify a

infinite repeating system, we stipulate the frame vectors:

$$\begin{aligned} |\boldsymbol{h}^1| &\leq |\boldsymbol{h}^1 + n_2\boldsymbol{h}^2 + n_3\boldsymbol{h}^3| \ (n_2, n_3 \text{ any integer}) \\ |\boldsymbol{h}^2| &\leq |n_1\boldsymbol{h}^1 + \boldsymbol{h}^2 + n_3\boldsymbol{h}^3| \ (n_1, n_3 \text{ any integer}) \\ |\boldsymbol{h}^3| &\leq |n_1\boldsymbol{h}^1 + n_2\boldsymbol{h}^2 + \boldsymbol{h}^3| \ (n_1, n_2 \text{ any integer}) \end{aligned} \tag{A.5}$$

Furthermore, if we fix the excessive degree of freedom by taking x-axis along $\boldsymbol{h}^1$, and y-axis on the plane of ($\boldsymbol{h}^1$, $\boldsymbol{h}^2$), i.e. take $h_2^1 = h_2^1 = h_3^2 = 0$, then we can uniquely identify the frame matrix for any infinitely repeating system. We call this choice of frame matrix the *proper frame.*

In MD simulations, the periodic boundary condition(PBC) is usually used. Similar to the conventional crystal system, the PBC requires three linear independent frame vectors that form a rect-linear cell, which we call a *super-cell.* PBC require that any field or force must be the same at opposite surfaces of the super-cell. This is equivalent to a system that is infinitely repeated in all three diretions with identical copies of the super-cell, which we call *images.* By using PBC, one wants to simulate an infinite system with no boundaries, thus one has to avoid the artificial requirement that all the images are identical. So it's desirable that any interaction between atoms can be confined within a single super-cell, i.e. any atom interacts with at most one copy of any other atom and no atom can interact with its own image. This is called *minimum image convention.* If the interation has a cutoff range r_{C}, the convention state that:

$$r_{\mathrm{C}} < \frac{h_{\mathrm{min}}}{2} \tag{A.6}$$

here h_{min} is the minimum possible distance between any two images of the same atom.

For any proper frame, we have

$$h_{\mathrm{min}} = \min(|\boldsymbol{h}^1|, |\boldsymbol{h}^2|, |\boldsymbol{h}^3|) \tag{A.7}$$

In general MD simulations, condition (A.6) does not ensure that the shortest distance between atoms $|\Delta\boldsymbol{r}|$ are given by shortest interanl coordinate distance $|\Delta\boldsymbol{s}|$.

Thus MD program has to check many different images to evaluate the shortest distance between two atoms in super-cell. If one enhances the requirement of (A.6) to

$$r_C < \frac{d_{\min}}{2} \tag{A.8}$$

(here $d_{\min}$ is the minimum distance between any two parallel planes of super-cell), then it can be proved that any interacting pair of atoms has the shortest distance in internal coordinate space as well as real coordinate space. This greatly simplifies the MD program.

It is not hard to show the shortest plane distance $d_{\min}$ to be:

$$d_{\min} = \min\left(\frac{|\boldsymbol{h}^2 \times \boldsymbol{h}^3|}{\det(\underline{\underline{h}})}, \frac{|\boldsymbol{h}^3 \times \boldsymbol{h}^1|}{\det(\underline{\underline{h}})}, \frac{|\boldsymbol{h}^1 \times \boldsymbol{h}^2|}{\det(\underline{\underline{h}})}\right) \tag{A.9}$$

The minimum image convention is easily achievable with short range interation models. But for any long range interations, either the PBC is not applicable, such as astrology simulations of gravity, or has to be taken special care with its meaning, such as Coulomb interation with Ewald construction (see 2.4 for detail).

Reciprocal Lattice and Brillouin Zone

The reciprocal lattice is defined by all the vectors that satisfy $\exp(i\boldsymbol{K}\cdot\boldsymbol{R}) = 1$. Similar to real space lattices, the reciprocal lattice frame vectors $\boldsymbol{g}_1$, $\boldsymbol{g}_2$ and $\boldsymbol{g}_3$ defines all the lattice points

$$\boldsymbol{K} = n_1\boldsymbol{g}^1 + n_2\boldsymbol{g}^2 + n_3\boldsymbol{g}^3 \ (n_1, n_2, n_3 \text{ integers}) \tag{A.10}$$

The reciprocal frame matrix $\underline{\underline{g}}$ satisfy

$$\underline{\underline{g}} = \left[\boldsymbol{g}^1\boldsymbol{g}^2\boldsymbol{g}^3\right] = 2\pi\left(\underline{\underline{h}}^{-1}\right)^{\mathrm{T}} \tag{A.11}$$

For a proper frame $\underline{\underline{h}}$, the reciprocal frame vector $\boldsymbol{g}^3$ is along z-axis, $\boldsymbol{g}^2$ is on yz-plane.

Interaction and Dynamics

The MD simulation is based on classical mechanics. The interaction is given by a *potential function* $U(\{\boldsymbol{r}_a\})$. The particle dynamics is governed by the Newton's equation of motion

$$\boldsymbol{f}_a = -\frac{\partial U(\{\boldsymbol{r}_a\})}{\partial \boldsymbol{r}_a} \tag{A.12}$$

Usually, the potential function U is short ranged and only depends on the distance between atoms that are within interaction range of each other. That means, for most models we can write the interation potential in the following form:

$$U(\{\boldsymbol{r}_a\}) = U(\{r_{ab}\}) \tag{A.13}$$

Specificly, in the pairwise potential models, one assumes U can be expressed in the linear combination of all the pairs.

$$U(\{r_{ab}\}) = \sum_{ab} U(r_{ab}) \text{ for pairwise potential models} \tag{A.14}$$

Because of translational symmetry, the functional form $U(r)$ should be identical to all the pairs of same species.

Following (A.13), the force on atoms can be calculated as:[1]

$$\boldsymbol{f}_a = \sum_{b\neq a} \left(-\frac{1}{r_{ab}} \frac{\partial U(\{r_{ab}\})}{\partial r_{ab}} \right) \boldsymbol{r}_{ab} \tag{A.15}$$

$$\boldsymbol{f}_a = \sum_{b\neq a} \left(-\frac{1}{r} \frac{\partial U(r)}{\partial r} \right)_{r=r_{ab}} \boldsymbol{r}_{ab} \text{ for pairwise potential models} \tag{A.16}$$

The instantaneous temperature of the system is just kinetic energy per degree of freedom.

$$T_{\mathrm{MD}} = \frac{2}{3N} \sum_{a=1}^{N} \frac{m_a \dot{\boldsymbol{r}}_a^2}{2} \tag{A.17}$$

[1]Here $\boldsymbol{r}_{ab} \equiv \boldsymbol{r}_a - \boldsymbol{r}_b$

The stress of the system are written in two parts, the kinetic stress and virial stress

$$\underline{\underline{\tau}} = \frac{1}{V}\sum_a \left(\frac{\boldsymbol{p}_a\boldsymbol{p}_a}{m_a} + \boldsymbol{r}_a\boldsymbol{f}_a\right) \tag{A.18}$$

In a PBC system such as an MD supercell, the second term of (A.18) is not clearly defined. It has to be converted into terms of the localized interating pairs. Substituting the force from (A.15), with a little derivation we arrive at:

$$\underline{\underline{\tau}}_{\mathrm{MD}} = \frac{1}{V}\left[\sum_{a=1}^{N} m_a\dot{\boldsymbol{r}}_a\dot{\boldsymbol{r}}_a - \sum_{ab}\frac{1}{r_{ab}}\frac{\partial U(\{r_{ab}\})}{\partial r_{ab}}\boldsymbol{r}_{ab}\boldsymbol{r}_{ab}\right] \tag{A.19}$$

The pressure is one-third of the trace of stress tensor:

$$P_{\mathrm{MD}} = \frac{\mathrm{tr}(\underline{\underline{\tau}}_{\mathrm{MD}})}{3} = \frac{1}{3V}\left[\sum_{a=1}^{N} m_a\dot{\boldsymbol{r}}_a^2 - \sum_{ab}\frac{\partial U(\{r_{ab}\})}{\partial r_{ab}}r_{ab}\right] \tag{A.20}$$

Harmonic Approximations

At the limit of low temperature, one can expand the interaction potential around it minimum and only keep harmonic terms (to the second order). This converts the equations of motion into a set of linear equations. It is called *harmonic approximation.* From the matrix equation a set of eigen value and eigen vector can be solved, each correspond to certain vibrational normal mode, those modes are called *phonons.* The phonon information obtained from the expansion gives important thermal and mechanical properites at low temperatures. High temperature effects can be studied by comparing MD simulations with harmonic approximations. This section mainly follows the discussion by Maradudin *et al.*[79].

Denote $\boldsymbol{u}_a^{\boldsymbol{R}}$ as the displacement of atom at $\boldsymbol{r}_a^{\boldsymbol{R}}$ from its original position, then we

can rewrite energies of the system in terms of $\boldsymbol{u}$:

$$K = \sum_{\boldsymbol{R}ai} \frac{m_a \left(\dot{u}_{ai}^{\boldsymbol{R}}\right)^2}{2} \tag{A.21}$$

$$U = U_0 + \sum_{\boldsymbol{R}ai} \left(\frac{\partial U}{\partial u_{ai}^{\boldsymbol{R}}}\right)_0 u_{ai}^{\boldsymbol{R}} + \frac{1}{2} \sum_{\boldsymbol{R}ai} \sum_{\boldsymbol{R}'bj} \left(\frac{\partial U}{\partial u_{ai}^{\boldsymbol{R}} \partial u_{bj}^{\boldsymbol{R}'}}\right)_0 u_{ai}^{\boldsymbol{R}} u_{bj}^{\boldsymbol{R}'} + \ldots \tag{A.22}$$

Harmonic approximation assumes higher order expansion in U can be ignored when atomic displacement ($u_a^{\boldsymbol{R}}$) is small.

In (A.22) the first term is just a constant, and the second term is zero because we assume there is no net force when atoms stay at original position. So the Hamiltonian can be written as:

$$\mathcal{H} = U_0 + \sum_{\boldsymbol{R}ai} \frac{m_a \left(\dot{u}_{ai}^{\boldsymbol{R}}\right)^2}{2} + \frac{1}{2} \sum_{\boldsymbol{R}ai} \sum_{\boldsymbol{R}'bj} \left(\frac{\partial U}{\partial u_{ai}^{\boldsymbol{R}} \partial u_{bj}^{\boldsymbol{R}'}}\right)_0 u_{ai}^{\boldsymbol{R}} u_{bj}^{\boldsymbol{R}'} \tag{A.23}$$

the equation of motion follows immediately:

$$m_a \ddot{u}_{ai}^{\boldsymbol{R}} = -\sum_{\boldsymbol{R}'bj} \left(\frac{\partial U}{\partial u_{ai}^{\boldsymbol{R}} \partial u_{bj}^{\boldsymbol{R}'}}\right)_0 u_{bj}^{\boldsymbol{R}'} \tag{A.24}$$

If we Fourier transform the displacements as

$$u_{ai}^{\boldsymbol{R}}(t) = \int \frac{1}{\sqrt{m_a}} \tilde{u}_{ai}(\boldsymbol{k}) e^{-i\omega t + i\boldsymbol{k}\cdot\boldsymbol{r}_a^{\boldsymbol{R}}} \mathrm{d}\boldsymbol{k} d\omega \tag{A.25}$$

the equation of motion transforms into

$$\omega^2 \tilde{u}_{ai}(\boldsymbol{k}) = \sum_{bj} \tilde{C}_{ai;bj}(\boldsymbol{k}) \tilde{u}_{bj}(\boldsymbol{k}) \tag{A.26}$$

where $\tilde{C}_{ai;bj}(\boldsymbol{k})$ is the Fourier transformed dynamic matrix ($3N \times 3N$)

$$\tilde{C}_{ai;bj}(\boldsymbol{k}) = \frac{1}{\sqrt{m_a m_b}} \sum_{\boldsymbol{R}'} \left(\frac{\partial U}{\partial u_{ai}^{\boldsymbol{R}} \partial u_{bj}^{\boldsymbol{R}'}}\right)_0 e^{i\boldsymbol{k}\cdot(\boldsymbol{r}_b^{\boldsymbol{R}'} - \boldsymbol{r}_a^{\boldsymbol{R}})} \tag{A.27}$$

This is a $3N$ eigen value problem, which gives $3N$ phonon bands, and the solution of $3N$ relations $\omega = \omega(\boldsymbol{k})$ are called *phonon dispersion relations.*

It is not hard to prove the following property of the dynamical matrix:

$$\tilde{C}_{ai;bj}(\boldsymbol{k}) = \tilde{C}^*_{bj;ai}(\boldsymbol{k}) = \tilde{C}^*_{ai;bj}(-\boldsymbol{k}) \tag{A.28}$$

In the special case where atomic interaction is pairwise, we can write

$$U = \sum_{ab} V(r_{ab}) = \frac{1}{2} \sum_{\boldsymbol{R}a} \sum_{\boldsymbol{R}'b} V(r)|_{\boldsymbol{r}=\boldsymbol{r}_b^{\boldsymbol{R}'} - \boldsymbol{r}_a^{\boldsymbol{R}}} \tag{A.29}$$

first we can write second derivative of V as

$$V_{ij}(r) \equiv \frac{\partial^2}{\partial r_i \partial r_j} V(r) = \frac{r_i r_j}{r^2} \left[V''(r) - \frac{1}{r} V'(r) \right] + \frac{\delta_{ij}}{r} V'(r) \tag{A.30}$$

the second derivative of U can be written as

$$\begin{aligned} \frac{\partial U}{\partial u_{ai}^{\boldsymbol{R}} \partial u_{bj}^{\boldsymbol{R}'}} &= -V_{ij}(r)|_{\boldsymbol{r}=\boldsymbol{r}_b^{\boldsymbol{R}'} - \boldsymbol{r}_a^{\boldsymbol{R}}} \qquad (\boldsymbol{R}a \neq \boldsymbol{R}'b) \\ \frac{\partial U}{\partial u_{ai}^{\boldsymbol{R}} \partial u_{aj}^{\boldsymbol{R}}} &= \sum_{\boldsymbol{R}'b \neq \boldsymbol{R}a} V_{ij}(r)|_{\boldsymbol{r}=\boldsymbol{r}_b^{\boldsymbol{R}'} - \boldsymbol{r}_a^{\boldsymbol{R}}} \end{aligned} \tag{A.31}$$

With this, we can write down the explicit expression for the dynamic matrix

$$\tilde{C}_{ai;bj}(\boldsymbol{k}) = -\frac{1}{\sqrt{m_a m_b}} \sum_{\boldsymbol{R}'} V_{ij}(|\boldsymbol{r}_b^{\boldsymbol{R}'} - \boldsymbol{r}_a^{\boldsymbol{R}}|) e^{i\boldsymbol{k}\cdot(\boldsymbol{r}_b^{\boldsymbol{R}'} - \boldsymbol{r}_a^{\boldsymbol{R}})} \qquad (a \neq b) \tag{A.32}$$

$$\tilde{C}_{ai;aj}(\boldsymbol{k}) = \frac{1}{m_a} \left[\sum_{\boldsymbol{R}'b \neq \boldsymbol{R}a} V_{ij}(|\boldsymbol{r}_b^{\boldsymbol{R}'} - \boldsymbol{r}_a^{\boldsymbol{R}}|) - \sum_{\boldsymbol{R}' \neq \boldsymbol{R}} V_{ij}(|\boldsymbol{r}_a^{\boldsymbol{R}'} - \boldsymbol{r}_a^{\boldsymbol{R}}|) e^{i\boldsymbol{k}\cdot(\boldsymbol{r}_a^{\boldsymbol{R}'} - \boldsymbol{r}_a^{\boldsymbol{R}})} \right]$$

If we write out the short-hand notations of $\boldsymbol{r}_a^{\boldsymbol{R}}$

$$\boldsymbol{r}_b^{\boldsymbol{R}'} - \boldsymbol{r}_a^{\boldsymbol{R}} = \boldsymbol{r}_{ab} + (\boldsymbol{R}' - \boldsymbol{R}) \tag{A.33}$$

and set $\boldsymbol{R} = 0$, then change all the summation over $\boldsymbol{R}'$ to $\boldsymbol{R}$, we will get the following:

$$\begin{aligned}
\tilde{C}_{ai;bj}(\boldsymbol{k}) &= -\frac{1}{\sqrt{m_a m_b}} \sum_{\boldsymbol{R}} V_{ij}(|\boldsymbol{r}_{ab} + \boldsymbol{R}|) e^{i\boldsymbol{k}\cdot(\boldsymbol{r}_{ab}+\boldsymbol{R})} \qquad (a \neq b) \\
\tilde{C}_{ai;aj}(\boldsymbol{k}) &= \frac{1}{m_a} \left[\sum_{b \neq a} \sum_{\boldsymbol{R}} V_{ij}(|\boldsymbol{r}_{ab} + \boldsymbol{R}|) + \sum_{\boldsymbol{R} \neq 0} V_{ij}(R) \left(1 - e^{i\boldsymbol{k}\cdot\boldsymbol{R}}\right) \right] \qquad \text{(A.34)}
\end{aligned}$$

A.2 Potential Models

Among the techniques deployed in the field of atomistic simulation, empirical potential models is often adopted for its relatively low computational cost. The typical system studied with empirical potential models is usually about several thousands of atoms. This makes the empirical potential model perfect for studying the microstructures.

Empirical potential is based on the cluster expansion of total energy of the system:

$$U = \sum_{ab} U_2(\boldsymbol{r}_a, \boldsymbol{r}_b) + \sum_{abc} U_3(\boldsymbol{r}_a, \boldsymbol{r}_b, \boldsymbol{r}_c) + \ldots \qquad \text{(A.35)}$$

Most empirical potential model cutoff the series at 3 or 4 body term. Usually, only 2 body interaction suffices the purpose. Three body interactions are brought in to describe bond angle dependence, so it is usually expressed in the bonding angle θ_{abc} form.

Another approach of potential model is based on the second moment approximation, which leads to EAM type potential, as we descussed below.

The Potential Cutoff Scheme

In MD simulations, most interaction have an effective range. Ignoring the interaction beyond a radius R_c is called "interaction cutoff". In order to maintain the continuation of atomic motions, it is desired that both the energy and the interaction force is continuous. Thus, for a simple formed interaction, a cutoff scheme is used to ensure that the value and first order derivative of the potential is zero at the cutoff radius

R_c. Suppose the potential function is $U(r)$, the generic cutoff potential is defined as:

$$U_c(r) = U(r) - U(R_c) - \left(\frac{dU(r)}{dr}\right)_{r=R_c} (r - R_c) \tag{A.36}$$

Other cutoff scheme are also used with simple formed potentials such as Lennard-Jones pair potential, as we will see in the following sections.

Simple Form Pair Potential Models

In many situations, a simple form pair potential is needed to describe atom-atom interaction, which gives attraction force at distance and repulsion force when two atoms are close. This kind of potential is often called "soft ball" potential. The most used ones are

- Lennerd-Jones[139, 140]

$$U(r) = 4\varepsilon \left[\left(\frac{\sigma}{r}\right)^{12} - \left(\frac{\sigma}{r}\right)^{6} \right] \tag{A.37}$$

Lennard-Jones potential is good for FCC close packed materials. It is mostly used to represent rare-gas elements such as Argon.

The parameters ε and σ defines the energy well depth and core size of each atom.

The specific parameters for Argon is usually choosen as

$$\varepsilon = 119.8\ [^\circ\mathrm{K}] = 0.01032\ [\mathrm{eV}] \qquad \sigma = 3.405\ [\text{Å}] \tag{A.38}$$

The cutoff radius is choosen as $R_c = 2.37343\sigma$, which lies exactly at the 2/3 interval between 4th and 5th neighbors at 0°K equilibrated FCC lattice.[2] As recommended in J.Li's Thesis[19], a special cutoff scheme is used for Lennard-Jones potential. It minimized the artificial cutoff effect and can speed-up the

[2]For detailed discussion of this choice, see *Appendix G* of Ju Li's Doctral Thesis[19]

potential calculation at same time.

$$U_c(r) = 4\varepsilon \left[\left(\frac{\sigma}{r}\right)^{12} - \left(\frac{\sigma}{r}\right)^{6} + \left(2\left(\frac{\sigma}{R_c}\right)^{18} - \left(\frac{\sigma}{R_c}\right)^{12} \right) \left(\frac{r}{\sigma}\right)^{6} - 3\left(\frac{\sigma}{R_c}\right)^{12} + 2\left(\frac{\sigma}{R_c}\right)^{6} \right] \quad \text{(A.39)}$$

- Born-Mayer

$$U(r) = Ae^{-Br} \quad \text{(A.40)}$$

- Buckingham

$$U(r) = Ae^{-Br} - \frac{C}{r^6} \quad \text{(A.41)}$$

- Moorse

$$U(r) = A\left[e^{-Br} - e^{-2Br}\right] \quad \text{(A.42)}$$

"ZrC-II" Potential

"ZrC-II" potential is an earlier development of the ZrC potential model. It is based on binary Moorse potential form. With a cutoff scheme of $W(r) = V(r) - V(r_c) - V'(r_c)(r - r_c)$, the ZrC-II potential has a form of

$$\begin{aligned} V(r) &= D_0\left[e^{2\beta(r_0 - r)} - 2e^{\beta(r_0 - r)} - A + B(r - r_c)\right] \quad \text{(A.43)} \\ A &\equiv e^{2\beta(r_0 - r_c)} - 2e^{\beta(r_0 - r_c)} \\ B &\equiv 2\beta\left[e^{2\beta(r_0 - r_c)} - e^{\beta(r_0 - r_c)}\right] \end{aligned}$$

Interaction	D_0[eV]	r_0[Å]	β[Å^{-1}]
Zr-Zr	0.51603557035733	4.08888282515727	0.97703114535312
Zr-C	0.92231006075817	2.21570837209438	1.94740518295180
C-C	0.37742291628244	3.57823943232922	0.80848585672605

Table A.1: Optimized Parameters for ZrC-II Potential

The optimized parameter set is shown in Table A.1, combined with a cutoff scheme with r_c=10Å for all Zr-Zr, Zr-C, C-C interactions.

Stillinger-Weber Potential

Stillinger-Weber potential[141] is a three-body covalent potential for silicon, it favors the diamond cubic structure explicity.

$$\begin{aligned} E &= \sum_{a,b} U_2(r_{ab}) + \sum_{a,b,c} U_3(\boldsymbol{r}_a, \boldsymbol{r}_b, \boldsymbol{r}_c) \\ U_2(r) &= A\left(\frac{B}{r^p} - \frac{1}{r^q}\right)\exp\left(\frac{1}{r-a}\right) \\ U_3(\boldsymbol{r}_a, \boldsymbol{r}_b, \boldsymbol{r}_c) &= h(r_{ab}, r_{ac}, \theta_{bac}) + h(r_{ba}, r_{bc}, \theta_{abc}) + h(r_{ca}, r_{cb}, \theta_{acb}) \\ h(r_1, r_2, \theta) &= \lambda \exp\left[\left(\frac{\gamma}{r_1 - a}\right) + \left(\frac{\gamma}{r_2 - a}\right)\right]\left(\cos\theta + \frac{1}{3}\right)^2 \end{aligned} \tag{A.44}$$

The parameters are:

$$\begin{aligned} A = 7.049556277\ [\text{eV}] \qquad & B = 0.6022245584\ [\text{Å}^4] \\ p = 4 \qquad q = 0 \qquad & a = 1.80\ [\text{Å}] \\ \lambda = 21.0\ [\text{eV}] \qquad & \gamma = 1.20\ [\text{Å}] \end{aligned} \tag{A.45}$$

EAM Potential for hcp and bcc zirconium

Willaime *et al.*[117] proposed a (EAM??) type potential for zirconium in 1991. The interaction energy can be written as:

$$E = \sum_a F_a[\rho_a] + \sum_{a,b} U(r_{ab}) \tag{A.46}$$

where F_a is the embeded energy functional for atom a, ρ_a is the electron density of atom a and $U(r)$ is the repulsive interaction between atoms.

The WM potential is the following:

$$\begin{aligned} E &= \sum_a E_a \\ E_a &= \sum_{b\neq a} U(r_{ab}) - \left[\sum_{b\neq a} f^2(r_{ab})\right]^{1/2} \\ U(r_{ab}) &= A\exp\left[-p\left(\frac{r_{ab}}{r_0}-1\right)\right] \\ f(r_{ab}) &= B\exp\left[-q\left(\frac{r_{ab}}{r_0}-1\right)\right] \end{aligned} \tag{A.47}$$

The parameters proposed by Willaime *et al.* [117] are:

$$\begin{aligned} R_c = 0.68\ [\text{Å}] \qquad & r_0 = 0.31744\ [\text{Å}] \\ A = 0.16702\ [\text{eV}] \qquad & p = 9.3 \\ B = 2.254948\ [\text{eV}] \qquad & q = 2.1 \end{aligned} \tag{A.48}$$

Potential Model for ZrC: Second Moment Approximation

The potential for ZrC first appears in the Thesis of J.Li[19]. It has the following form:

$$\begin{aligned} U^{tot} &= \sum_{a\in Zr} U_a^{\mathrm{Zr}} + \sum_{a\in C} U_a^C \\ U_a^{\mathrm{Zr}} &= \sum_{b\in Zr\neq a} \phi_{\mathrm{ZrZr}}(r_{ab}) + \sum_{b\in C} \phi_{\mathrm{ZrC}}(r_{ab}) - \left(X_a^{\mathrm{Zr}}\right)^{1/2} \\ X_a^{\mathrm{Zr}} &= \sum_{b\in Zr\neq a} h^2_{\mathrm{ZrZr}}(r_{ab}) + \sum_{b\in C} \tilde{h}^2_{\mathrm{ZrC}}(r_{ab}) \\ U_a^C &= \sum_{b\in Zr} \phi_{\mathrm{ZrC}}(r_{ab}) + \sum_{b\in C\neq a} \phi_{CC}(r_{ab}) - \left(X_a^C\right)^{1/2} \\ X_a^C &= \sum_{b\in Zr} \tilde{h}^2_{\mathrm{ZrC}}(r_{ab}) + \sum_{b\in C\neq a} h^2_{CC}(r_{ab}) \end{aligned} \tag{A.49}$$

The definition of pair interaction and second moments are:

$$\begin{aligned}
\phi_{CC}(r) &= 0 \qquad h_{CC}(r) = 0 \\
\phi_{\mathrm{ZrZr}}(r) &= \exp\left(A_{\mathrm{ZrZr}}(B_{\mathrm{ZrZr}} - r) + \frac{K}{r - R_c^{\mathrm{ZrZr}}}\right) \\
h^2_{\mathrm{ZrZr}}(r) &= \exp\left(C_{\mathrm{ZrZr}}(D_{\mathrm{ZrZr}} - r) + \frac{K}{r - R_c^{\mathrm{ZrZr}}}\right) \\
\phi_{\mathrm{ZrC}}(r) &= \exp\left(A_{\mathrm{ZrC}}(B_{\mathrm{ZrC}} - r) + \frac{K}{r - R_c^{\mathrm{ZrC}}}\right) \\
h_{\mathrm{ZrC}}(r) &= \exp\left(C_{\mathrm{ZrC}}(D_{\mathrm{ZrC}} - r) + \frac{K}{r - R_c^{\mathrm{ZrC}}}\right)
\end{aligned} \tag{A.50}$$

The screened second moment $\tilde{h}_{\mathrm{ZrC}}$ is defined with environment dependent terms as:

$$\tilde{h}_{\mathrm{ZrC}}(a \in Zr, b \in C) = h_{\mathrm{ZrC}}(r_{ab}) \exp\left(-\frac{\sqrt{s_{ab}}}{h_{\mathrm{ZrC}}(r_{ab})}\right) \tag{A.51}$$

Here s_{ab} is the screening strength:

$$s_{ab} = \sum_{c \in C} \left(\frac{1 + \cos\theta_{cab}}{\alpha}\right)^{\beta} h^2_{\mathrm{ZrC}}(r_{ac}) + \sum_{c \in C} \left(\frac{1 + \cos\theta_{cba}}{\alpha}\right)^{\beta} h^2_{\mathrm{ZrC}}(r_{bc}) \tag{A.52}$$

The fitted parameters are listed below (K, R_c^{ZrZr} and R_c^{ZrC} are chosen by hand)

$$\begin{aligned}
A_{\mathrm{ZrZr}} &= 2.9296875\ [\text{Å}^{-1}] & B_{\mathrm{ZrZr}} &= 2.58787395638939\ [\text{Å}] \\
C_{\mathrm{ZrZr}} &= 1.32308467741935\ [\text{Å}^{-1}] & D_{\mathrm{ZrZr}} &= 4.3672464262563\ [\text{Å}] \\
A_{\mathrm{ZrC}} &= 3.24589393669854\ [\text{Å}^{-1}] & B_{\mathrm{ZrC}} &= 2.05679804919117\ [\text{Å}] \\
C_{\mathrm{ZrC}} &= 0.82303818052368\ [\text{Å}^{-1}] & D_{\mathrm{ZrC}} &= 4.15482225815134\ [\text{Å}] \\
\alpha &= 1.80853303846249 & \beta &= 14.59345494373451 \\
K &= 0.1\ [\text{Å}] & & \\
R_c^{\mathrm{ZrZr}} &= 7\ [\text{Å}] & R_c^{\mathrm{ZrC}} &= 3.5\ [\text{Å}]
\end{aligned} \tag{A.53}$$

A.3 MD in Different Ensembles

It is very important to be able to do MD in different ensembles. Currently, the widely accepted standard for constant temperature simulation is the Nosé-Hoover thermostat[110, 142, 111, 143, 144], and the constant stress simulation are done with Parrinello-Rahman's[62, 145] shape varying simulation cells. In the section, we will mainly follow the works by Melchoinna *et al.*[93]

It should be noted that even without any modification of equations of motion. MD does not strictly simulate microcanonical ensemble. According to Ray *et al.*[146], the fact that MD conserves total momentum makes it slightly deviates from the commonly known microcanonical ensembe, in proportion to $1/N$. This is also true in the canonical ensemble and NTP ensemble described below. In almost all MD simulations, this slight deviation can be safely ignored.

Nosé-Hoover Thermostat (NTV ensemble)

The equation of motions which generates the canonical ensemble can be written as:

$$\begin{aligned} \dot{\boldsymbol{r}}_a &= \frac{\boldsymbol{p}_a}{m_a} \\ \dot{\boldsymbol{p}}_a &= -\frac{\partial U}{\partial \boldsymbol{r}_a} - \zeta \boldsymbol{p}_a \\ \dot{\zeta} &= v_T^2 \left(\frac{T_{\mathrm{MD}}}{T_{\mathrm{ext}}} - 1 \right) \end{aligned} \tag{A.54}$$

Where ζ is a control variable monitors the deviation of MD temperature from the externally applied temperature. With some algebra, it can be proved the distribution function is:

$$f(\boldsymbol{r}_a, \boldsymbol{p}_a, \zeta) \propto \exp[-\frac{\mathcal{A}}{T_{\mathrm{ext}}}] \tag{A.55}$$

Here the Helmholtz free energy is defined as

$$\mathcal{A} = \sum_{a=1}^{N} \frac{\boldsymbol{p}_a^2}{2m_a} + U(\{r_a\}) + \frac{3NT_{\mathrm{ext}}\zeta^2}{2v_T^2} \tag{A.56}$$

If an additional dynamic variable $z = \int^t \mathrm{d}t'\zeta(t')$ is introduced, we can write (A.54) as second order Newton's equation of motions:

$$\begin{aligned} \ddot{\boldsymbol{r}}_a &= -\frac{1}{m_a}\frac{\partial U}{\partial \boldsymbol{r}_a} - \dot{z}\dot{\boldsymbol{r}}_a \\ \ddot{z} &= v_T^2\left(\frac{T_{\mathrm{MD}}}{T_{\mathrm{ext}}} - 1\right) \end{aligned} \tag{A.57}$$

This can be easily integrated. A conserved quantity is found as the extended Helmholz free energy:

$$\mathcal{A}' = \sum_{a=1}^{N}\frac{m_a\dot{\boldsymbol{r}}_a^2}{2} + U(\{r_a\}) + \frac{3NT_{\mathrm{ext}}\dot{z}^2}{2v_T^2} + 3NT_{\mathrm{ext}}z \tag{A.58}$$

This can be used to check the correctness of MD simulation.[3]

[3]It is notable that the equation of motion (A.57) can be directly derived from a Langrangian formulation:

$$\mathcal{L}_{NTV} = \sum_{a=1}^{N}\frac{m_a z\dot{\boldsymbol{r}}_a^2}{2} - U(\{\boldsymbol{r}_a\}) + \frac{3NT_{\mathrm{ext}}}{4v_T^2}\dot{z}^2 - \frac{3NT_{\mathrm{ext}}}{2}z \tag{A.59}$$

Thus we can convert it into Hamiltonian formulation and get another conserved quantity:

$$\begin{aligned} \boldsymbol{p}_a &= \frac{\partial\mathcal{L}}{\partial\dot{\boldsymbol{r}}_a} = m_a z\dot{\boldsymbol{r}}_a \\ p_z &= \frac{\partial\mathcal{L}}{\partial\dot{z}} = \frac{3NT_{\mathrm{ext}}}{2v_T^2}\dot{z} \\ \mathcal{H}_{NTV} &= \sum_{a=1}^{N}\frac{\boldsymbol{p}_a^2}{2m_a z} + U(\{\boldsymbol{r}_a\}) + \frac{v_T^2}{3NT_{\mathrm{ext}}}p_z^2 + \frac{3NT_{\mathrm{ext}}}{2}z \end{aligned} \tag{A.60}$$

The dynamic variable z does not appear in the original equation of motion (A.54), we introduced it solely for the purpose of getting Newtonian form (A.57). Because of this redundancy, it is not surprising we can find more than one conserved quantity.

Isothermal-isobaric ensemble (NTP ensemble)

Also from Melchoinna *et al.*[93], equation of motion for isothermal-isobaric ensemble can be written as

$$\begin{aligned}
\dot{\boldsymbol{r}}_a &= \frac{\boldsymbol{p}_a}{m_a} + \underline{\underline{\eta}}(\boldsymbol{r}_a - \boldsymbol{R}_0) \\
\dot{\boldsymbol{p}}_a &= -\frac{\partial U}{\partial \boldsymbol{r}_a} - (\underline{\underline{\eta}} + \zeta \underline{\underline{I}})\boldsymbol{p}_a \\
\dot{\zeta} &= v_T^2 \left(\frac{T_{\mathrm{MD}}}{T_{\mathrm{ext}}} - 1 \right) \\
\dot{\underline{\underline{\eta}}} &= \frac{v_P^2}{N T_{\mathrm{ext}}} V (\underline{\underline{\tau}}_{\mathrm{MD}} - \underline{\underline{\tau}}_{\mathrm{ext}}) \\
\dot{\underline{\underline{h}}} &= \underline{\underline{\eta}}\,\underline{\underline{h}}
\end{aligned} \tag{A.61}$$

where $\boldsymbol{R}_0 = \sum_a m_a \boldsymbol{r}_a / \sum_a m_a$ is the center of mass of the system. Only 6 degrees of freedom is needed in specifying the lattice frame, $\underline{\underline{h}}$ has 9 free variables, therefore a convention must be taken to restrict the values of $\underline{\underline{h}}$. We assert that if we always restrict $\underline{\underline{h}}$ to be an upper triangular matrix, we can prove the distribution function of the ensemble as

$$f(\boldsymbol{r}_a, \boldsymbol{p}_a, \{h_1^1, h_2^2, h_3^3\}, \underline{\underline{\eta}}, \zeta) \propto \exp[-\frac{\mathcal{H}}{T_{\mathrm{ext}}}] \tag{A.62}$$

$$\mathcal{H} \equiv \sum_{a=1}^{N} \frac{\boldsymbol{p}_a^2}{2m_a} + U(\{r_a\}) + \int \mathrm{tr}(\underline{\underline{\eta}}^{\mathrm{T}} \underline{\underline{\tau}}_{\mathrm{ext}}) V \mathrm{d}t + \frac{3NT_{\mathrm{ext}}}{2} \left(\frac{\zeta^2}{v_T^2} + \frac{\mathrm{tr}(\underline{\underline{\eta}}^{\mathrm{T}} \underline{\underline{\eta}})}{3v_P^2} \right)$$

Remember the V in $\mathcal{H}$ equals to $\det(\underline{\underline{h}})$, in the case of upper triangular $\underline{\underline{h}}$, $V = h_1^1 h_2^2 h_3^3$. To prove (A.62), first notice the off-diagonal values of $\underline{\underline{h}}$ only appears in the last equation in (A.61), since volume V only depends on diagonal terms. So the off-diagonal terms of $\underline{\underline{h}}$ are decoupled and can be integrate out of the distribution function.[4] That's why we can write only diagonal terms into the distribution function.

[4]Here we have made an assumption that the periodic boundary condition effect can be ignored. Because the dynamics in (A.61) depends explicitly on $\underline{r}_a$, it is alright to ignore PBC effects as long as no atom interact with its image. Usually, interaction between atoms are short ranged, and this assumption holds. But in case of ionic systems, this is not true. Strictly speaking, the scheme showed here does not give true NTP ensemble for ionic system, but on the other hand, in an ionic system, atoms interacting with infinite many of its own images are already quite unphysical, the

To prove (A.62), we only need to show that distribution function satisfies

$$\frac{1}{f}\frac{\mathrm{d}f}{\mathrm{d}t} = -\frac{1}{T_{\mathrm{ext}}}\frac{\mathrm{d}\mathcal{H}}{\mathrm{d}t} \tag{A.63}$$

Using the general probablity flow equation, LHS of the above equation is($\{x_\alpha\}$ are all the dynamical variables)

$$\frac{1}{f}\frac{\mathrm{d}f}{\mathrm{d}t} = -\sum_\alpha \frac{\partial \dot{x}_\alpha}{\partial x_\alpha} \tag{A.64}$$

It is trivial to verify that RHS of (A.63) and (A.64) are indeed equal.

In general, (A.62) does not describe an NTP ensemble except in the case where external stress is homogeneous: $\underline{\underline{\tau}}_{\mathrm{ext}} = P_{\mathrm{ext}}\underline{\underline{I}}$. In this case, using the identity(λ_i are eigenvalues of $\underline{\underline{A}}$)

$$\mathrm{tr}(\underline{\underline{A}}^{-1}\dot{\underline{\underline{A}}}) = \sum_i \frac{\dot{\lambda}_i}{\lambda_i} = \frac{\mathrm{d}}{\mathrm{d}t}\left[\det(\underline{\underline{A}})\right] / \det(\underline{\underline{A}}) \tag{A.65}$$

We can write:

$$\int \mathrm{tr}(\underline{\underline{\eta}}^{\mathrm{T}}\underline{\underline{\tau}}_{\mathrm{ext}})V\mathrm{d}t = \int P_{\mathrm{ext}}\mathrm{tr}(\dot{\underline{\underline{h}}}\underline{\underline{h}}^{-1})V\mathrm{d}t = \int P_{\mathrm{ext}}\frac{\dot{V}}{V}V\mathrm{d}t = P_{\mathrm{ext}}V \tag{A.66}$$

In this case, the distribution function does not depend on h_1^1, h_2^2 or h_3^3 separately, instead it only depends on V

$$\begin{aligned} &f(\boldsymbol{r}_a, \boldsymbol{p}_a, V, \underline{\underline{\eta}}, \zeta) \propto \exp[-\frac{\mathcal{H}}{T_{\mathrm{ext}}}] \\ &\mathcal{H} \equiv \sum_{a=1}^{N}\frac{\boldsymbol{p}_a^2}{2m_a} + U(\{r_a\}) + P_{\mathrm{ext}}V + \frac{3NT_{\mathrm{ext}}}{2}\left(\frac{\zeta^2}{v_T^2} + \frac{\mathrm{tr}(\underline{\underline{\eta}}^{\mathrm{T}}\underline{\underline{\eta}})}{3v_P^2}\right) \end{aligned} \tag{A.67}$$

similar as last section, we can write down the conserved Gibbs free energy of the

justification for ionic system MD simulation says that there are always enough screening effects around any charge that the apparent long range interaction have little artificial effect. This justifys the NTP simulation scheme too.

whole system. (z is defined as in last section):

$$\mathcal{G} = \sum_{a=1}^{N} \frac{\boldsymbol{p}_a^2}{2m_a} + U(\{r_a\}) + P_{\text{ext}}V + \frac{3NT_{\text{ext}}}{2}\left(\frac{\zeta^2}{v_T^2} + \frac{\text{tr}(\underline{\underline{\eta}}^{\text{T}}\underline{\underline{\eta}})}{3v_P^2}\right) + 3NT_{\text{ext}}z \qquad \text{(A.68)}$$

Under any other loading condition, the term $\int \text{tr}(\underline{\underline{\eta}}^{\text{T}}\underline{\underline{\tau}}_{\text{ext}})V dt$ is dissipative and there is no conserved quantity in the system. Under these situations, it is not recommended to use the dynamical system described by (A.61) for property calculation. Even so, it is a good choice to quickly achieve desired external loading condition. After certain external condition is achieved, an NEV or NTV simulation can be done to get properties.

In MD simulation, it is more convenient to work with the internal coordinates instead of the absolute ones, after some algebra, we arrive at the Newton's equations of motion:

$$\begin{aligned}
\ddot{\boldsymbol{s}}_a &= \frac{\underline{\underline{h}}^{-1}\boldsymbol{F}_a}{m_a} - \left(2\underline{\underline{h}}^{-1}\dot{\underline{\underline{h}}} + \dot{z}\right)\dot{\boldsymbol{s}}_a - \left[\underline{\underline{h}}^{-1}\left(\dot{\underline{\underline{h}}}\dot{z} + \ddot{\underline{\underline{h}}}\right)\right]\boldsymbol{S}_0 \\
\ddot{z} &= v_T^2\left(\frac{T_{\text{MD}}}{T_{\text{ext}}} - 1\right) \\
\ddot{\underline{\underline{h}}} &= \dot{\underline{\underline{h}}}\underline{\underline{h}}^{-1}\dot{\underline{\underline{h}}} + \frac{v_P^2}{NT_{\text{ext}}}V(\underline{\underline{\tau}}_{\text{MD}} - \underline{\underline{\tau}}_{\text{ext}})\underline{\underline{h}}
\end{aligned} \qquad \text{(A.69)}$$

where $\boldsymbol{F}_a = -\frac{\partial U}{\partial \boldsymbol{r}_a}$ is the force on each atom. For the PBC boundary conditions, there is no well-defined center-of-mass coordinate. The center-of-mass appears in the equations of motion because we need a local balance so that the system won't drift away from the original center of mass. In PBC systems, as long as we start at a configuration of $\boldsymbol{S}_0 = 0$, we do not need to worry about the last term in equation of motion of $\boldsymbol{s}_a$.

The conserved quantity to check dynamics is the Gibbs free energy defined in (A.68). In the case of $\boldsymbol{S}_0 = 0$ we can write it in terms of only the dynamical variables

in (A.69):

$$\mathcal{G} = \sum_{a=1}^{N} \frac{m_a(\underline{\underline{h}}\dot{\boldsymbol{s}}_a)^2}{2} + U + P_{\text{ext}}V + \frac{3NT_{\text{ext}}}{2}\left(\frac{\dot{z}^2}{v_T^2} + \frac{\text{tr}\left[(\dot{\underline{\underline{h}}}\underline{\underline{h}}^{-1})^{\text{T}}(\dot{\underline{\underline{h}}}\underline{\underline{h}}^{-1})\right]}{3v_P^2}\right) + 3NT_{\text{ext}}z \tag{A.70}$$

A.4 Property Evaluation

From MD simulations one have the full phase space trajactory of the system. Thus a great varieties of properties can be calculated for the system. Some can be directly compared with experimental measurements as verifications, others can serve as predictions or easy substitute for complicated experiments, but the most important ones are those inaccessible by the experiments, these are the unique contributions of MD simulations.

Below is a brief list of the useful properties to MD simulation:

General Properties

- **Mean Square Displacement**

$$\langle r^2 \rangle = \frac{1}{N}\sum_{a=1}^{N}\left[\boldsymbol{r}_a(t) - \boldsymbol{r}_a(0)\right]^2 \tag{A.71}$$

- **Radial Distribution Function**

$$g(r) = \frac{V}{N}\left[\frac{\Delta n(r)}{4\pi r^2 \Delta r}\right] \tag{A.72}$$

The radial distribution function $g(r)$ is normalized such that

$$\lim_{r\to\infty} g(r) = 1 \tag{A.73}$$

- **Heat Capacity**

It can be shown (for details see [6]) that in a microcanonical ensemble, the isometric heat capacity can be expressed using fluctuation formulation

$$\frac{C_v}{N} = \left[N - \left(N - \frac{2}{3} \right) \langle K \rangle \left\langle K^{-1} \right\rangle \right]^{-1} \tag{A.74}$$

In another study, the fluctuation formula of C_v is derived by Lebowitz *et al.*[147]

$$\frac{C_v}{N} = \frac{3}{2} \left[1 - \frac{2}{3NT^2} \left\langle (\Delta K)^2 \right\rangle \right]^{-1} \tag{A.75}$$

Both formulae applys to microcanonical ensemble simulations.

Elastic Constants

From Ray *et al.*[148], we have the fluctuation formulation for adaibatic elastic constant C_{ijkl}

$$C_{ijkl} = -\frac{V}{T} \langle (\Delta \tau_{ij})(\Delta \tau_{kl}) \rangle + \frac{2NT}{V} (\delta_{il}\delta_{jk} + \delta_{ik}\delta_{jl}) + \frac{1}{V} \left\langle \sum_{b>a}^{N} f(r_{ab}) r_{abi} r_{abj} r_{abk} r_{abl} \right\rangle \tag{A.76}$$

where $f(r)$ is defined as

$$f(r) \equiv \frac{1}{r^2} \left(\frac{\partial^2 U(r)}{\partial r^2} - \frac{1}{r} \frac{\partial U(r)}{\partial r} \right) \tag{A.77}$$

Thermal Conductivity

A.5 Notations and Units

Throughout the book, scalars are represented by normal italic letters, such as T, r, ξ. Vectors are bold italic letters, like $\boldsymbol{r}$, $\boldsymbol{J}$ and second order tensors (*i.e.* 3×3 matrices) are bold italic letters with double underlines: $\underline{\underline{h}}$, $\underline{\underline{\tau}}$. To avoid confusion, different subscript systems are used to separate different meanings, a, b, ...are indices of atoms, usually within simulation cell or unit cell, i, j *etc.* are used for Cartesian

indices, takes value 1, 2 or 3 in three dimensional systems.

Here is a list of symbols used in the book:

$\underline{\underline{h}}$, $\underline{\underline{g}}$	real and reciprocal space frame matrix ($\underline{\underline{g}}^{\mathrm{T}} = 2\pi\underline{\underline{h}}^{-1}$)
$\boldsymbol{r}_a$, $\boldsymbol{s}_a$	real coordinate and internal coordinate ($\boldsymbol{r}_a = \underline{\underline{h}}\boldsymbol{s}_a$)
$\boldsymbol{k}_a$, $\boldsymbol{q}_a$	reciprocal coordinate and internal coordinate ($\boldsymbol{k}_a = \underline{\underline{g}}\boldsymbol{q}_a$)
$\boldsymbol{R}$, $\boldsymbol{K}$	lattice vectors of real and reciprocal space (see (A.2) and (A.10)
N, V	number of atoms, volume ($V = det(\underline{\underline{h}})$)
E, U, K	total, configurational and kinetic energy ($E = U + K$)
e_a, m_a, $\boldsymbol{p}_a$	charge, mass, position and momentum of atom a
$\boldsymbol{r}_{ab}$	distance between atom a and b ($\boldsymbol{r}_{ab} = \boldsymbol{r}_a - \boldsymbol{r}_b$)

The default atomic units are chosen as electron volts for energy[eV], angstroms for length[Å] and atomic mass units for mass[u]. The temperature is taken to have the same unit as energy, the Bolzmann constant k_{B} is ignored in all formulae.

Appendix B

A Programmer's View of MD Simulation

So far we have only talked about physics and formulations of MD simulation. The underlying theories and approximations of MD simulations are indeed vitally important, but people involving in the business often forget about the importance of programming. It is true that most common tasks can be done with available programs such as Moldy(cite). But being a researcher, the ability to do uncommon tasks and test different ideas is indespensible. In the old time, the algorithms are simple, the programs are written in FORTRAN and easy to understand and modify. More and more, the algorithms are getting complicated, as the ones we present earlier, and formulations are harder to incorporate into old FORTRAN codes. What's more, with the new multi-processor supercomputers available, the parallel computing is a very realistic problem to most researchers. Ignoring the importance of programming is a fatal error in researcher's career.

This chapter we want to look at MD simulation with a programmer's view and briefly discuss the make of a MD program. It is not recommended that everyeone write his own program, but knowing how to write an MD program will definitely help in choosing, using, understanding and improving any existing MD program.

B.1 Components of an MD simulation

The idea of MD simulation if quite simple, it is just solving a many body Newton's equation of motion:

$$m_n \frac{\mathrm{d}^2 \boldsymbol{r}_n}{\mathrm{d}t^2} = \frac{\partial U(\{\boldsymbol{r}_n\})}{\partial \boldsymbol{r}_n} \; (n = 1, 2.., N) \tag{B.1}$$

Obviously, one needs to record the position and velocity of each atom, $\{\boldsymbol{r}_n\}$ and $\{\boldsymbol{v}_n\}$. One needs to evaluate the interaction between atoms, i.e. the r.h.s of (B.1). In order to effectively evaluate the forces on each atoms, because most interaction potential are of short range, a **neighbor list** algorithm is used. Using neighbor list, one can evaluate the acceleration of each atom. In the course of evaluating accelerations, one usually evaluate various different properties too. The conserved quantity, usually total energy of the system, should be evaluated to verify the whose simulation. Other properties including the temperature, the system pressure, the mean square displacement are among the usually choosen properties to evaluate, because they are very easily got and gives important indications to the system as it evolves through time. In mature MD simulation program, the **propertie evaluation** is usually configurable.

In order to know the time evolution of the system, the position and velocity as a function of time has to be discretized into segments. It is usually done by choosing a small time unit called *time step*, and the properties as function of time are discretized uniformly by the *time step*. If the descretization is not done uniformly, one calls it a *varying time step scheme*. The *varying time step scheme* can be used if the system is inhomogeneous in time. A typical case of the usage is simulation of hard spheres, where two atom comes into interaction only when the distance is less than the sum of their radii. Actually in hard sphere simulations the time progress by the collision events. For the purpose of this chapter, we always assume the time evolution is slice into equal timesteps. Many different **numerical integration** algorithms can be used to evolve the equation of motion (B.1). As we described earlier, the Gear's[36] predictor-corrector is a favorite choice for MD simulation.

So far we have described all the key components of a MD simulation program, below is a brief summary:

- **Neighbor List**: Listing all the possible neighbors of each atom, used to facilitate the interaction evaluation

- **Propertiy Evaluator**: Evaluate interaction forces and various other properties of the system.

- **Numerical Integrator**: Integrate the Newton's equation of motion.

Besides the main MD program, some utilities are also desireable. These include visualization tools, configuration manipulation tools, property calculation tools etc.

B.2 Parallelized MD

Due to the different architecture of parallel computers, there are several ways of doing parallel computing. Below briefly summerized three ways of doing parallelization:

- **Shared Memory Parallelization**: In the shared memory multi-processor computers, all the processors can read/write from the same globalized memory. By copying the common informations to a public shared memory block, all the processes can work on the same data. This scheme takes advantage of the hardware and ensues least overhead of parallel computing. In this schemem, different locking/signaling mechanisms must be deployed to maintain data consistancy, e.g. prevent two preocessor writing same data at same time.

- **Message Passing Parallelization**: In the clustered multi-processor computers, each processor has its own local memory, and information are passed between processors by some data channel. In these kinds of computers, parallelization are implemented by passing relavent data as "messages" from one processor to another, e.g. scattering the data before computation, and gather the results after. The overhead of copying the information could be fairly large, and the difficulty in implementation also hinders the creation and maintenance of the program. Nevertheless, because this scheme is suitable in many different situations and take advantage of almost all kinds of systems, it is quite popular.

There are several standard for this kind of parallelization, notably, the MPI[149] and PVM[150]

In this section, the discussion will focus on the first type of paralleliation, and comparisons with the second type are given from time to time.

When running MD program in parallel, with M processors, parallelization of most of the components of MD simulation can be done intuitively, but cares must be taken to make sure all the processes run synchronized with as little blocking as possible. Writing to shared information such as neighbor lists must be protected from overlapping with each other. In this section all the parallelization techniques are briefly described.

The most used operation is `synchronize`, which means block until every process arrives this point and then proceed together.

There are more than one way to implement `synchronize`, in order to accommodate various operations that implied `synchronize`, a two step approach is adopted. As shown in Fig. B-1, one of the processor is designated as "master", and all others as "slave". In the first step slaves are blocked until master gives permission to proceed. In the second step the master is blocked until every slave gives permission to proceed.[1]

In the two step implementation of `synchronize`, shown in Fig. B-1, there are two event slots, `event1` is for master processor to prepare before any slave processor, `event2` is for slave processors to do tasks before synchronization is finished. Putting different operations in the two slots allows different synchronized task to be performed.

[1]Those steps are implemented by atomic operations of `semaphores`, which are inherent parts of any multi-processor operating system.

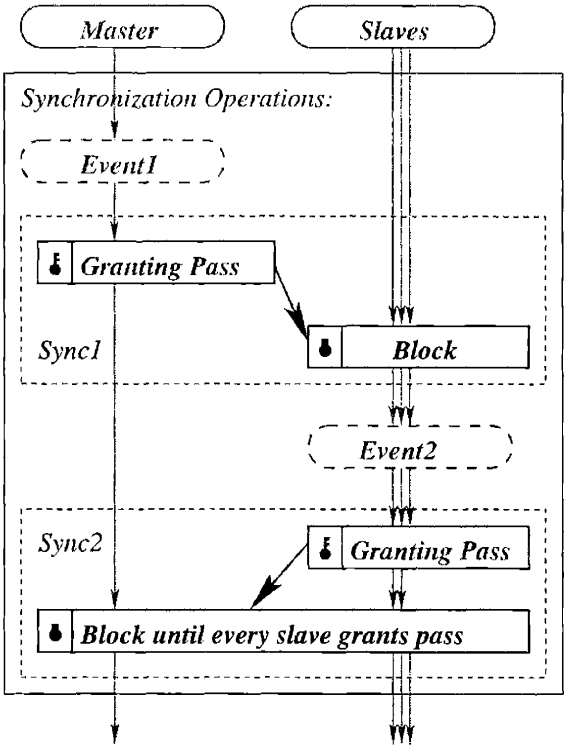

Figure B-1: Block diagram showing the two step approach to implement the `synchronize` operation.

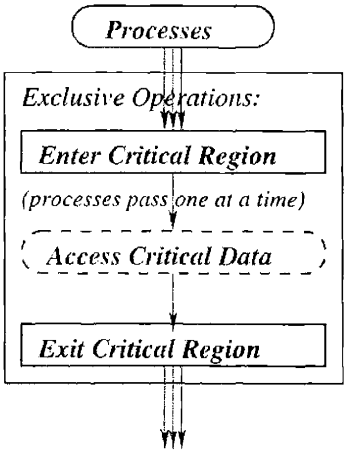

Figure B-2: Block diagram showing exclusive operations used to access critical resources.

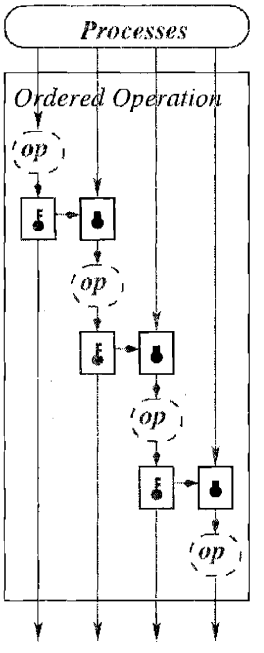

Figure B-3: Block diagram showing ordered operations used to access resources sequencially according to process number.

Bibliography

[1] W. D. Kingery, H. K. Bowen, and D. R. Uhlmann. *Introduction to Ceramics* (John Wiley and Sons, 1976), 2nd edition.

[2] A. Kelly and N. H. Macmillan. *Strong Solids* (Clarendon Press, 1986), 3rd edition.

[3] F. F. Abraham. "Computational statistical mechanics: Methodology, applications and supercomputing." *Advances in Physics* **35**(1), 1–111 (1986).

[4] S. Yip. "Atomistic simulations in material science." In G. Ciccotti and W. G. Hoover, editors, "Molecular Dynamics Simulation of Statistical Mechanical systems," pages 523–561 (1986).

[5] M. P. Allen and D. J. Tildesley. *Computer Simulation of Liquids* (Oxford Science Publications, 1987).

[6] J. M. Haile. *Molecular Dynamics Simulation: Elementary Methods* (John Willey and Sons, Inc., 1997).

[7] B. W. H. van Beest, G. J. Kramer, and R. A. van Santen. "Force fields for silicas and aluminophosphates based on ab initio calculations." *Phys. Rev. Lett.* **64**(16), 1955 (1990).

[8] J. S. Tse and D. D. Klug. "The structure and dynamics of silica polymorphs using a tow-body effective potential model." *J. Chem. Phys.* **95**(12), 9176 (1991).

[9] J. S. Tse, D. D. Klug, Y. L. Page, and M. Bernasconi. "High-pressure four-coordinated structure of SiO_2." *Phys. Rev. B* **56**(17), 10878 (1997).

[10] J. Badro, J.-L. Barrat, and P. Gillet. "Numerical simulation of α-quartz under nonhydrostatic compression: Memory glass and five-coordinated crystalline phases." *Phys. Rev. Lett.* **76**(5), 772 (1996).

[11] M. S. Somayazulu, S. M. Sharma, and S. K. Sikka. "Structure of a new high pressure phase in α-quartz determined by molecular dynamics studies." *Phys. Rev. Lett.* **73**(1), 98 (1994).

[12] N. Binggeli, N. R. Keskar, and J. R. Chelikowsky. "Pressure-induced amorphization, elastic instability, and soft modes in α-quartz." *Phys. Rev. B* **49**(5), 3075 (1994).

[13] G. W. Watson and S. C. Parker. "Dynamical instabilities in α-quartz and α-berlinite: A mechanism for amorphization." *Phys. Rev. B* **52**(18), 13306 (1995).

[14] S. L. Chaplot and S. K. Sikka. "Molecular-dynamics simulation of shock-stress-induced amorphization of α-quartz." *Phys. Rev. B* **61**(17), 11205 (2000).

[15] L. E. McNeil and M. Grimsditch. "Pressure-amorphized SiO_2 α-quartz: An anisotropic amorphous solid." *Phys. Rev. Lett.* **68**(1), 83 (1992).

[16] E. Demiralp, T. Çağin, and W. A. Goddard III. "Morse stretch potential charge equilibrium force field for ceramics: application to the quartz-stishovite phase transition and to silica glass." *Phys. Rev. Lett.* **82**(8), 1708 (1999).

[17] J. Badro, P. Gillet, and J.-L. Barrat. "Melting and pressure induced amorphization of quartz." *Europhysics Letters* **42**(6), 643 (1998).

[18] K. Vollmayr, W. Kob, and K. Binder. "Cooling-rate effects in amorphous silica: A computer-simulation study." *Phys. Rev. B* **54**(22), 15808 (1996).

[19] J. Li. *Modeling Microstructural Effects on Deformation Resistance and Thermal Conductivity.* Ph.D. thesis, Massachusetts Institute of Technology (2000).

[20] J. Li, D. Liao, and S. Yip. "Many-body interatomic potential for zrc." (2001). To be published in *Phil. Mag. A.*

[21] J. Li, D. Liao, and S. Yip. "High temperature thermal conductivity of zrc_x: Vibrational or electronic." (2001). To be published in *Phys. Rev. B.*

[22] M. Born. "On the stability of crystal lattices." *Proc. Camb. Philos. Soc.* **36**, 160–172 (1940).

[23] J. Wang, J. Li, S. Yip, S. R. Phillpot, and D. Wolf. "Mechanical instabilities of homogeneous crystals." *Phys. Rev. B* **52**, 12627 (1995).

[24] J. Wang, S. Yip, S. R. Phillpot, and D. Wolf. "Crystal instabilities at finite strain." *Phys. Rev. Lett.* **71**(25), 4182 (1993).

[25] C. A. Arguello, D. L. Rousseau, and S. P. S. Porto. "First-order raman effect in wurtzite-type crystals." *Phys. Rev.* **181**(3), 1351–1363 (1969).

[26] D. Strauch and B. Dorner. "Lattice dynamics of α-quartz:I. Experiment." *J. Phys. Condens. Matter* **5**, 6149 (1993).

[27] B. Dorner, H. Grimm, and H. Rzany. "Phonon dispersion branches in α-quartz." *J. Phys. C: Solid State Physics* **13**, 6607 (1980).

[28] H. L. Chatelier. "Sur la dilatation du quartz." *C. R. Ac. Sci. Paris* **108**, 1046 (1889).

[29] G. Dolino. "The α-inc-β transitions of quartz: A century of research on displacive phase transitions." *Phase Transitions* **21**, 59 (1990).

[30] S. Tsuneyuki, H. Aoki, M. Tsukada, and Y. Matsui. "Molecular-dynamics study of the α to β structural phase transition of quartz." *Phys. Rev. Lett.* **64**(7), 776 (1990).

[31] E. K. H. Salje, A. Ridgewell, B. Güttler, B. Wruck, M. T. Dove, and G. Dolino. "On the displacive character of the phase transition in quartz: a hard-mode spectroscopy study." *J. Phys. Condens. Matter* **4**, 571 (1992).

[32] D. J. Bergman and B. I. Halperin. "Critical behavior of an Ising model on a cubic compressible lattice." *Phys. Rev. B* **13**(5), 2145 (1976).

[33] L. Verlet. "Computer experiments on classical fluids. I. Thermodynamical properties of Lennard-Jones molecules." *Phys. Rev.* **159**(1), 98 (1967).

[34] B. Quentrec and C. Brot. "New methods for searching for neighbours in molecular dynamics computations." *J. Comp. Phys.* **13**, 430 (1973).

[35] D. Fincham and B. J. Ralston. "Molecular dynamics simulation using the CRAY-1 vector processing computer." *Comput. Phys. Commun.* **23**, 127 (1981).

[36] C. W. Gear. *Numerical Initial Value Problems in Ordinary Differential Equations* (Prentice-Hall, Inc., 1971).

[37] J.-C. Doukhan and L. Trépied. "Plastic deformation of quartz single crystals." *Bull. Minéral.* **108**, 97–123 (1985).

[38] J. H. Simmons. "What is so exciting about non-linear viscous flow in glass, molecular dynamics simulations of brittle fracture and semiconductor-glass quantum composites." *J. Non-Cryst. Solids* **239**(1), 1 (1998).

[39] R. Ochoa, T. P. Swiler, and J. H. Simmons. "Molecular dynamics studies of brittle failure in silica: effect of thermal vibrations." *J. Non-Cryst. Solids* **128**, 57 (1991).

[40] A. A. Griffith. "The phenomena of rapture and flow in solid." *Phil. Trans. R. Soc.* **A221**, 163 (1920).

[41] T. L. Anderson. *Fracture mechanics: fundamentals and applications* (CRC Press, 1995), 2nd edition.

[42] M. Iwasa and T. Ueno. "Fracture toughness of quartz and sapphire single crystals at room temperature." *Zairyo* **30**(337), 1001–1004 (1981).

[43] C. Maerky, M.-O. Guillou, J. L. Henshall, and R. M. Hooper. "Indentation hardness and fracture toughness in single crystal $TiC_{0.96}$." *Mater. Sci. Eng.* **A209**, 329–336 (1996).

[44] R. J. Hemley, A. P. Jephcoat, H. K. Mao, L. C. Ming, and M. H. Manghnani. "Pressure-induced amorphization of crystalline silica." *Nature* **334**(6177), 52 (1988).

[45] K. J. Kingma, R. J. Hemley, H. kwang Mao, and D. R. Veblen. "New high-pressure transformation in α-quartz." *Phys. Rev. Lett.* **70**(25), 3927 (1993).

[46] D. W. Dean, R. M. Wentzcovitch, N. Keskar, and J. R. Chelikowsky. "Pressure-induced amorphization in crystalline silica: soft phonon modes and shear instabilities in coesite." *Phys. Rev. B* **61**(5), 3303 (2000).

[47] N. L. Carter, J. M. Christie, and D. T. Griggs. "Experimental deformation and recrystallization of quartz." *J. Geol.* **72**, 687 (1964).

[48] J. M. Christie, H. C. Heard, and P. N. LaMori. "Experimental deformation of quartz single crystals at 27 to 30 kilobars confining pressure and 24°c." *Amer. J. Sci.* **262**, 26 (1964).

[49] R. D. Baëta and K. H. G. Ashbee. "Mechanical deformation of quartz. I. Constant strain-rate compression experiments." *Philos. Mag.* **22**(177), 601 (1970).

[50] B. E. Hobbs, A. C. McLaren, and M. S. Paterson. "Plasticity of single crystals of quartz." In H. C. Heard, I. Y. Borg, N. L. Carter, and C. B. Raleigh, editors, "Flow and Fracture of Rocks(The Griggs Volume)," volume 16 of *Geophysical Monograph Series*, page 29 (American Geophysical Union, 1972).

[51] F. A. McClintock and A. S. Argon. *Mechanical behavior of materials* (Addison-Wesley, Reading, Mass., 1966).

[52] B. A. Proctor, I. Whitney, and J. W. Johnson. "The strength of fused silica." *Proc. Roy. Soc. Lond.* **A297**, 534 (1967).

[53] J. G. Morley. "Strong fibres and fibre-reinforced metals." *Proc. Roy. Soc. Lond.* **A282**, 43 (1964).

[54] J. Schiøzt, F. D. di Tolla, and K. W. Jacobsen. "Softening of nanocrystalline metals at very small grain sizes." *Nature* **391**, 561 (1998).

[55] E. O. Hall. "The deformation and ageing of mild steel:III discussion of results." *Proc. Phys. Soc. Lond. B* **64**, 747–753 (1951).

[56] N. J. Petch. "The cleavage of polycrystals." *J. Iron Steel Inst.* **174**, 25–28 (1953).

[57] S. Yip. "The strongest size." *Nature* **391**, 532 (1998).

[58] A. Post and J. Tullis. "The rate of water penetration in experimentally deformed quartzite: implications for hydrolytic weakening." *Tectonophysics* **295**, 117 (1998).

[59] A. A. Chialvo and P. G. Debenedetti. "On the use of the verlet neighbor list in molecular dynamics." *Comput. Phys. Commun.* **60**, 215 (1990).

[60] R. W. Hockney, S. P. Goel, and J. W. Eastwood. "A 10000 particle molecular dynamics model with long range forces." *Chem. Phys. Lett.* **21**, 589 (1973).

[61] D. Fincham. "Optimization of the Ewald sum for large systems." *Molec. Simul.* **13**(1), 1 (1994).

[62] M. Parrinello and A. Rahman. "Polymorphic transitions in single crystals: A new molecular dynamics method." *J. Appl. Phys.* **52**(12), 7182 (1981).

[63] S. Blanes, F. Casas, and J. Ros. "Symplectic integratation with processing: A general study." *SIAM J. Sci. Comput.* **21**(2), 711–727 (1999).

[64] C. Schlier and A. Seiter. "Symplectic integration of classical trajectories: a case study." *J. Phys. Chem. A* **102**, 9399–9404 (1998).

[65] M. P. Calvo and J. M. Sanz-Serna. "High-order symplectic runge-kutta-nyström methods." *SIAM J. Sci. Comput.* **14**(5), 1237–1252 (1993).

[66] J. Koplik and J. R. Banavar. "Continuum deductions from molecular dynamics." *Annu. Rev. Fluid Mech.* **27**, 257 (1995).

[67] S. T. O'Connell and P. A. Thompson. "Molecular dynamics-continuum hybrid computations: A tool for studying complex fluid flows." *Phys. Rev. E* **52**(6), 5792 (1995).

[68] N. G. Hadjicostantinou. "Combining atomistic and continuum simulations of contact-line motion." *Phys. Rev. E* **59**(2), 2457 (1999).

[69] N. G. Hadjicostantinou. "Hybrid atomistic-continuum formulations and the moving contact-line problem." *J. Comp. Phys.* **154**(2), 245 (1999).

[70] B. F. Smith, P. E. Bjorstad, and W. D. Gropp. *Domain Decomposition: Parallel Multilevel Methods for Elliptic Partial Differential Equations* (Cambridge University Press, 1996).

[71] J. Li, D. Liao, and S. Yip. "Coupling continuum to molecular-dynamics simulation: Reflecting particle method and the field estimator." *Phys. Rev. E* **57**(6), 7259 (1998).

[72] A. L. Greensite. *Control Theory* (Spartan Books, 1970).

[73] P. A. Thompson and M. O. Robbins. "Shear flow near solids: Epitaxial order and flow boundary conditions." *Phys. Rev. A* **41**(12), 6830 (1990).

[74] E. B. Tadmor, M. Ortiz, and R. Phillips. "Quasicontinuum analysis of defects in solids." *Philos. Mag. A* **73**(6), 1529 (1996).

[75] W. Cai, M. de Koning, V. V. Bulatov, and S. Yip. "Minimizing boundary reflections in coupled-domain simulations." *Phys. Rev. Lett.* **85**(15), 3213 (2000).

[76] M. Born and K. Huang. *Dynamical Theory of Crystal Lattices* (Oxford University Press, 1962).

[77] S. W. de Leeuw, J. W. Perram, and E. R. Smith. "Simulation of electrostatic systems in periodic boundary conditions. I. Lattice sums and dielectric constants." *Proc. Roy. Soc. Lond.* **373A**, 27 (1980).

[78] S. W. de Leeuw, J. W. Perram, and E. R. Smith. "Simulation of electrostatic systems in periodic boundary conditions. II. Equivalence of boundary conditions." *Proc. Roy. Soc. Lond.* **373A**, 57 (1980).

[79] A. A. Maradudin, E. W. Montroll, G. H. Weiss, and I. P. Ipatova. *Theory of Lattice Dynamics in the Harmonic Approximation* (Academic Press, 1971).

[80] A. L. Fetter and J. D. Walecka. *Quantum Theory of Many-particle Systems* (McGraw Hill Book Company, 1990).

[81] S. Tsuneyuki, M. Tsukada, H. Aoki, and Y. Matsui. "First-principles interatomic potential of silica applied to molecular dynamics." *Phys. Rev. Lett.* **61**(7), 869 (1988).

[82] R. D. Baëta and K. H. G. Ashbee. "Slip systems in quartz: I. Experiments." *Amer. Mineral.* **54**, 1511–1573 (1969).

[83] R. D. Baëta and K. H. G. Ashbee. "Slip systems in quartz: II. Interpretation." *Amer. Mineral.* **54**, 1574–1582 (1969).

[84] R. W. G. Wyckoff. *Crystal Structures*, volume 1 (New York Interscience Publishers, 1963).

[85] G. Dolino and P. Bastie. "Phase transitions of quartz." *Key Engineering Materials* **101-102**, 285 (1995).

[86] G. Dolino, P. Bastie, B. Berge, M. Vallade, J. Bethke, L. P. Regnault, and C. M. E. Zeyen. "Stress-induced $< 3-q > - < 1-q >$ incommensurate phase transition in quartz." *Europhysics Letters* **3**(5), 601 (1987).

[87] T. A. Aslanyan, A. P. Levanyuk, M. Vallade, and J. Lajzerowicz. "Various possibilities for formation of incommensurate superstructure near the α-β transition in quartz." *J. Phys. C: Solid State Physics* **16**, 6705 (1983).

[88] P. Vashishta, R. K. Kalia, J. P. Rino, and I. Ebbsjö. "Interaction potential for SiO_2: A molecular-dynamics study of structural correlations." *Phys. Rev. B* **41**(17), 12197 (1990).

[89] S. Tsuneyuki, Y. Matsui, H. Aoki, and M. Tsukada. "New pressure-induced structural transformations in silica obtained by computer simulation." *Nature* **339**(6221), 209 (1989).

[90] E. de Vos Burchart, H. van Bekkum, and B. van de Graaf. "Molecular mechanics study on the α-quartz/β-quartz transition." *Journal of Chemical Society-Faraday Transactions* **88**(8), 1161 (1992).

[91] B. Silvi, P. D'arco, and M. Causà. "Periodic pseudopotential Hartree-Fock study of α-quartz tructure SiO_2 and geo_2." *J. Chem. Phys.* **93**(10), 7225 (1990).

[92] P. P. Ewald. "Die berechnung optischer und elektrostatischer gitterpotentiale." *Ann. Phys.(Leipzig)* **64**, 253 (1921).

[93] S. Melchionna and G. Ciccotti. "Hoover NPT dynamics for systems varying in shape and size." *Molec. Phys.* **78**(3), 533 (1993).

[94] J. P. Bachheimer and G. Dolino. "Measurement of the order parameter of α-quartz by second-harmonic generation of light." *Phys. Rev. B* **11**(8), 3195 (1975).

[95] J. S. Tse and D. D. Klug. "Mechanical instability of alpha -quartz: A molecular dynamics study." *Phys. Rev. Lett.* **67**(25), 3559 (1991).

[96] J. S. Tse and D. Klug. "Anisotropy in the structure of pressure-induced disordered solids." *Phys. Rev. Lett.* **70**(2), 174 (1993).

[97] V. V. Murashov. "Quartz family of silica polymorphs: comparative simulation study of quartz, moganite, and orthorhombic silica, and their phase transitions." *Phys. Rev. B* **57**(10), 5639 (1998).

[98] S. L. Chaplot and S. K. Sikka. "Molecular-dynamics simulation of pressure-induced crystalline-to-amorphous transition in some corner-linked polyhedral compounds." *Phys. Rev. B* **47**(10), 5710 (1993).

[99] N. Binggeli and J. R. Chelikowsky. "Elastic instability in α-quartz under pressure." *Phys. Rev. Lett.* **69**(15), 2220 (1992).

[100] Y. Uemura. "Atomistic model for the evaluation of the stability of diamond under uniaxial tensile force." *Phys. Rev. B* **49**(10), 6528 (1994).

[101] Y. Uemura. "Atomistic simulation of the behavior of diamond under compressive stress." *Phys. Rev. B* **51**(10), 6704 (1995).

[102] N. R. Keskar and J. R. Chelikowsky. "Theoretical predictions of negative poisson ratios in crystalline SiO_2." *Nature* **358**, 222 (1992).

[103] N. R. Keskar and J. R. Chelikowsky. "Anomalous elastic behavior in crystalline silica." *Phys. Rev. B* **48**(22), 16227 (1993).

[104] N. L. Carter, J. M. Christie, and D. T. Griggs. *J. Geophys. Res.* **66**, 2518 (1961).

[105] J. M. Christie, D. T. Griggs, and N. L. Carter. "Experimental evidence of basal slip in quartz." *J. Geol.* **72**, 734 (1964).

[106] B. E. Hobbs. "Recrystallization of single crystals of quartz." *Tectonophysics* **6**, 353 (1968).

[107] R. D. Baëta and K. H. G. Ashbee. "Mechanical deformation of quartz. II. Stress relaxation and thermal activation parameters." *Philos. Mag.* **22**(177), 625 (1970).

[108] J. S. Tse, D. D. Klug, and D. C. Allan. "Structure and stability of several high-pressure crystalline polymorphs of silica." *Phys. Rev. B* **51**(22), 16392 (1995).

[109] I. M. Svishchev, P. G. Kusalik, and V. V. Murashov. "Orthorhombic quartzlike polymorph of silica: A molecular-dynamics simulation study." *Phys. Rev. B* **55**(2), 721 (1997).

[110] S. Nosé. "A molecular dynamics method for simulations in the canonical ensemble." *Molec. Phys.* **52**(2), 255 (1984).

[111] W. G. Hoover. "Canonical dynamics: equilibrium phase-space distributions." *Phys. Rev. A* **31**(3), 1695 (1985).

[112] O. H. Wyatt and D. Dew-Hughes. *Metals Ceramics and Polymers* (Cambridge University Press, 1974).

[113] D. I. Grimley, A. C. Wright, and R. N. Sinclair. "Neutron scattering from vitreous silica IV. time-of-flight diffraction." *J. Non-Cryst. Solids* **119**, 49 (1990).

[114] J. H. Konnert and J. Karle. "The computation of radial distribution functions for glassy materials." *Acta Cryst.* **A29**, 702 (1973).

[115] M. W. Finnis and J. E. Sinclair. "A simple empirical N-body potential for transition metals." *Philos. Mag. A* **50**, 45 (1984).

[116] F. Willaime and C. Massobrio. "Temperature-induced hcp-bcc phase transformation in zirconium: A lattice and molecular-dynamics study based on an n-body potential." *Phys. Rev. Lett.* **63**(20), 2244 (1989).

[117] F. Willaime and C. Massobrio. "Development of an N-body interatomic potential for hcp and bcc zirconium." *Phys. Rev. B* **43**(14), 11653 (1991).

[118] T. B. Massalski, editor. *Binary Alloy Phase Diagrams* (ASM International, 1990), 2nd edition.

[119] J. C. Slater. "Atomic radii in crystals." *J. Chem. Phys.* **39**, 3199–3204 (1964).

[120] L. E. Toth. *Transition metal carbides and nitrides* (Academic Press, New York, 1971).

[121] W. S. Williams. "The thermal conductivity of metallic ceramics." *Journal of the Minerals Metals and Materials Society* **50**, 62–66 (1998).

[122] J. Li, L. J. Porter, and S. Yip. "Atomistic modeling of finite-temperature properties of crystalline β-SiC: II. Thermal conductivity and effects of point defects." *J. Nucl. Mater.* **255**, 139 (1998).

[123] J. P. Boon and S. Yip. *Molecular Hydrodynamics* (Dover, 1990).

[124] C. Kittel. *Introduction to solid state physics* (Wiley, 1996), 7th edition.

[125] Y. S. Touloukian, R. W. Powell, C. Y. Ho, and P. G. Klemens, editors. *Thermophysical Properties of Matter*, volume 2 (IFI/Plenum, 1970).

[126] J. F. Shackelford, W. Alexander, and J. S. Park, editors. *CRC Materials Science and Engineering Handbook* (CRC Press, 1994), 2nd edition.

[127] G. C. Sih, editor. *Methods of analysis and solutions of crack problems* (Noordhoff International Publishing, 1973).

[128] R. W. Siegel and G. E. Fougere. In G. C. Hadjipanayis and R. W. Siegel, editors, "Nanophase Materials: Synthesis–Properties–Applications," (Kluwer, Dordrecht, 1994).

[129] R. W. Siegel. "What do we really know about the atomic-scale structure of nanophase materials?" *J. Phys. Chem. Solids* **55**, 1097–1106 (1994).

[130] F. H. Streitz and J. W. Mintmire. "Molecular dynamics simulations of elastic response and tensile failure of alumina." *Langmuir* **12**(19), 4605 (1996).

[131] R. D. Oeffner and S. R. Elliott. "Interatomic potential for germanium dioxide empirically fitted to an ab initio energy surface." *Phys. Rev. B* **58**(22), 14791 (1998).

[132] L. J. Porter, J. Li, and S. Yip. "Atomistic modeling of finite-temperature properties of crystalline:I. Lattice vibrations, heat capacities and thermal expansion." *J. Nucl. Mater.* **246**, 53 (1997).

[133] W. Cai. *Atomistic and Mesoscale Modeling of Dislocation Mobility.* Ph.D. thesis, Massachusetts Institute of Technology (2000).

[134] W. R. Cannon and T. G. Langdon. "Review creep of ceramics." *J. Mater. Sci.* **18**, 1 (1983).

[135] J.-P. Poirier. *Creep of crystals* (Cambridge University Press, 1985).

[136] J. P. Poirier. "Plastic rheology of crystals." In T. J. Ahrens, editor, "Mineral Physics and Crystallography: A handbook of physical constants," pages 237–247 (American Geophysical Union, 1995).

[137] A. F. Voter. "Hyperdynamics: Accelerated molecular dynamics of infrequent events." *Phys. Rev. Lett.* **78**, 3908 (1997).

[138] A. F. Voter. "A method for accelerating the molecular dynamics simulation." *J. Chem. Phys.* **106**(11), 4665 (1997).

[139] J. E. Lennard-Jones. "The determination of molecular fields I. From the variation of the viscosity of a gas with temperature." *Proc. Roy. Soc. Lond.* **106A**, 441 (1924).

[140] J. E. Lennard-Jones. "The determination of molecular fields II. From the equation of state of a gas." *Proc. Roy. Soc. Lond.* **106A**, 463 (1924).

[141] F. H. Stillinger and T. A. Weber. "Computer simulation of local order in condensed phase of silicon." *Phys. Rev. B* **31**(8), 5262 (1985).

[142] S. Nosé. "A unified formulation of the constant temperature molecular dynamics methods." *J. Chem. Phys.* **81**(1), 511 (1984).

[143] S. Nosé. "An extension of the canonical ensemble molecular dynamics method." *Molec. Phys.* **57**(1), 187 (1986).

[144] W. G. Hoover. "Constant-pressure equations of motion." *Phys. Rev. A* **34**(3), 2499 (1986).

[145] M. Parrinello and A. Rahman. "Strain fluctuations and elastic constants." *J. Chem. Phys.* **76**(5), 2662 (1982).

[146] J. R. Ray and H. Zhang. "Correct microcanonical ensemble in molecular dynamics." *Phys. Rev. E* **59**(5), 4781 (1999).

[147] J. L. Lebowitz, J. K. Percus, and L. Verlet. "Ensemble dependence of fluctuations with application to machine computations." *Phys. Rev.* **153**, 250 (1967).

[148] J. R. Ray, M. C. Moody, and A. Rahman. "Molecular dynamics calculation of elastic constants for a crystalline system in equilibrium." *Phys. Rev. B* **32**(2), 733 (1985).

[149] W. Gropp, E. Lusk, and A. Skjellum. *Using MPI : Portable Parallel Programming With the Message-Passing Interface* (MIT Press, 1999), 2nd edition.

[150] A. Geist, A. Beguelin, J. Dongarra, W. Jiang, R. Manchek, and V. Sunderam. *PVM : Parallel Virtual Machine : A Users' Guide and Tutorial for Networked Parallel Computing* (MIT Press, 1994).

Thanks to the internet, the author can always be reached by email

`liaody@alum.mit.edu`

The errata and future developments of this thesis can be found at

`http://asm.mit.edu/~liaody/Research`